Interaction Notes

Note 339

August 1976

Selected Topics in EMP Interaction

C. M. Butler, D. R. Wilton
University of Mississippi
University, MS

K. F. Casey
Kansas State University
Manhattan, KS

S. K. Chang, F. M. Tesche, T. K. Liu
Science Applications, Inc.
Berkeley, CA

ABSTRACT

This report contains formulas and data pertinent to electromagnetic pulse (EMP) penetration through: (1) apertures, (2) cable shields, (3) connectors, and (4) skin panels.

PREFACE

During the course of preparing the manuscript, many helpful suggestions were received from the following persons, to whom the authors are greatly in debt: Drs. C.E. Baum, J.P. Castillo, and K.C. Chen of the Air Force Weapons Laboratory, and Dr. K.S.H. Lee of Dikewood Industries, Inc.

Considerable revisions have been made by the Air Force and Dikewood technical staff to achieve the objectives of the report.

CONTENTS

CHAPTER I
INTRODUCTION

A. Objective

Energy associated with electromagnetic pulse (EMP) can penetrate into a structure (such as an aircraft, a missile, a cable, etc.) by one of the following processes:

(a) Penetration through apertures. The apertures are usually in the wall (or skin) of the structure and may be deliberate such as in the cases of windows, wheel bays, etc., or they may be inadvertent such as in the cases of cracks around doors, seams between panels or imperfections of the walls.

(b) Penetration through walls by diffusion. Since the walls are at best conductors with very high, but finite, conductivity, electromagnetic energy can penetrate the walls by the process of diffusion (skin effect). Although generally this process is dominated by the other two processes of penetration, it is severe at very low frequencies when the walls offer virtually no shielding of the magnetic field.

(c) Penetration through deliberate antennas. Overall, this process may pick up most electromagnetic energy since the antennas are designed for that purpose. Usually the narrowband nature of, and the lightning protection mechanisms associated with most antennas somewhat reduce the EMP penetration into the structure.

There are a large number of papers in the open literature and reports in various organizations dealing with the problem of electromagnetic field penetration. In this report, useful information selected from these sources is presented with the following conditions:

(a) Only the first two processes listed above are included. This means that the penetration through apertures and penetration by diffusion are considered.

(b) The materials presented are relevant to EMP problems. This means that much information included is for low frequencies when the typical dimensions of the structure are small compared with the wavelength.

(c) The materials presented are readily usable without requiring the use of computers or complicated mathematical methods of solution. Thus, as far as possible, information is presented in graphical form, tabular form, or as simple formulas involving only elementary mathematical functions. Care has been exercised to avoid the presentation of the results in unsolved integral equations or differential equations which require computers for their solution. Results involving complicated series or complicated mathematical functions are also avoided when possible.

The vast majority of results available in the literature is in the frequency domain. Although EMP is a transient phenomenon, the use of frequency domain results has its values. Once the spectrum of the system frequency response is known, the time domain response due to a particular excitation waveform can be found by taking the inverse Fourier transform of the product of the frequency spectra of the system response and the excitation waveform. Throughout this report most results presented are in the frequency domain. However, when possible, the time responses of some particular excitation waveforms are presented.

Most of the problems presented in this report involve the penetration of plane waves into the structure.

B. Organization of the Report

The materials are divided into four major topics. They are: apertures, cable shields, connectors and skin panels.

In Chapter II, the subject of penetration through apertures is discussed. The chapter includes topics on small apertures, slots, apertures on parallel plates, wires behind apertures, large apertures and cavity-backed apertures. Most of the configurations involve apertures on an infinitely large planar conductor. However, non-planar geometries are also studied in the cases of cavity-backed apertures.

The subject of cable shields has been studied for some time. It is important to limit the amount of electromagnetic energy induced in the shielded conductors of a cable so that the instrument circuits at the ends of the cable are protected from the induced energy. The cable shields may contain apertures such as in the cases of braided shields, tape-wound shields. Energy may also penetrate through the shields by diffusion. The problem of penetration through cable shields is presented in Chapter III.

In Chapter IV, penetrations through coaxial connectors are discussed. Due to the uncertainty in the physical descriptions of the imperfection on connectors, very limited amounts of theoretical work have been done. Results presented in Chapter IV are mostly experimental and qualitative.

Finally, in Chapter V, penetrations through skin panels by diffusion are presented. Most of the results are for the cases of thin-walled shields which have small wall thickness when compared with the characteristic dimensions of the structures. In this chapter, results are presented in the form of simple formulas which are valid at low frequencies.

C. Units and Notations

All electrical units are presented in MKSA units. However, due to the popular usage of British units in some non-electrical work, limited quantities are in the latter units. Specifically, some panels' thickness are in inches since they are available in 1/16", 1/8", etc.

When presenting results in the time-harmonic forms (frequency domain), the time variation $\exp(j\omega t)$ is used, where $j = \sqrt{-1}$, ω is the radian frequency and t is the time variable. Sometimes the more general time factor $\exp(st)$ is used where s is the complex frequency.

Since each chapter is reasonably independent, the symbols are consistently used within chapters. However, there may be some variation between chapters. For example, in Chapter III, γ is used to denote the complex propagation constant, whereas k is used in Chapter V.

General References

"Electromagnetic pulse handbook for missiles and aircraft in flight EMP Interaction 1-1," AFWL TR-73-68, September 1972.

"State-of-the-art review on apertures/cable shields/connectors/skin panels," AFWL, August 1976.

"EMP engineering and design principles," Bell Laboratories, Whippany, New Jersey, 1975.

CHAPTER II
APERTURE PENETRATION

A. Introduction

In designing hardened systems, one must be able to characterize and quantitatively determine the penetration of EMP signals through apertures of general shapes in structures of varying configurations. In this chapter a tutorial overview is given of electromagnetic penetration through apertures in conducting surfaces. The emphasis of this chapter is upon simplicity and it is intended to be informative rather than theoretical.

Apertures of interest here are in the outer, conducting skins of aircraft and missiles, among other units of interest to the EMP community, and usually they are electromagnetically small over the spectrum of the EMP. Furthermore, their existence may be intentional, e.g., windows, open access holes, and bombay doors, or they may be inadvertent as in the case of cracks around doors and plates covering access ports or poor electrical seams in outer skins. Obviously, harmful internal currents can be determined and avoided only if EMP penetration through apertures in outer skins is understood and can be computed.

Even though the classic problem of penetration of time-harmonic electromagnetic fields through an aperture in a planar conducting screen of infinite extent has been the subject of intensive research for many years, still the body of theory pertaining to this simplest of aperture problems remains a rather complicated subject, and only in the case of scalar diffraction by a circular aperture are analytical results available in the three dimensional problem. Greater progress has been achieved for small apertures in planar screens, where, in this context, small means that the maximum dimension across the aperture is small relative to the wavelength of the time-harmonic electromagnetic field, as well as in the two-dimensional problem of diffraction by an infinite slot of uniform width. For apertures in nonplanar surfaces, far less progress has been made. Fortunately, for many problems of practical interest, the introduction of an infinite, planar screen in place of a finite one, or one with gradual curvature relative to aperture size and, in some cases, wavelength, does

not seriously degrade accuracy of the solution of a problem.

Due to its importance in EMP studies, appropriate attention is given in the following sections to the electrically small aperture and to the determination of penetration through such small holes. Bethe's equivalent dipole moment representation of an aperture is reviewed and its use to compute penetration is outlined. Copious data are presented, illustrating penetration through small apertures. Infinite slots of uniform width approximate reasonably well certain practical situations, so this two-dimensional problem is treated briefly. The important, finite-length, narrow slot is mentioned and data are given in a form which shows the behavior of the electric field behind a slot in a conducting skin. Next a discussion is provided of the problem of penetration into the region between two parallel plates through a hole in one plate. A small elliptic hole as well as a slot is considered and data are presented for both. Turning to a problem of great significance in EMP, the authors characterize the behavior of current induced on a wire behind a screen by excitation which passes through a hole in the screen. Also, with the wire viewed as a transmission line, an equivalent circuit representation of the problem is presented. Selected results are provided for penetration through large apertures and apertures in nonplanar surfaces. The penetration into closed regions is of interest in EMP and, thus, data available in the literature are given for this situation usually classified as a cavity-backed aperture problem.

Ultimate interest in EMP investigations lies, of course, in the time history of the electromagnetic field at critical points in a system under evaluation. Usually such a time history is computed (via Fourier inversion) from knowledge of the corresponding time-harmonic field over a frequency spectrum of practical limits. For this reason and, also, due to the insight gained therefrom, it is of value to become familiar with available information in the frequency domain. In addition, when one has time-domain results (probably measured) for a problem under study, he can Fourier transform his data and compare with frequency-domain results provided here or elsewhere. Such provides a good check on the accuracy of the time-domain information. Due to the paucity of time-domain data available in the present state of knowledge, one must glean whatever he can from the frequency domain.

B. Small Apertures

B.1 Introduction

In many EMP-related applications, apertures of interest are electromagnetically small, a property which leads to very helpful simplifications in computations. Small used here is taken to mean that the maximum dimension across the aperture is short relative to the wavelength of the electromagnetic wave and that the radii of curvature of the conducting surface near the aperture are large compared to this wavelength. In the case of a (transient) EMP signal, the wavelength in question is the smallest of significance in the spectrum of the signal.

Diffraction by small circular and elliptic apertures has been investigated by numerous workers employing a wide variety of different approaches. Lord Rayleigh (Ref. 2.1) proposed a solution in the form of a series in ascending powers of the wavenumber k ($= 2\pi/\lambda$) where λ is the wavelength. Bethe (Ref. 2.2) obtained results for the leading terms in the series expansion by means of a scalar potential approach. Later, Bouwkamp (Ref. 2.3) investigated the same problem using a more complete set of coupled integro-differential equations and pointed out errors in Bethe's solution. A comprehensive review of articles pertaining to aperture diffraction in general is given in Ref. 2.4, and an extensive bibliography is accumulated in Ref. 2.5. The low frequency scalar diffraction problem also has been analyzed by Van Bladel (Ref. 2.6). Rahmat-Samii and Mittra (Ref. 2.7) have solved the aperture problem for a small circular hole, and, recently, numerical solution techniques have been advanced with the goal of attacking nonseparable geometries, e.g., rectangular apertures (Refs. 2.8-2.12).

One can demonstrate that the electromagnetic field which penetrates a small hole in a conducting surface can be represented approximately by the radiation from equivalent electric and magnetic dipoles plus a linear magnetic quadrupole. These point sources are located on the shadow side of the shorted aperture; that is, the conducting screen is made continuous. If the hole is very small and the point of observation is distant from it relative to the hole's maximum dimension, then this equivalence provides a good approximation. Usually the quadrupole

contribution is negligibly small and it is most convenient to locate the equivalent sources at the geometric "center" of the shorted aperture. This equivalent problem is illustrated in Fig. 2.1, where one sees the original excitation ($\bar{E}^i$, $\bar{H}^i$) plus the equivalent magnetic and electric dipoles located on the continuous conducting surface at a point originally in the aperture (unshorted).

Bethe (Ref. 2.2) has shown that the equivalent dipole moments of a given small aperture in a screen are related to the specified excitation by the so-called aperture polarizabilities (Refs. 2.2, 2.11, 2.13-2.16). Knowing the polarizabilities for an aperture and the illumination of the perforated screen, one can determine dipole moments and, subsequently, the diffraction caused by the presence of a small aperture in the screen. For a small aperture A in a planar conducting screen of infinite extent (Fig. 2.2), the electric polarizability α_e is defined by

$$p = \varepsilon \alpha_e \; E_z^{sc}(\bar{0}-) \tag{2.1}$$

and the components, $\alpha_{m,xx}$ and $\alpha_{m,yy}$, of the magnetic polarizability are defined by

$$m_x = - \alpha_{m,xx} \; H_x^{sc}(\bar{0}-) \tag{2.2a}$$

$$m_y = - \alpha_{m,yy} \; H_y^{sc}(\bar{0}-) \tag{2.2b}$$

In Eqs. 2.1 and 2.2, ($\bar{E}^{sc}$, $\bar{H}^{sc}$) is the total field which exists on the shorted conducting surface at the point (0,0,0-) (illuminated side). $p\hat{z}$ and $\bar{m}$ are the moments of the equivalent electric and magnetic dipoles, respectively; these dipoles are located on the shadow side of the shorted surface at (0,0,0+).

We point out that, at the surface of a perfect conductor, only a normal component of electric field can exist and only tangential components of magnetic field exist. Of course, the normal electric field is related to the surface charge density σ and the tangential magnetic

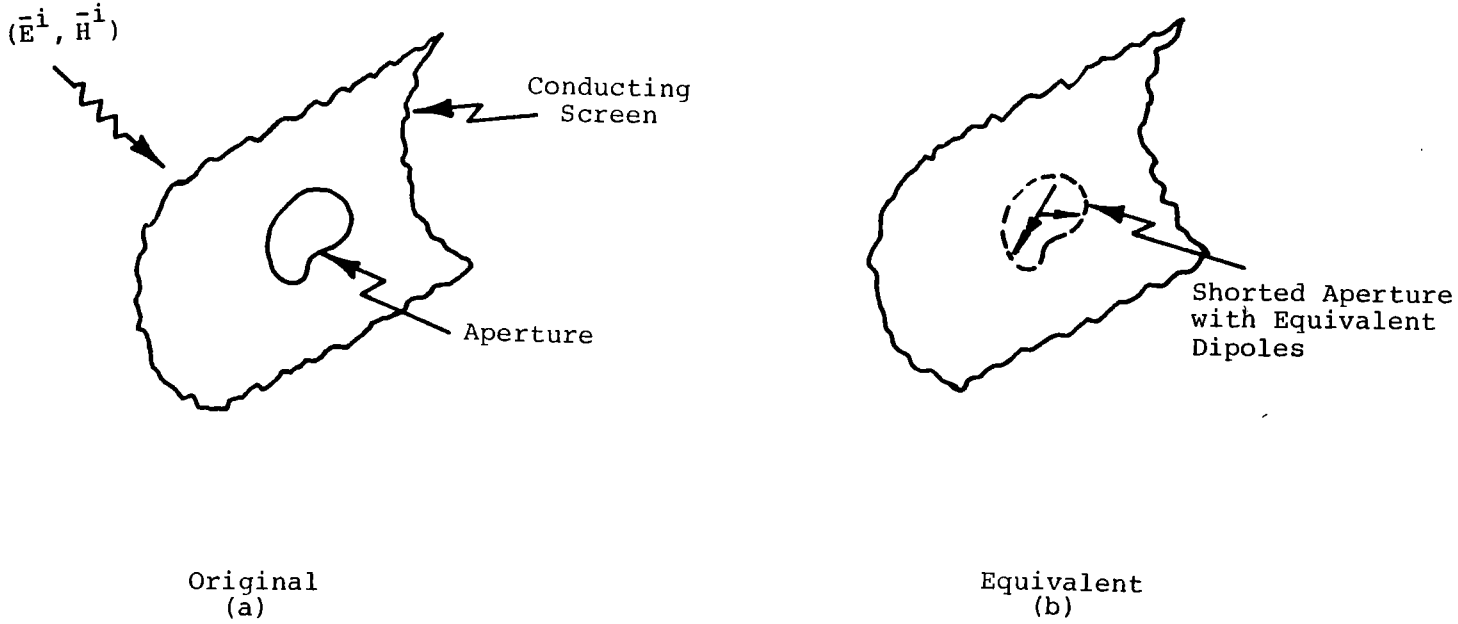

Fig. 2.1. (a) Section of Conducting Surface with Aperture.
(b) Shorted Aperture with Equivalent Dipoles on Shadow Side of Surface.

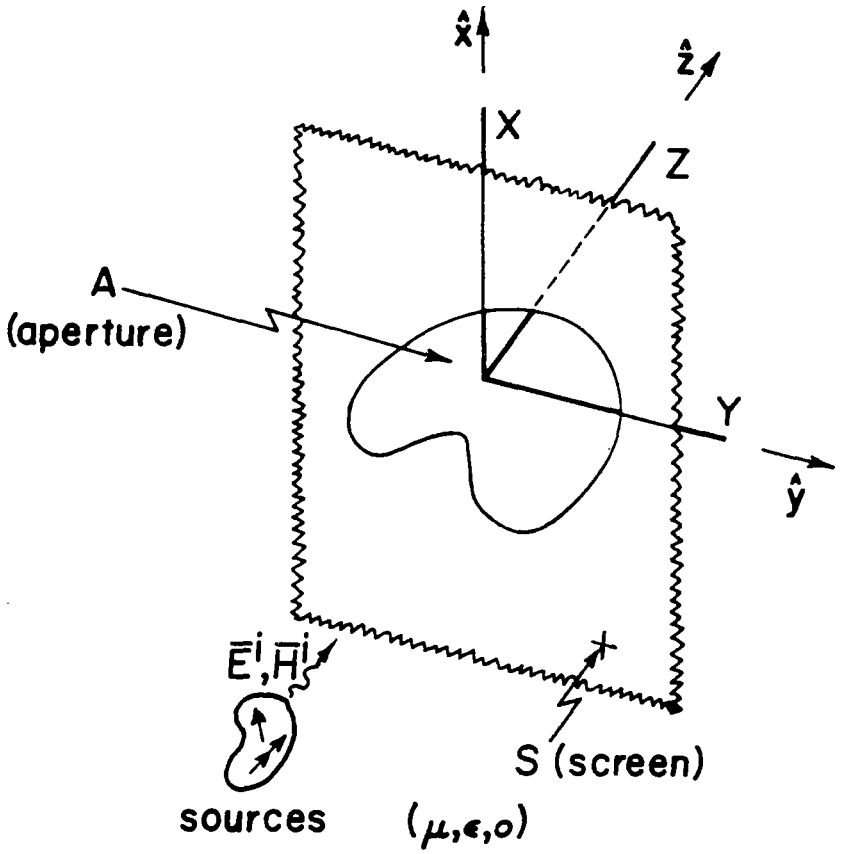

Fig. 2.2. Aperture in Planar Conducting Screen of Infinite Extent.

field is related to the surface current density $\bar{K}$. If $\hat{n}$ is the outward normal at a point $\bar{r}$ on the surface, then

$$\varepsilon E_n^{sc}(\bar{r}) = \sigma(\bar{r}) \tag{2.3a}$$

and

$$\hat{n} \times \bar{H}^{sc}(\bar{r}) = \bar{K}(\bar{r}) \tag{2.3b}$$

If, in addition, the conducting surface is planar and of infinite extent, the incident field and short-circuit field are simply related at the conducting surface:

$$E_n^{sc} = 2 E_n^i \tag{2.4a}$$

and

$$\bar{H}^{sc} \times \hat{n} = 2 \bar{H}^i \times \hat{n} \tag{2.4b}$$

For a small aperture in a planar conducting surface of infinite extent, polarizabilities are available in the literature for several aperture shapes. An important example is the small circular hole for which

$$\alpha_e = \frac{1}{12} D^3 \tag{2.5a}$$

and

$$\alpha_{m,xx} = \alpha_{m,yy} = \frac{1}{6} D^3 \tag{2.5b}$$

where D is the diameter of the circle. For an electrically small ellipse whose length ℓ is much greater than its width w, the polarizability components are ($w << \ell$)

$$\alpha_e = \frac{\pi}{24} w^2 \ell \tag{2.6a}$$

$$\alpha_{m,xx} = \frac{\pi}{24} \frac{\ell^3}{\left[\ell n\left(\frac{4\ell}{w}\right) - 1\right]} \tag{2.6b}$$

$$\alpha_{m,yy} = \frac{\pi}{24} w^2 \ell \tag{2.6c}$$

Polarizabilities for other apertures have been obtained by measurements and still others by various numerical techniques. A selection of polarizability values is presented below.

B.2 Dipole Moments and Polarizabilities

The electromagnetic field which is diffracted by a small aperture in a conducting surface can be approximated by the radiation from equivalent electric and magnetic dipoles. Due to the simplicity and utility of such an equivalence, a great amount of attention has been devoted to the problem of determining the moments of the dipoles. The diffracted field is, of course, dependent upon the excitation of the aperture/screen and upon the shape and size of the aperture. In the case of a planar conducting screen of infinite extent having an aperture whose maximum dimension is very small relative to the wavelength of the electromagnetic signal of interest, the moments of the equivalent dipoles are proportional to the components of the exciting field. These constants of proportionality, the electric and magnetic polarizabilities, are dependent only upon the shape and size of the aperture. In addition, whenever the aperture possesses one symmetry axis about an axis, only three constants are needed for computation of the dipole moments: one for the moment of the electric dipole and two for that of the magnetic dipole. Knowing the polarizabilities for an aperture and the illumination of the perforated screen, one can determine the equivalent dipole moments, and, subsequently, the distance diffracted field caused by the presence of a small aperture in the screen.

Below we discuss aperture polarizabilities and equivalent dipoles and

provide a collection of polarizability data for numerous aperture shapes.

For a small aperture A of a given size and shape in a planar, conducting screen of infinite extent, a section of which is depicted in Fig. 2.3a, the electric polarizability α_e is defined by Eq. 2.1 in which $p\hat{z}$ is the moment of the equivalent electric dipole located at the aperture (shorted) center on the shadow side of the screen (Fig. 2.3). We point out that only a normal component of electric field exists on the surface of the perfectly conducting screen with the aperture shorted; so, relative to the location of the planar screen in Fig. 2.3, $E_z^{sc}\hat{z}$ is the total electric field on the surface of the shorted screen. Also, the equivalent electric dipole is oriented perpendicular to the conducting plane and is located at $\bar{0}$ on the upper-side surface of the shorted screen.

The magnetic polarizability has two components, $\alpha_{m,xx}$ and $\alpha_{m,yy}$, defined by Eq. 2.2. The magnetic dipole $\bar{m} = m_x\hat{x} + m_y\hat{y}$ is located at (0,0,0+) on the shadow-side surface of the shorted screen and is parallel to the screen. The negative signs in Eq. 2.2 account for the fact that the equivalent magnetic dipole on the shadow side is in the direction opposite to that of $\bar{H}^{sc}(\bar{0}-)$.

In Fig. 2.3 we depict the original problem, the excitation, and the equivalent problem. The original problem is seen in Fig. 2.3a, while the illustration of Fig. 2.3b shows the aperture shorted with the short-circuit electric and magnetic fields, $E_z^{sc}(\bar{0}-)\hat{z}$ and $H_x^{sc}(\bar{0}-)\hat{x} + H_y^{sc}(\bar{0}-)\hat{y}$, at $\bar{0}$ on the under-side surface of the shorted screen. Fig. 2.3c shows the dipoles on the upper surface of the short screen, which forms the equivalent of the original problem. Radiation from these dipoles is computed by standard methods; they radiate in the presence of the screen and its effect must be included in any calculation of radiated field.

At the surface of a perfect conductor, only a normal component of electric field can exist and only tangential components of magnetic field exist. The normal electric field is related to the surface charge density and the tangential magnetic field is rleated to the surface current density as specified in Eq. 2.3, valid for a surface of any size and shape. If the conducting surface is planar and of infinite extent,

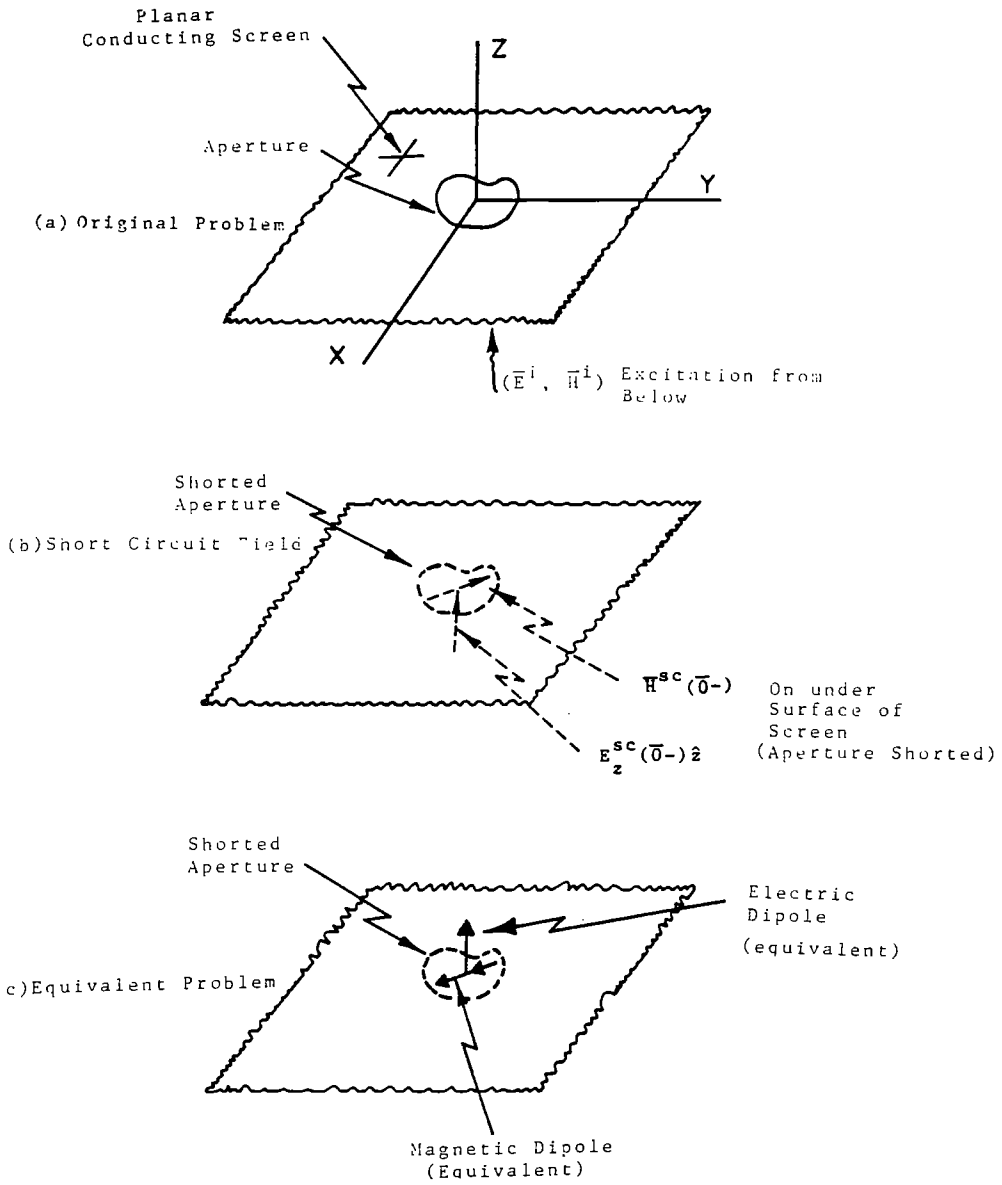

Fig. 2.3. Illustration of Aperture in a Screen, Short Circuit Fields, and Equivalent Problem.

the incident field and short-circuit field are simply related at the conducting surface by

$$E_z^{sc}(x,y,0-) = 2E_z^{i}(x,y,0-) \tag{2.7a}$$

and

$$\bar{H}^{sc}(x,y,0-) \times \hat{z} = 2\bar{H}^{i}(x,y,0-) \times \hat{z} \tag{2.7b}$$

From knowledge of the polarizabilities for a given small aperture, the moments of the equivalent dipoles are readily available, and from them one can compute the field which reaches the shadow side of the perforated surface. In the case of an infinite plane the shadow-side field is equivalent to that radiated by dipoles of moments $2\,p\hat{z}$ and $2\,\bar{m}$ located at $\bar{0}$ in a uniform space of infinite extent characterized by (μ,ε).

The polarizabilities for the circle, the ellipse, and the narrow slit can be computed theoretically and values for these shapes are available in the literature (Refs. 2.11, 2.15, 2.16). Formulas for the polarizabilities are presented in Table 2.1 for these shapes (Figs. 2.4a and 2.4b).

Cohn (Refs. 2.13, 2.14) has experimentally confirmed the expressions in Table 2.1 and has determined values for several other shapes. His data, together with values based upon Table 2.1 are presented in Figs. 2.5 through 2.8; Figs. 2.6 through 2.8 were taken from Ref. 2.17. Notice that the polarizabilities are normalized with respect to ℓ^3 which results in dimensionless quantities. As an aid to the reader, the direction for the short-circuit magnetic field for a given magnetic polarizability is indicated in the figures.

De Meulenaere and Van Bladel (Ref. 2.11) have computed by numerical methods the polarizabilities for a rectangle, a diamond, a cross, and a rounded-off rectangle, all of which are illustrated in Fig. 2.4. Their results have been compared with Cohn's experimental values and with the well-known values for the ellipse, and they find that their data are

TABLE 2.1

APERTURE POLARIZABILITIES*

Shape	α_e	$\alpha_{m,xx}$	$\alpha_{m,yy}$
Circle (D = Diameter)	$\frac{1}{12} D^3$	$\frac{1}{6} D^3$	$\frac{1}{6} D^3$
Ellipse+	$\frac{\pi}{24} \frac{w^2 \ell}{E(\epsilon)}$	$\frac{\pi}{24} \frac{\ell^3 \epsilon^2}{K(\epsilon) - E(\epsilon)}$	$\frac{\pi}{24} \frac{\ell^3 \epsilon^2}{\left(\frac{\ell}{w}\right)^2 E(\epsilon) - K(\epsilon)}$
Narrow Ellipse ($w << \ell$)	$\frac{\pi}{24} w^2 \ell$	$\frac{\pi}{24} \frac{\ell^3}{\ln\left(\frac{4\ell}{w}\right) - 1}$	$\frac{\pi}{24} w^2 \ell$
Narrow Slit‡ ($w << \ell$)	$\frac{\pi}{16} w^2 \ell$	no theoretical value	$\frac{\pi}{16} w^2 \ell$

*See Refs. 2.2, 2.15, 2.16.

+Ellipse Eccentricity $\epsilon = \sqrt{1 - \left(\frac{w}{\ell}\right)^2}$

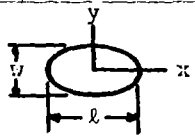

K and E are the complete elliptic integrals of the first and second kind, respectively:

$$K(\epsilon) = \int_{\phi=0}^{\pi/2} \frac{1}{\left[1 - \epsilon^2 \sin^2\phi\right]^{\frac{1}{2}}} d\phi \quad , \quad E(\epsilon) = \int_{\phi=0}^{\pi/2} \left[1 - \epsilon^2 \sin^2\phi\right]^{\frac{1}{2}} d\phi$$

‡Valid for $\tilde{H}^{sc}(0-)$ transverse to and constant along slit axis (See Fig. 2.4a).

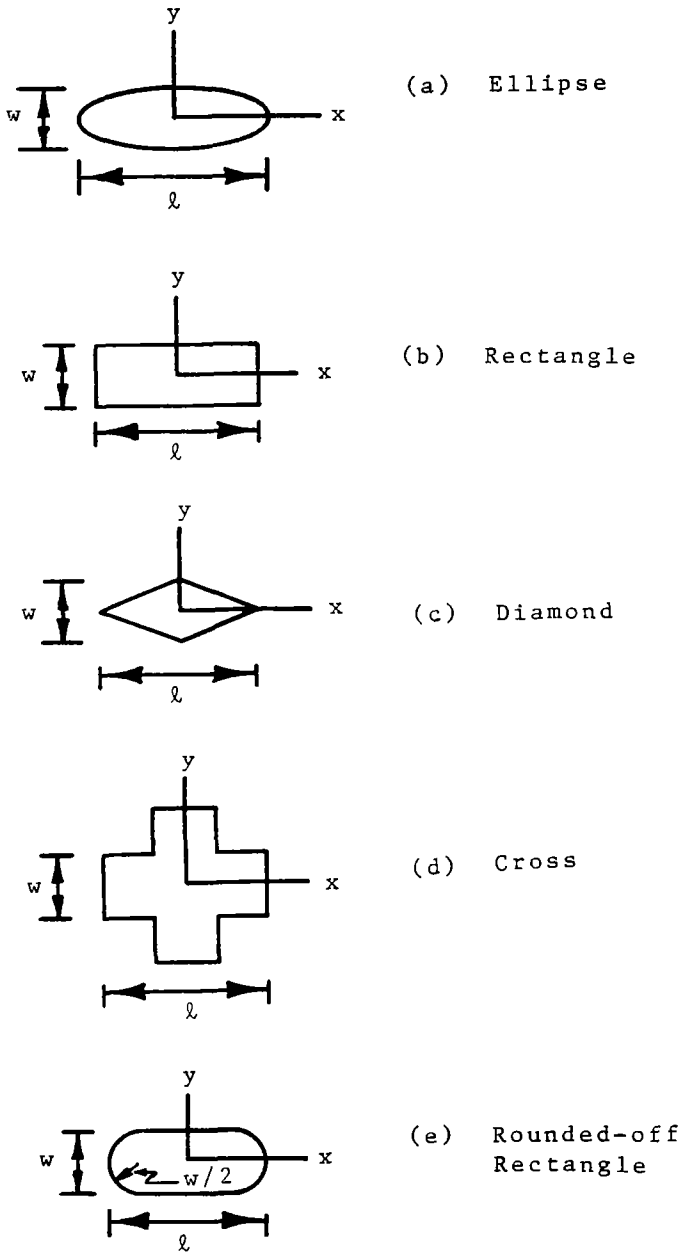

Fig. 2.4. Various Aperture Shapes.

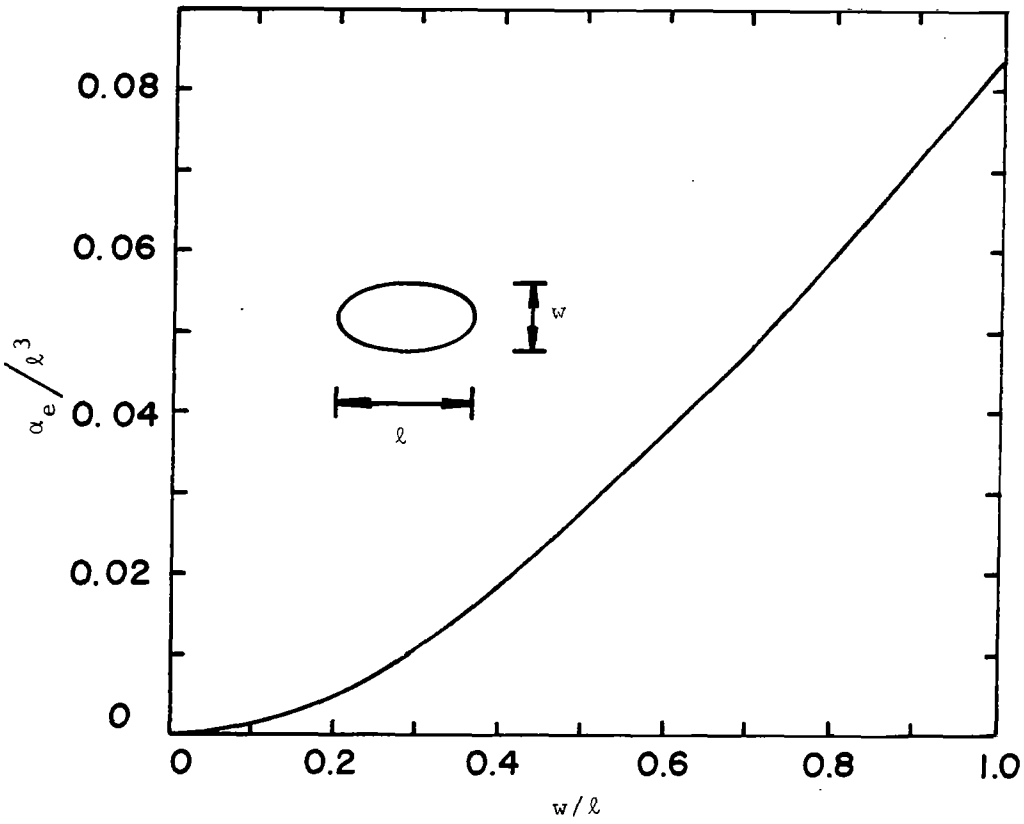

Fig. 2.5. Normalized Electric Polarizability $\left(\alpha_e/\ell^3\right)$.

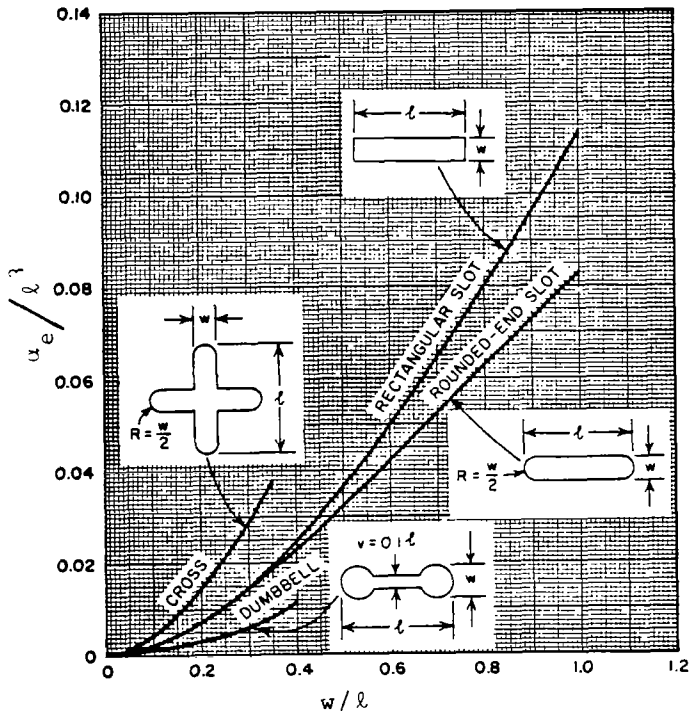

Fig. 2.6. Normalized Electric Polarizability $\left(\alpha_e / \ell^3\right)$.

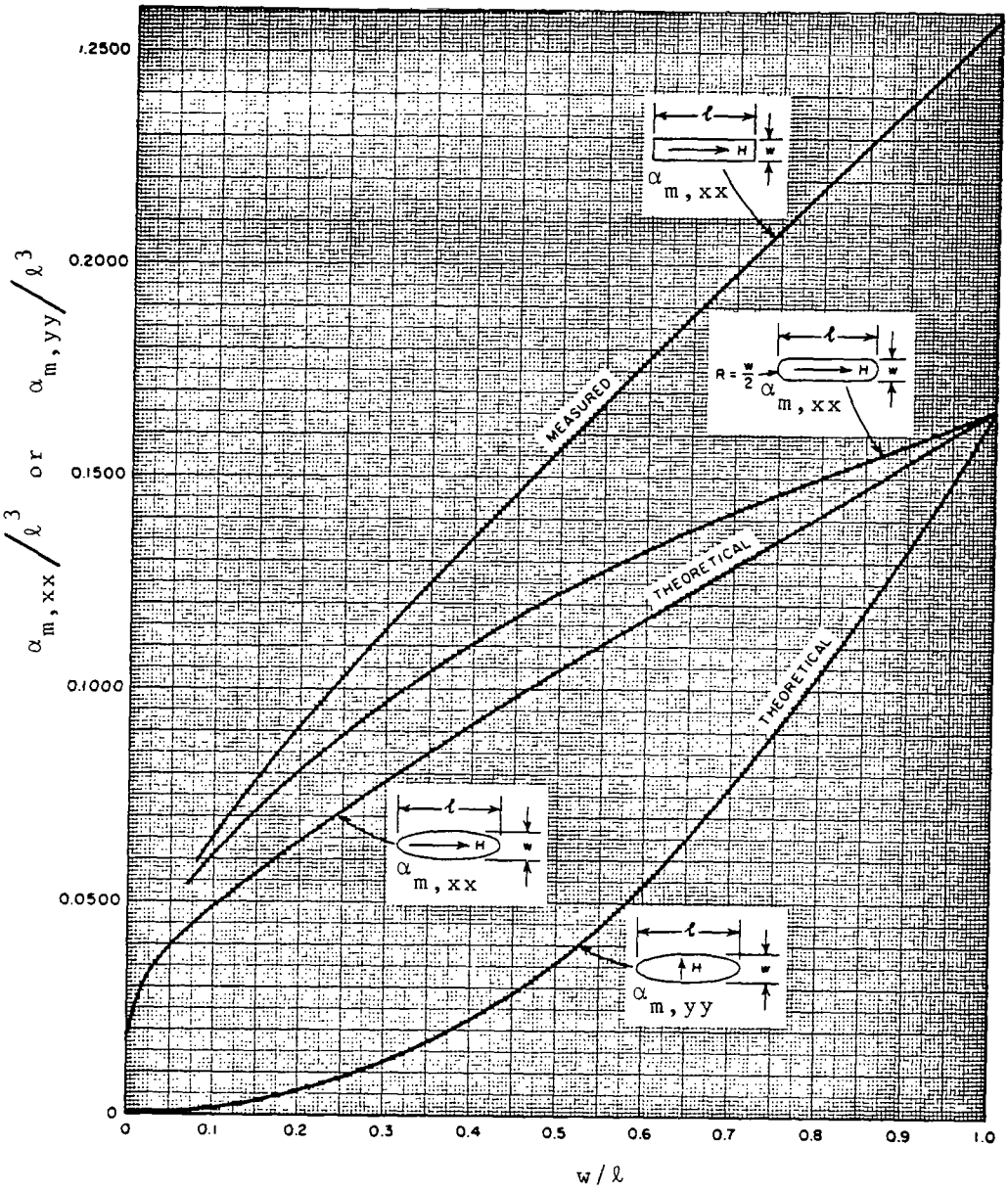

Fig. 2.7. Normalized Magnetic Polarizability $\left(\alpha_{m,xx}/\ell^3 \text{ or } \alpha_{m,yy}/\ell^3\right)$.

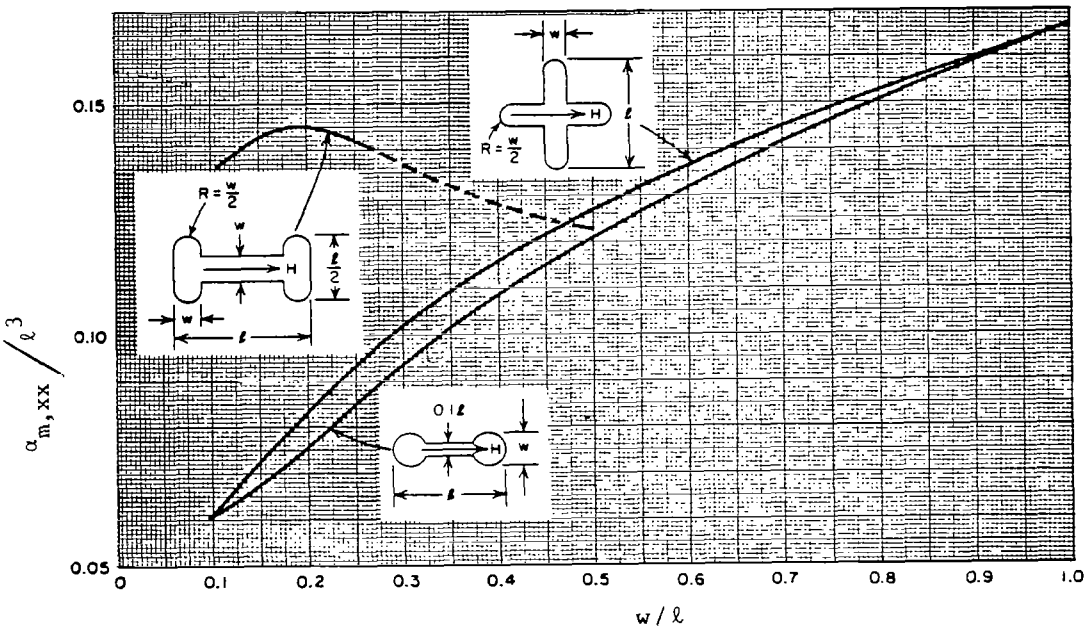

Fig. 2.8. Normalized Magnetic Polarizability $\left(\alpha_{m,xx} / \ell^3\right)$.

highly accurate, having maximum error of ±2%.

De Meulenaere and Van Bladel present polarizability data in the form of curves, and, for convenience, their curves are normalized. Electric polarizability is normalized with respect to the 3/2 power of the aperture area; that is, they plot $\alpha_e / A^{3/2}$ vs. w/ℓ, where A is the aperture area (Fig. 2.9). The meaning of the length ℓ and width w of the shapes is suggested in Fig. 2.4. As pointed out by De Meulenaere and Van Bladel and supported by the data of Fig. 2.9, electric polarizability normalized with respect to $A^{3/2}$ is highly insensitive to aperture shape and depends almost entirely upon the width-to-length ratio w/ℓ.

In Figs. 2.10 and 2.11 are presented data provided by De Meulenaere and Van Bladel from which magnetic polarizability components $\alpha_{m,xx}$ and $\alpha_{m,yy}$ can be readily computed. In Fig. 2.10 is plotted $A^{3/2}/\alpha_{m,xx}$ and in Fig. 2.11 is plotted $\alpha_{m,yy} / A^{3/2}$. Again, excluding the cross, one sees very similar values for the various shapes. Since values for the ellipse are almost identical to those of the rounded-off rectangle, the ellipse curve is omitted.

Latham (Ref. 2.18) also has computed by numerical methods the polarizabilities for the rectangle and diamond, and, because he employs a normalization factor different from those discussed above, it is of interest to consider his findings too. He chooses A^2/P, where A is again the aperture area while P is the length of its perimeter, as his normalization factor and presents data for $\alpha_e/(A^2/P)$, $\alpha_{m,xx}/(A^2/P)$, and $\alpha_{m,yy}/(A^2/P)$. It is interesting to observe from Figs. 2.12 and 2.13 that $\alpha_e/(A^2/P)$ for the rectangle and diamond is only slightly dependent upon aspect ratio. (Note carefully the ordinate ranges in Figs. 2.12 and 2.13.) Furthermore, Latham claims that $\alpha_e/(A^2/P)$ is in the neighborhood of 0.4 or 0.5 for any hole of reasonable shape. To support his claim he mentions that, for an elliptic aperture,

$$\alpha_e/(A^2/P) = \frac{4}{3\pi} = 0.424 \qquad (2.8)$$

independent of the ellipse eccentricity,

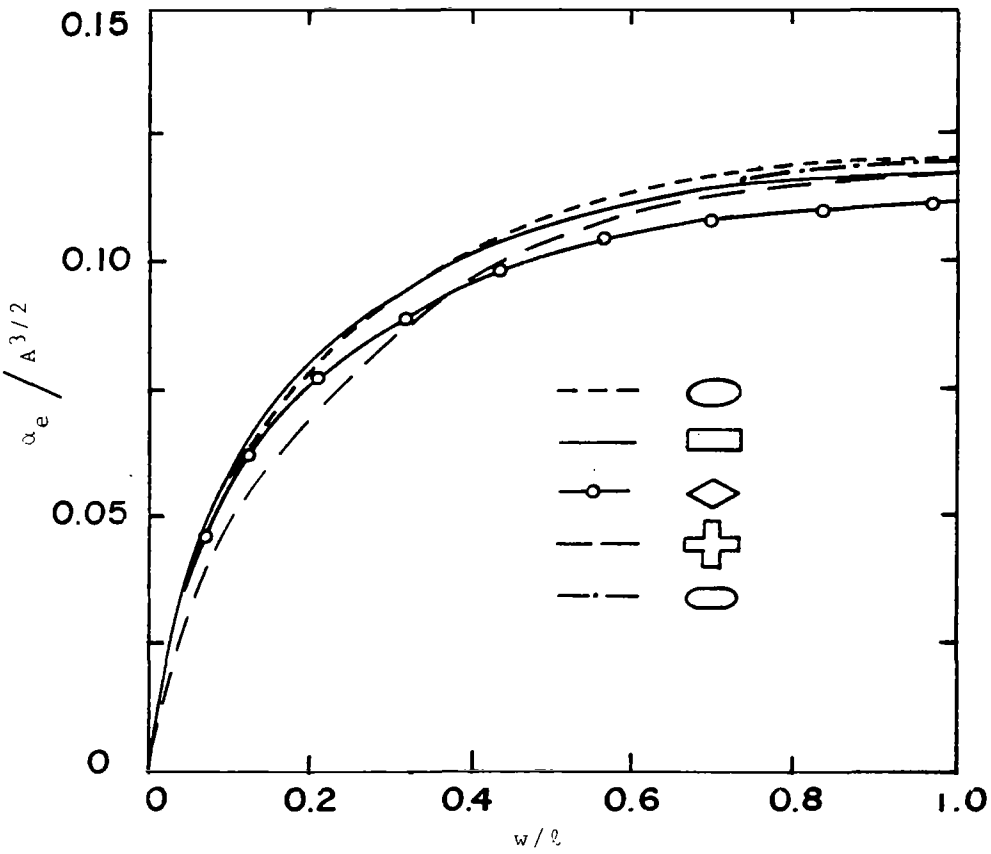

Fig. 2.9. Normalized Electric Polarizability $\left(\alpha_e \Big/ A^{3/2} \right)$.

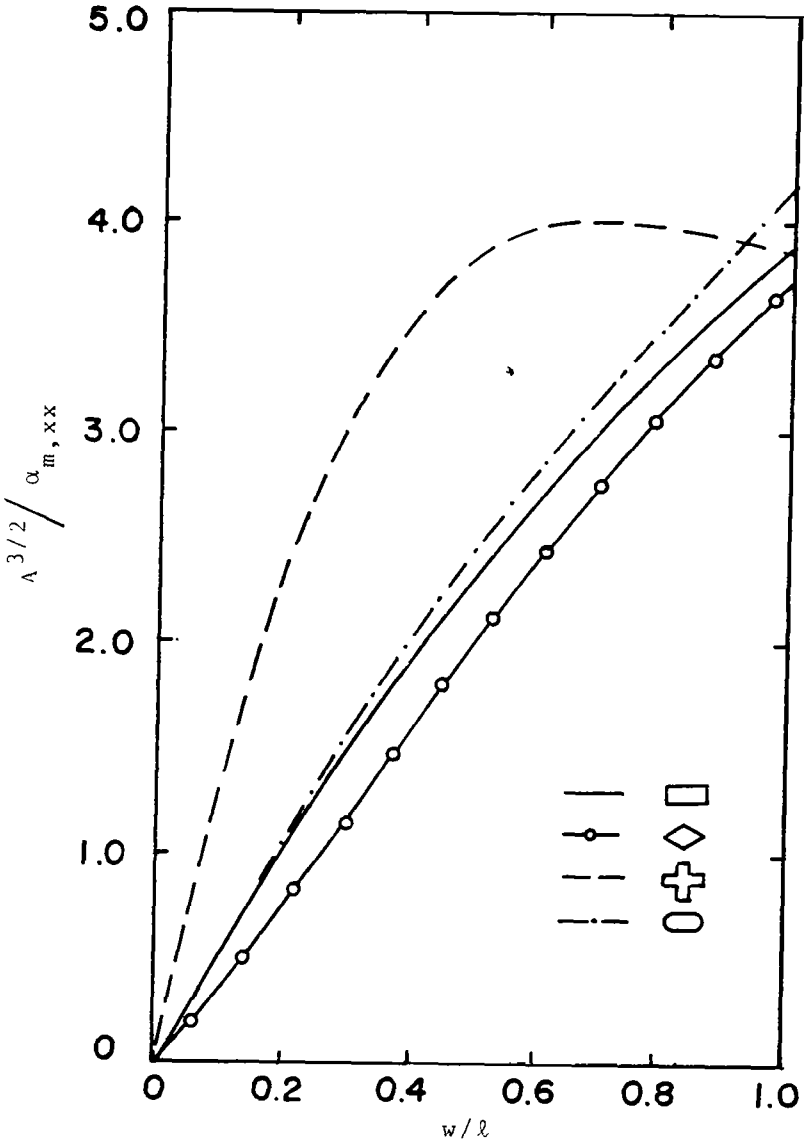

Fig. 2.10. Normalized Reciprocated Magnetic Polarizability $\left(A^{3/2}/\alpha_{m,xx}\right)$.

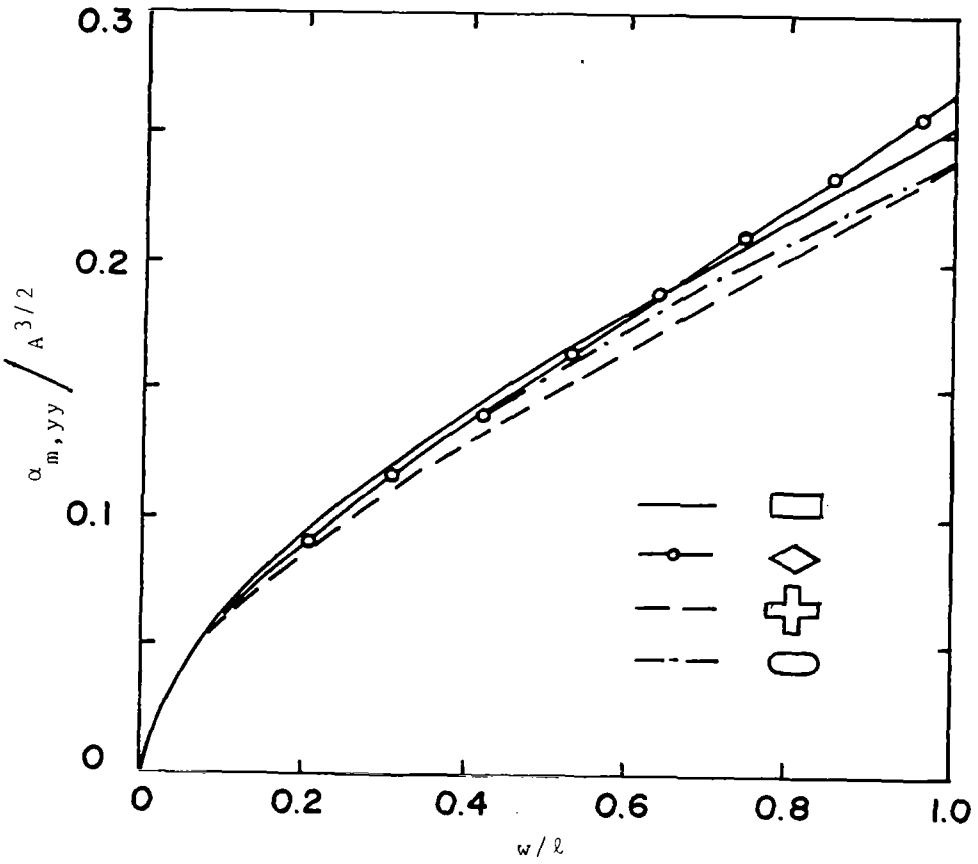

Fig. 2.11. Normalized Magnetic Polarizability $\left(\alpha_{m,yy} \Big/ A^{3/2}\right)$.

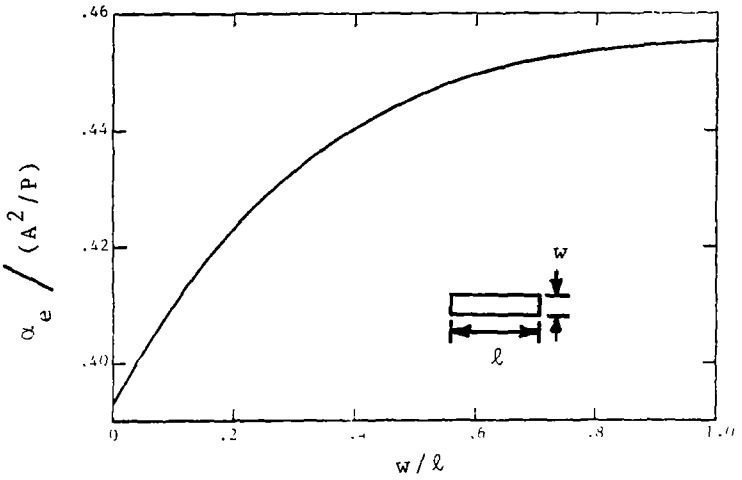

Fig. 2.12. Normalized Electric Polarizability $\left(\alpha_e / (A^2/P)\right)$ for a rectangle.

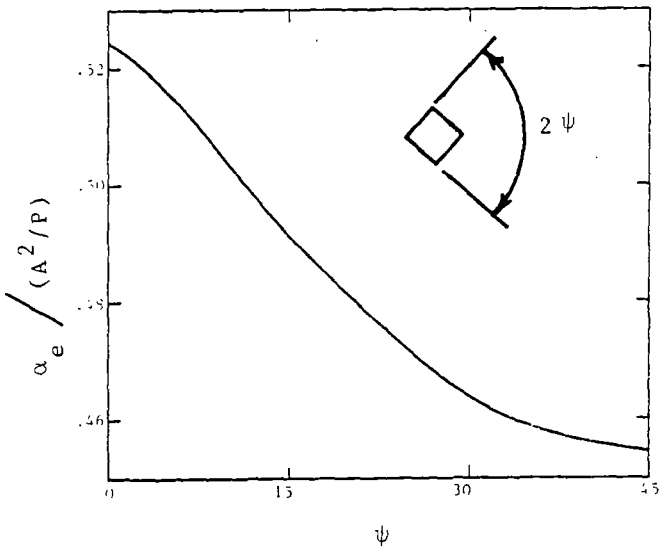

Fig. 2.13. Normalized Electric Polarizability $\left(\alpha_e / (A^2/P)\right)$ for a diamond.

$$\sqrt{1 - \left(\frac{w}{\ell}\right)^2}$$

The reader is invited to compare $\alpha_e/(A^2/P)$ of (2.8) with values from Figs. 2.9 and 2.12.

From computed data, Latham observes that a useful empirical formula can be given for $\alpha_{m,yy}/(A^2/P)$ for a rectangle:

$$\alpha_{m,yy}/(A^2/P) = \frac{\pi}{8}\left[1 + 0.55\left(\frac{w}{\ell}\right)\right] \tag{2.9}$$

Eq. 2.9 differs from computed values by less than 3% for $\left(\frac{w}{\ell}\right) < \frac{1}{2}$.

In addition to computation of penetration through an aperture of one of the relatively simple shapes considered above, one often faces the problem of determining the penetration (leakage) through very narrow slots which exist around the perimeter of a poorly (poor in the electromagnetic sense) closed door or cover plate. When such apertures are considered from the EMP viewpoint, they are called hatch apertures (Ref. 2.19). Examples of hatch apertures are illustrated in Fig. 2.14, each figure of which is intended to represent a narrow slot of width g cut in a thin, conducting surface. In all cases, the slot width g is much smaller than any dimension across an aperture, i.e., $g \ll \ell$, $g \ll w$, and $g \ll d$. Of course, for the equivalent dipole representation of the aperture to be a good approximation, the maximum dimension across the aperture must be very small relative to the wavelength λ ($w \ll \lambda$, $\ell \ll \lambda$, $d \ll \lambda$) as well as relative to the radii of curvature of the conducting surface in which such an aperture has been cut. Figs. 2.14a and 2.14b might represent a "covered" access hole or doorway while Fig. 2.14c might be a circular access hole with a cover hinged on one side (at $y = -d/2$) and latched on the other (at $y = d/2$). The final example (Fig. 2.14d) could be representative of a doorway closed by means of double doors.

Polarizabilities for the hatch apertures of Fig. 2.14 have been determined by Yang, Lee, and Marin (Ref. 2.20), by Lee (Ref. 2.21), and by Chen (Ref. 2.22), and simple formulas for them are given in Table 2.2. One should note that the presence of the hinge and latch has no effect

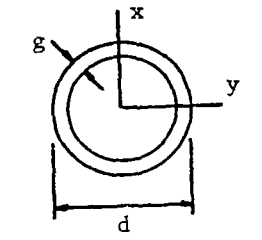

(a)

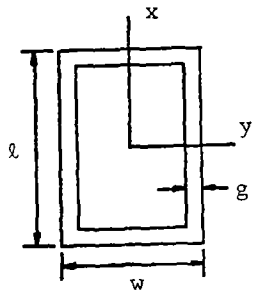

(b)

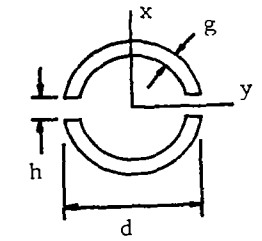

(c)

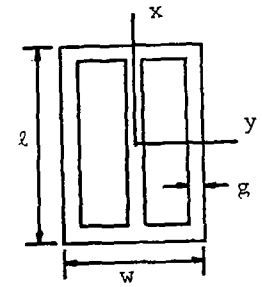

(d)

Fig. 2.14. Hatch Apertures

TABLE 2.2

POLARIZABILITIES* OF HATCH APERTURES

Aperture	α_e	$\alpha_{m,xx}$	$\alpha_{m,yy}$
Fig. 2.14a	$\frac{\pi^2}{32}\frac{d^3}{\ln\left(16\frac{d}{g}\right)-2}$	$\frac{\pi^2}{16}\frac{d^3}{\ln\left(16\frac{d}{g}\right)-2}$	$\frac{\pi^2}{16}\frac{d^3}{\ln\left(16\frac{d}{g}\right)-2}$
Fig. 2.14b	$\frac{\pi}{4}\frac{\ell^2 w}{\left(1+\frac{\ell}{w}\right)\ln\left[4(\ell+w)/g\right]}$	$\frac{\pi}{12}\frac{\ell^3\left[1+3\left(\frac{w}{\ell}\right)\right]}{\ln\left[4(\ell+w)/g\right]}$	$\frac{\pi}{12}\frac{w^3\left[1+3\left(\frac{\ell}{w}\right)\right]}{\ln\left[4(\ell+w)/g\right]}$
Fig. 2.14c		$\frac{\pi^2 d^3}{8\Omega}\left[1-\frac{8/\pi 2}{1+\Omega g^2/(8\pi dh)}\right]$**	$\frac{\pi^2}{16}\frac{d^3}{\ln\left(16\frac{d}{g}\right)-2}$
Fig. 2.14d	$\frac{\pi}{4}\frac{\ell^2 w}{\left(1+\frac{\ell}{w}\right)\ln\left[4(\ell+w)/g\right]}$	$\frac{\pi}{24}\frac{\ell^3\left[\frac{8}{3}+7\left(\frac{w}{\ell}\right)+2\left(\frac{w}{\ell}\right)^2\right]}{\ln\left[4(\ell+w)/g\right]}$	$\frac{\pi}{12}\frac{w^3\left[1+3\left(\frac{\ell}{w}\right)\right]}{\ln\left[4(\ell+w)/g\right]}$

*Refs. 2.20~2.22.

**$\Omega = 2\ \ell n\ (16\ d/g)$

on $\alpha_{m,yy}$ of Fig. 2.14c while it does modify $\alpha_{m,xx}$ and α_e, as is seen from a comparison of the polarizabilities of the apertures of Figs. 2.14a and 2.14c. Similarly, the presence of the center slot in Fig. 2.14d influences only $\alpha_{m,xx}$.

B.3 Computation of Penetrated Field by Dipole Moment Approximation

From knowledge of the equivalent dipoles one can compute the field which reaches the shadow side of the perforated surface. If the surface is an infinite plane, image theory applies and the shadow-side field is equivalent to that radiated by dipoles of moments $2p\hat{z}$ and $2\bar{m}$ located at $\bar{0}$ in a uniform space of infinite extent characterized by (μ,ε). Radiation from such dipoles is easy to compute (Ref. 2.23). After some algebra, one can show that an electric dipole of moment $p\hat{z}$ and a magnetic dipole of moment $\bar{m} = m_x\hat{x} + m_y\hat{y}$, both located at $\bar{0}+$ on the shorted screen and radiating in concert, produce the field components given in Table 2.3.

Now we summarize how the time-harmonic field, which penetrates a screen through a small hole, can be computed from knowledge of the excitation and polarizabilities. First, from known short circuit field components $(E_z^{sc};H_x^{sc},H_y^{sc})$ and known polarizabilities $(\alpha_e;\alpha_{m,xx},\alpha_{m,yy})$ for a specified hole shape, one computes the dipole moment components $(p;m_x,m_y)$. Then, these moments are substituted into Eqs. 2.10 and 2.11 of Table 2.3 which leads to the desired field components.

For a circular aperture of radius R which is sufficiently small relative to the wavelength, the cylindrical coordinate electric field components E_ρ^a and E_ϕ^a in the hole have been determined (Ref. 2.7) to be

$$E_\phi^a = +\frac{8j}{3\pi}k\gamma\left(E_y^i\cos\phi - E_x^i\sin\phi\right)\left(R^2-\rho^2\right)^{\frac{1}{2}} + \frac{4j}{3\pi}k\left(\alpha\sin\phi - \beta\sin\phi\right)\left(R^2-\rho^2\right)^{\frac{1}{2}}E_z^i \qquad (2.12a)$$

TABLE 2.3

ELECTRIC FIELD COMPONENTS IN REGION $z > 0$ DUE TO AN ELECTRIC DIPOLE OF MOMENT $p\hat{z}$ AND A MAGNETIC DIPOLE OF MOMENT $\bar{m}$ $(= m_x\hat{x} + m_y\hat{y})$ BOTH LOCATED AT $(0,0,0+)$ ON AN INFINITE, CONDUCTING SCREEN*

$$E_x = \frac{1}{2\pi}\frac{e^{-jkr}}{r}\left\{-\frac{p}{\epsilon}\frac{xz}{r^2}\left(k^2 - j\frac{3k}{r} - \frac{3}{r^2}\right) + \eta m_y \frac{z}{r}\left(k^2 - j\frac{k}{r}\right)\right\} \tag{2.10a}$$

$$E_y = -\frac{1}{2\pi}\frac{e^{-jkr}}{r}\left\{\frac{p}{\epsilon}\frac{yz}{r^2}\left(k^2 - j\frac{3k}{r} - \frac{3}{r^2}\right) + \eta m_x \frac{z}{r}\left(k^2 - j\frac{k}{r}\right)\right\}. \tag{2.10b}$$

$$E_z = \frac{1}{2\pi}\frac{e^{-jkr}}{r}\left\{\frac{p}{\epsilon}\left[\left(k^2 - j\frac{k}{r} - \frac{1}{r^2}\right) - \frac{z^2}{r^2}\left(k^2 - j\frac{3k}{r} - \frac{3}{r^2}\right)\right]\right.$$

$$\left. + \frac{\eta}{r}\left(ym_x - xm_y\right)\left(k^2 - j\frac{k}{r}\right)\right\} \tag{2.10c}$$

* The screen is embedded in a homogeneous medium characterized by (μ,ϵ); $\eta = \sqrt{\mu/\epsilon}$.

TABLE 2.3 (cont'd)

MAGNETIC FIELD COMPONENTS IN REGION $z > 0$ DUE TO AN ELECTRIC DIPOLE OF MOMENT $p\hat{z}$ AND A MAGNETIC DIPOLE OF MOMENT $\bar{m}$ $(= m_x\hat{x} + m_y\hat{y})$ BOTH LOCATED AT (0,0, 0+) ON AN INFINITE, CONDUCTING SCREEN*

$$H_x = \frac{1}{2\pi}\frac{e^{-jkr}}{r}\left\{\frac{p}{\varepsilon\eta}\frac{y}{r}\left(k^2 - j\frac{k}{r}\right) + m_x\left(k^2 - j\frac{k}{r} - \frac{1}{r^2}\right)\right.$$

$$\left. - \frac{x}{r^2}\left(xm_x + ym_y\right)\left(k^2 - j\frac{3k}{r} - \frac{3}{r^2}\right)\right\} \qquad (2.11a)$$

$$H_y = \frac{1}{2\pi}\frac{e^{-jkr}}{r}\left\{-\frac{p}{\varepsilon\eta}\frac{x}{r}\left(k^2 - j\frac{k}{r}\right) + m_y\left(k^2 - j\frac{k}{r} - \frac{1}{r^2}\right)\right.$$

$$\left. - \frac{y}{r^2}\left(xm_x + ym_y\right)\left(k^2 - j\frac{3k}{r} - \frac{3}{r^2}\right)\right\} \qquad (2.11b)$$

$$H_z = -\frac{1}{2\pi}\frac{e^{-jkr}}{r}\left\{\frac{z}{r^2}\left(xm_x + ym_y\right)\left(k^2 - j\frac{3k}{r} - \frac{3}{r^2}\right)\right\} \qquad (2.11c)$$

*The screen is embedded in a homogeneous medium characterized by (μ,ε); $\eta = \sqrt{\mu/\varepsilon}$.

$$E_\rho^a = \frac{2j}{3\pi} k\gamma \left(E_x^i \cos\phi + E_y^i \sin\phi \right) \left[4\left(R^2 - \rho^2 \right)^{\frac{1}{2}} + \frac{2\rho^2}{\left(R^2 - \rho^2 \right)^{\frac{1}{2}}} \right]$$

$$+ \frac{2}{\pi} \left[\rho - \frac{2}{3} jk \left(\alpha \cos\phi + \beta \sin\phi \right) \left(\rho^2 + R^2 \right) \right] \frac{1}{\left(R^2 - \rho^2 \right)^{\frac{1}{2}}} E_z^i \qquad (2.12b)$$

where (α,β,γ) are the usual direction cosines of the ray along which the incident field propagates and (E_x^i, E_y^i, E_z^i) are the components of the incident field evaluated at the center of the circular hole.

We point out that Eqs. 2.10 and 2.11 are exact for the case of the specified dipoles on the infinite, planar screen, but the equivalent representation of the aperture field is not accurate at points close to the aperture, measured relative to the maximum dimension across A. Eqs. 2.12 are exact in the aperture for a vanishingly small radius R. However, for a surface which is large and whose radii of curvature are large, relative to the aperture size, Eqs. 2.10, 2.11, and 2.12 are good approximations at points close to the surface relative to the smaller dimension measured across the conducting surface. If an object which scatters energy back into the aperture resides on the shadow side of the screen, corrections must be made to account for this additional aperture excitation due to the back scatter. Usually such a correction is very small for cases where the aperture is small unless some resonance is caused by the presence of the obstacle behind the screen. Even for an aperture in a wall of a closed surface, the equivalent dipole representation leads to good results in many (nonresonant) situations. Of course, the field produced inside the enclosure must be computed by interior boundary value problem techniques, not by the expressions of Table 2.3 except under very special circumstances.

B.4 Sample Data

For an electrically small aperture one may approximate the aperture-produced fields by making use of Table 2.3 and the dipole moments calculated for the given aperture. How good the dipole moment approximation

to the actual fields is depends upon the electrical size of the aperture, the distance from the aperture to the point at which the field is evaluated, and the choice of the coordinate origin with respect to which the dipole moments are calculated. Therefore, since one wishes to take advantage of the simplicity afforded by use of dipole moments to characterize the electromagnetic behavior of an aperture, it is of interest to compare the field computed this way with those computed by more accurate means.

Fig. 2.15 shows the electric field which penetrates a small square aperture ($2a = 2b = 0.15\lambda$) subject to normally incident illumination with a 1 volt/meter electric field directed along the y axis (Ref. 2.10). In this case the electric dipole moment is zero ($E_z^{sc} = 0$), so the total field is approximated by that of a magnetic dipole. These approximate values of fields together with values determined from numerical computations (Ref. 2.10) are both displayed for comparison. One sees good agreement at a radial distance r = 10a but sees significant differences at 3a and 2a. In Fig. 2.16 is displayed the field which penetrates the same aperture subject to edge-on incident illumination with $E_z^{i-}(0) = 1$ volt/meter and with the direction of propagation along either the x axis or the y axis (Ref. 2.10).

The primary reason for the departure of the two results is the approximate nature of the dipole moment equivalence, which incorrectly predicts an infinite field for $z/\lambda \to 0$. Thus, one must exercise caution in using the dipole moment approach to compute the diffracted field very close to an aperture.

B.5 Transient Fields

For cases where the polarizabilities are known, one can compute time histories of the field which passes through a small aperture. This is done by making use of Fourier transform techniques.

We point out that the polarizabilities of small, unloaded apertures are frequency independent so, in view of Eqs. 2.10 and 2.11, the behavior of the dipole moments with frequency ω is seen to be the same as that of the short-circuit field. Since the dependence of $p\hat{z}$ upon $j\omega$ is the same as that of E_z^{sc} and since $\bar{m}$ has the same behavior as does $\bar{H}^{sc}$, one can

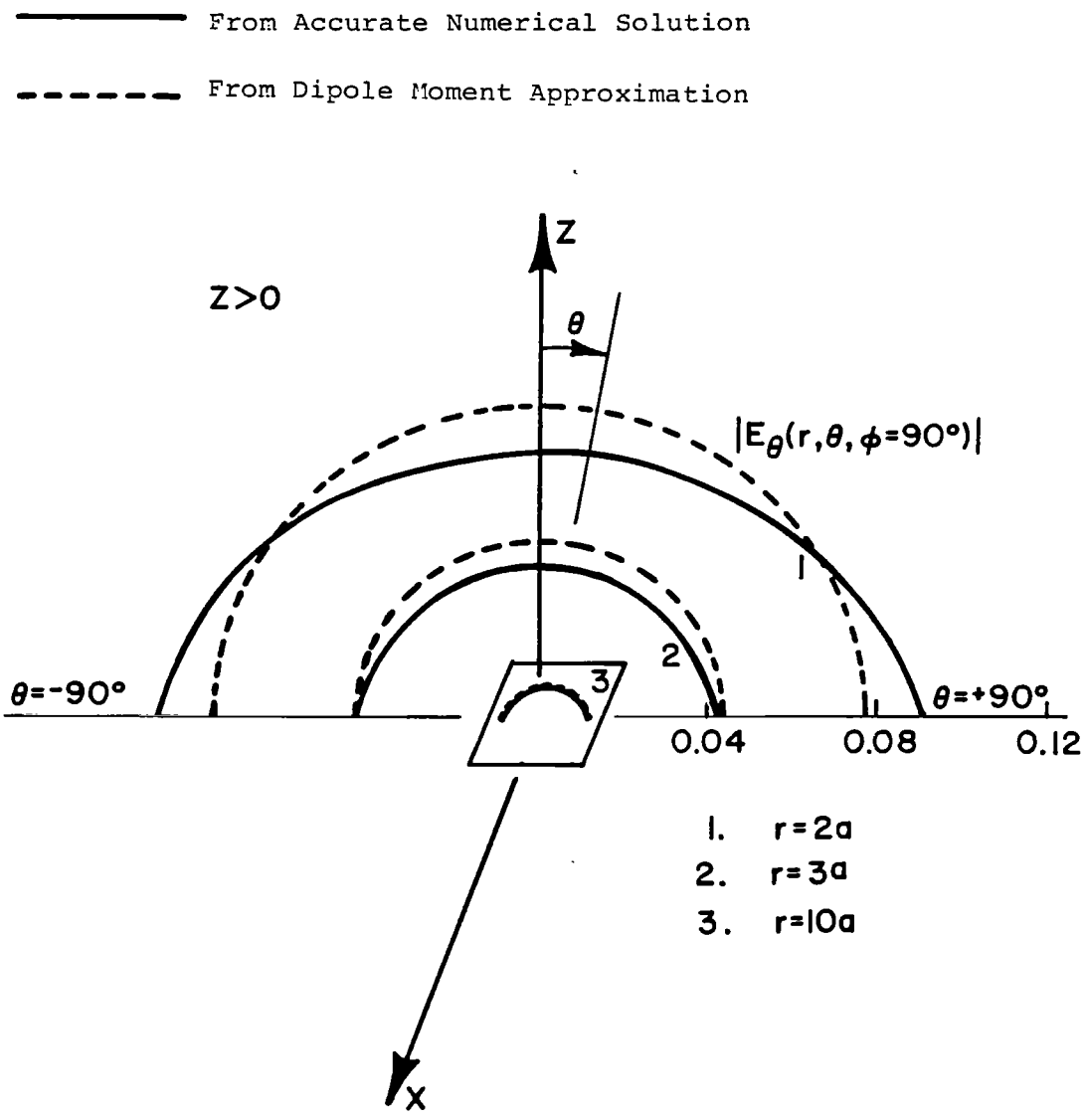

Fig. 2.15. Electric Field on Shadow Side of Square Aperture ($2a = 2b = 0.15\lambda$, $E_y^{i-} = 1$ volt/meter, normal incidence).

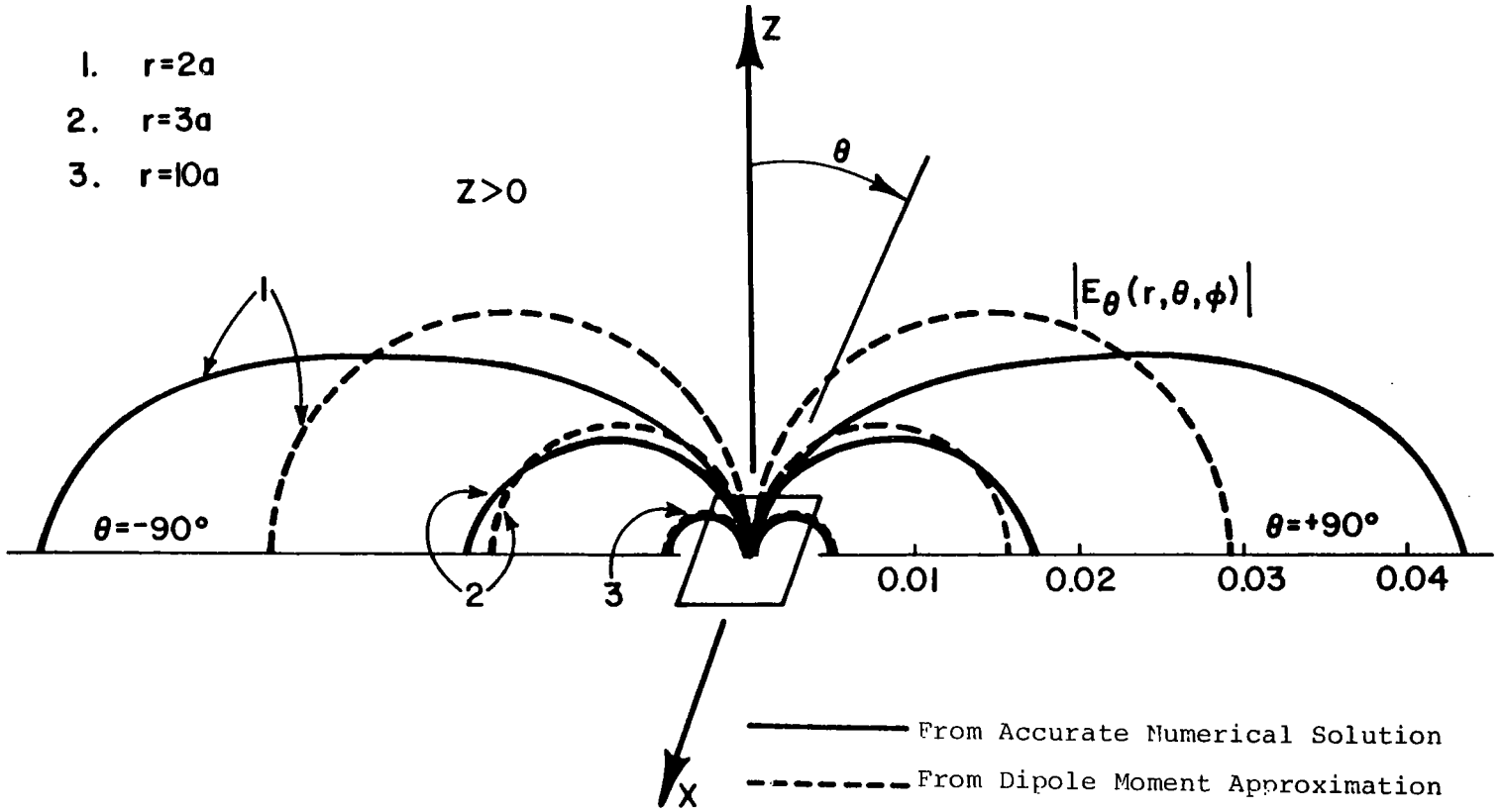

Fig. 2.16. Electric Field on Shadow Side of Square Aperture

(2a = 2b = 0.15λ, E_z^{i-} = 1 volt/meter, edge-on incidence).

obtain time histories of the fields from the expressions in Table 2.3 whenever the short-circuit fields are known as functions of time.

If we denote the time dependent dipole moments components by $p(t)$, $m_x(t)$, and $m_y(t)$, then

$$p(t) = \varepsilon\alpha_e \, E_z^{sc}(\bar{0}-,t) \tag{2.13}$$

$$m_x(t) = -\alpha_{m,xx} \, H_x^{sc}(\bar{0}-, t) \tag{2.14a}$$

and

$$m_y(t) = -\alpha_{m,yy} \, H_y^{sc}(\bar{0}-,t) \tag{2.14b}$$

We emphasize that the polarizabilities in Eqs. 2.13 and 2.14 are independent of time and that, once the short-circuit field is known as a function of time, so are the dipole moments.

If the ω-domain field components of Table 2.3 are inverted by the Fourier integral

$$f(t) = \mathscr{F}^{-1}\{f(\omega)\} = \frac{1}{2\pi}\int_{\omega=-\infty}^{\infty} f(\omega) \, e^{j\omega t} d\omega \tag{2.15}$$

one obtains the time-domain field components given in Table 2.4. The differential operators in Table 2.4 are defined by

$$D_1[f(\tau)] = \frac{1}{c^2}\left(\frac{\partial^2}{\partial\tau^2} f(\tau) + \frac{c}{r}\frac{\partial}{\partial\tau} f(\tau)\right) \tag{2.16a}$$

$$D_2[f(\tau)] = \frac{1}{c^2}\left(\frac{\partial}{\partial\tau^2} f(\tau) + \frac{c}{r}\frac{\partial}{\partial\tau} f(t) + \frac{c^2}{r^2} f(\tau)\right) \tag{2.16b}$$

and

TABLE 2.4

TRANSIENT ELECTRIC FIELD COMPONENTS IN REGION $z > 0$ DUE TO AN ELECTRIC DIPOLE OF MOMENT $p(t)\hat{z}$ AND A MAGNETIC DIPOLE OF MOMENT $\bar{m}(t)(= m_x(t)\hat{x} + m_y(t)\hat{y})$ BOTH LOCATED AT (0,0,0+) ON AN INFINITE, CONDUCTING SCREEN*

$$E_x(\bar{r},t) = \frac{\eta}{2\pi}\left\{ cxzr^{-3}D_3\,[p(\tau)] - zr^{-2}D_1\,[m_y(\tau)]\right\} \tag{2.17a}$$

$$E_y(\bar{r},t) = \frac{\eta}{2\pi}\left\{ cyzr^{-3}D_3\,[p(\tau)] + zr^{-2}D_1\,[m_x(\tau)]\right\} \tag{2.17b}$$

$$E_z(\bar{r},t) = \frac{\eta}{2\pi}\left\{ - cr^{-1}D_2\,[p(\tau)] + cz^2r^{-3}D_3\,[p(\tau)] - r^{-2}D_1\,[ym_x(\tau) - xm_y(\tau)]\right\} \tag{2.17c}$$

Note: $\tau = (t - r/c)$

*The screen is embedded in a homogeneous medium characterized by (μ,ε); $\eta = \sqrt{\mu/\varepsilon}$.

TABLE 2.4 (cont'd)

TRANSIENT MAGNETIC FIELD COMPONENTS IN REGION $z > 0$ DUE TO AN ELECTRIC DIPOLE OF MOMENT $p(t)\hat{z}$ AND A MAGNETIC DIPOLE OF MOMENT $\bar{m}(t)(= m_x(t)\hat{x} + m_y(t)\hat{y})$ *BOTH LOCATED AT (0,0,0+) ON AN INFINITE, CONDUCTING SCREEN**

$$H_x(\bar{r},t) = \frac{1}{2\pi}\left\{- cyr^{-2}D_1\,[p(\tau)] - r^{-1}D_2\,[m_x(\tau)] + xr^{-3}D_3\,[xm_x(\tau) + ym_y(\tau)]\right\} \quad (2.18a)$$

$$H_y(\bar{r},t) = \frac{1}{2\pi}\left\{cxr^{-2}D_1\,[p(\tau)] - r^{-1}D_2\,[m_y(\tau)] + yr^{-3}D_3\,[xm_x(\tau) + ym_y(\tau)]\right\} \quad (2.18b)$$

$$H_z(\bar{r},t) = \frac{1}{2\pi}\,zr^{-3}D_3\,[xm_x(\tau) + ym_y(\tau)] \quad (2.18c)$$

Note: $\tau = (t - r/c)$

*The screen is embedded in a homogeneous medium characterized by (μ,ε); $\eta = \sqrt{\mu/\varepsilon}$.

$$D_3[f(\tau)] = \frac{1}{c^2}\left(\frac{\partial^2}{\partial\tau^2} f(\tau) + 3\frac{c}{r}\frac{\partial}{\partial\tau} f(\tau) + 3\frac{c^2}{r^2} f(\tau)\right) \qquad (2.16c)$$

where c is the speed of light in the lossless medium characterized by (μ,ε).

C. Slotted Planar Screen

C.1 Infinite Slot

Very long slots of uniform width in a planar screen, subject to illumination which is transverse electric (TE) to the slot axis, can be approximated in many typical practical applications by infinitely long slots. If the slot is very narrow and the excitation is known, one can compute the slot electric field directly, but for wider slots integral equations can be solved numerically. Care should be exercised in approximating a finite-length slot by one of infinite length especially when the slot length is near resonance or antiresonance. However, the field pattern behind a long slot is quite similar to that behind one of infinite length when the point of observation is near the slotted screen and not near the slot ends or a point at which the slot field has a null. Of further interest in EMP applications is the fact that penetration through a slot subject to TE excitation is typically much greater than subject to TM excitation. Hence data for TE-excited slots represent worse-case fields insofar as EMP hardness is concerned.

For TE illumination of an infinitely long narrow slot in a planar screen as illustrated in Fig. 2.17, the electric field E_x^a in the slot is (Ref. 2.24)

$$E_x^a(x) = \frac{1}{2}\left\{ j \frac{\eta H_y^{sc}(0-)}{\left(\gamma + \ell n\left(\frac{kw}{8}\right) + j\frac{\pi}{2}\right)} + E_z^{sc}(0-)kx \right\} \frac{1}{\sqrt{\left(\frac{kw}{2}\right)^2 - \left(kx\right)^2}}$$

$$|kw| << 1 \qquad (2.19)$$

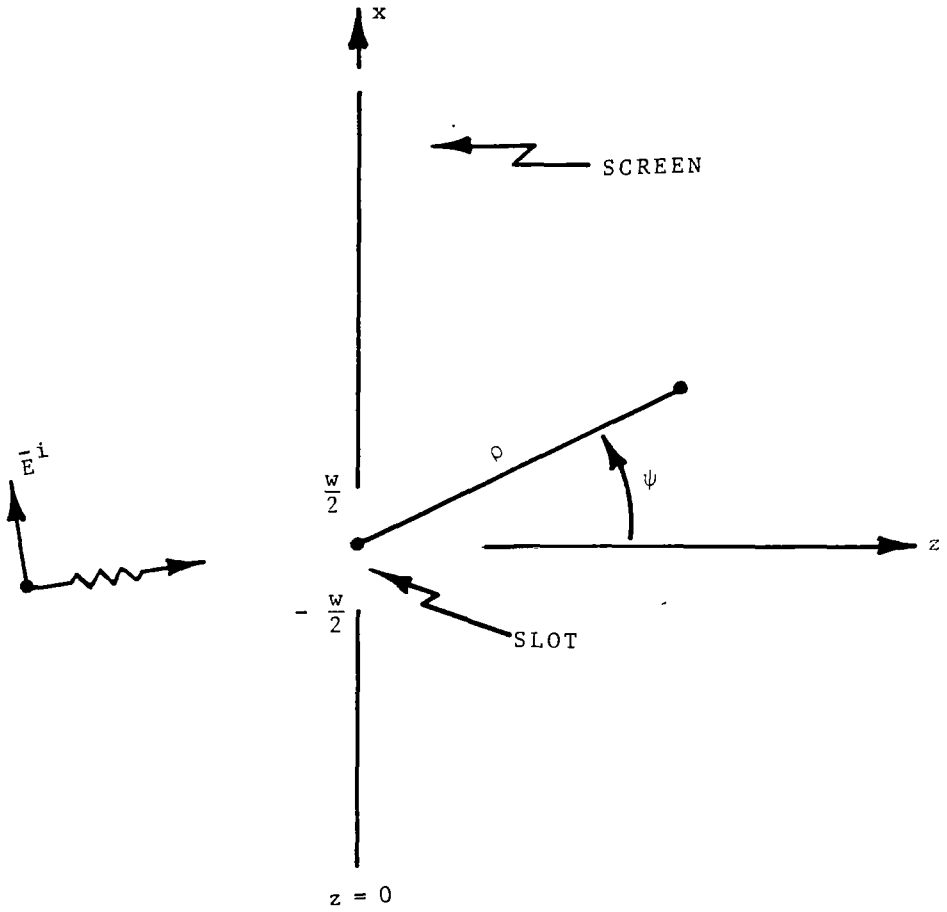

Fig. 2.17. Infinite Slot in Conducting Screen Subject to TE Illumination (Cross Sectional View).

where $\gamma = 0.57722$ used here is Euler's constant and where w is the slot width as depicted in Fig. 2.17. In view of the typical EMP spectrum, usually encountered slots are narrow and one usually wishes to know fields behind a slotted screen at points close to the slot relative to the wavelength. At a distance ρ from the slot axis which is large relative to slot width w and small relative to wavelength λ, the magnetic field H_y is (Ref. 2.24)

$$H_y(\rho,\psi) = \frac{1}{2}\left\{\frac{H_y^{sc}(0-)}{\left(\gamma + \ell n\left(\frac{kw}{8}\right) + j\,\frac{\pi}{2}\right)}\left[\gamma + f_e + j\,\frac{\pi}{2}\right] + j\left(\frac{kw}{8}\right)\frac{E_z^{sc}(0-)}{\eta}\,f_o\right\}$$

$$|kw| << 1$$

$$w < \rho << \lambda \qquad (2.20a)$$

where

$$f_e \doteq \ell n\left(\frac{k\rho}{2}\right) - \frac{1}{8}\left(\frac{w}{\rho}\sin\psi\right)^2 - \frac{3}{64}\left(\frac{w}{\rho}\sin\psi\right)^4 \qquad (2.20b)$$

and

$$f_o \doteq \frac{w}{\rho}\sin\psi + \frac{1}{4}\left(\frac{w}{\rho}\sin\psi\right)^3 \qquad (2.20c)$$

C.2 Finite-Length Slot

For a finite-length slot (Fig. 2.18) whose width w is much smaller than the wavelength of the excitation and the length ℓ of the slot, the transverse component of slot electric field E_x^a is far stronger than the axial component E_y^a. In almost all cases of practical interest, the latter can be neglected compared with the former. Maximum penetration occurs when the slot length ℓ is near $\lambda/2$, or an odd multiple thereof, and when the magnetic field of the excitation is directed along the slot

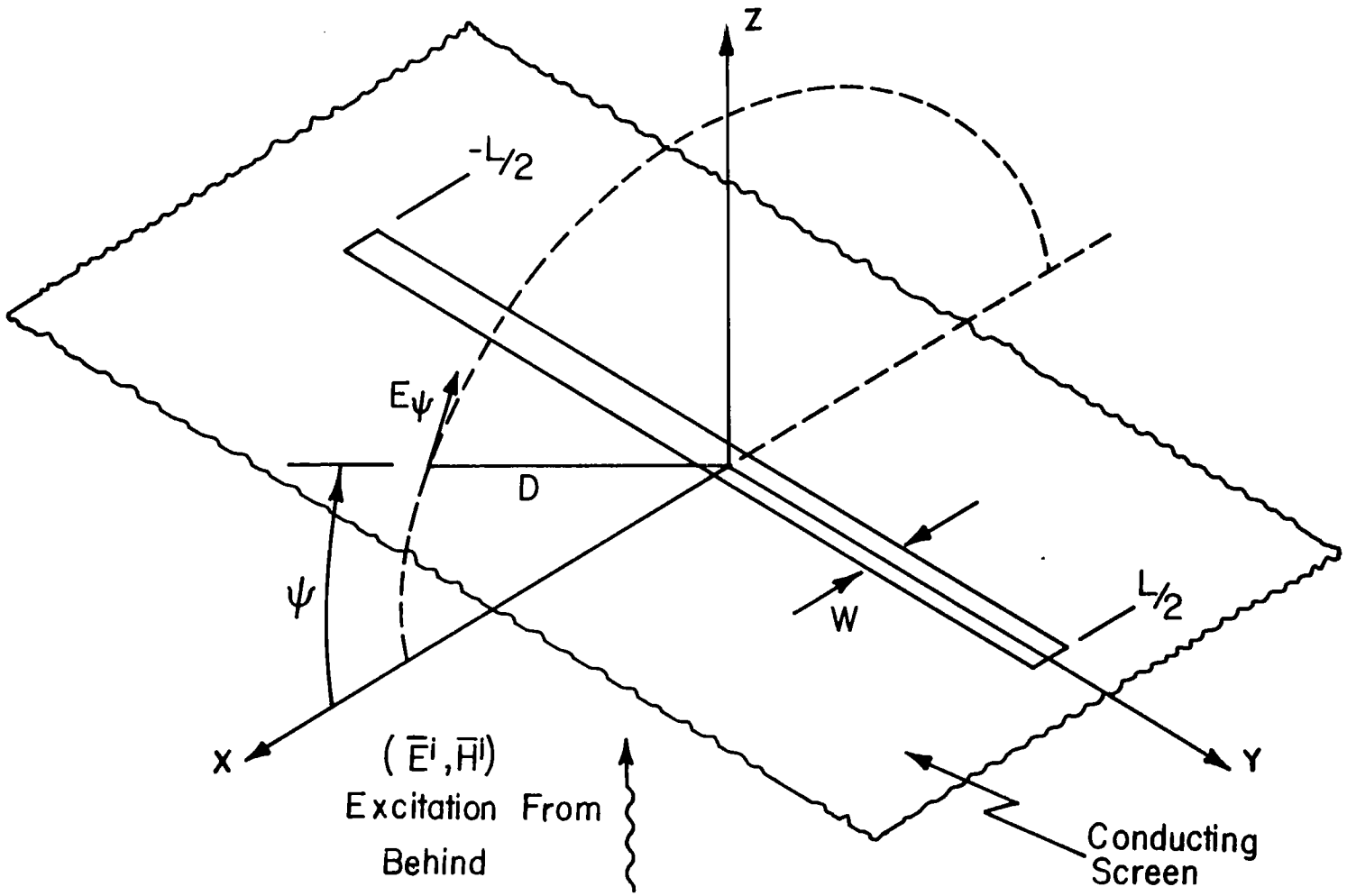

Fig. 2.18. Finite-Length, Narrow Slot.

axis and is an even function relative to the slot center. Strong penetration occurs too through slots whose length is a multiple of one wavelength when the axially directed magnetic field possesses a rich odd-function component. Such "worse case" data can be computed from the dual results available for thin wires.

As an example illustrative of the EMP field which might pass through a finite-length slot, $H_y^{sc}(0-,t)$ is selected to be constant along the slot axis with the double exponential pulse time variation shown in Fig. 2.19. Fig. 2.20 displays the time history of the electric field $E_x(t)$ (at a point two meters behind the screen) which passed through a 115 cm × 1.3 cm slot (Ref. 2.25).

D. Parallel Plates

D.1 Introduction

The determination of the field which reaches the interior region between two parallel, conducting plates through an aperture in one plate is of considerable interest. Such a configuration is representative of the penetration into a semi-closed region through an aperture, and it is a geometry of sufficient simplicity to permit careful analysis (Refs. 2.26-2.28).

D.2 Elliptic Aperture in "Front" Plate

Taylor (Refs. 2.26, 2.27) has investigated penetration into a parallel-plate region through very small elliptic apertures (Fig. 2.21). He considers general plane wave excitation and provides copious data, which are reproduced here in Figs. 2.22-2.27. For the purpose of normalizing his data to render it applicable to a large variety of situations, Taylor introduces

$$\alpha'_{11} = -8\,\alpha_{m,xx}/\ell^3 \tag{2.21a}$$

$$\alpha'_{22} = -8\,\alpha_{m,yy}/\ell^3 \tag{2.21b}$$

$$\alpha'_{33} = 8\,\alpha_e/\ell^3 \tag{2.21c}$$

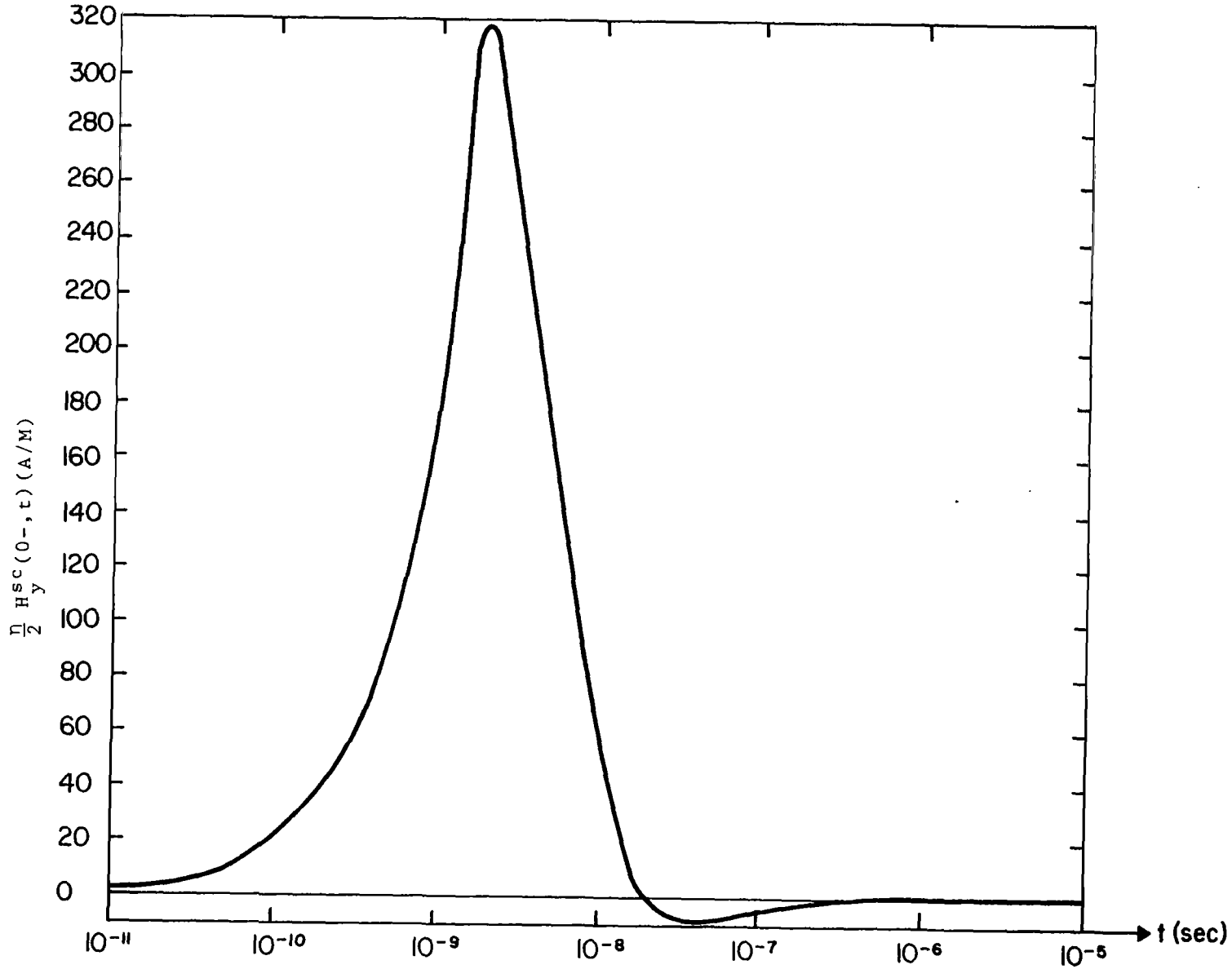

Fig. 2.19. Time Domain Plot of $H_y^{sc}(0-,t)$.

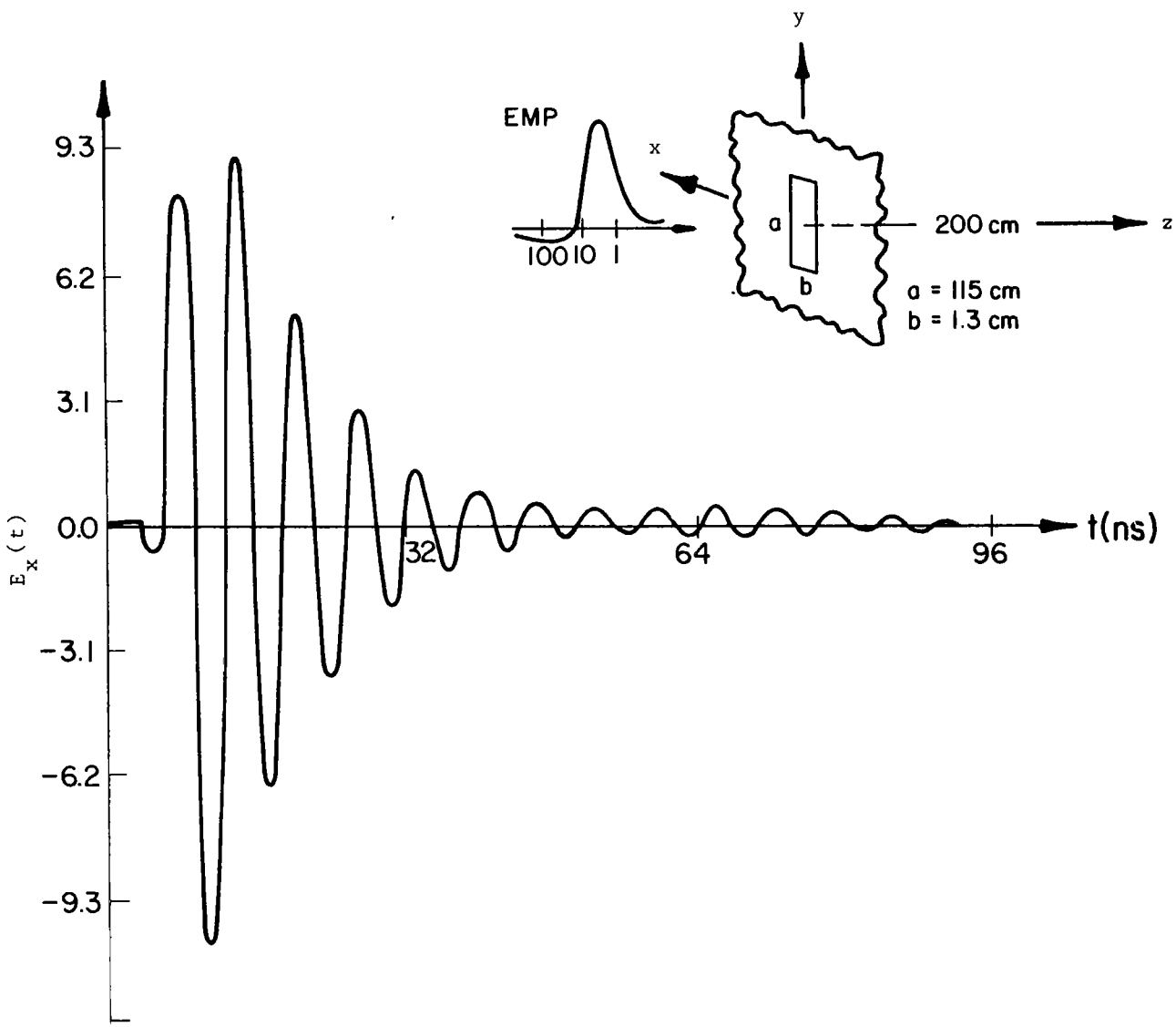

Fig. 2.20. Time Domain Behavior of the $E_x(t)$ Field Sampled at a Point 2 Meters behind a Single Aperture.

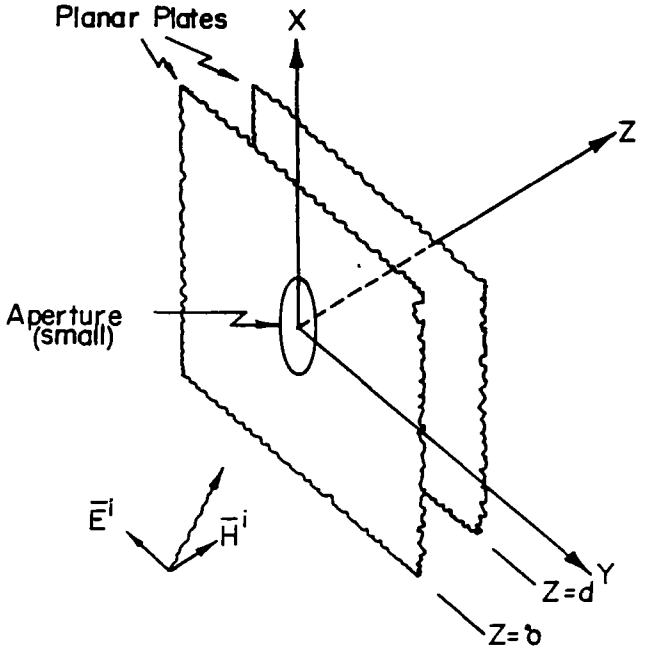

Fig. 2.21a. Parallel Plates with Aperture in Front Plate.

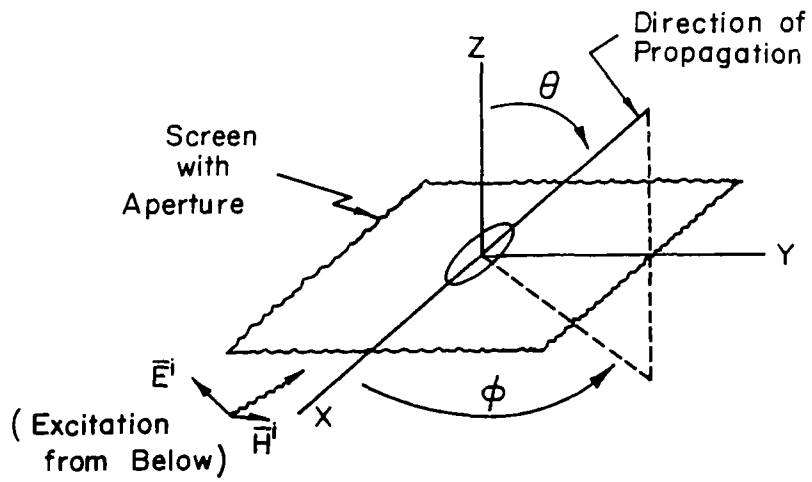

Fig. 2.21b. Illustration of Propagation Direction (Back Plate Removed).

where $\alpha_{m,xx}$, $\alpha_{m,yy}$, α_e, and ℓ^3 are defined in Section B; also,

$$a_2 = \begin{cases} -\alpha'_{22} \cos\theta \sin\phi \ , & \text{E polarization} \\ \\ -\alpha'_{22} \sin\phi \ , & \text{H polarizaton} \end{cases} \tag{2.22}$$

and

$$a_3 = \begin{cases} 0 \ , & \text{E polarization} \\ \\ \alpha'_{33} \sin\theta \ , & \text{H polarization} \end{cases} \tag{2.23}$$

E-polarization is taken to mean, in the notation* of Taylor's paper, that the time-domain field components of an incident plane wave are

$$E_z^{inc} = 0 \tag{2.24a}$$

$$E_x^{inc}(t) = -\frac{1}{\eta} E^{inc}(t) \cos\theta \cos\phi \tag{2.24b}$$

$$H_y^{inc}(t) = -\frac{1}{\eta} E^{inc}(t) \cos\theta \sin\phi \tag{2.24c}$$

while H-polarization implies field components

$$E_z^{inc}(t) = E^{inc}(t) \sin\theta \tag{2.25a}$$

*Taylor's notation is adopted here for compatibility with curves from this paper (Ref. 2.27).

$$H_x^{inc}(t) = \frac{1}{\eta} E^{inc}(t) \cos\phi \qquad (2.25b)$$

$$H_y^{inc}(t) = \frac{1}{\eta} E^{inc}(t) \sin\phi \qquad (2.25c)$$

The angles θ and ϕ (see Fig. 2.21) define the ray in spherical coordinates along which the incident plane wave propagates. The reader is reminded that $\bar{E}^{inc}$, $\bar{H}^{inc}$, and the above-mentioned ray are mutually perpendicular for a plane wave. In E-polarization, $\bar{E}^{inc}$ is rotated about the ray along which the wave propagates until it has no (z-component) component perpendicular to the conducting plane ($E_z^{inc} = 0$), while in H-polarization $\bar{H}^{inc}$ is adjusted until it has no z-component ($H_z^{inc} = 0$). This way of specifying the incident field allows Taylor (Ref. 2.27) to present minimum data to cover general cases of excitation.

Figs. 2.22-2.25 provide time-harmonic data indicative of the behavior of field components between the plates, subject to the excitation discussed above, for different plate separations. In Figs. 2.24 and 2.25 $\bar{B}^{inc} = \mu \bar{H}^{inc}$ and $\bar{B} = \mu \bar{H}$, and ℓ_1 is the length of the major semi-axis of the ellipse ($2\ell_1 = \ell$ where ℓ is illustrated in Fig. 2.4a).

Computation of the equivalent electric and magnetic dipoles by means of Eqs. 2.1 and 2.2 from knowledge of $E_z^{sc}(0-)$ and $\bar{H}^{sc}(0-)$ and the polarizabilities leads to accurate results so long as the field scattered back from the back plate into the aperture is small relative to the excitation. Such would be the case for plate spacing d different from odd integer multiples of $\lambda/2$ or with lossy material between the plates. If d differs from $\lambda/2$ by less than 10%, then resonance effects take place and this back scatter must be taken into account (Ref. 2.27).

To show that his results for penetration into the region between parallel plates provide information valid for penetration (in certain cases) into regions bounded by conducting walls of another geometry, Taylor compares his time-domain findings with those of Bombardt (Ref. 2.29) computed and measured for cylindrical walls (Fig. 2.26). Bombardt adopted

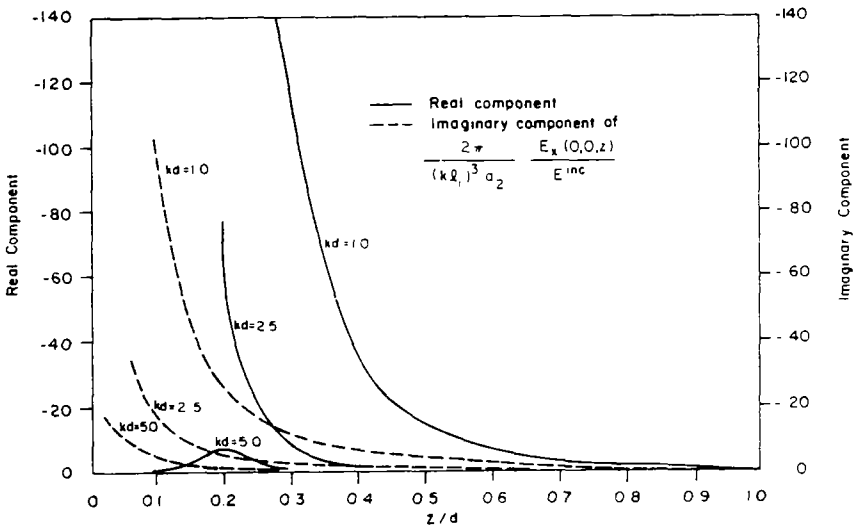

Fig. 2.22. x Component of Electric Field between Plates along a Line Passing through Center of Aperture and Perpendicular to Plates.

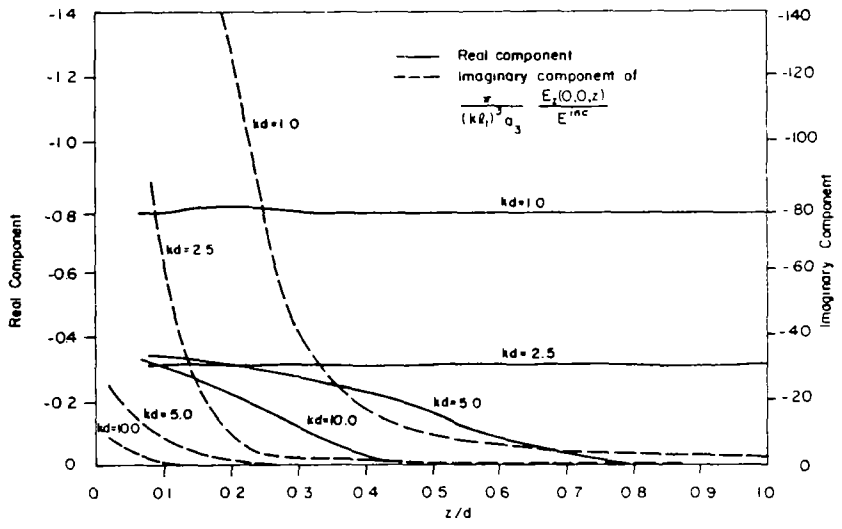

Fig. 2.23. z Component of Electric Field between Plates along a Line Passing through Center of Aperture and Perpendicular to Plates.

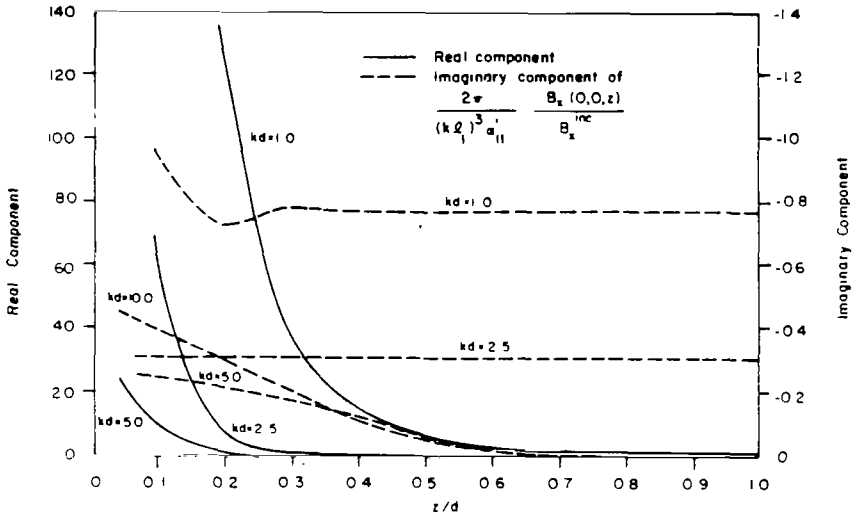

Fig. 2.24. x Component of Magnetic Field between Plates along a Line Passing through Center of Aperture and Perpendicular Plates.

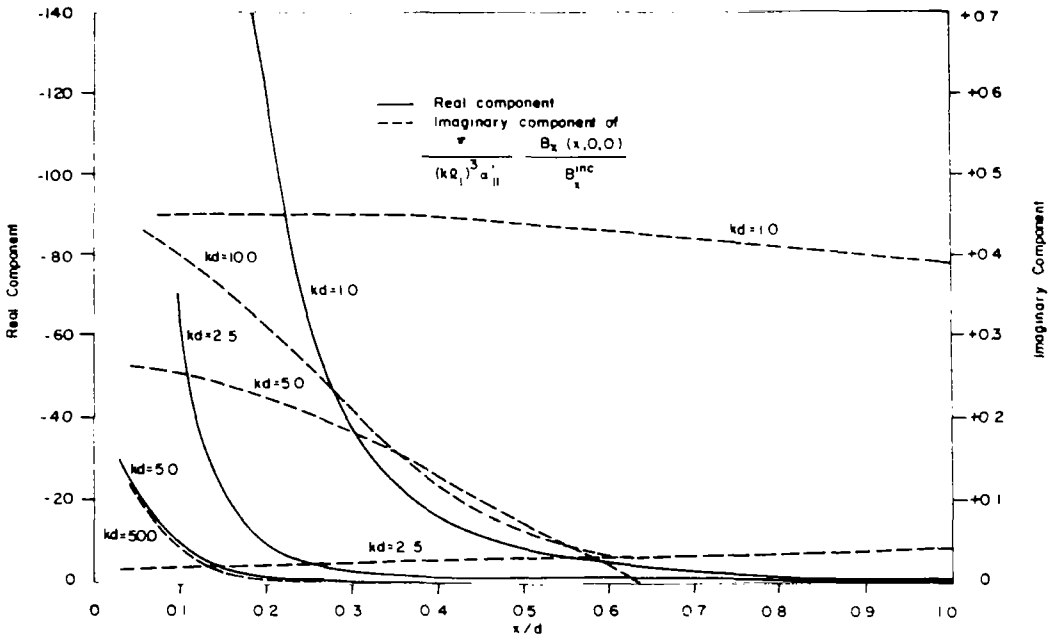

Fig. 2.25. x Component of Magnetic Field at Surface of Plate with Aperture.

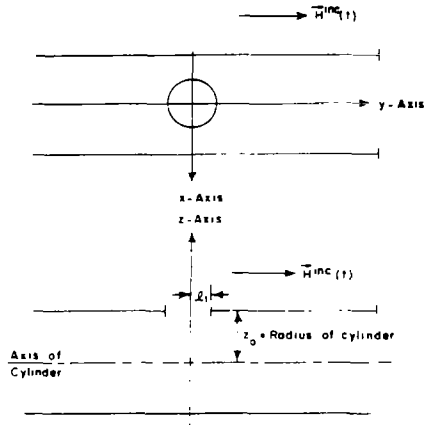

Fig. 2.26. Small Aperture in Long Cylindrical Shell Immersed in Uniform Axial Magnetic Field, $H^{inc}(t)$.

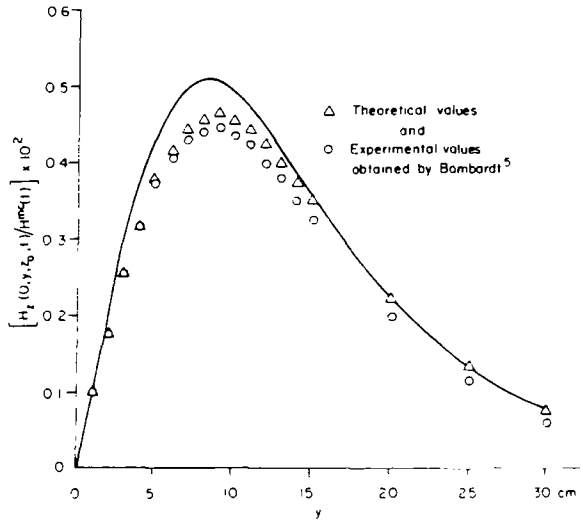

Fig. 2.27. Penetration Field for Circular Aperture in Long Cylindrical Shell Immersed in Uniform Axial Magnetic Field, $H^{inc}(t)$, z_0 = 16.5 cm and ℓ_1 = 5 cm.

$$E^{inc}(t) = \frac{e}{t_r} E^{inc}(t_r) t e^{-t/t_r} \qquad (2.26)$$

as his excitation, where t_r is the rise time of the incident field, $E^{inc}(t_r)$ is its peak value, and e = 2.71828. The polarization is shown in Fig. 2.26, and the normalized magnetic field at points on the cylinder axis is shown in Fig. 2.27. Notice that Taylor's results (solid line) based on his parallel-plate theory agree quite well with those obtained by Bombardt. The reader should observe that the curves of Fig. 2.27 provide the field as a function of position; for the geometries under study, the time variation of the field on the axis is the same as that of the excitation.

D.3 Slot in Front Plate

If the aperture in the front plate is a uniform-width slot of infinite length and is excited by an incident plane wave whose electric field is in a direction transverse to the slot axis, as illustrated in Fig. 2.28, the field which reaches the interior region can be computed, and the TEM wave which is guided by the plates away from the slot can be determined (Ref. 2.28). When the slot is narrow compared with the wavelength and the plate separation, the slot field retains the essential features of that found in such a slot in a single, isolated plate, i.e., the distribution of Eq. 2.19. However, as is evident from Fig. 2.29, the strength of the field differs from that of the field in the isolated, slotted plane, and, as expected, depends upon the distance between the two conducting planes. For $h < \lambda/2$, only the TEM mode exists in the guide remote from the slot. The electric field of this propagating TEM mode, apart from the factor $e^{\pm jkx}$, is given as a function of h in Fig. 2.30.

From a study of Fig. 2.29, one observes that approximating the field in the narrow slot by means of Eq. 2.19 is justifiable for a narrow slot, if extreme accuracy is not required in a given application. This observation enables one to greatly simplify the labor of estimating the field which reaches the interior region between the plates.

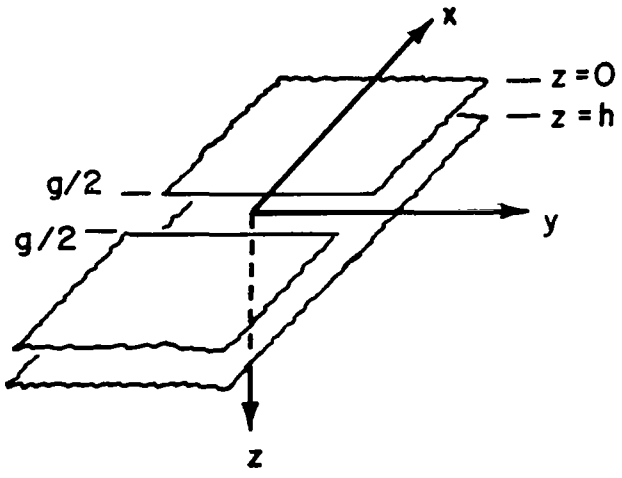

Fig. 2.28. Slotted Parallel-Plate Waveguide.

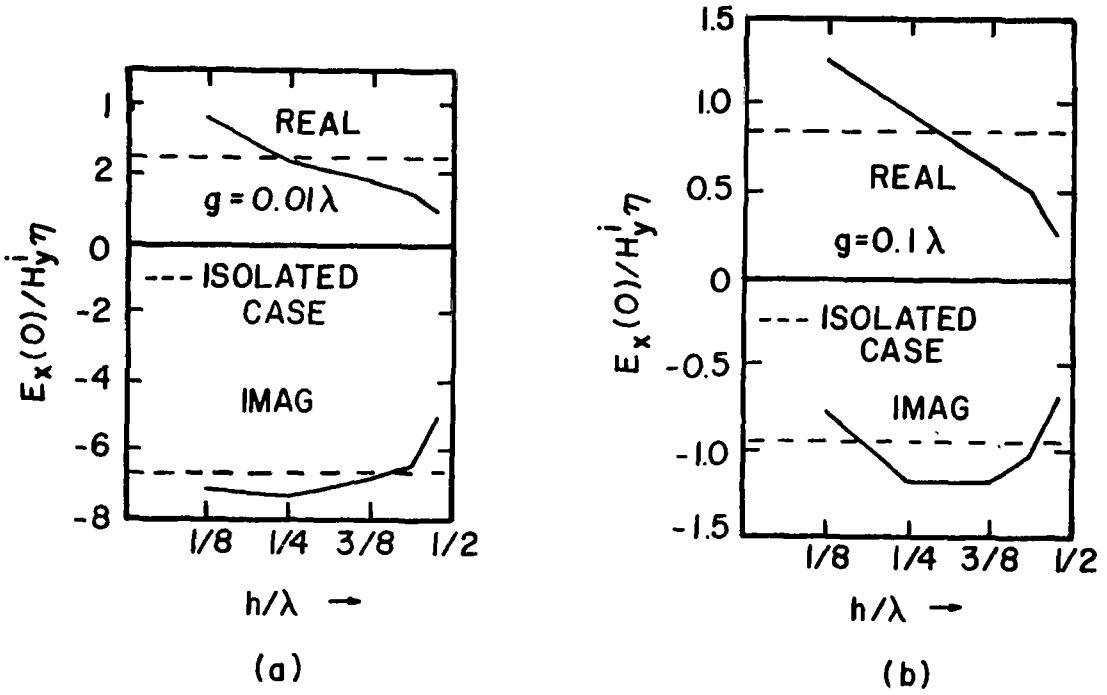

Fig. 2.29. Electric Field E_x at Center of Slot in Plate of Parallel-Plate Waveguide as a Function of Plate Separation h (Normally Incident, TE Illumination).

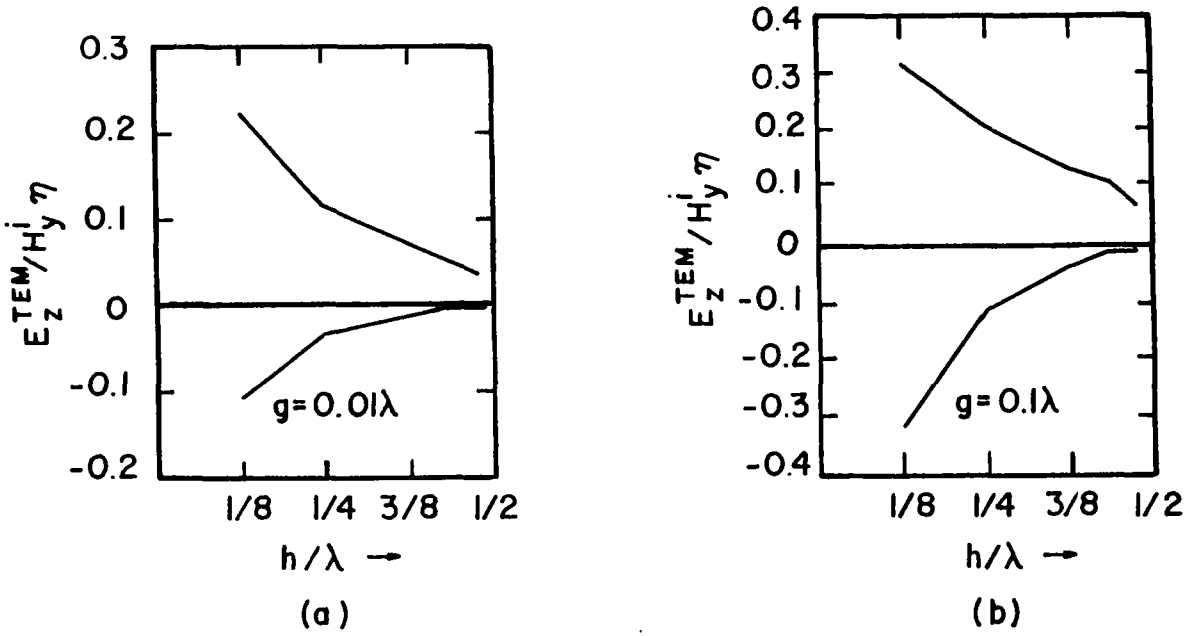

Fig. 2.30. TEM Electric Field in Slotted Parallel-Plate Guide Due to Normally Incident TE Illumination.

E. Wire Behind Aperture/Screen

E.1 Introduction

In this section results are presented for the problem of a wire excited by an electromagnetic field which penetrates an aperture-perforated conducting screen (Refs. 2.30, 2.31). A problem to be considered here is shown in Fig. 2.31 where one sees an infinitely long wire behind a planar conducting screen in which a slot has been cut. The screen is assumed to be perfectly conducting, vanishingly thin, and of infinite extent. The wire is also perfectly conducting and excited by the electromagnetic field which passes through the aperture. Results are given for the case of an infinitely long, thin wire and a small hole.

E.2 Transmission Line Equivalent Circuit for Wire Behind Aperture

In Fig. 2.31 is shown a thin wire of radius $a (a/d << 1)$ whose axis is parallel to the x-axis and at a distance d from a ground screen containing an electrically small aperture. The wire axis is located a distance ρ from the center of the aperture, which is centered at the coordinate origin. The distance ρ from the wire to the aperture is assumed to be somewhat larger than the maximum aperture dimension so that the field illuminating the wire through the aperture can be assumed to emanate from equivalent dipole moments.

Further, it is assumed that we are interested only in currents and/or voltages sufficiently far removed from the aperture that only TEM modes need be considered. The reflections caused by terminating loads on the line can thus be accounted for by standard transmission line techniques. With these assumptions, the transmission line-aperture interaction can be represented by the lumped circuit and source models of Fig. 2.32 (Ref. 2.31). The sources account for the TEM current induced on the line caused by fields illuminating the aperture from the region $z < 0$, while the lumped capacitance and inductance circuit elements account for the wire-aperture interaction caused by reflected TEM fields due to mismatched terminations. For nearly all combinations of the parameters, k, ρ,d, and a for which the assumptions hold, the elements C and L may be

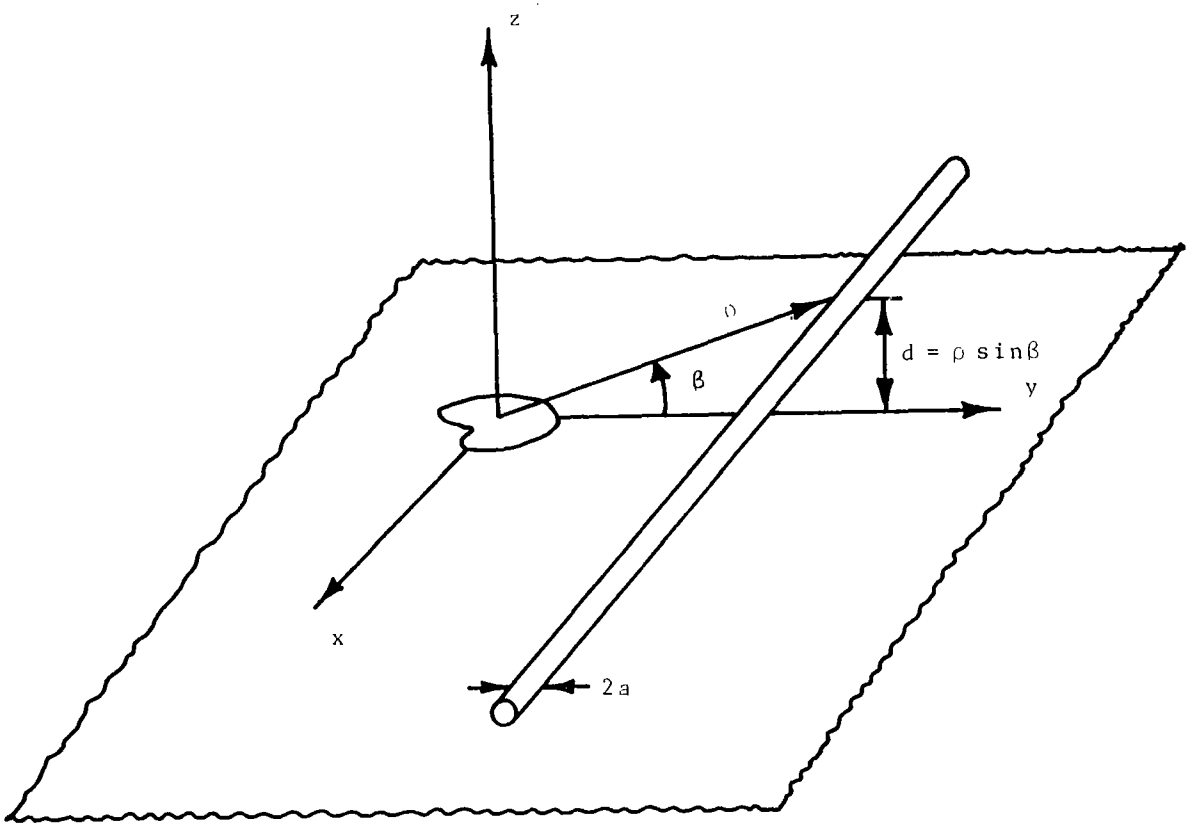

Fig. 2.31. Geometry of a Transmission Line Behind an Aperture in an Infinite Planar Ground Screen.

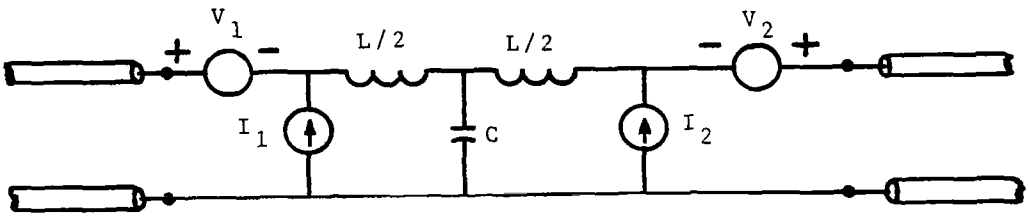

$$V_1 = \frac{jk \sin\beta}{2\pi\rho} \left[\alpha_e E_z^{sc}(\bar{0}-) - \alpha_{m,yy} \eta H_y^{sc}(\bar{0}-)\right]$$

$$V_2 = \frac{jk \sin\beta}{2\pi\rho} \left[\alpha_e E_z^{sc}(\bar{0}-) + \alpha_{m,yy} \eta H_y^{sc}(\bar{0}-)\right]$$

$$I_1 = V_1/Z_0$$

$$I_2 = V_2/Z_0$$

$$C = \frac{-4\varepsilon \alpha_e \sin^2\beta}{\left(\rho \ell \frac{2d}{a}\right)^2}$$

$$L = \frac{\mu \alpha_{m,yy} \sin^2\beta}{\pi^2 \rho^2}$$

$$Z_0 = \frac{\eta}{2\pi} \ell n\left(\frac{2d}{a}\right)$$

Fig. 2.32. Equivalent Circuit for Aperture Coupling to a Transmission Line Parallel to a Ground Screen.

ignored. It is, however, instructive to point out that the negative capacitance in Fig. 2.32 represents the lumped effect of the decrease in transmission line capacitance per unit length resulting from the decreased charging surface near the aperture. On the other hand, the additional magnetic flux paths which may penetrate the aperture may be thought of as increasing the inductance per unit length near the aperture, which effect is accounted for by adding a lumped inductance.

The equivalent voltage sources V_1 and V_2 of Fig. 2.32 may be expressed in the time domain by merely replacing the factor jk by $\frac{1}{c}\frac{\partial}{\partial t}$ where c is the speed of light in the surrounding medium. Thus, the time domain voltage sources are approximately proportional to the time derivative of the aperture fields. Fig. 2.33 shows a typical incident EMP waveform of the form

$$E^i(t) = A_0(e^{-\alpha t} - e^{-\beta t})$$

with

$$A_0 = 100 \text{ kV/m}, \quad \beta = 10^8 s^{-1}, \quad \alpha = 3 \times 10^6 s^{-1}$$

and arriving at an angle such that

$$E_t^{sc}(\bar{0}-, t) = \sqrt{2}\, E^i(t)$$

$$H_y^{sc}(\bar{0}-, t) = \frac{1}{\eta} E^i(t)$$

We assume a set of aperture and wire parameters as follows:

radius of circular aperture	10 mm
distance from aperture to transmission line	ρ = 22.4 mm
height of wire above ground plane	d = 10 mm
line length in (+x) direction	2.1 m
line length in (-x) direction	3.0 m
load resistance at (+x) port	10 kΩ
load resistance at (-x) port	10 Ω

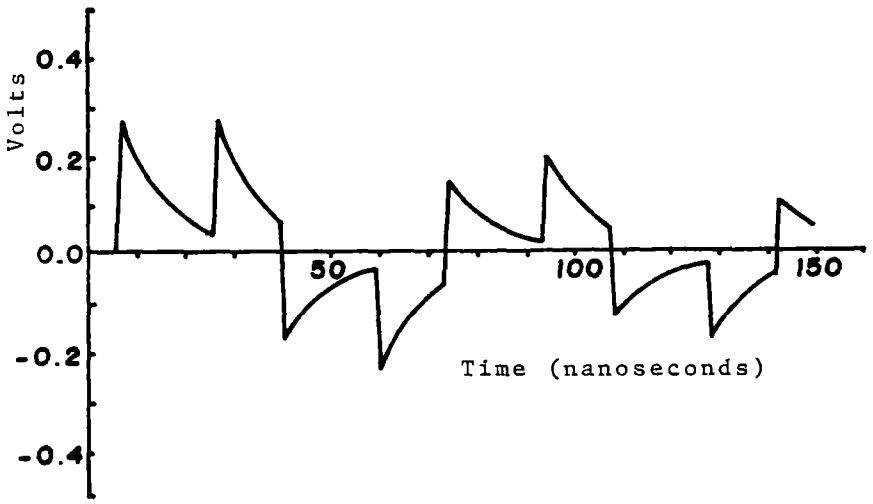

Fig. 2.33. Time Domain Voltage Observed on a Transmission Line Excited through an Aperture by a Transient Waveform.

The resulting voltage across the 10 kΩ resistor is shown in Fig. 2.33 as computed from the time domain source model by following in time the various induced waveforms and their reflections on the line (Ref. 2.31). The differentiating effect of the aperture is apparent in the highly peaked signal that first arrives at the load. The succeeding discontinuities represent contributions from reflections at the terminations. Because the two terminations almost constitute a short and an open circuit, respectively, there is only a small decay in the peaks as a function of time.

F. Large Apertures

If the size of an aperture is large or the frequency sufficiently high that the largest dimension of an aperture is no longer a small fraction but is rather on the order of a wavelength, then the small-aperture approximations used in the previous sections are no longer valid. Fortunately, in the EMP applications this situation is relatively rare because of the band-limited nature of an incident EMP pulse. Almost never occurring in EMP problems are cases when aperture dimensions are several wavelengths long, where the Kirchhoff diffraction approximation or the more accurate geometrical diffraction theory (GTD) would be appropriate. Consequently, we restrict our consideration to apertures whose maximum dimensions are on the order of no more than a few wavelengths. For such apertures, numerical techniques must be employed to accurately determine aperture penetration.

The penetration of fields through circular apertures of moderate size has been examined by numerical methods by Graves, et al (Ref. 2.32). Although the results obtained exhibit some numerical convergence difficulties, they nevertheless illustrate features of the transistion from the electrically small to the moderate-sized aperture. Figs. 2.34 and 2.35 show the aperture electric field in both principal planes for a circular aperture of radius 0.25λ. The illumination is a normally incident plane wave whose electric vector is polarized along the y-axis.

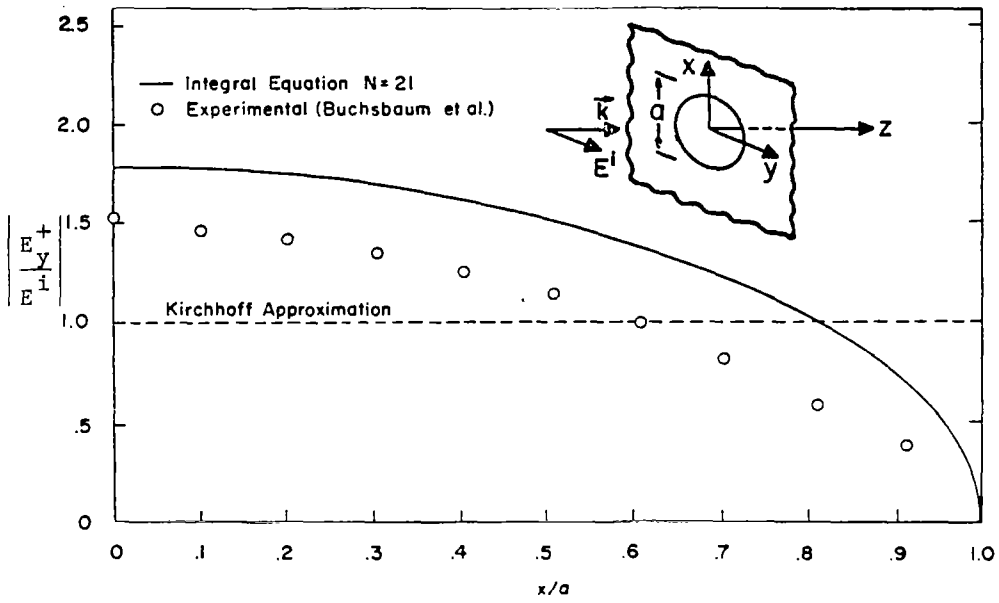

Fig. 2.34. H-Plane Distribution of Electrical Field within Aperture of 0.5λ in Diameter for Normal Incidence.

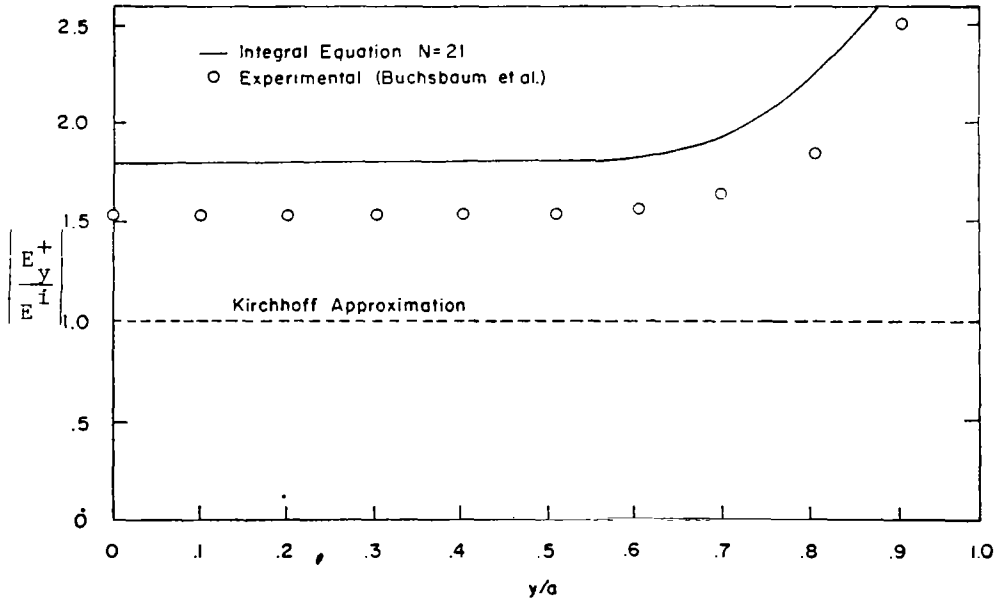

Fig. 2.35 E-Plane Distribution of Electrical Field within Aperture of 0.5λ in Diameter for Normal Incidence.

Note the nearness of the aperture field distribution to the Kirchhoff approximation. Also observe that according to the Kirchhoff approximation the aperture field distribution is close to the incident field in the aperture region. Some comparisons with experimental results (Ref. 2.33) are also given in the figures.

Aperture fields in square apertures have been computed by Mittra and Rahmat-Samii (Ref. 2.34), and they present comparison of the dominant aperture field component along the two principal planes for a square and circular aperture given in Fig. 2.36 The dashed line curves (---) represent measured data (Ref. 2.35).

Figs. 2.37 and 2.38 show the field penetrations of the electric and magnetic field along the axis of a circular aperture. The components of the penetrating fields shown correspond to those of the incident plane wave.

G. Cavity-Backed Apertures

G.1 Introduction

Apertures in missiles or aircraft skins often should be treated as cavity-backed apertures wherein the dipole moments used to represent the aperture are corrected for the multiple reflections which take place from the walls of the cavity-like region behind the aperture. These reflections often influence the aperture field levels, particularly near frequencies at which the cavity itself is resonant. Unfortunately, there is little data available on this important problem.

In this section, results are given for the magnetic field penetration into an open-ended circular cylindrical tube, both with and without an aperture (Ref. 2.29). A simple formula for the magnetic field penetrating a rectangular cavity in an infinite ground plane is also given (Ref. 2.36). The field penetration of a slotted circular cylinder with the incident electric field polarized along the slot axis has been solved by Senior (Ref. 2.37). Finally, penetration into a sphere through a circular aperture is also treated by Senior (Ref. 2.38).

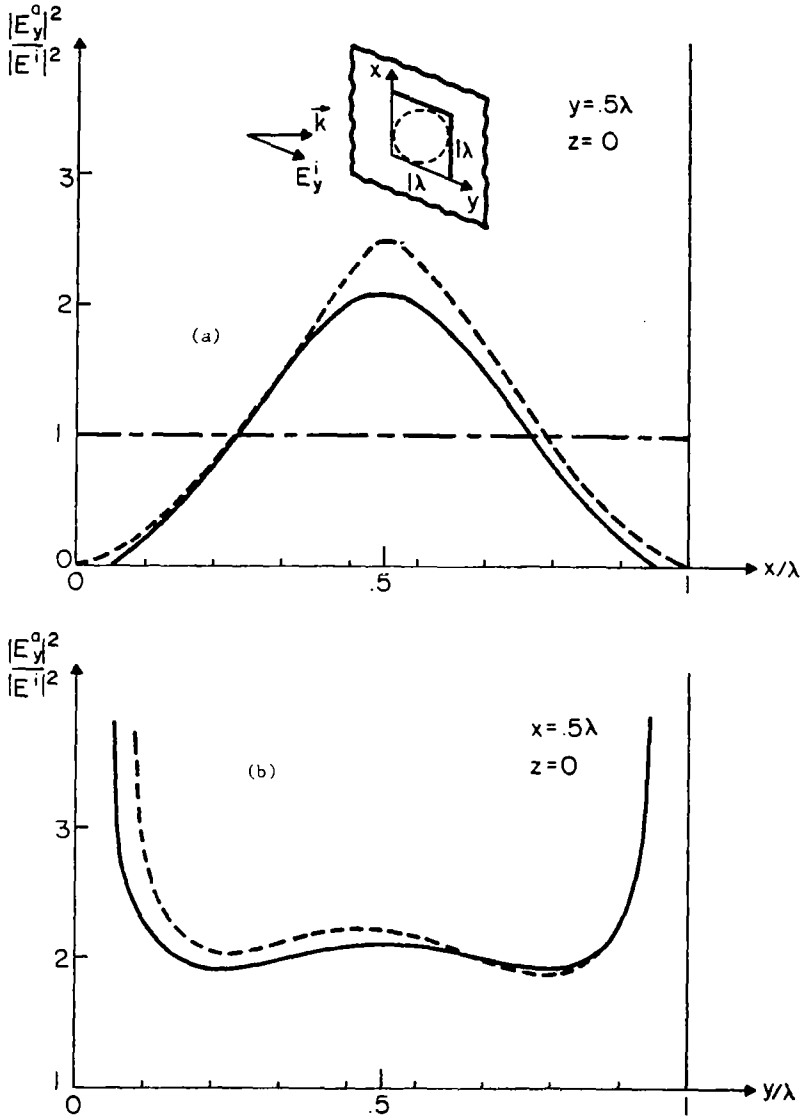

Fig. 2.36. Intensity distribution of the E_y-field sampled along the principal axes of a 1λ × 1λ square aperture and a circular aperture of radius 1λ. (a) Intensity distribution sampled along a line parallel to the x-axis and passing through the center. (b) Intensity distribution sampled along a line parallel to the y-axis and passing through the center. Integral equation solution (———). Experimental results (---) from Robinson (Ref. 2.35).

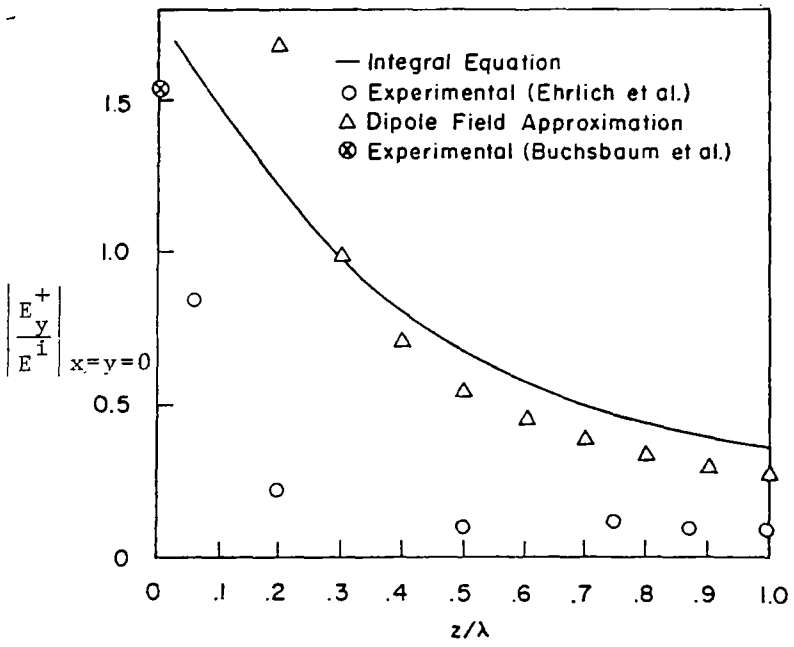

Fig. 2.37. Distribution of y Component of Electric Field Penetrating Aperture of 0.5λ Diameter for Normal Incidence.

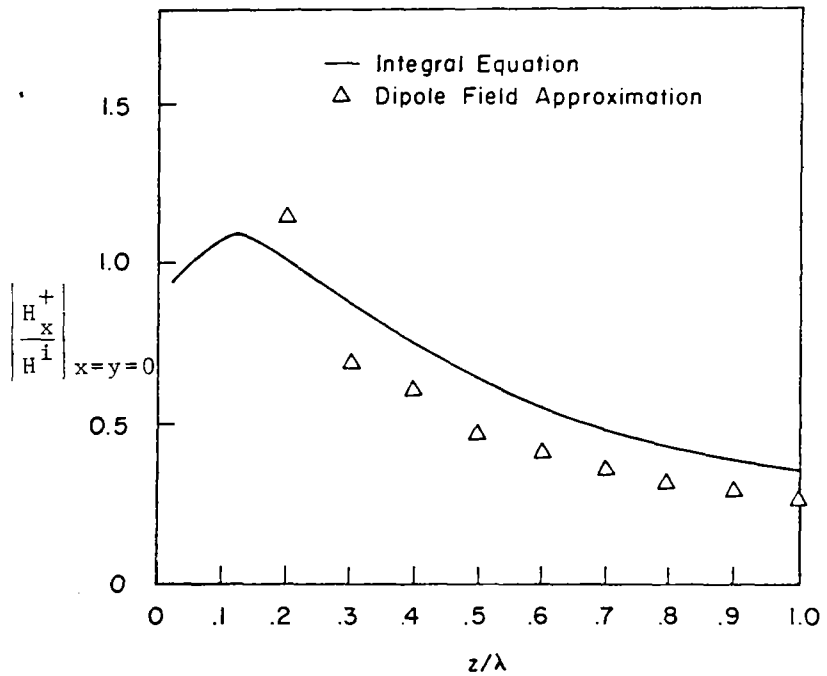

Fig. 2.38. Distribution of x Component of Magnetic Field Penetrating Aperture of 0.5λ in Diameter for Normal Incidence.

G.2 Magnetic Field Penetration into an Open-Ended Circular Cylinder, with and without an Aperture

Bombardt (Ref. 2.29) considers the degradation in magnetic field shielding by the presence of an aperture in a long, open-ended hollow conducting tube. He considers a transient exciting field which is essentially uniform in the region about the cylinder and whose temporal variation is

$$B_z^{inc} = A\, e^{-\alpha t} \sin\beta t \qquad (2.27)$$

$$A = 2.07 \times 10^{-2}\ \omega/m^2$$

$$\alpha = 2.09 \times 10^{5}\ s^{-1}$$

$$\beta = 0.73 \times 10^{5}\ s^{-1}$$

The internal axial field in the cylinder resulting from the incident field above is found to be (Ref. 2.29)

$$B_z^{int} = \frac{A(a/b)^{\frac{1}{2}}\,\omega_1}{\alpha^2 + (\beta - \omega_1)^2} \left\{ \alpha\, e^{-\omega_1 t} - \left[\alpha\cos\alpha t + (\beta - \omega_1)\sin\alpha t \right] e^{-\beta t} \right\} \qquad (2.28)$$

where

a = outer radius of the cylinder

b = inner radius of the cylinder

$$\omega_1 = \frac{2}{\mu\sigma(a-b)}$$

$$\sigma = 5.56 \times 10^{7}\ \text{mho/m}$$

Fig. 2.39 compares experimental measurements with results computed from Eq. (2.28) above. For this axial field component, there is almost no

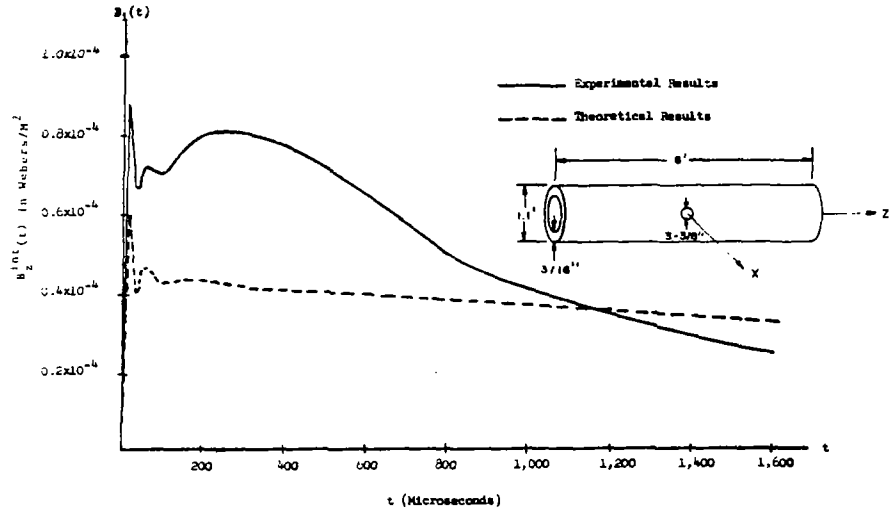

Fig. 2.39. Comparison of Theoretical and Experimental Results For a Hollow Copper Cylinder with no Apertures (Late Time).

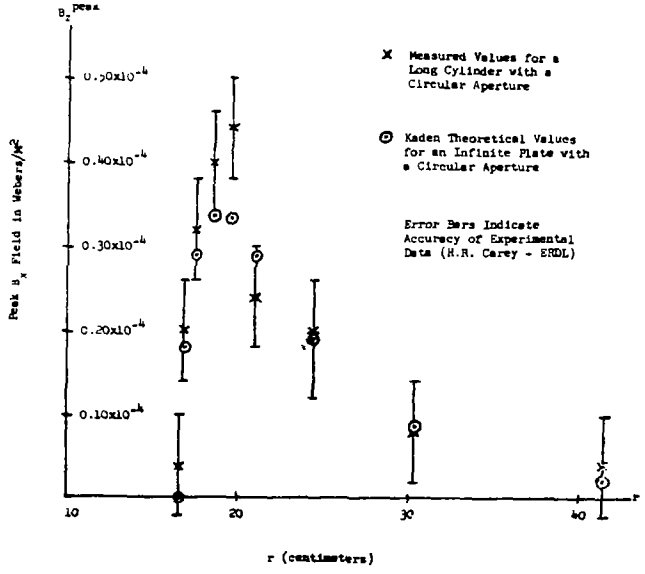

Fig. 2.40. Comparison of Theoretical and Experimental Peak Field Values for the Aperture Problem.

change when an aperture is introduced. For the component transverse to the cylinder axis, however, the corresponding change is much greater. The transient peak of this transverse field component is plotted in Fig. 2.40. The abscissa represents the distance from the center of the aperture to a measuring point on the cylinder axis. Also shown for comparison are theoretical values for the field behind an infinite planar screen with a circular aperture. The peak transverse field is seen to occur almost directly behind the aperture edge at r = 20 cm and the field is small directly behind the aperture.

G.3 Magnetic Field Penetration into a Rectangular Cavity

The magnetic field penetration into an open rectangular cavity has been studied in Ref. 2.36. The magnetic field at the aperture is assumed to be constant and is oriented in the x direction. The cavity opening is b meters by a meters wide in the x and y directions, respectively, and the cavity is h units deep (Fig. 2.41). It is found that the $\bar{H}$ field internal to the cavity is given approximately by

$$\bar{H}(x,y,z) = \frac{4\,H_x(0,0,0+)}{\pi \cosh \frac{\pi h}{b}} \left[\hat{x} \cos \frac{\pi x}{b} \cosh \frac{\pi(z+h)}{b} + \hat{z} \sin \frac{\pi x}{b} \sinh \frac{\pi(z+h)}{b} \right] \tag{2.29}$$

It is assumed in the above that h/b > 0.5 and that the observation points are not close to the aperture, but are well down inside the cavity. Note that the field variation along the y direction is assumed uniform.

G.4 Field Penetration into a Finite Coaxial Cavity via a Hatch Aperture

Equivalent circuits have been developed to describe the quasi-static field penetration into multiply-connected cavities through hatch apertures (Ref. 2.20). One of the most interesting examples is the penetration into

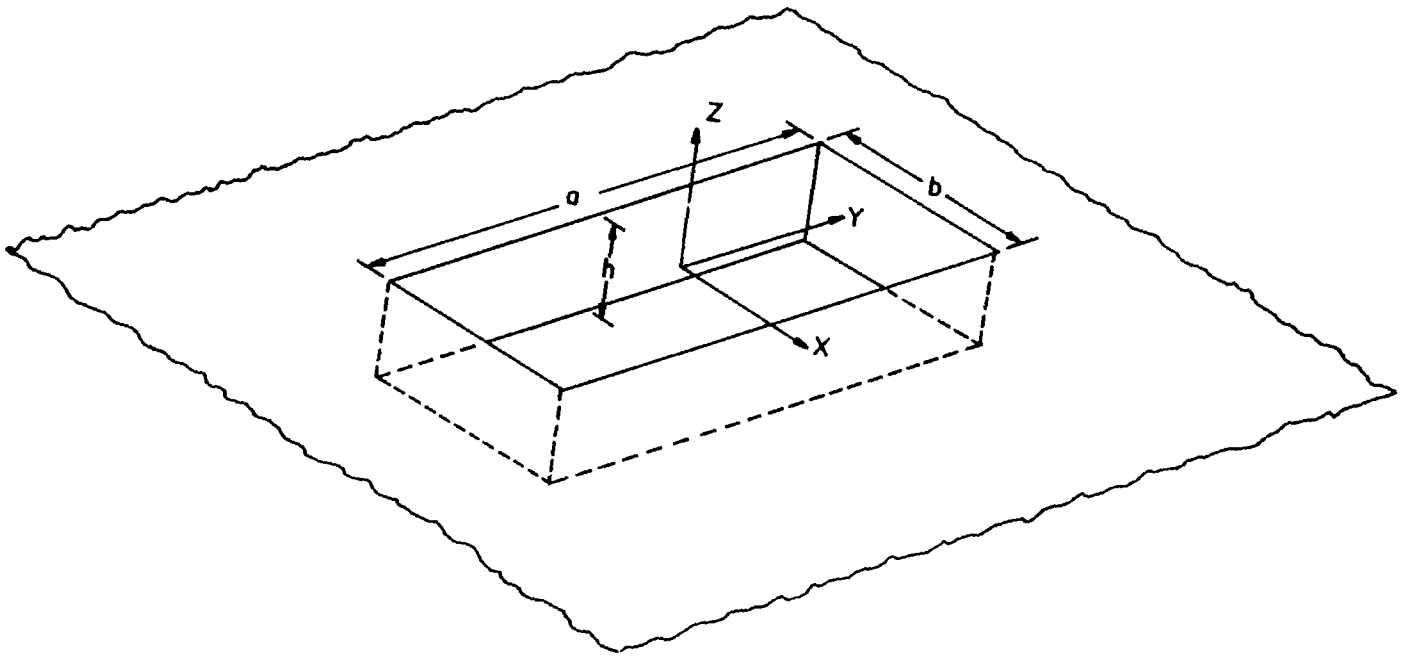

Fig. 2.41. Rectangular Cavity Opening into a Ground Plane.

a coaxial cavity via a two-adjacent-rectangular-hatch aperture as shown in Fig. 2.42. The coaxial cavity may be used to model a weapon bay, while the hatch aperture represents the door slits. The dominant magnetic field penetration can be represented by the equivalent circuit shown in Fig. 2.43, where

I_{sc}^{ℓ} = total current intercepted by the hatch aperture
= $a\theta_o \times$ (short-circuit skin current density)

R_ℓ = equivalent resistance of the door gasket

L_ℓ = self-inductance of the hatch

L_c = inductance of the coaxial cavity

M = mutual inductance between hatch aperture and the coaxial cavity

The total current I_c^i induced on the center conductor is given by

$$\frac{I_c^i}{I_{sc}^{\ell}} = \frac{M}{L_c} \frac{1}{1 + s\, L_\ell / R_\ell} \tag{2.30}$$

G.5 Slot in a Circular Cylinder

The problem of field penetration into a slotted circular cylinder has been treated by Senior (Ref. 2.37) by means of a numerical approach. The geometry, depicted in the inset of Fig. 2.44, consists of a circular cylinder with an angular sector of half-ange θ_0 removed. The electric field vector of the incident plane wave is polarized parallel to the cylinder axis. Although this polarization does not provide maximum coupling to the interior, it is, nevertheless, an important case of interest.

Figs. 2.45 and 2.46 show aperture field variations for normally illuminated apertures of half-angle $\theta_0 = 10°$ and 30°, respectively, for various values of ka. In all the figures, the incident field is assumed to be of the form

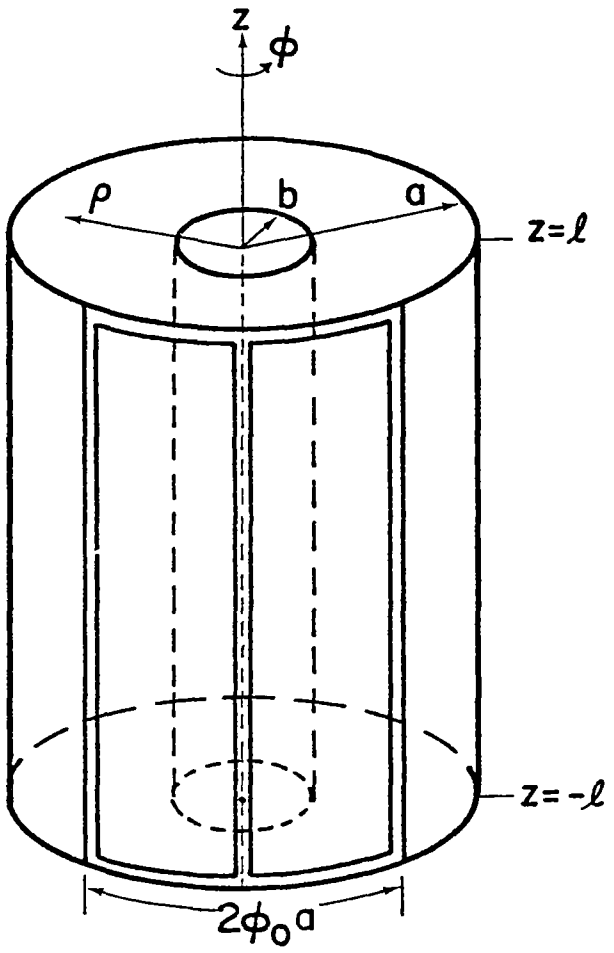

Fig. 2.42. Geometry of a coaxial cavity with slits.

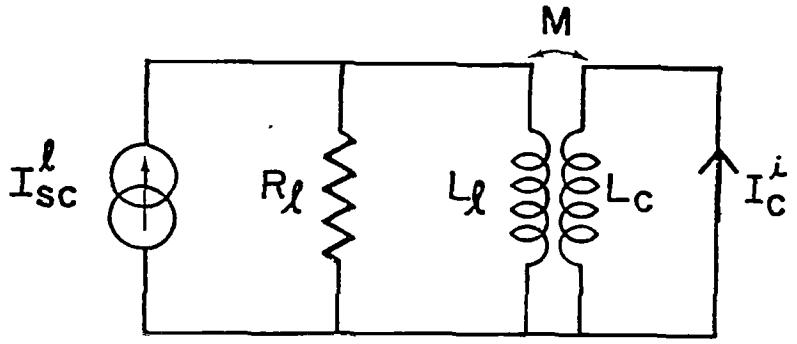

$$L_\ell = \frac{\mu\pi}{2\Omega}(a\phi_o + 2\ell)$$

$$L_c = \frac{\mu\ell}{\pi}\ell n\,(a/b)$$

$$M = \frac{\mu\phi_o}{3\pi\Omega}(a\phi_o + 3\ell)$$

$$L_\ell L_c \gg M^2$$

Fig. 2.43. Circuit representation of Fig. 2.42.

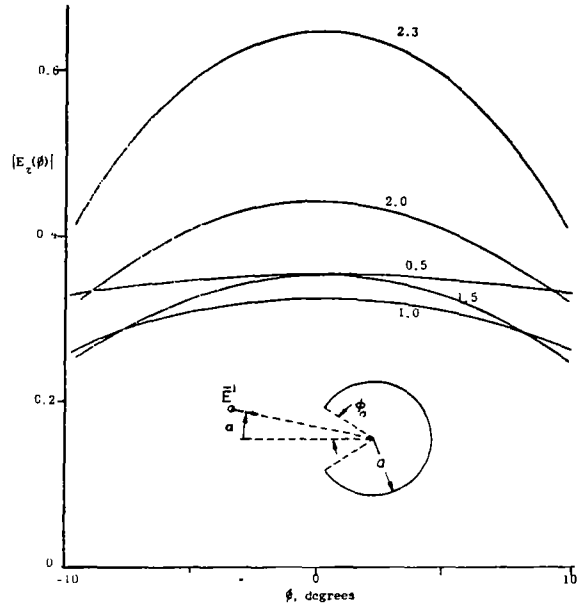

Fig. 2.44. Aperture Field Amplitudes for $\phi_o = 10^o$, $\alpha = 0$ and Various Values of ka.

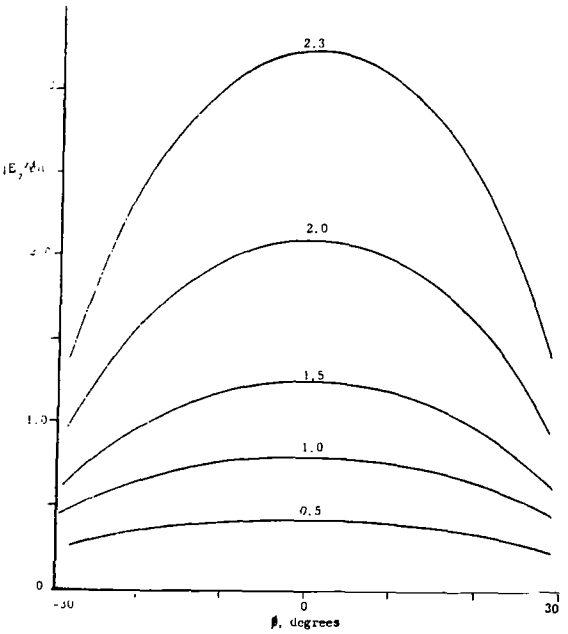

Fig. 2.45. Aperture field amplitudes for $\phi_o = 30^o$, $\alpha = 0$ and Various Values of ka.

$$\bar{E}^i = \hat{z}\, e^{+jk\rho\cos\phi}$$

It is noted that the shape of the aperture field is relatively insensitive to the frequency. The field at the aperture center is depicted in Fig. 2.46 which shows the dramatic effects of interior resonances near ka = 2.4. Figs. 2.47 and 2.48 show the electric field variation along the cylinder diameter from the aperture to the cylinder wall for various frequencies. Note the dramatic increase in interior fields for the wider aperture and for frequencies near the interior resonance. Fig. 2.49 shows the cavity field amplitude at the center of the cavity as a function of frequency. Again, the effects of resonance are seen to be quite dramatic.

G.6 Circular Aperture in a Spherical Cavity

Senior (Ref. 2.38) has considered the electromagnetic penetration of a spherical cavity through a circular aperture. As shown in Fig. 2.50 the aperture is centered about the polar axis and the angle θ_0 specifies the angular extent of the aperture. The illumination is a plane wave incident normal to the aperture and polarized with its electric vector along the x direction. The magnitude of the two components of aperture electric field are given in Figs. 2.51 and 2.52 for a sphere of radius ka = 2.5. The basic features of the shapes of these curves remains essentially the same with changes in frequency.

Figs. 2.53 through 2.68 show the variation of the electric and magnetic fields along the sphere diameter from the aperture to the back of the cavity. In addition to the exact solution, various approximate solutions are given. In approximation A, the distribution of the field in the aperture is assumed to be that of the incident field but with an adjusted amplitude. The interior fields are then represented as in expansion in modes whose coefficients are computed from mode matching. Approximation C is essentially the Kirchhoff approximation wherein the aperture field is just the incident field and the interior fields are then computed from the assumed aperture field by Huygen's principle. In approximation D, the aperture is considered to be so small that it can

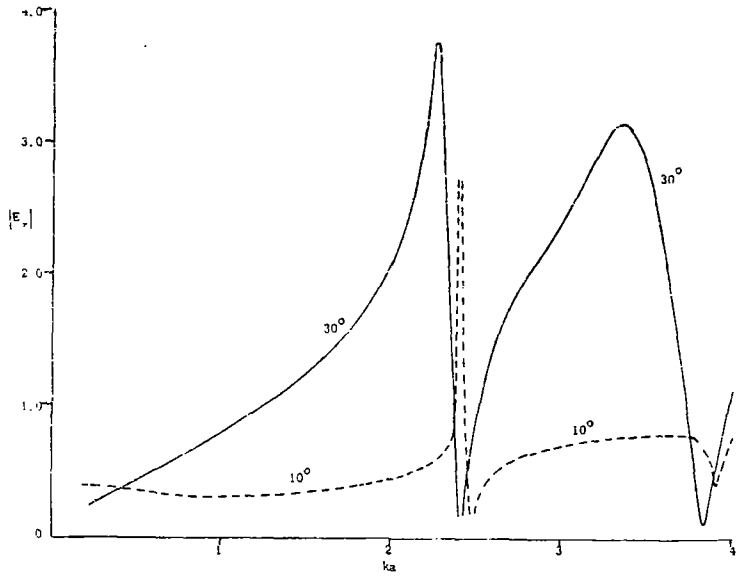

Fig. 2.46. Field Amplitude at the Center of the Aperture for $\emptyset_o = 10^o$ and 30^o, and $\alpha = 0$.

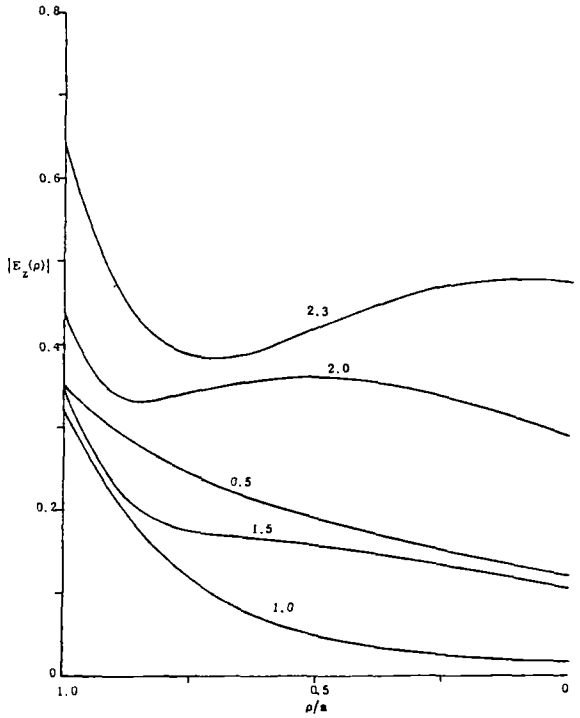

Fig. 2.47. Interior Field Amplitudes for $\emptyset_o = 10^o$, $\alpha = 0$ and Various Values of ka.

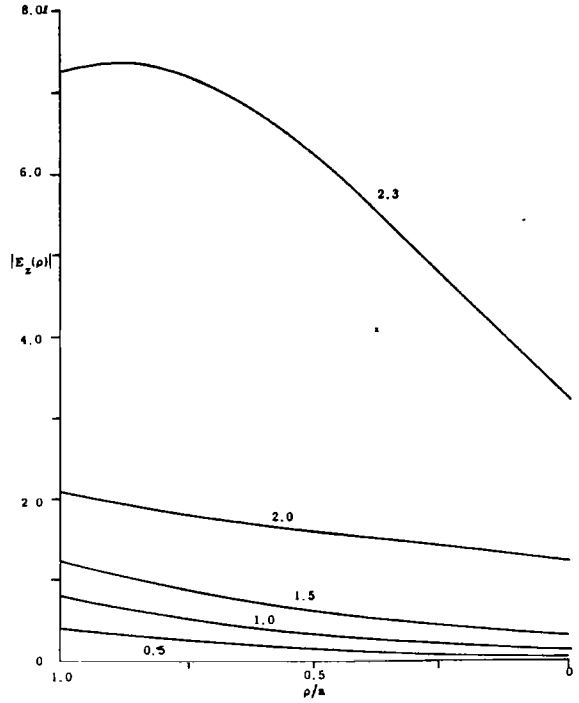

Fig. 2.48. Interior Field Amplitudes for $\phi_o = 30^\circ$, $\alpha = 0$ and Various Values of ka.

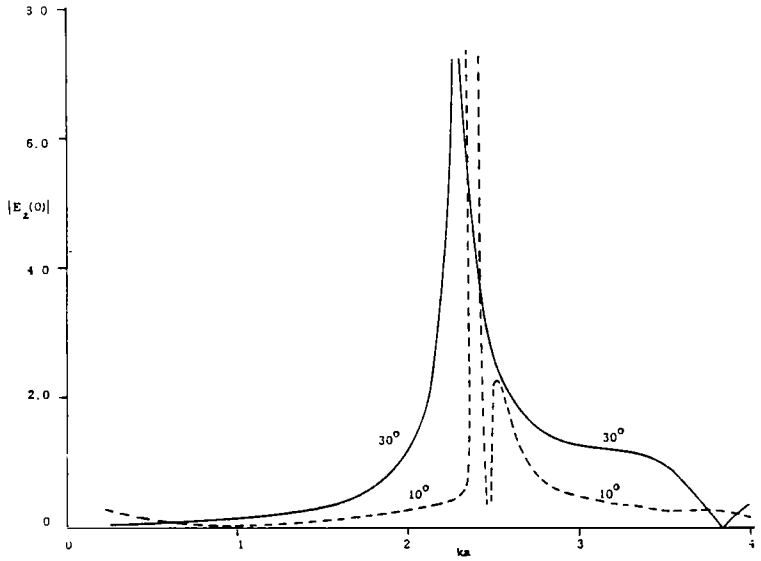

Fig. 2.49. Field Amplitude at the Center of the Cavity for $\phi_o = 10^\circ$ and 30°, and $\alpha = 0$.

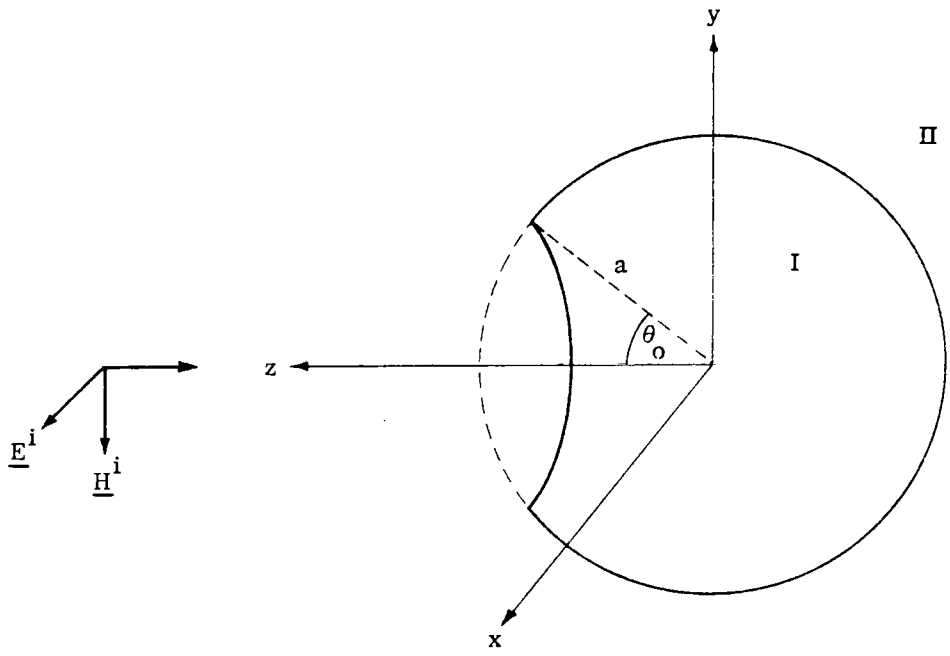

Fig. 2.50. Spherical Shell Geometry.

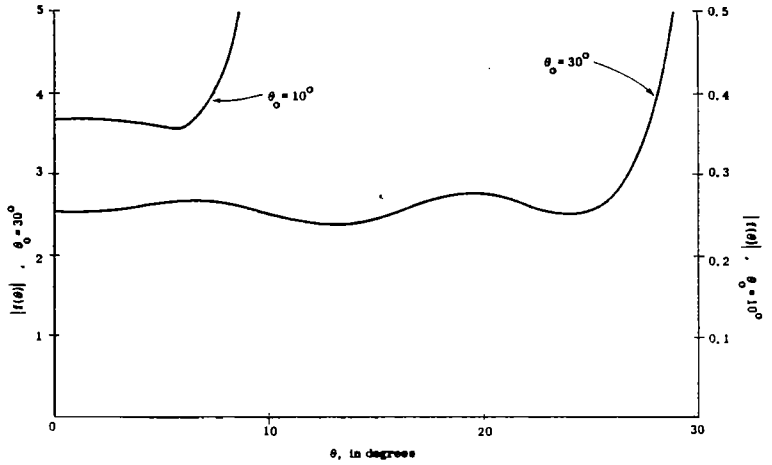

Fig. 2.51. The Amplitude of E_θ across the Aperture for ka = 2.5.

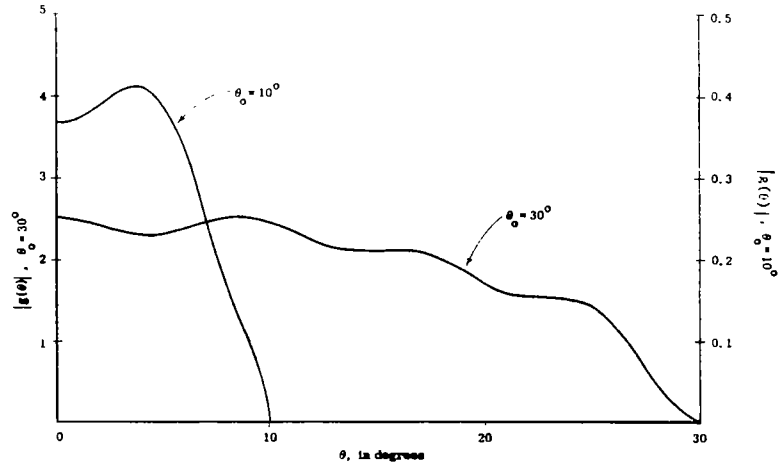

Fig. 2.52. The Amplitude of E_ϕ across the Aperture for ka = 2.5.

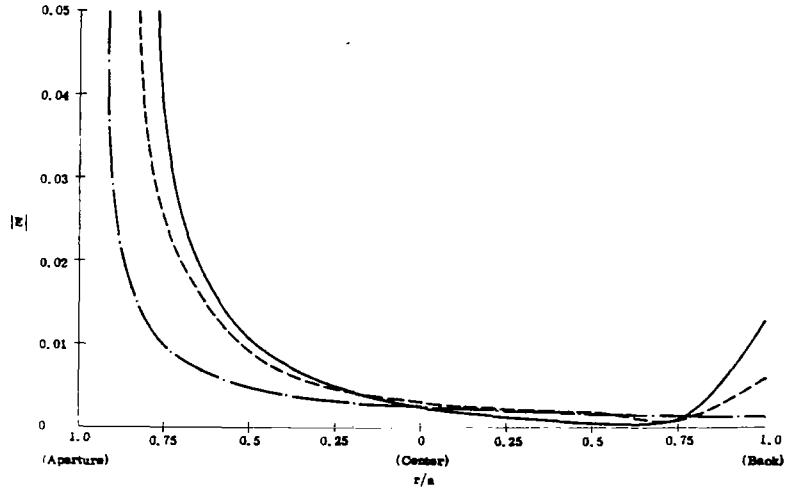

Fig. 2.53. Amplitude of the Electric Field along the Main Diameter for ka = 1.0, $\theta_o = 10^o$: Exact (———), Approx. A (----), Approx. D (— · —).

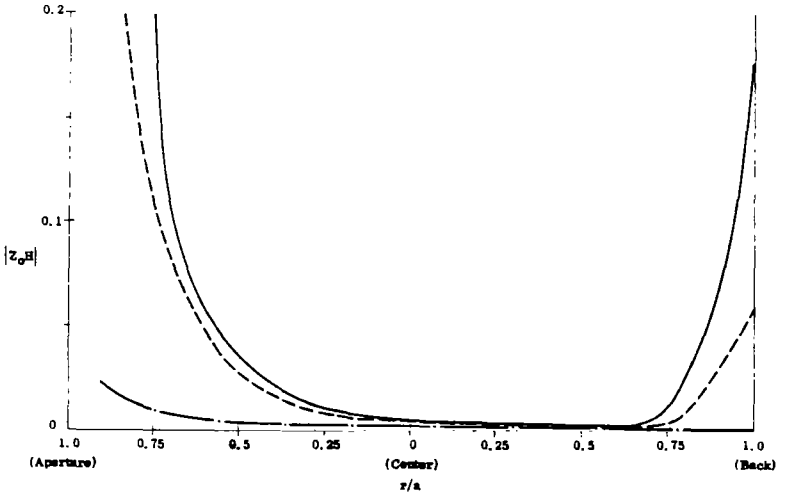

Fig. 2.54. Amplitude of the Magnetic Field along the Main Diameter for ka = 1.0, $\theta_o = 10^o$: Exact (———), Approx. A (----), Approx. D (— · —).

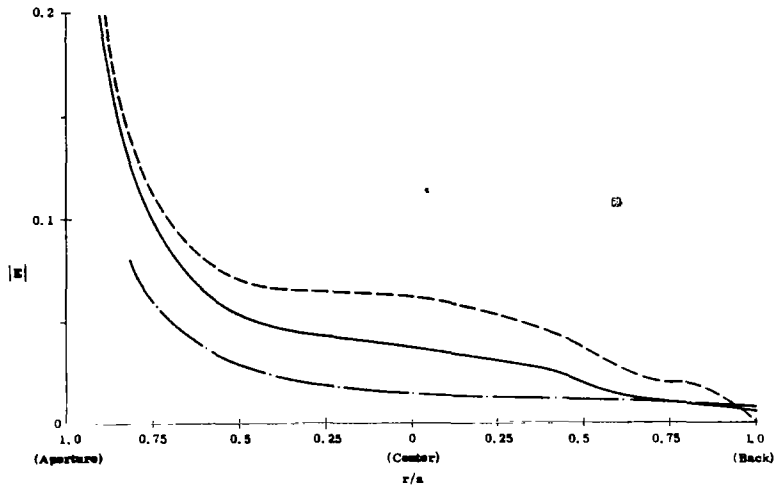

Fig. 2.55. Amplitude of the Electric Field along the Main Diameter for ka = 2.5, $\theta_o = 10^o$: Exact (———), Approx. A (----), Approx. D (— · —).

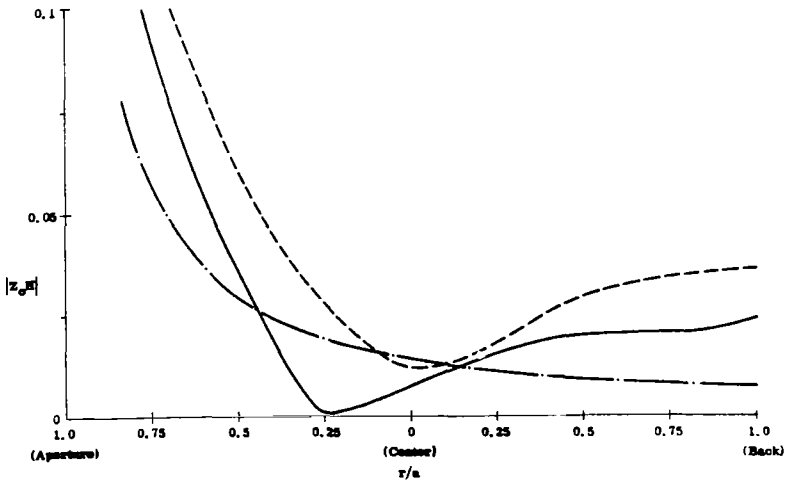

Fig. 2.56. Amplitude of the Magnetic Field along the Main Diameter of ka = 2.5, $\theta_o = 10^o$: Exact (———), Approx. A (----), Approx. D (— · —).

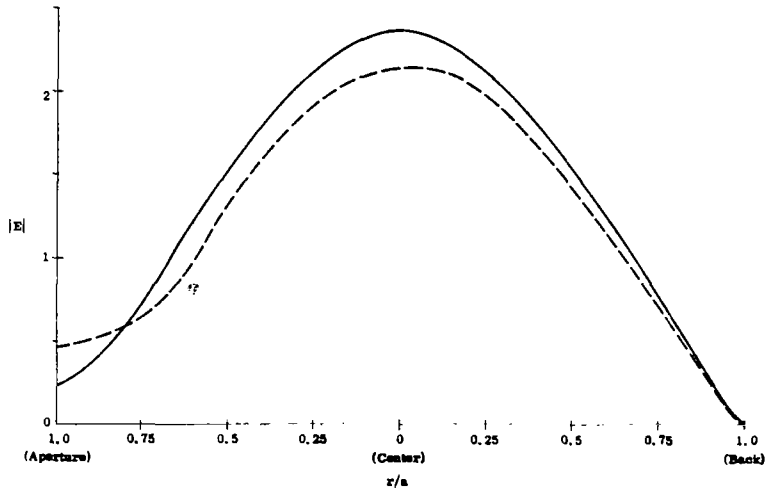

Fig. 2.57. Amplitude of the Electric Field along the Main Diameter for ka = 2.75, $\theta_o = 10^o$: Exact (———), Approx. A (----).

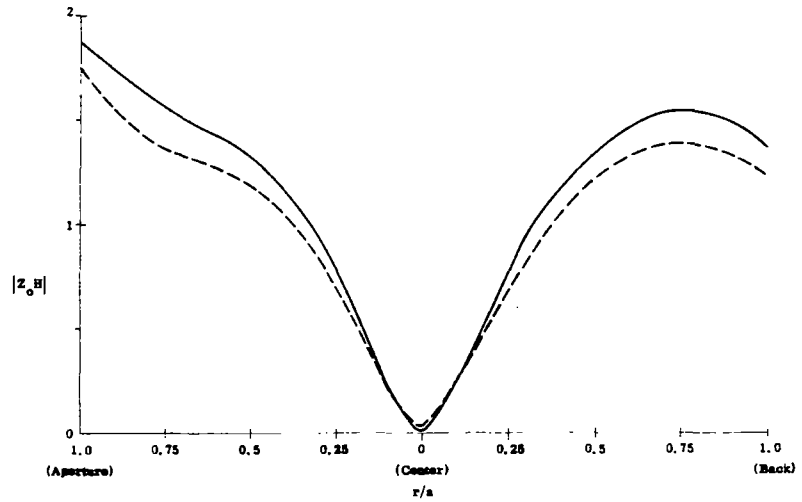

Fig. 2.58. Amplitude of the Magnetic Field along the Main Diameter for ka = 2.75, $\theta_o = 10^o$: Exact (———), Approx. A (----).

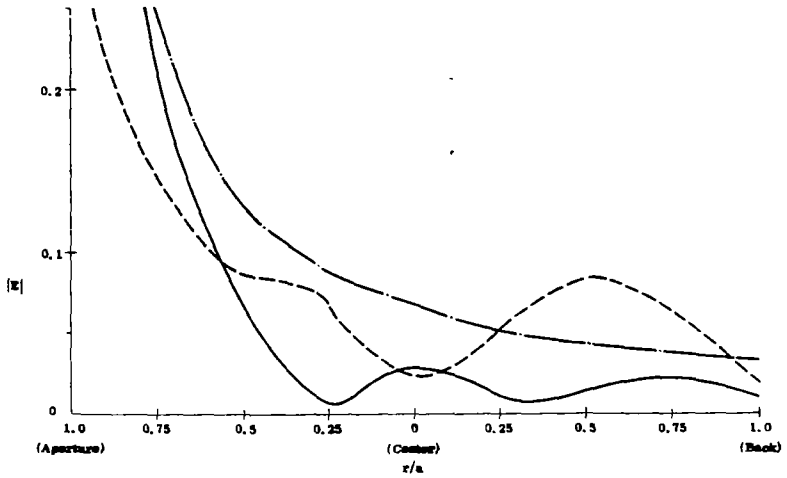

Fig. 2.59. Amplitude of the Electric Field along the Main Diameter for ka = 4.25, $\theta_o = 10^o$: Exact (———), Approx. A (----), Approx. C (— · —).

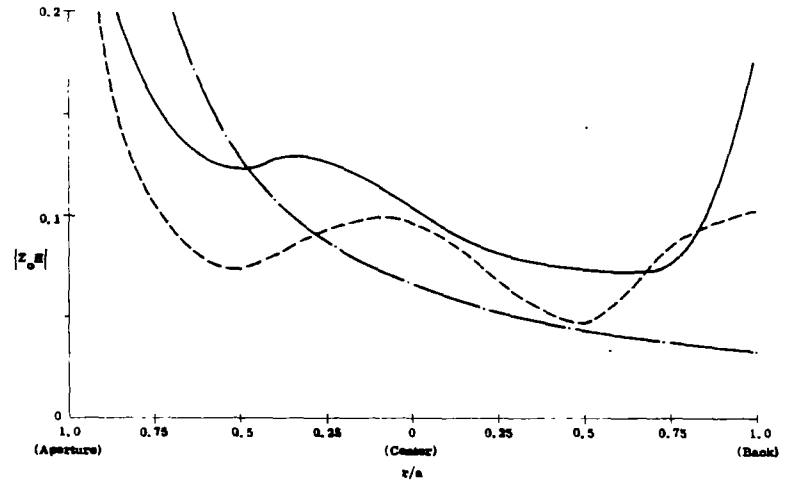

Fig. 2.60. Amplitude of the Magnetic Field along the Main Diameter for ka = 4.25, $\theta_o = 10^o$: Exact (———), Approx. A (----), Approx. C (— · —).

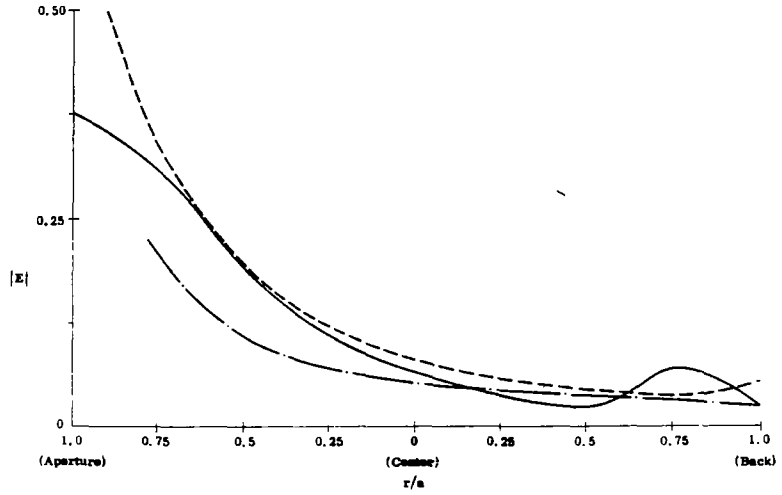

Fig. 2.61. Amplitude of the Electric Field along the Main Diameter for ka = 1.0, $\theta_o = 30^\circ$: Exact (———), Approx. A (----), Approx. D. (— · —).

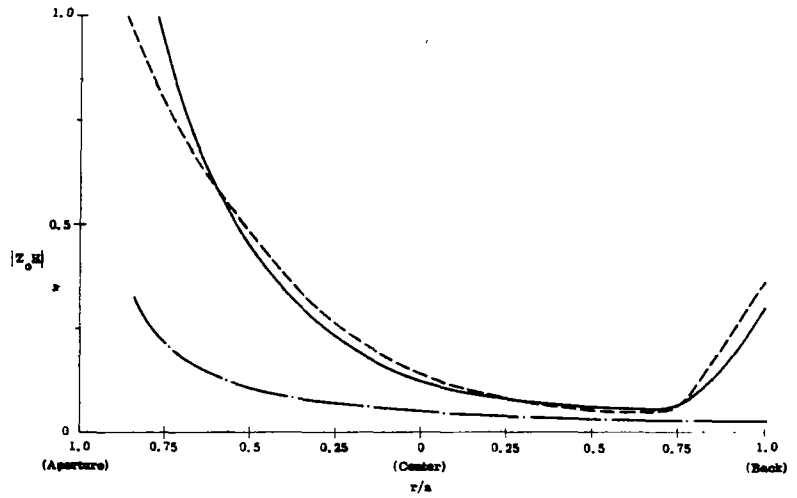

Fig. 2.62. Amplitude of the Magnetic Field along the Main Diameter for ka = 1.0, $\theta_o = 30^\circ$: Exact (———), Approx. A (----), Approx. D. (— · —)

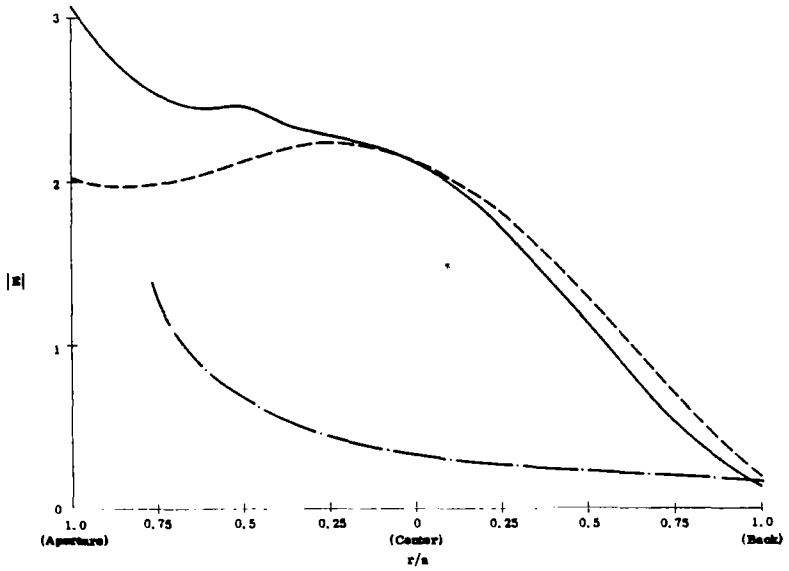

Fig. 2.63. Amplitude of the Electric Field along the Main Diameter for ka = 2.5, $\theta_o = 30^o$: Exact (———), Approx. A (----), Approx. D (— . —).

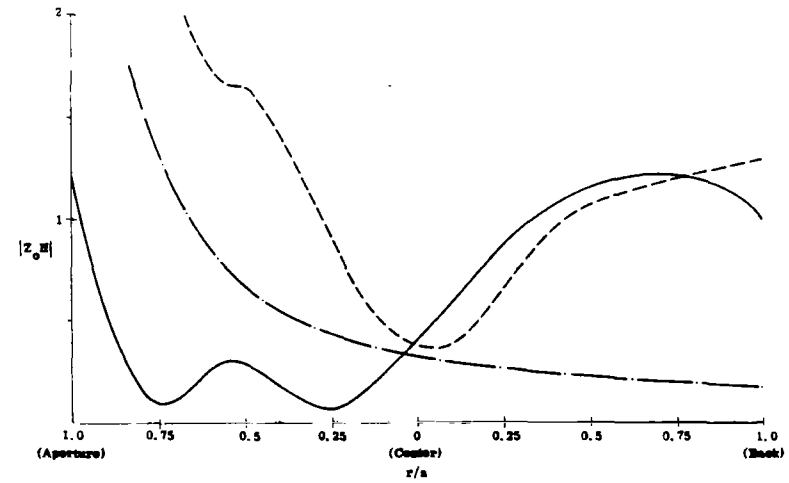

Fig. 2.64. Amplitude of the Magnetic Field along the Main Diameter for ka = 2.5, $\theta_o = 30^o$: Exact (———), Approx. A (----), Approx. D (— · —).

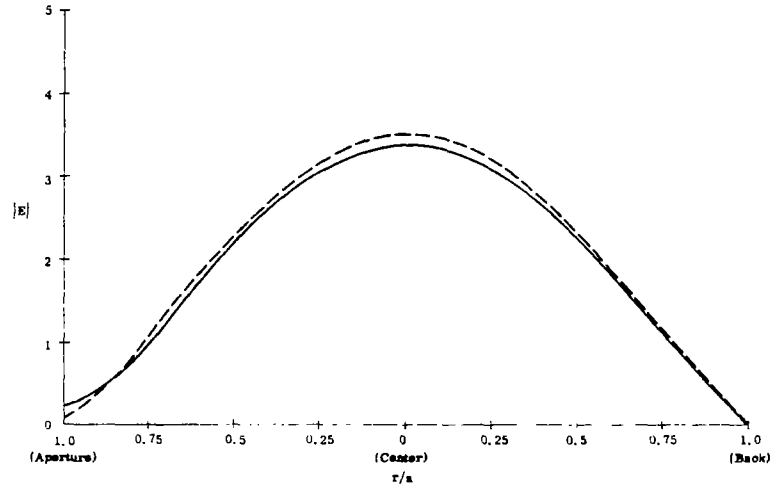

Fig. 2.65. Amplitude of the Electric Field along the Main Diameter for ka = 2.75, $\theta_o = 30^\circ$: Exact (———), Approx. A (----).

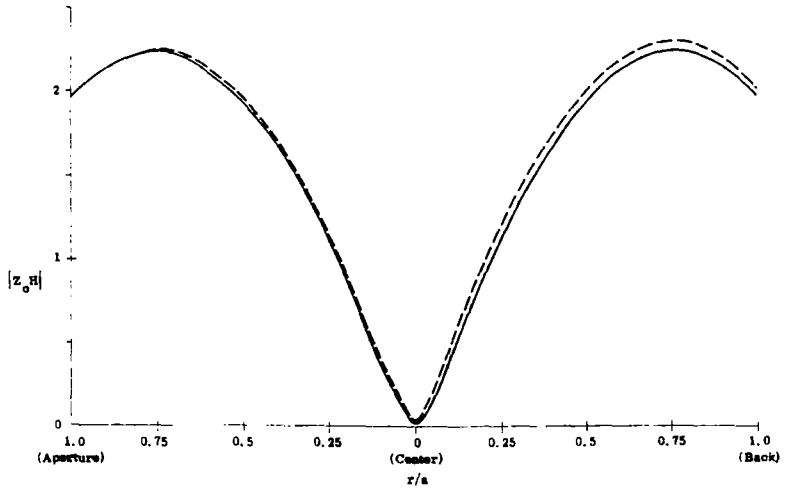

Fig. 2.66. Amplitude of the Magnetic Field along the Main Diameter for ka = 2.75, $\theta_o = 30^\circ$: Exact (———) Approx. A (----).

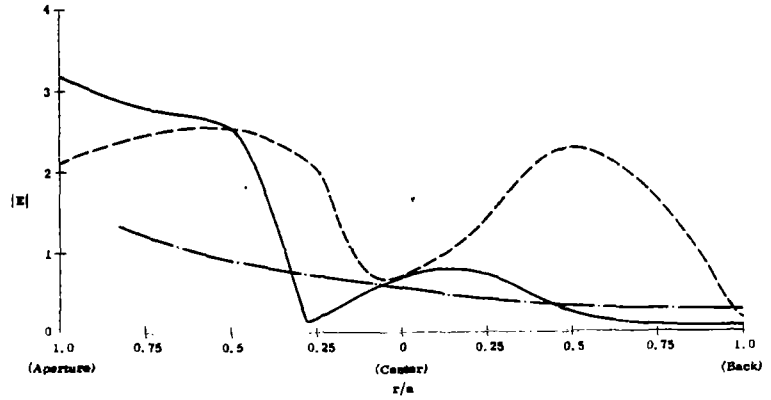

Fig. 2.67. Amplitude of the Electric Field along the Main Diameter for ka = 4.25, $\theta_o = 30^o$: Exact (———), Approx. A (----), Approx. C (— · —).

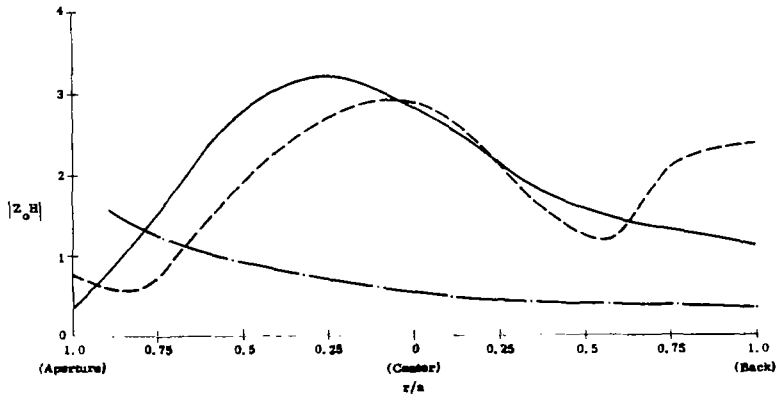

Fig. 2.68. Amplitude of the Magnetic Field along the Main Diameter for ka = 4.25, $\theta_o = 30^o$: Exact (———), Approx. A (----), Approx. C (— · —).

be represented by an equivalent magnetic current moment computed as if the aperture were in a planar sheet. The latter approximations, of course, do not take into account the presence of the cavity and hence, as the figures show, they exhibit no resonance effects. As can also be seen from the figures, such approximations should be confined only to very large cavities and to frequencies not near cavity resonances. The figures clearly show the strong influence of the cavity walls on the computed field distributions and indicate why it is usually necessary to include the cavity effects in computing aperture penetration.

References

2.1. Lord Rayleigh, "On the Incidence of Aerial and Electric Waves upon Small Obstacles in the Form of Ellipsoids or Elliptic Cylinders, and on the Passage of Electric Waves through a Circular Aperture in a Conducting Screen," Phil. Mag., Series 5, Vol. 44, No. 266, pp. 28 - 52; July, 1897.

2.2. Bethe, H. A., "Theory of Diffraction by Small Holes," Phys. Revs., Vol. 66, pp. 163 - 182; October, 1944.

2.3. Bouwkamp, C. J., "On Bethe's Theory of Diffraction by Small Holes," Philips Res. Repts., Vol. 5, pp. 321 - 332; October, 1950.

2.4. Bouwkamp, C. J., "Diffraction Theory," Repts. Prog. in Phys., Vol. 17, pp. 35 - 100; 1954.

2.5. Eggimann, W. H., "Higher-Order Evaluation of Electromagnetic Diffraction by Circular Disks," IRE Transactions on Microwave Theory and Techniques, Vol. MTT-9, No. 5, pp. 408 - 418; September, 1961.

2.6. Van Bladel, J., "Low Frequency Scattering through an Aperture in a Rigid Screen," J. Sound Vib., Vol. 6, pp. 386 - 395; 1967.

2.7. Rahmat-Samii, Y., and R. Mittra, "Electromagnetic Coupling through Small Apertures in a Conducting Screen," IEEE Transactions on Antennas and Propagation, Vol. AP-25, No. 2, pp. 180 - 187; March, 1977.

2.8. Butler, C. M., "Formulation of Integral Equations for an Electrically Small Aperture in a Conducting Screen," Interaction Note 149, Air Force Weapons Laboratory, Albuquerque, New Mexico; December, 1973.

2.9. Butler, C. M., "Formulation of Integral Equations for an Electrically Small Aperture in a Conducting Screen," 1974 IEEE International Symposium on Antennas and Propagation, Atlanta, Georgia; June, 1974 (Interaction Note 149, Air Force Weapons Laboratory, Albuquerque, New Mexico; December, 1973).

2.10. Wilton, D. R., C. M. Butler, and K. R. Umashankar, "Penetration of EM Fields through Small Apertures in Planar Screens: Selected Data," Interaction Note 213, Air Force Weapons Laboratory, Albuquerque, New Mexico; September, 1974.

2.11. De Meulenaere, F., and J. Van Bladel, "Polarizability of Some Small Apertures," IEEE Transactions on Antennas and Propagation, Vol. AP-25, No. 2, pp. 198 - 205; March, 1977.

2.12. Mittra, R., Y. Rahmat-Samii, D. V. Jamnejad, and W. A. Davis, "A New Look at the Thin-Plate Scattering Problem," Radio Science, Vol. 8, No. 10, pp. 869 - 875; 1973 (Interaction Note 155, Air Force Weapons Laboratory, Albuquerque, New Mexico; March, 1973).

2.13. Cohn, S. B., "Determination of Aperture Parameters by Electrolytic-Tank Measurements," Proceedings of the IRE, Vol. 39, pp. 1416 - 1421; November, 1951. (See Correction: Vol. 40, p. 33; January, 1952.)

2.14. Cohn, S. B., "The Electric Polarizability of Apertures of Arbitrary Shape," Proceedings of the IRE, Vol. 40, pp. 1069 - 1071; September, 1952.

2.15. Collin, R. E., Field Theory of Guided Waves, McGraw-Hill Book Company, New York; 1960.

2.16. Montgomery, C. G., R. H. Dicke, and E. M. Purcell (Eds.), Principles of Microwave Circuits, McGraw-Hill Book Company, New York; 1948.

2.17. Matthaei, G. L., L. Young, and E. M. T. Jones, Microwave Filters, Impedance-Matching Networks, and Coupling Structures, McGraw-Hill, New York; 1964.

2.18. Latham, R. W., "Small Holes in Cable Shields," Interaction Note 118, Air Force Weapons Laboratory, Albuquerque, New Mexico; September, 1972.

2.19. Baum, C. E., K. C. Chen, and B. K. Singaraju, "Categorization of the Types of Apertures," Interaction Note 219, Air Force Weapons Laboratory, Albuquerque, New Mexico; January, 1975.

2.20. Yang, F. C., K. S. H. Lee, and L. Marin, "Analysis of EMP Penetration into a Weapons Bay," AIP Memo #4, The Dikewood Corporation, Westwood Research Branch, Los Angeles; October, 1976.

2.21. Lee, K. S. H., (Private Communication).

2.22. Chen, K. C., K. S. H. Lee and F. C. Yang, "EMP Penetration Through Door/Hatch Seams," to be presented at the NEM 1978 Meeting, University of New Mexico, Albuquerque, NM, 6-8 June 1978.

2.23. Van Bladel, J., Electromagnetic Fields, McGraw-Hill Book Company, New York; 1964.

2.24. Butler, C. M., "Penetration through a Narrow Slot in a Screen Separating Different Media," in preparation.

2.25. Mittra, R. and Y. Rahmat-Samii (Private Communication).

2.26. Taylor, C. D., "Electromagnetic Pulse Penetration through Small Apertures," Interaction Note 74, Air Force Weapons Laboratory, Albuquerque, New Mexico; March, 1971.

2.27. Taylor, C. D., "Electromagnetic Pulse Penetration through Small Apertures," IEEE Transactions on Electromagnetic Compatibility, Vol. EMC-15, pp. 17 - 23; February, 1973 and also Interaction Note 74, 24 March 1974.

2.28. Butler, C. M., and E. Yung, "Properties of a Slotted Parallel-Plate Waveguide Excited by an Incident TEM Wave," 1976 IEEE/AP-S Symposium, Amherst, Massachusetts; October, 1976.

2.29. Bombardt, J. N., "Magnetic Field Shielding Degradation Due to Circular Apertures in Long Hollow Cylinders," Interaction Note 3, Air Force Weapons Laboratory, Albuquerque, New Mexico; September, 1966.

2.30. Butler, C. M., and K. R. Umashankar, "Electromagnetic Excitation of a Wire through an Aperture-Perforated, Conducting Screen," IEEE Transactions on Antennas and Propagation, Vol. AP-24, No. 4, pp. 456 - 462; July, 1976, also Interaction Note 251, June 1975.

2.31. Kajfez, D., "Excitation of a Terminated TEM Transmission Line through a Small Aperture," Interaction Note 215, July 1974.

2.32. Graves, B. D., T. T. Crow, and C. D. Taylor, "On the Electromagnetic Field Penetration through Apertures," Interaction Note 199, Air Force Weapons Laboratory, Albuquerque, New Mexico; August, 1974.

2.33. Buchsbaum, S. J., A. R. Milne, D. C. Hogg, G. Berkefi, and G. A. Woonton, "Microwave Diffraction by Apertures of Various Shapes," Journal of Applied Physics, Vol. 26, No. 6, pp. 706 - 715; June, 1955.

2.34. Rahmat-Samii, Y., and R. Mittra, "Integral Equation Solution and RCS Computation of a Thin Rectangular Plate," IEEE Transactions on Antennas and Propagation, Vol. AP-22, No. 4, pp. 608 - 610; July, 1974, and also Interaction Note 146, December 1973.

2.35. Robinson, H. L., "Diffraction Patterns in Circular Apertures Less than One Wavelength in Diameter," Journal of Applied Physics, Vol. 24, pp. 35 - 38; 1953.

2.36. Marin, Lennart, Quasi-Static Field Penetration Into a Two-Dimensional Rectangular Well in a Ground Plane, Interaction Note 171, March 1974.

2.37. Senior, T. B. A., "Electromagnetic Field Penetration into a Cylindrical Cavity," Interaction Note 221, Air Force Weapons Laboratory, Albuquerque, New Mexico; January, 1975.

2.38. Senior, T. B. A., and G. A. Desjardins, "Electromagnetic Field Penetration into a Spherical Cavity," IEEE Transactions on Electromagnetic Compatibility, Vol. EMC-16, no. 4, pp. 205 - 208; November, 1974 (Interaction Note 142, Air Force Weapons Laboratory, Albuquerque, New Mexico; August, 1973).

CHAPTER III
CABLE SHIELDS

A. Introduction

In this chapter we shall be concerned with the coupling of electromagnetic fields between the exterior and the interior of a cable through its shield, which forms the boundary between these two regions. If a cable shield were a perfect conductor without apertures, then the currents and charges induced on the shield by an external source of electromagnetic energy would reside strictly on its outer surface and would produce no electromagnetic fields in the interior region. No induced currents and voltages would appear on the conductor(s) inside the cable shield; such a shield would thus be perfect, in that the inner conductors would be completely protected from the effects of external electromagnetic interference.

Unfortunately, such a shield does not exist. The conductivities of typical shield materials are large but finite; furthermore, apertures may exist in the shield, either as a natural concomitant of the shield manufacturing process or because of the presence of connectors or actual flaws in the shield. Consequently, our objectives in this chapter are to examine the mechanisms by means of which electromagnetic fields can penetrate imperfect cable shields and to assess the effects of shield imperfections on the currents and voltages induced on the internal conductor(s). Where possible, we shall also attempt to illustrate problem-solving procedures with simple example calculations.

There exists a large body of literature dealing with various aspects of cable shielding. A review of this literature was conducted in mid-1976, and in the course of this presentation we shall draw heavily from some of the articles which were reviewed. It was found that the papers and technical reports on cable shielding could be categorized as follows:

1. works dealing with the transmission-line theory of shielded cables

2. works dealing with the excitation of the total currents and charges on cables in various environments by an external electromagnetic field
3. works dealing with the modeling of various types of cable shields
4. works dealing with experimental techniques for the determination of cable properties and measurement of the internal signals excited by external sources.

In the first category of papers and technical reports, the theory of transmission lines is studied and sets of equations applicable to imperfectly shielded cables are developed. It is found that for well-shielded cables, the total current and charge induced on the cable by an external field depend little on the detailed cable structure, so that these total currents and charges can be calculated under the assumption that the shield is perfect. Calculations of this kind are described in the papers in the second category. Since, as we shall see, the sources of the internal induced currents and voltages are the total current and the total charge per unit length on the cable, the internal induced signals can then be calculated if the descriptive parameters of the cable itself are known. These parameters are theoretically derived for various types of cable shields in the papers in the third category, and experimental procedures for determining the cable parameters are outlined in the papers in the fourth category.

An important limitation to the results which are presently available is that the great majority of the extant articles on various aspects of cable shielding deal with time-harmonic, rather than transient, signals. As a consequence, only a few representative time-domain calculations are available at the present time. Furthermore, multiconductor cables have not been as extensively studied as two-conductor (specifically, coaxial) cables. These limitations will be reflected in this presentation.

We shall discuss four types of cable shield in this chapter and concentrate our attention on coaxial cables, in which there is but a single conductor inside the shield. These four shield types are

1. tubular shields, both ferromagnetic and non-ferromagnetic
2. braided shields
3. helical and tape-wound shields
4. shields with isolated apertures.

The geometry of the tubular shields is shown in Fig. 3.1. These shields are physically thin cylindrical shells of inner radius b and thickness d. They are made of a highly conducting material and do not possess apertures. A braided shield is typically constructed of woven copper wire. The geometry of a braided-shield cable is shown in Fig. 3.2a and the developed surface of the shield is shown in Fig. 3.2b. The angle ψ denotes the pitch of the woven braid and is measured from the direction of the cable axis. Dielectric weatherproofing jackets are commonly found on these cables. The geometry of a tape-wound helical shield is shown in Fig. 3.3. Such shields commonly occur in flexible armored cables. Isolated apertures in cable shields may occur as a consequence of a break or other flaw in a shield; an isolated aperture may also represent a cable connector, which is discussed extensively elsewhere in this report.

In the next section (section B) we consider the transmission-line equations for imperfectly shielded cables and discuss the source terms in those equations. We also consider the approximate decoupling of the total electromagnetic problem of determining the induced internal currents and voltages, given the external field, into two simpler problems, one for the exterior and one for the interior of the cable. Tubular shields are discussed in section C, and leaky shields (shields with uniformly distributed apertures, e.g., braided or helical shields) in section D. Isolated shield aperture effects are considered in section E. Experimental procedures for determining cable properties are described in section F, and the chapter is summarized in section G.

B. General Considerations: Transmission-Line Equations

A two-conductor transmission line of any type, including a shielded line, can be described electrically by a pair of coupled first-order

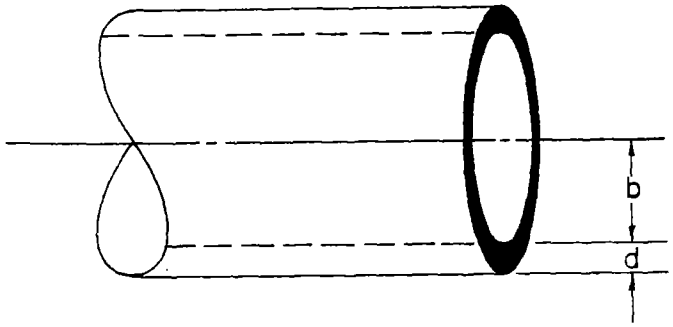

Fig. 3.1. Tubular-shield geometry. The shield thickness d is small in comparison to the inner radius b.

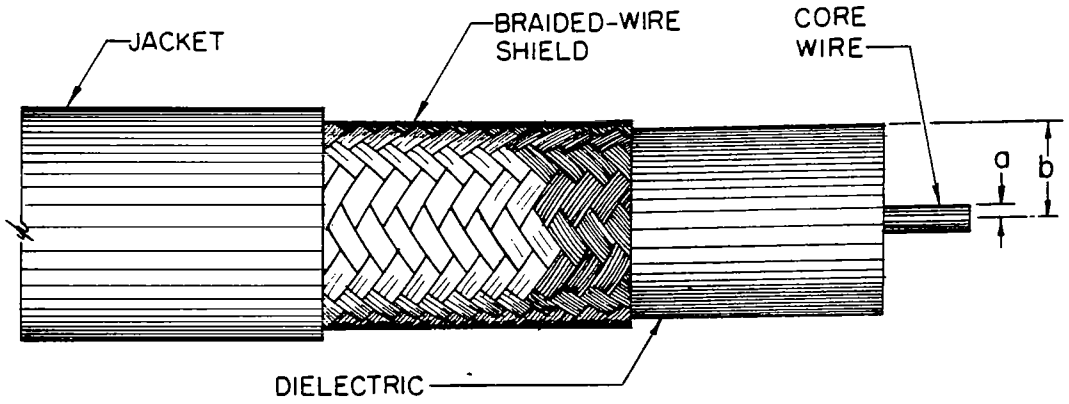

Fig. 3.2a. A braided-shield coaxial cable.

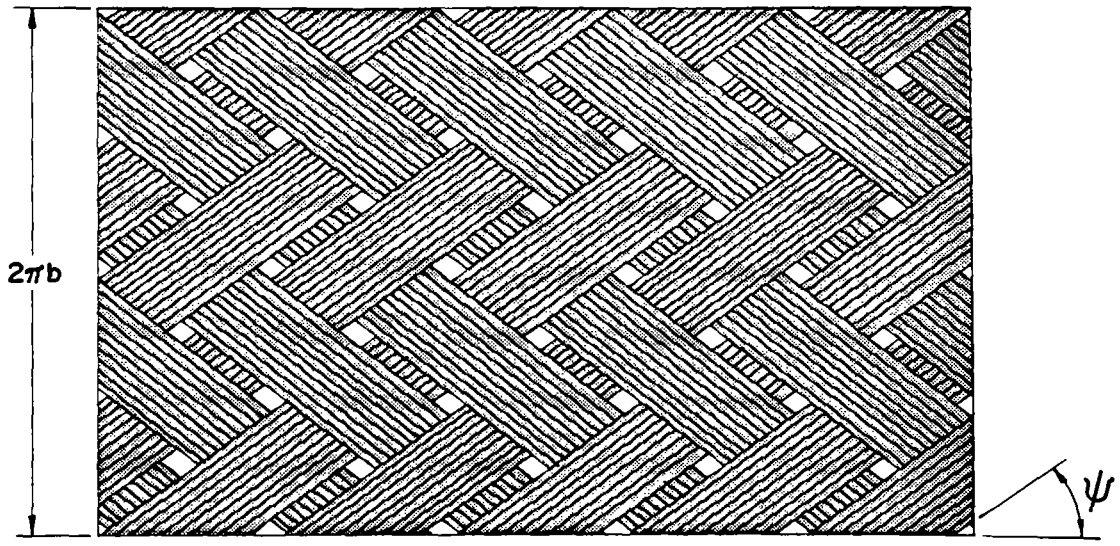

Fig. 3.2b. Developed surface of a braided shield.

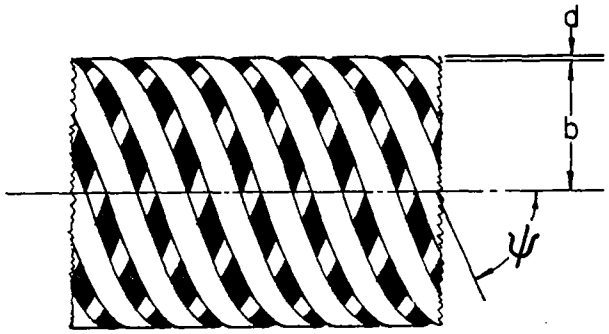

Fig. 3.3. Tape-wound helical shield geometry. The shield shown is 6-filar.

differential equations, the transmission-line equations. Assuming that all currents and voltages vary with time as exp(st)*, these equations may be written

$$\frac{dV}{dz} = -ZI + E(z)$$
$$\frac{dI}{dz} = -YV - K(z) \qquad (3.1)$$

in which z is the coordinate parallel to the axis of the line and V and I denote the line voltage and current respectively: I is the current on the center conductor and is taken to be positive in the +z-direction; V is the potential of the center conductor with respect to the shield. These conventions are shown in Fig. 3.4. Z and Y denote respectively the series impedance per unit length and the shunt admittance per unit length of the cable. E(z), the source term in the "voltage-change" equation, has dimensions volt m^{-1}; K(z), the source term in the "current-change" equation, has dimensions ampere m^{-1}. We shall discuss these source terms more fully below.

Equations 3.1 can be used to construct a linear equivalent circuit for an incremental length dz of the cable. Such an equivalent circuit is shown in Fig. 3.5. One will note that the source terms E(z) and K(z) appearing in Eq. 3.1 enter the incremental equivalent circuit as a series voltage source E(z)dz and a shunt current source K(z)dz respectively.

Latham (Ref. 3.1) has shown that for a shielded coaxial cable with a periodic shield structure, the source term E(z) is proportional to the total current I_t flowing on the cable (i.e., the sum of the currents flowing on the inner conductor and the shield) and the source term K(z) is proportional to the total charge per unit length Q_t carried by the cable. Equivalently (Ref. 3.2), K(z) is proportional to the potential difference between the cable shield and an external "return" conductor. We have, therefore,

---

*The time-harmonic case corresponds to $s = j\omega$. More generally $s = \sigma + j\omega$, the Laplace-transform variable.

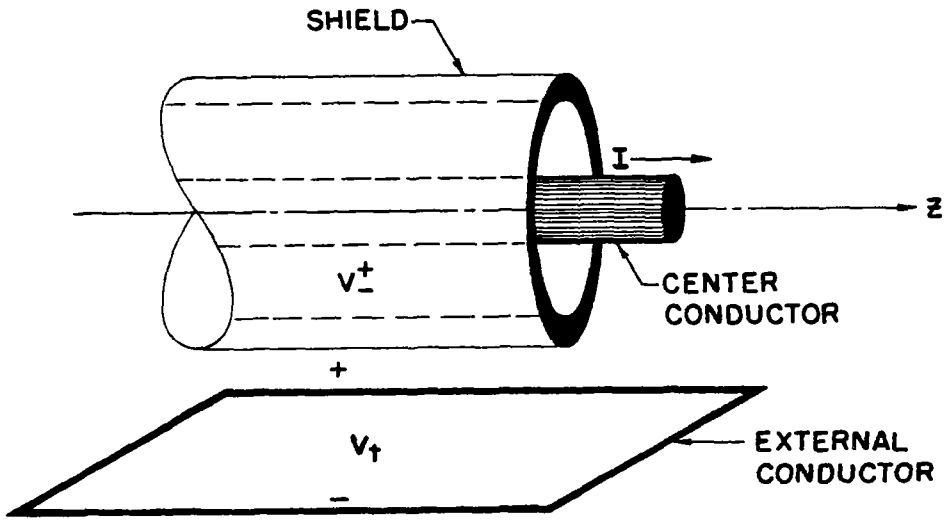

Fig. 3.4. Sign conventions for cable current and voltage.

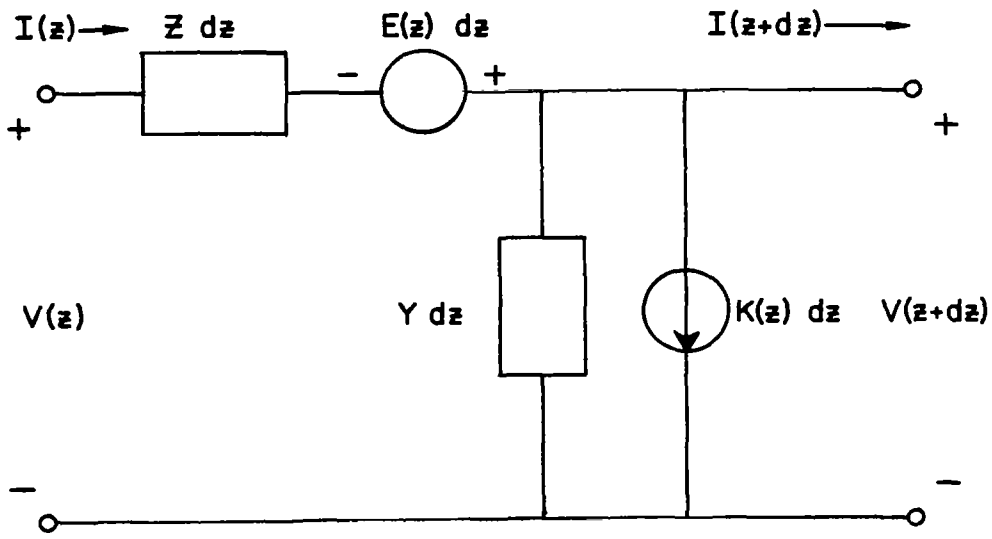

Fig. 3.5. Linear equivalent circuit for a length dz of transmission line.

$$E(z) = Z_T I_t$$
$$K(z) = s\Gamma_T Q_t \qquad (3.2)$$
$$= Y_T V_t$$

in which Z_T is the shield transfer impedance per unit length, Y_T is the shield transfer admittance per unit length*, and Γ_T is the (dimensionless) charge coupling coefficient. I_t and Q_t have already been defined, and V_t is the potential between the shield and an external return conductor, as shown in Fig. 3.4.

Some auxiliary relationships among the source quantities I_t, V_t, and Q_t and between the parameters Y_T and $s\Gamma_T$ can be found. For example, the charge continuity equation

$$\frac{dI_t}{dz} + sQ_t = 0 \qquad (3.3)$$

yields the result that

$$K(z) = -\Gamma_T \frac{dI_t}{dz} \qquad (3.4)$$

Furthermore, defining an "external capacitance per unit length" C_e via the relation

$$Q_t = C_e V_t \qquad (3.5)$$

we find that

$$\Gamma_T = \frac{Y_T}{sC_e} \qquad (3.6)$$

It is often convenient to define a parameter Y_s through the relation

$$\Gamma_T = \frac{Y}{Y_s} \qquad (3.7)$$

so that

$$Y_T Y_s = sC_e Y \qquad (3.8)$$

Y_s may be termed the shield coupling admittance per unit length.

---

*But note that $Y_T \neq 1/Z_T$.

It is apparent that the source quantity of greatest interest is I_t, since by Eq. 3.3,

$$Q_t = -\frac{1}{s}\frac{dI_t}{dz} \tag{3.9}$$

Once I_t is determined, both E(z) and K(z) can be found if the parameters Z_T and Γ_T are known. The determination of I_t is facilitated, for well-shielded cables at least, by the fact that the cable may be modeled as a perfectly conducting cylinder for this "external" calculation (Ref. 3.3)*. Thus the interior and exterior problems are approximately uncoupled, and the process of determining the induced internal voltage and current on a given cable in a given environment involves two distinct steps. These are:

1. First, calculate the total current and charge per unit length induced on the cable by the external field, assuming the shield to be a perfectly conducting cylinder whose outer radius is equal to that of the cable shield.

2. Second, evaluate E(z) and K(z) and solve the transmission-line equations 3.1, subject to appropriate boundary conditions, for the internal voltage and current. It is assumed that the cable parameters are known.

If the transient response to the excitation is desired, then the final step would be to invert the Laplace-transformed current and voltage I(z,s) and V(z,s) to obtain the time-domain quantities i(z,t) and v(z,t).

In this chapter, we shall concentrate our attention on the second of these steps, assuming that the exterior problem has been solved and thus that the total current and the total charge per unit length induced by the external field are known. The solution of the exterior problem is beyond the scope of this presentation, and the reader is referred to Refs. 3.4-3.6 for some examples of exterior-problem calculations.

---

*If the cable has an outer dielectric jacket, the proper "exterior" model is a perfectly conducting cylinder (whose radius is equal to that of the shield) coated with a dielectric jacket (Ref. 3.14).

The solution of the transmission-line equations 3.1 is straightforward. We shall present a few of the most important formulae relevant to the calculation of induced terminal voltages and currents. First, we note that V(z) and I(z) take the form

$$\begin{aligned} V(z) &= Ae^{-\gamma z} + Be^{\gamma z} + V_p(z) \\ I(z) &= \frac{A}{Z_o} e^{-\gamma z} - \frac{B}{Z_o} e^{\gamma z} + I_p(z) \end{aligned} \tag{3.10}$$

in which A and B are constants to be determined, $\gamma = \sqrt{ZY}$ is the (complex) propagation constant, and $Z_o = \sqrt{Z/Y}$ is the characteristic impedance of the transmission line. $V_p(z)$ and $I_p(z)$ are the <u>particular integrals</u> of the differential equations

$$\begin{aligned} \frac{d^2V}{dz^2} - \gamma^2 V &= ZK(z) + \frac{dE(z)}{dz} \\ \frac{d^2I}{dz^2} - \gamma^2 I &= -YE(z) - \frac{dK(z)}{dz} \end{aligned} \tag{3.11}$$

I_p and V_p are related to each other by

$$\begin{aligned} I_p &= \frac{1}{Z}\left[E(z) - \frac{dV_p}{dz}\right] \\ V_p &= -\frac{1}{Y}\left[K(z) + \frac{dI_p}{dz}\right] \end{aligned} \tag{3.12}$$

Expressing E(z) and K(z) in terms of the total current I_t, Eqs. 3.11 become

$$\begin{aligned} \frac{d^2V}{dz^2} - \gamma^2 V &= (Z_T - Z\Gamma_T)\frac{dI_t}{dz} \\ \frac{d^2I}{dz^2} - \gamma^2 I &= \Gamma_T \frac{d^2I_t}{dz^2} - YZ_T I_t \end{aligned} \tag{3.13}$$

Now, Eqs. 3.13 can be solved by several means, depending upon the form of I_t. Let us assume for the moment that $V_p(z)$ and $I_p(z)$ are known.

Let the transmission line run between z=0 and z=ℓ, and let the terminating impedances at each end be denoted Z(0) and Z(ℓ) respectively, as shown in Fig. 3.6, so that

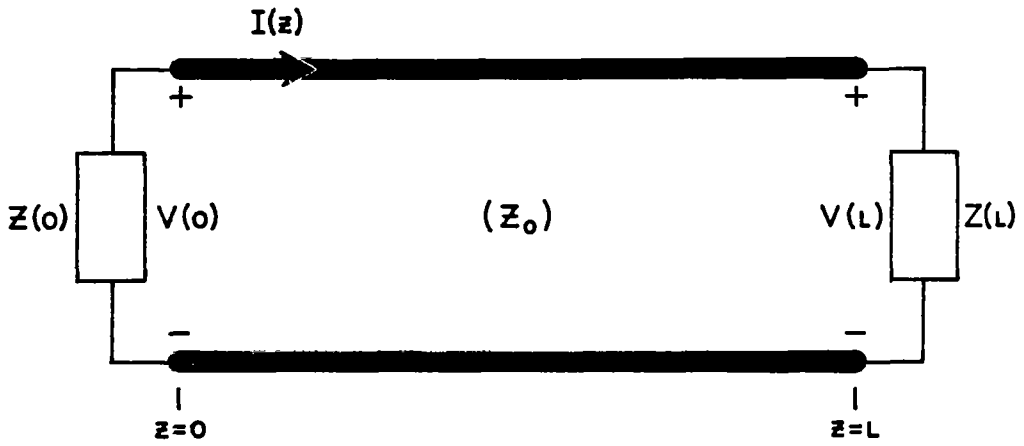

Fig. 3.6. A terminated transmission line of characteristic impedance Z_o.

$$V(0) = -Z(0)I(0)$$
$$V(\ell) = Z(\ell)I(\ell) \tag{3.14}$$

Now by imposing conditions (3.14) we may determine the constants A and B and thus evaluate the terminal voltages and currents excited by the external field. Substituting Eqs. 3.10 into 3.14, we find that A and B satisfy

$$\begin{bmatrix} 1 + \frac{Z(0)}{Z_o} & 1 - \frac{Z(0)}{Z_o} \\ e^{-\gamma\ell}[1 - \frac{Z(\ell)}{Z_o}] & e^{\gamma\ell}[1 + \frac{Z(\ell)}{Z_o}] \end{bmatrix} \begin{bmatrix} A \\ B \end{bmatrix} = \begin{bmatrix} -S_o \\ -S_\ell \end{bmatrix} \tag{3.15}$$

where

$$S_o = V_p(0) + Z(0)I_p(0)$$
$$S_\ell = V_p(\ell) - Z(\ell)I_p(\ell) \tag{3.16}$$

Solving for A and B, we obtain

$$A = \frac{-e^{\gamma\ell}[1 + \frac{Z(\ell)}{Z_o}]S_o + [1 - \frac{Z(0)}{Z_o}]S_\ell}{2\cosh \gamma\ell[\frac{Z(0) + Z(\ell)}{Z_o}] + 2\sinh \gamma\ell[1 + \frac{Z(0)Z(\ell)}{Z_o^2}]}$$
$$B = \frac{e^{-\gamma\ell}[1 - \frac{Z(\ell)}{Z_o}]S_o - [1 + \frac{Z(0)}{Z_o}]S_\ell}{2\cosh \gamma\ell[\frac{Z(0) + Z(\ell)}{Z_o}] + 2\sinh \gamma\ell[1 + \frac{Z(0)Z(\ell)}{Z_o^2}]} \tag{3.17}$$

The induced terminal voltages and currents are now given by Eq. 3.10 with z=0 or ℓ and with A and B given by Eq. 3.17.

As a simple example of the use of these equations, let us consider the case where I_t is a constant, independent of z and given by I_{to}, and the transmission line is terminated at each end in its characteristic impedance, so that $Z(0) = Z(\ell) = Z_o$. Let us further assume that at the highest frequency of interest, $|\gamma\ell| << 1$. Eq. 3.13 reveals that $V_p = 0$, and from the first of Eqs. 3.12, we obtain

$$I_p(z) = \frac{Z_T}{Z} I_{to} \tag{3.18}$$

Thus, from Eq. 3.16,

$$S_o = -S_\ell = \frac{1}{\gamma} Z_T I_{to} \tag{3.19}$$

A and B are given approximately by

$$A \simeq \frac{-Z_T I_{to}}{2\gamma}$$
$$B \simeq \frac{Z_T I_{to}(1-\gamma\ell)}{2\gamma} \tag{3.20}$$

so that

$$V(0) = -V(\ell) = \frac{-Z_T \ell\ I_{to}}{2}$$
$$I(0) = I(\ell) = Z_T \ell\ I_{to}/2Z_o \tag{3.21}$$

In this example, as in the general case, the final results depend upon the total induced cable current I_t and upon the parameters of the line. The evaluation of the parameters Z, Y, Z_T, and Γ_T for several types of coaxial cables is the subject of the following two sections of this chapter.

C. Tubular Shields

C.1 Non-ferromagnetic tubular shields

The simplest type of imperfect coaxial cable shield to analyze is a non-ferromagnetic tubular shield made of a highly conductive metal (e.g., aluminum or copper). The geometry of such a shielded cable is shown in Fig. 3.7. Tubular shields were originally studied by Schelkunoff (Ref. 3.7). The mechanism by which an external electromagnetic field couples to the interior of a cable with a tubular shield is <u>diffusion</u> of the magnetic field through the imperfectly conducting shield metal. A good discussion of this phenomenon is given in the text by Ramo, Whinnery, and Van Duzer (Ref. 3.8).

Schelkunoff's analysis is readily adapted to the determination of the cable parameters Z, Y, Z_T, and Γ_T. The following general results are obtained:

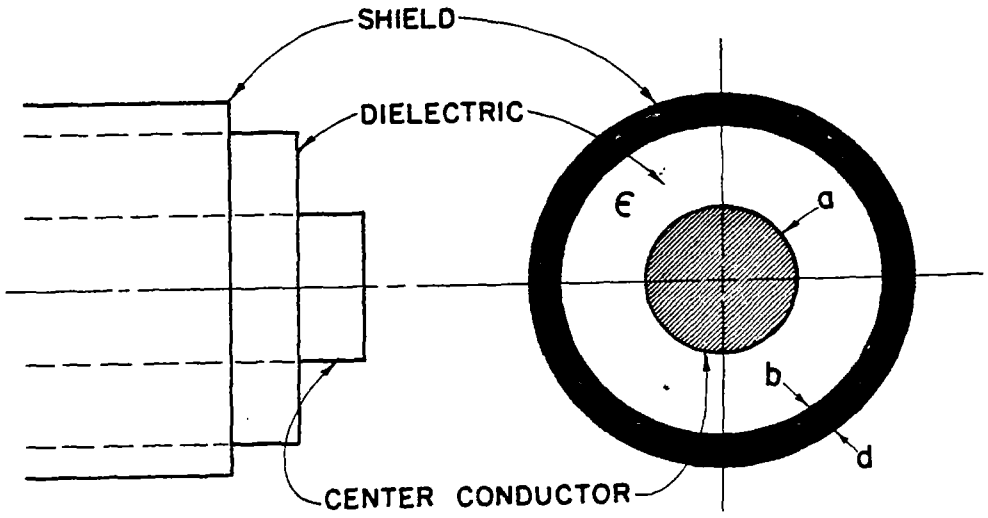

Fig. 3.7. Tubular shielded coaxial cable geometry.

$$
\begin{aligned}
Z &= \frac{s\mu_o}{2\pi} \ln \frac{b}{a} + Z_i + Z_{bb} \\
Y &= 2\pi s\varepsilon / \ln \frac{b}{a} \\
Z_T &= \frac{1}{2\pi\sigma_s b(b+d)D} \\
\Gamma_T &= 0
\end{aligned}
\tag{3.22}
$$

in which μ_o and ε are the permeability and permittivity of the dielectric material between the center conductor and the shield, a is the radius of the center conductor, and b is the inner radius of the shield. The shield thickness is d and the conductivity of the shield material is σ_s. Z_i denotes the impedance per unit length of the center conductor, and is given by

$$
Z_i = \frac{\sqrt{s\mu_o/\sigma_c}}{2\pi a} \frac{I_o(\sqrt{s\mu_o\sigma_c}\, a)}{I_1(\sqrt{s\mu_o\sigma_c}\, a)} \tag{3.23}
$$

in which σ_c is the conductivity of the center conductor and $I_n(\cdot)$ denotes the modified Bessel function of the first kind. Z_{bb} is given by

$$
\begin{aligned}
Z_{bb} = \frac{\sqrt{s\mu_o/\sigma_s}}{2\pi bD} \; & [I_o(\sqrt{s\mu_o\sigma_s}\, b) K_1(\sqrt{s\mu_o\sigma_s}\, c) \\
& + I_o(\sqrt{s\mu_o\sigma_s}\, c) K_o(\sqrt{s\mu_o\sigma_s}\, b)]
\end{aligned}
\tag{3.24}
$$

where $c = b+d$, $K_n(\cdot)$ denotes the modified Bessel function of the second kind, and

$$
D = I_1(\sqrt{s\mu_o\sigma_s}\, c) K_1(\sqrt{s\mu_o\sigma_s}\, b) - I_1(\sqrt{s\mu_o\sigma_s}\, b) K_1(\sqrt{s\mu_o\sigma_s}\, c) \tag{3.25}
$$

When d is small in comparison to b, Z_T is reliably approximated by the simpler expression

$$
Z_T \simeq \frac{\sqrt{s\mu_o\sigma_s}\, d}{2\pi\sigma_s bd} \operatorname{csch} \sqrt{s\mu_o\sigma_s}\, d \tag{3.26}
$$

It is interesting to note that Z comprises contributions from the finite impedances per unit length of both the center conductor and the shield as well as the usual inductive impedance contribution. It should

also be pointed out that Y is identical to the result obtained for an ideal coaxial cable and that $\Gamma_t = 0$. This occurs because the induced charge per unit length resides entirely on the outer surface of the shield and no radial electric field penetrates from the exterior region to the interior of the cable. Thus the coupling between the exterior and interior of the cable occurs via the magnetic field alone; and the coupling is referred to as purely inductive.

In most practical situations, the purely inductive term in Z is dominant and Z_T can be approximated by the expression given in Eq. 3.26. Thus the transmission-line parameters of a tubular shielded cable are approximately

$$\begin{aligned} Z &\simeq \frac{s\mu_o}{2\pi} \ln \frac{b}{a} \\ Y &\simeq \left(\frac{1}{2\pi s\varepsilon} \ln \frac{b}{a}\right)^{-1} \\ Z_T &\simeq R_o \sqrt{s\tau_{ds}}\ \mathrm{csch} \sqrt{s\tau_{ds}} \\ \Gamma_T &= 0 \end{aligned} \tag{3.27}$$

in which we have introduced the notation

$$\tau_{ds} = \mu_o \sigma_s d^2 \tag{3.28}$$

for the "diffusion time constant" of the shield, and

$$R_o = \frac{1}{2\pi\sigma_s bd} \tag{3.29}$$

denotes the dc resistance per unit length of the shield.

Curves of the magnitude and phase of $Z_T(s=j\omega)/R_o$ as a function of normalized frequency $f\tau_{ds}$ are given in Fig. 3.8. These curves, together with a knowledge of the conductivity σ_s and the shield radius b and thickness d, permit the calculation of the transfer impedance per unit length for any given non-ferromagnetic tubular shield.

As an example of the transient behavior of the induced voltage and current on a tubular-shielded cable, let us consider an electrically short cable terminated at both ends in its characteristic impedance. We found in the previous section that the induced currents I(0) and I(ℓ) were given by

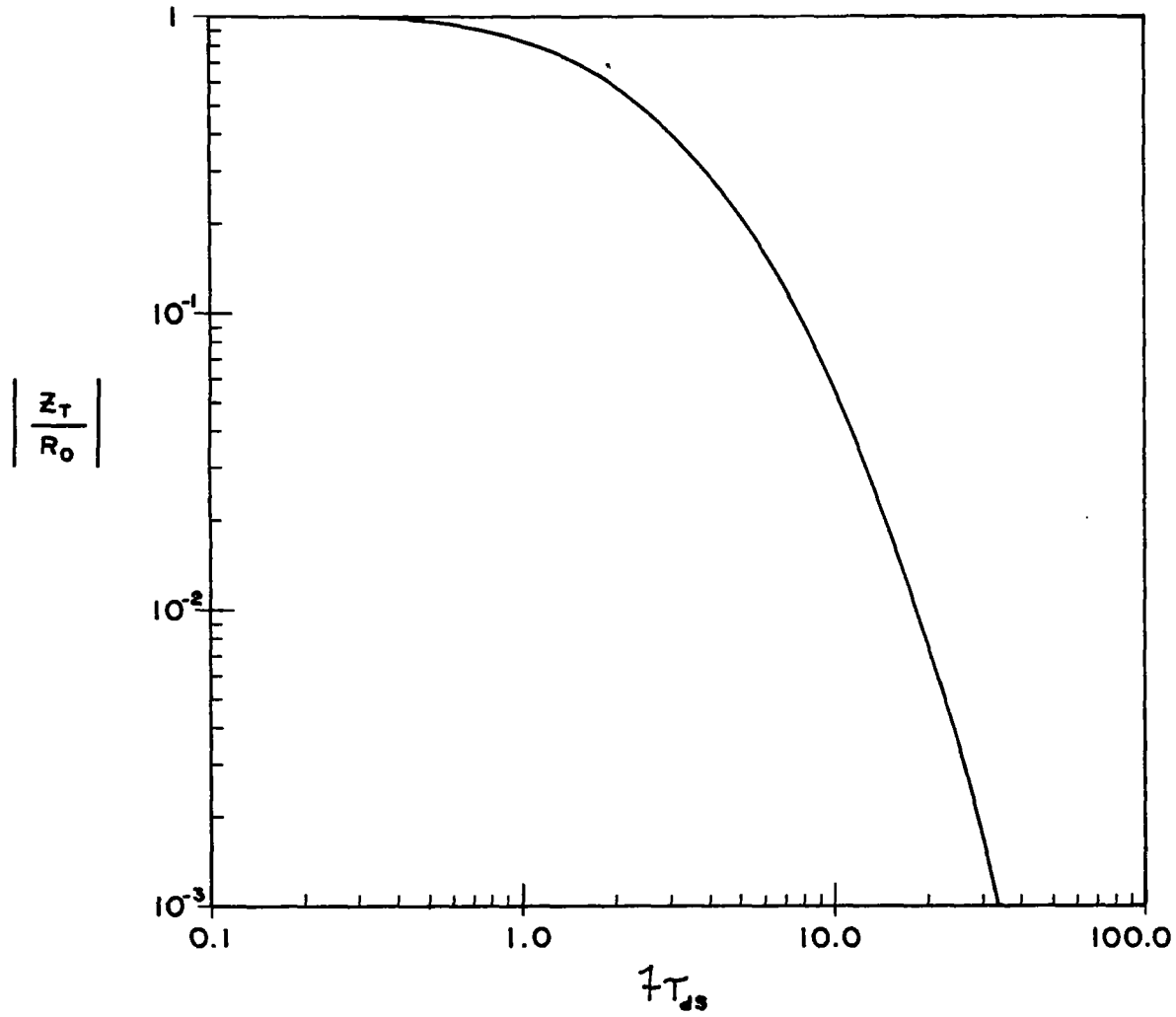

Fig. 3.8a. Magnitude of Z_T/R_o as a function of normalized frequency $f\tau_{ds}$.

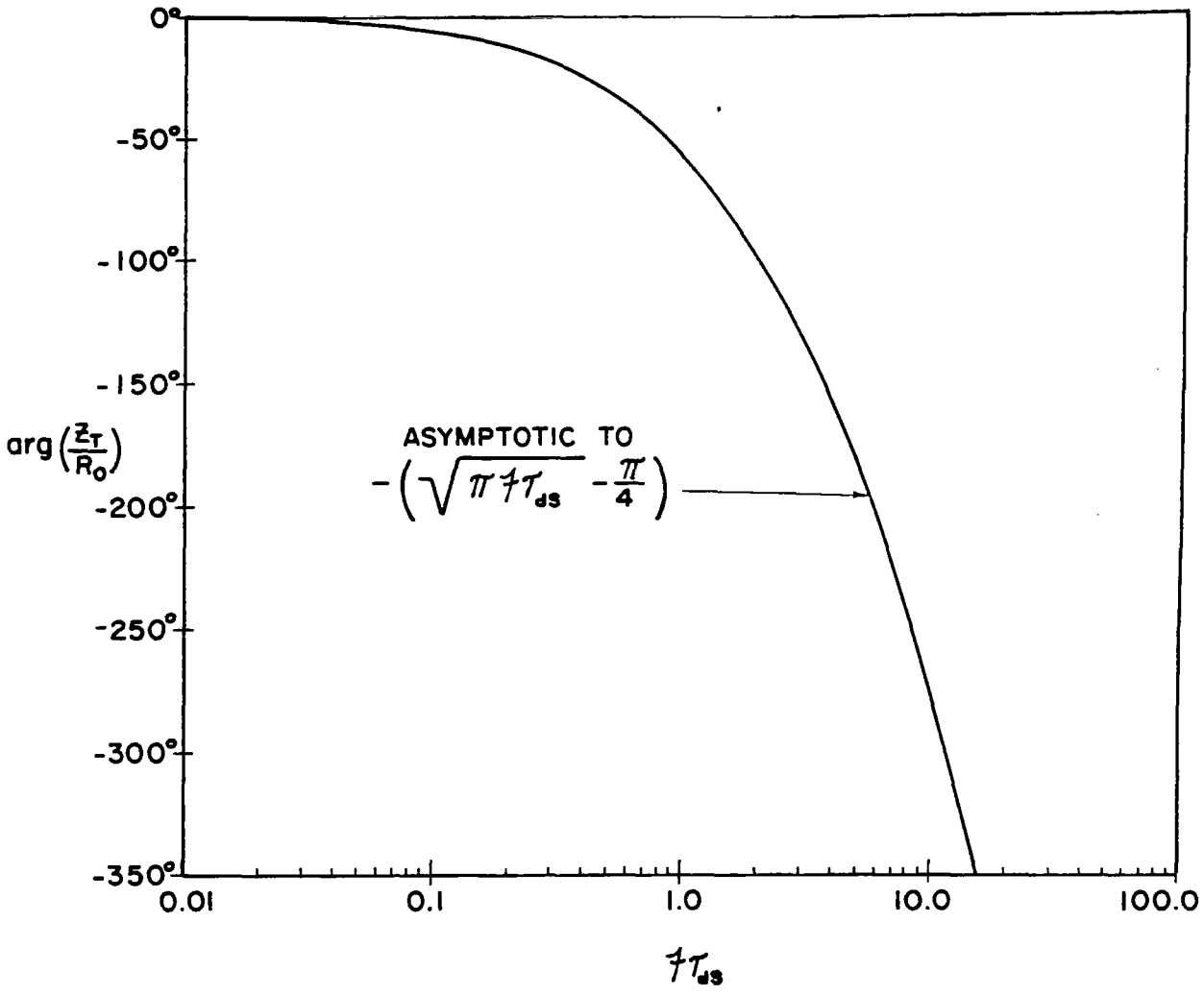

Fig. 3.8b. Phase of Z_T/R_o as a function of normalized frequency $f\tau_{ds}$.

$$I(0) = I(\ell) = \frac{Z_T \ell \, I_{to}}{2Z_o} \tag{3.30}$$

where I_{to} was the (spatially uniform) total cable current. If the temporal behavior of the total current is given by

$$i_{to}(t) = I_o U(t) \tag{3.31}$$

where U(t) denotes the unit step function, then

$$I_{to} = \frac{I_o}{s} \tag{3.32}$$

Now let Z_T be given by Eq. 3.27. We obtain

$$I(0) = I(\ell) = \frac{R_o \ell \, I_o \tau_{ds}}{2Z_o} \frac{\operatorname{csch}\sqrt{s\tau_{ds}}}{\sqrt{s\tau_{ds}}} \tag{3.33}$$

as the Laplace transform of the currents i(t,z=0) and i(t,z=ℓ). This transform can be readily inverted, and a plot of $2Z_o i(t,z=0)/R_o I_o \ell$ as a function of t/τ_{ds} is shown in Fig. 3.9 (Ref. 3.4). The final value of the induced current normalized to I_o is simply $R_o\ell/2Z_o$.

As an additional example, consider the same situation as above, but let

$$i_{to}(t) = q_t \delta(t) \tag{3.34}$$

where q_t has dimensions of charge (Coulombs) and $\delta(t)$ denotes the Dirac delta-function. Thus $I_{to} = q_t$ and

$$I(0) = I(\ell) = \frac{R_o \ell q_t}{2Z_o} \sqrt{s\tau_{ds}} \operatorname{csch}\sqrt{s\tau_{ds}} \tag{3.35}$$

is the Laplace transform of i(t,z=0) and i(t,z=ℓ). A plot of $2Z_o\tau_{ds} i(t,z=0)/R_o \ell q_t$ as a function of t/τ_{ds} is shown in Fig. 3.10 (Ref. 3.4). One will note that the peak value reached by the induced current is

$$i(t,z=0)\Big|_{peak} \approx 6\left(\frac{R_o \ell q_t}{2Z_o \tau_{ds}}\right) \tag{3.36}$$

and q_t is related to $i_{to}(t)$ by

$$q_t = \int_0^\infty i_{to}(t)dt \tag{3.37}$$

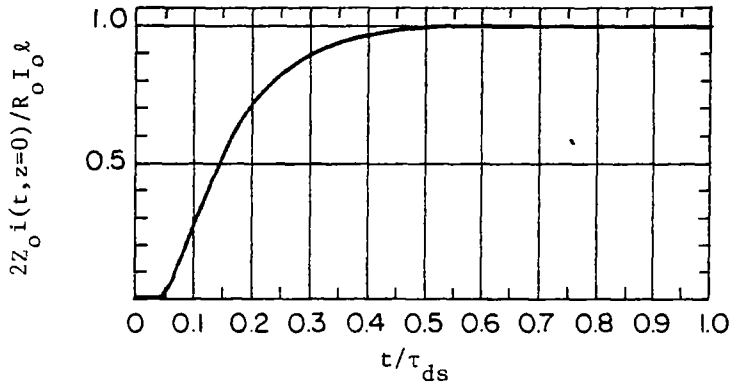

Fig. 3.9. Normalized step-function response of internal current vs. t/τ_{ds}.

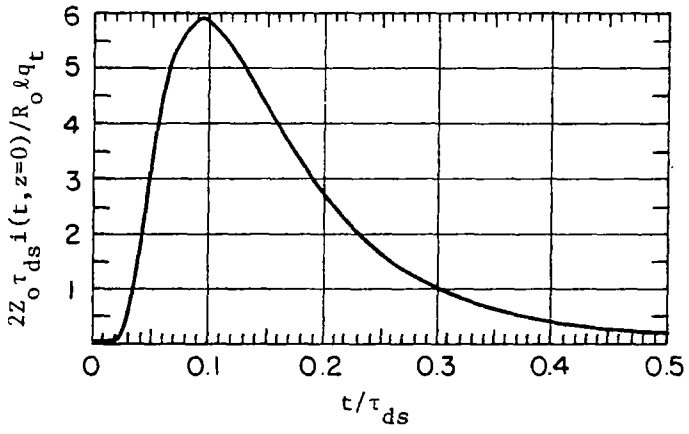

Fig. 3.10. Normalized delta-function response of internal current vs. t/τ_{ds}.

The preceding examples will serve to give the reader an idea of the responses to be expected when the total cable current $i_{to}(t)$ is an exponential-form transient whose time constant is either very long or very short in comparison to the shield diffusion time constant τ_{ds}.

C.2 Ferromagnetic tubular shields

Because of the very large equivalent relative permeability of unsaturated ferromagnetic materials, cable shields made of such materials can be very effective. This is so because of the increase in the shield diffusion time constant (cf. Eq. 3.28) by a factor of $\mu_{r,eff}$. When the shield carries a large current, however, the resulting magnetic field can saturate the shield through a part of, or throughout, its thickness. When complete shield saturation occurs, the relative permeability of the shield drops essentially to unity and its effectiveness decreases.

Ferber and Young (Ref. 3.9) have developed an expression for the depth of saturation of a thin tubular ferromagnetic shield of radius b, thickness d, conductivity σ_s, and saturation flux density B_s, which is carrying a current $i_s(t)$. Hysteresis effects are ignored and it is assumed that the shield material is either completely saturated or completely unsaturated with infinite effective relative permeability. The B-H curve appropriate to these assumptions is shown in Fig. 3.11. Denoting by x the depth to which the shield saturates ($x \leq d$), Ferber and Young find that

$$x = d\left[\frac{\int_0^t i_s(t)dt}{\pi b \tau_{ds} B_s/\mu_o}\right]^{1/2} \tag{3.38}$$

where $\tau_{ds} = \mu_o \sigma_s d^2$. B_s is typically 1.6 Wb m^{-2} for the steel used in electrical conduit.

Partial saturation of the shield (i.e., $x<d$) is far less serious than complete saturation, since most of the shield current flows in the saturated portion (the outer portion) of the shield and the current carried on the inner unsaturated portion remains small. When complete saturation occurs, however, this is no longer true. The condition for complete saturation is that

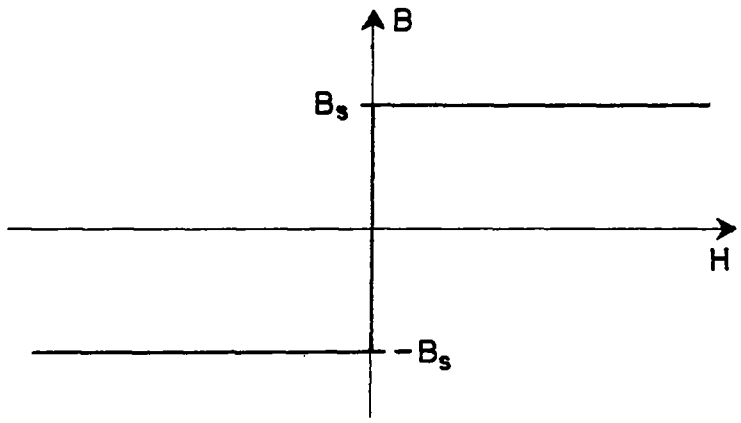

Fig. 3.11. Idealized B-H curve for saturable ferromagnetic shield material.

$$\int_0^t i_s(t)dt \geq \pi b \tau_{ds} B_s/\mu_o \tag{3.39}$$

Eq. 3.39 may be used to develop a design criterion for ferromagnetic tubular shields if the maximum expected value of the total transferred charge (i.e., the integral of $i_s(t)$) is known (Ref. 3.10).

D. Leaky Shields

Helical and braided shields do not generally completely "cover" the center conductor. Braided shields commonly possess a periodic distribution of small diamond-shaped apertures appearing where the bands of shield wires overlap. Helical shields usually have gaps between turns. Braided and helical shields have been shown in Figs. 3.2 and 3.3.

The presence of these openings or apertures in the shield gives rise to the possibility of electromagnetic field coupling directly through the apertures between the exterior and the interior of the shield. Both electric and magnetic fields can couple through shield apertures; this coupling is indicated in Fig. 3.12. Thus in shields with apertures, both inductive and capacitive coupling mechanisms are present, and the inductive coupling can occur both via diffusion and via direct aperture penetration.

Electrically small apertures can be modeled as equivalent electric and magnetic dipoles (Ref. 3.11). As a consequence, the electromagnetic quantities of interest for the analysis of aperture effects, especially in braided shields, are the electric and magnetic polarizabilities of the apertures. When these polarizabilities are known, the transmission-line parameters Z_T and Γ_T for braided shields may be expressed in terms of them as follows:

$$\begin{aligned} Z_T &= Z_{Td} + s\,\frac{n\mu_o\alpha_m}{(2\pi b)^2} \\ \Gamma_T &= \frac{n\alpha_e C}{\epsilon\,(2\pi b)^2} \end{aligned} \tag{3.40}$$

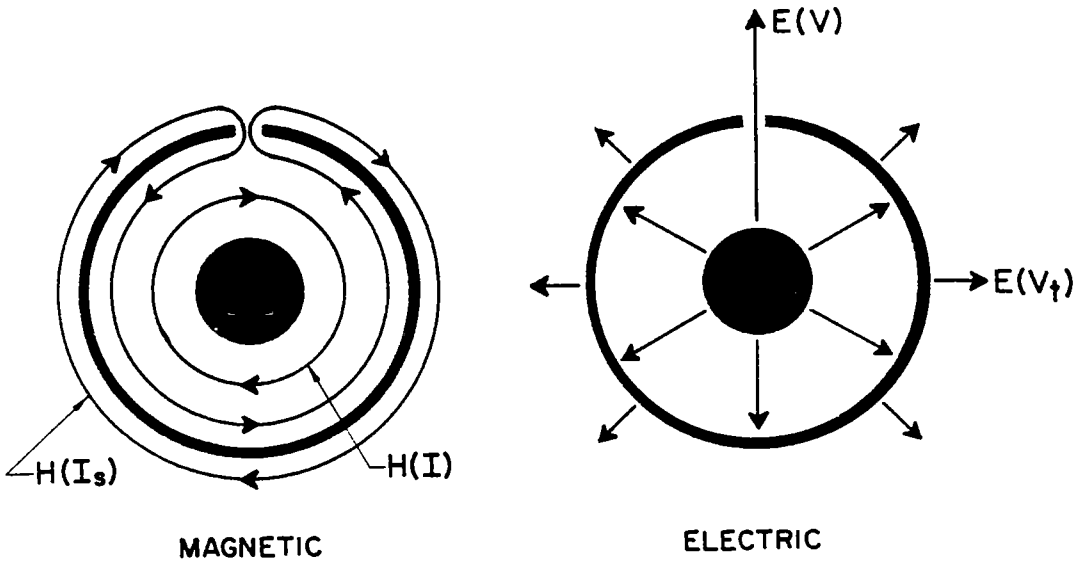

Fig. 3.12. Illustrating coupling of magnetic and electric fields through a shield aperture. I_s denotes the shield current.

in which α_e and α_m denote respectively the electric and magnetic polarizabilities of the apertures, n is the number of apertures per unit length of shield, and b is the shield radius. C denotes the capacitance per unit length between the center conductor and the shield and ε is the permittivity of the inner dielectric. Z_{Td} is the diffusion contribution to Z_T; it is given by (Ref. 3.2)

$$Z_{Td} = \frac{R_o}{\nu} \sqrt{s\tau_{ds}} \operatorname{csch} \sqrt{s\tau_{ds}} \tag{3.41}$$

where ν is the optical coverage of the shield, and the other quantities in Eq. 3.41 have been previously defined.

The aperture polarizabilities appearing in Eq. 3.40 depend on several factors, the most important of which are:

a. the size and shape of the aperture
b. neighboring apertures
c. the dielectric materials inside and outside the shield

Latham (Ref. 3.12) has studied the first two effects in detail. He found that the polarizabilities of an isolated diamond-shaped aperture α_{ei} and α_{mi} are given by

$$\begin{aligned} \alpha_{ei} &= \left(\frac{\delta}{2}\right)^3 \frac{\sin^2\psi}{\cos\psi} \bar{\alpha}_e(\psi) \\ \alpha_{mi} &= \left(\frac{\delta}{2}\right)^3 \frac{\sin^2\psi}{\cos\psi} \bar{\alpha}_m(\psi) \end{aligned} \tag{3.42}$$

in which δ denotes the dimension of the aperture along the direction of the cable axis and ψ denotes the pitch of the braid shield. The geometry of the shield apertures is shown in Fig. 3.13. $\bar{\alpha}_e$ and $\bar{\alpha}_m$ denote normalized polarizabilities which depend only on ψ. Curves of $\bar{\alpha}_e(\psi)$ and $\bar{\alpha}_m(\psi)$ as functions of ψ are shown in Fig. 3.14.

The effect of neighboring apertures on the polarizabilities of a given aperture in an array is to modify the polarizabilities of an isolated aperture as follows:

$$\alpha_e = \frac{\alpha_{ei}}{1 + (\alpha_{ei}/w_x^3)\Sigma_e(\psi)} \tag{3.43}$$

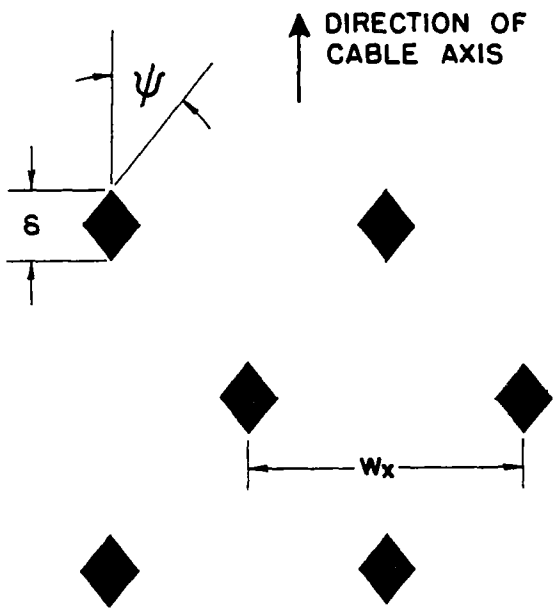

Fig. 3.13. Geometry of aperture array for braided-shield cable.

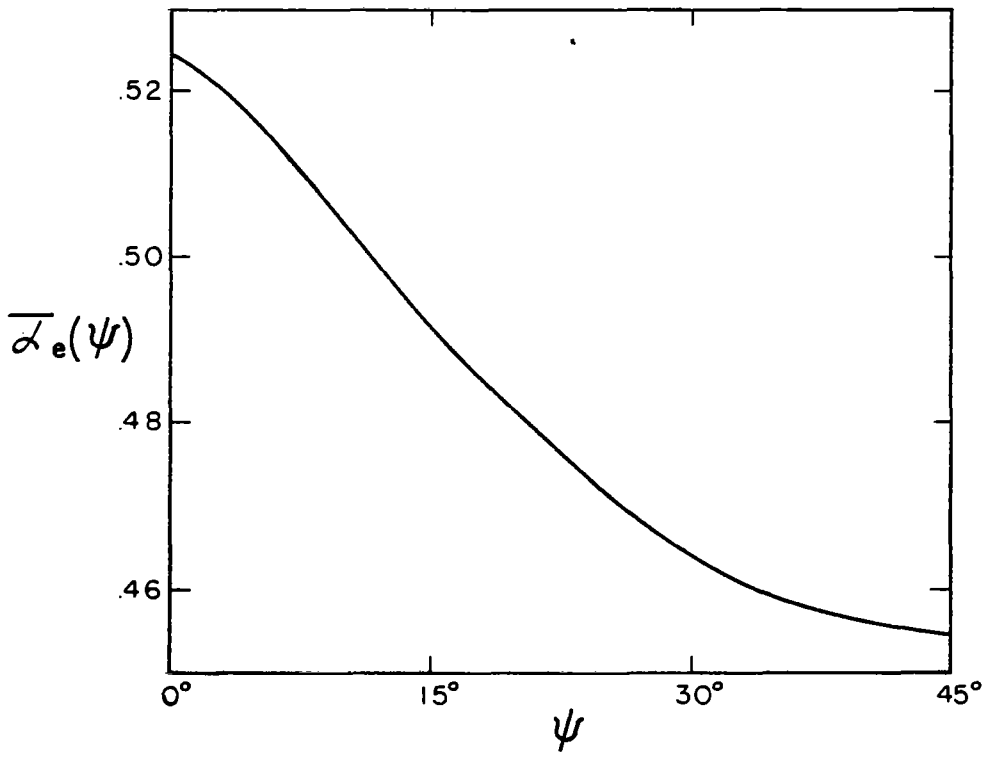

Fig. 3.14a. Normalized electric polarizability for diamond-shaped apertures.

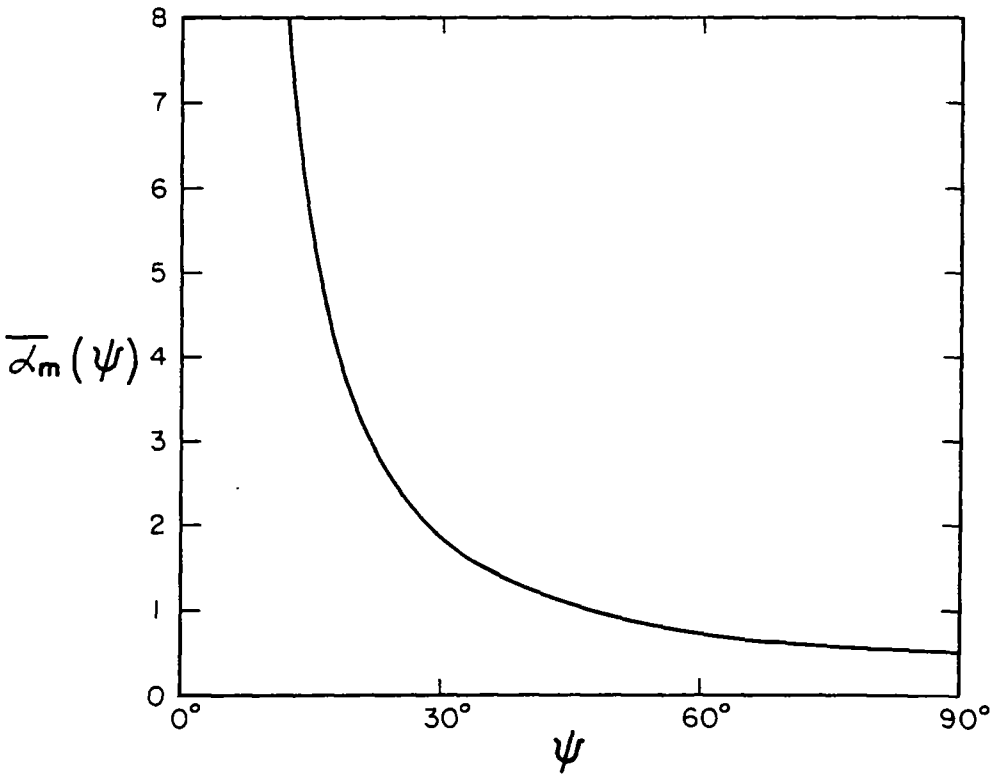

Fig. 3.14b. Normalized magnetic polarizability for diamond-shaped apertures.

$$\alpha_m = \frac{\alpha_{mi}}{1 + (\alpha_{mi}/w_x^3)\Sigma_h(\psi)}$$

w_x is the distance between apertures in the direction normal to the cable axis as shown in Fig. 3.13, and Σ_e and Σ_h are "interaction sums" whose dependences on ψ are shown in Fig. 3.15.

Marin (Ref. 3.13) considered the effect on the electric polarizability of an isolated aperture of the inner and outer dielectrics (i.e., the dielectric between the center conductor and the shield, and the outer dielectric weatherproofing jacket). He found that α_{ei}, the electric polarizability of an isolated aperture in the presence of dielectrics, was related to α_{eio}, the electric polarizability of an isolated aperture when no dielectric materials are present, by

$$\alpha_{ei} = \alpha_{eio}\left(\frac{2\varepsilon}{\varepsilon + \varepsilon_{j,eff}}\right) \tag{3.44}$$

in which ε is the permittivity of the inner dielectric and $\varepsilon_{j,eff}$ denotes either ε_j, the permittivity of the outer jacket, if one is present; or ε_o, if the cable has no jacket*.

Equations 3.40-3.44 permit one to evaluate the coupling parameters of a braided-shield coaxial cable when the permittivities of the dielectrics involved and the shield geometry are known. The remaining parameters Z and Y are affected by the presence of the shield apertures, but the changes are small for well-shielded cables. Thus for a braided-shield cable, Z and Y are given approximately by

$$Z \simeq \frac{\mu_o s}{2\pi} \ln \frac{b}{a}$$
$$\frac{1}{Y} \simeq \frac{1}{2\pi s\varepsilon} \ln \frac{b}{a} \tag{3.45}$$

To illustrate the effect of aperture coupling to a braided-shield cable, let us consider as an example an electrically short section of cable on which a constant total current I_{to} is induced by an external

*Actually, of course, $\varepsilon_{j,eff}$ is a function of the jacket thickness; but it turns out that for practicable jacket thickness, $\varepsilon_{j,eff}$ is essentially equal to ε_j if a jacket is present.

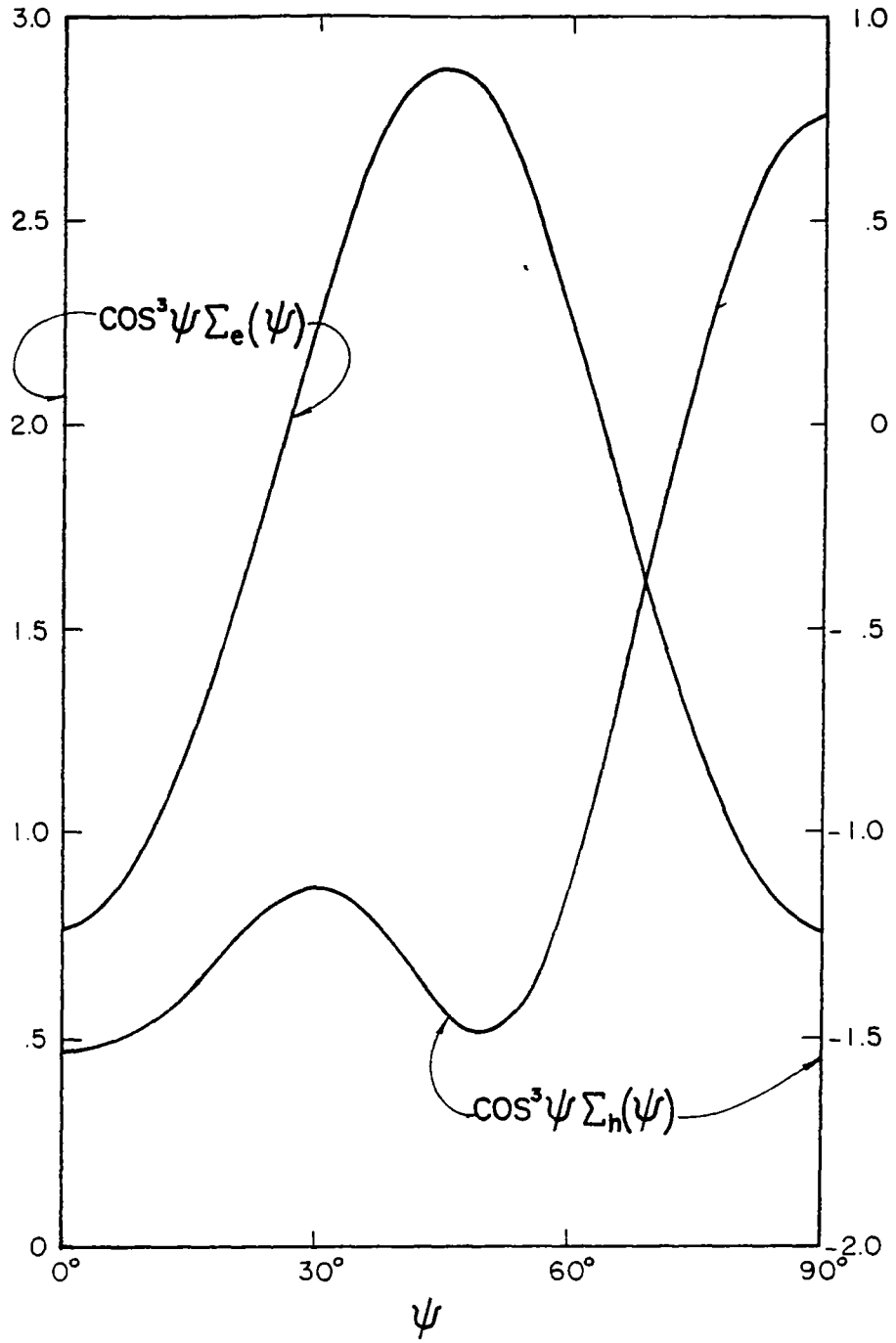

Fig. 3.15. "Normalized" interaction sums $\cos^2\psi\Sigma_e$ and $\cos^3\psi\Sigma_h$ vs. ψ.

source. We shall further assume that $Z_{Td} = 0$ so that only the effects of the apertures will be present. The cable extends from z=0 to z=ℓ and the terminating impedances at each end are Z(0) and Z(ℓ), as in our previous example in section B. When $Z(0) = Z(\ell) = Z_o$, the induced current on the internal conductor is

$$I(0) = I(\ell) = \frac{Z_T \ell \, I_{to}}{2Z_o} \tag{3.46}$$

Now let us denote Z_T by sL_s, where L_s is the "transfer inductance per unit length" due to the aperture coupling. If the time-domain total current $i_{to}(t)$ is a step function of magnitude I_o as given in Eq. 3.31, then

$$I(0) = I(\ell) = \frac{L_s \ell \, I_o}{2Z_o} \tag{3.47}$$

so that

$$i(t, z=0) = i(t, z=\ell) = \frac{L_s \ell \, I_o}{2Z_o} \delta(t) \tag{3.48}$$

and the induced terminal voltages are

$$v(t, z=0) = -v(t, z=\ell) = \frac{-L_s \ell \, I_o}{2} \delta(t) \tag{3.49}$$

so that this type of shield tends to act as a "differentiator" of the total current in producing the internal voltage and current.

If both terms in Z_T are present, i.e., if $Z_T = Z_{Td} + sL_s$, then the total internal current response to a step function current on the cable will consist of a term identical to that given in Eq. 3.49 plus a term like that plotted in Fig. 3.9 with R_o replaced by R_o/ν.

We now turn our attention to tape-wound helical shields. The most important feature of helical shields, whether filamentary or tape-wound, is that a significant azimuthal component of shield current density is present. If the total current carried by a helical shield is I_s, then the average azimuthal shield surface current density is

$$J_{s\phi} = \frac{I_s}{2\pi b} \tan\psi \tag{3.50}$$

This "solenoidal" component of the shield current density gives rise to a large inductive contribution to Z_T having the form (Ref. 3.1)

$$Z_T\Big|_{\substack{\text{due to solenoidal}\\ \text{shield current component}}} = \frac{s\mu_o}{4\pi}\left(1 - \frac{a^2}{b^2}\right)\tan^2\psi \qquad (3.51)$$

This contribution to Z_T generally dominates that due to the aperture coupling contribution which is due to the finite gaps between turns. That contribution is, for a M-filar filamentary shield (Ref. 3.14),

$$Z_T\Big|_{\text{due to gaps}} = \frac{s\mu_o \sec\psi}{2\pi M}\,\ell n\left(2\sin\frac{\pi\nu}{2}\right)^{-1} \qquad (3.52)$$

where ν denotes the optical coverage of the shield. For an M-filar tape-wound shield, the contribution to Z_T due to the gaps between turns is (Ref. 3.15)

$$Z_T\Big|_{\text{due to gaps}} = \frac{s\mu_o w_o^2 \sec\psi}{64\pi b^2 M} \qquad (3.53)$$

in which w_o denotes the gap width between turns.

Electric field coupling through gaps in the shield also occurs; the coefficient Γ_T is given by

$$\Gamma_T = \frac{2Cw_o^2 \sec\psi}{64\pi b^2 M(\varepsilon + \varepsilon_{j,\text{eff}})} \qquad (3.54)$$

for an M-filar tape-wound shield.

In general, the series impedance per unit length Z of a cable consists of terms arising from the finite impedances per unit length of the center conductor and the shield, an inductive term of the form given in Eq. 3.45, and Z_T itself. In the cases of tubular shields and braided shields, the inductive term alone is a satisfactory approximation to Z for well-shielded cables, because the remaining contributions are generally negligible in an engineering approximation. However, a contribution of the form given in Eq. 3.51 may not be negligible, so that for helical shields, Z is approximately given by

$$Z \approx \frac{s\mu_o}{2\pi}\left[\ell n\,\frac{b}{a} + \frac{1}{2}\left(1 - \frac{a^2}{b^2}\right)\tan^2\psi\right] \qquad (3.55)$$

while Y is given approximately by the second equation in 3.45.

The diffusion contribution to Z_T is generally of little interest, since the solenoidal-current contribution given in Eq. 3.51 is so large in comparison. It should also be mentioned that when a tape-wound shield carries a large transient current, the solenoidal-current inductive contribution to Z_T can cause sufficiently large voltages to develop between turns that arcover occurs. Under this condition, the shielding actually improves (Ref. 3.16).

E. Isolated Apertures

An isolated small aperture in a cable shield can be represented in terms of a transmission-line circuit model by a series voltage source V_a, a shunt current source I_a, series impedance Z_a, and a shunt admittance Y_a, as shown in Fig. 3.16. These quantities can be expressed as follows (Ref. 3.17):

$$\begin{aligned} V_a &= Z\delta_m I^{ext} \\ I_a &= s\delta_e Q^{ext} \\ Z_a &= s\delta_m L + R_a \\ Y_a &= s\delta_e C \end{aligned} \tag{3.56}$$

in which I^{ext} and Q^{ext} denote the induced current and charge per unit length on the outside surface of a "perfect" shield; Z, L, and C denote the line's series impedance, series inductance, and shunt capacitance per unit length; R_a is a "contact resistance" usually given from measurements*, and

$$\begin{aligned} \delta_m &= \frac{Z_w \alpha_m}{(2\pi b)^2 Z_o} \\ \delta_e &= \frac{Z_w \alpha_e}{(2\pi b)^2 Z_o} \end{aligned} \tag{3.57}$$

*R_a is usually important when the isolated aperture is used to model a connector.

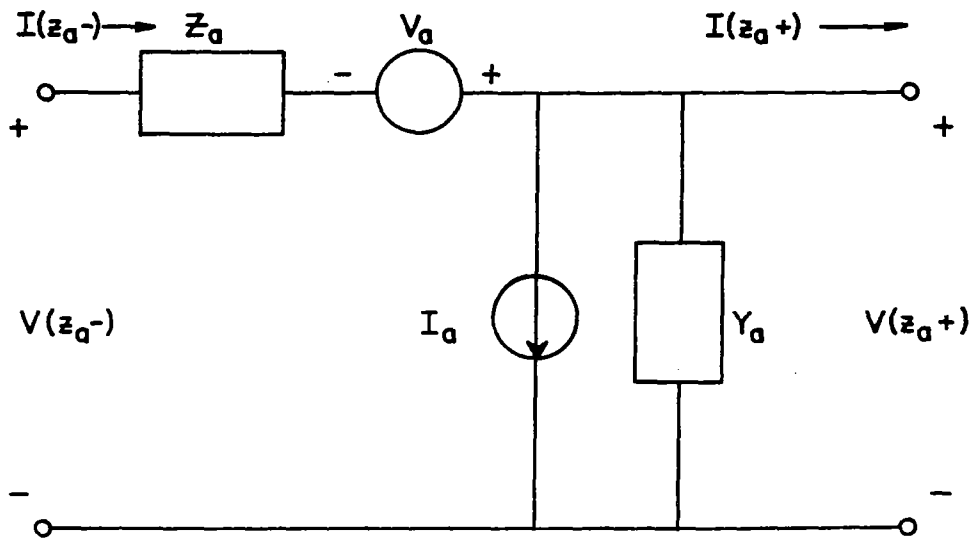

Fig. 3.16. Equivalent circuit for an isolated aperture at $z = z_a$.

in which α_e and α_m denote the electric and magnetic polarizabilities of the aperture, Z_o is the characteristic impedance of the line, and $Z_w = \sqrt{\mu_o/\epsilon}$ is the intrinsic wave impedance of the internal medium. The polarizabilities of apertures of various shapes are given in Ref. 3.17. Modifications to α_e due to the presence of inner and outer dielectrics have already been discussed (cf. Eq. 3.44).

The currents and voltages induced in the terminations of a cable by coupling through a single aperture can be found by means of a straightforward transmission-line analysis. Let the line run between z=0 and z=ℓ, and let the aperture be located at $z=z_a$. The terminating impedances are Z(0) and Z(ℓ), as in our previous examples. We find in general that

$$\begin{aligned} I(0) &= \frac{-V(0)}{Z(0)} = \left[\cosh \gamma z_a + \frac{Z(0)}{Z_o} \sinh \gamma z_a\right]^{-1} I_1 \\ I(\ell) &= \frac{V(\ell)}{Z(\ell)} = \left[\cosh \gamma(\ell - z_a) + \frac{Z(\ell)}{Z_o} \sinh \gamma(\ell - z_a)\right]^{-1} I_2 \end{aligned} \tag{3.58}$$

where

$$\begin{aligned} I_1 &= \frac{\frac{I_a}{Y_a}\left(Z_{e\ell} + \frac{Z_a}{2}\right) + \frac{V_a}{2}\left(Z_{e\ell} + \frac{Z_a}{2} + \frac{2}{Y_a}\right)}{\left(Z_{eo} + \frac{Z_a}{2}\right)\left(Z_{e\ell} + \frac{Z_a}{2}\right) + \frac{1}{Y_a}\left(Z_{e\ell} + Z_{eo} + Z_a\right)} \\ I_2 &= \frac{-\frac{I_a}{Y_a}\left(Z_{eo} + \frac{Z_a}{2}\right) + \frac{V_a}{2}\left(Z_{eo} + \frac{Z_a}{2} + \frac{2}{Y_a}\right)}{\left(Z_{eo} + \frac{Z_a}{2}\right)\left(Z_{e\ell} + \frac{Z_a}{2}\right) + \frac{1}{Y_a}\left(Z_{e\ell} + Z_{eo} + Z_a\right)} \end{aligned} \tag{3.59}$$

and

$$\begin{aligned} Z_{eo} &= Z_o \frac{Z(0)\cosh \gamma z_a + Z_o \sinh \gamma z_a}{Z(0)\sinh \gamma z_a + Z_o \cosh \gamma z_a} \\ Z_{e\ell} &= Z_o \frac{Z(\ell)\cosh \gamma(\ell - z_a) + Z_o \sinh \gamma(\ell - z_a)}{Z(\ell)\sinh \gamma(\ell - z_a) + Z_o \cosh \gamma(\ell - z_a)} \end{aligned} \tag{3.60}$$

are the impedances Z(0) and Z(ℓ) referred to the position of the aperture, and in which $\gamma = \sqrt{ZY}$ and $Z_o = \sqrt{Z/Y}$. In the special case where the line

is electrically short ($|\gamma\ell| << 1$) and terminated in its characteristic impedance at each end, we have

$$I(0) \simeq \frac{\frac{I_a}{Y_a}(Z_o + \frac{Z_a}{2}) + \frac{V_a}{2}(Z_o + \frac{Z_a}{2} + \frac{2}{Y_a})}{(Z_o + \frac{Z_a}{2})(Z_o + \frac{Z_a}{2} + \frac{2}{Y_a})}$$

$$I(\ell) \simeq \frac{-\frac{I_a}{Y_a}(Z_o + \frac{Z_a}{2}) + \frac{V_a}{2}(Z_o + \frac{Z_a}{2} + \frac{2}{Y_a})}{(Z_o + \frac{Z_a}{2})(Z_o + \frac{Z_a}{2} + \frac{2}{Y_a})} \qquad (3.61)$$

If it is further assumed that the total current induced on the cable is a constant*, then $I_a = 0$ and

$$I(0) = I(\ell) = \frac{V_a}{2Z_o + Z_a} = \frac{Z\delta_m}{2Z_o + Z_a} I^{ext} \qquad (3.62)$$

If $Z = sL$, i.e., if the series resistance per unit length is neglected, and if $I^{ext} = I_{to}/s$ (i.e., the exterior induced current is a step function of current I_{to}), and $R_a = 0$, then

$$I(0) = I(\ell) = \frac{I_{to}}{s + \frac{2Z_o}{L\delta_m}} \qquad (3.63)$$

and

$$i(t,z=0) = i(t,z=\ell) = I_{to} e^{-(2Z_o/L\delta_m)t} \qquad (3.64)$$

is the induced current in the terminations. The terminal voltages are

$$-v(t,z=0) = v(t,z=\ell) = Z_o I_{to} e^{-(2Z_o/L\delta_m)t} \qquad (3.65)$$

F. Experimental Procedures

In this section we shall mention briefly some of the procedures commonly employed or proposed for the experimental determination of the transmission-line coupling parameters. Consider first the voltage-change

---

* i.e., with respect to z.

equation in Eq. 3.1 with E(z) as given in Eq. 3.2:

$$\frac{dV}{dz} = -ZI + Z_T I_t \tag{3.66}$$

Clearly, Z_T can be expressed as

$$Z_T = \frac{1}{I_t} \frac{dV}{dz}\bigg|_{I=0} \tag{3.67}$$

so that Z_T may be determined experimentally by appropriate measurements of V and I_t under open-circuit (I=0) conditions. A configuration appropriate to such measurements is shown in Fig. 3.17. A length of the coaxial cable under test is mounted in a concentric conducting cylinder and the shield is driven by a current source at one end. The current provided by the source is I_o. The center conductor is open at the other end and the potential difference between the center conductor and the shield is measured. If the measured value of this potential is denoted V and the length of the cable sample is ℓ_s, then

$$Z_T = \frac{V}{\ell_s I_o} \tag{3.68}$$

It is assumed that ℓ_s is small in comparison to the wavelength over the frequency range of interest. Measurements taken with a system of this type are discussed in more detail in Refs. 3.18 and 3.19.

Another approach to the problem of measuring Z_T has been suggested by Lee and Baum (Ref. 3.3). Their approach is based on the same equation 3.66,

$$Z_T = Z \frac{I}{I_t}\bigg|_{\frac{dV}{dz} = 0} \tag{3.69}$$

An experimental configuration based on this approach is shown in Fig. 3.18. A current source I_o drives both the center conductor and the shield at one end of the cable and its concentric conducting cylindrical enclosure and the center-conductor current is measured at the other end. If the measured value of current is I, then

$$Z_T = Z\ (I/I_o) \tag{3.70}$$

The measurement of the electrical coupling parameters is based on considerations similar to those given above. Writing the current-change

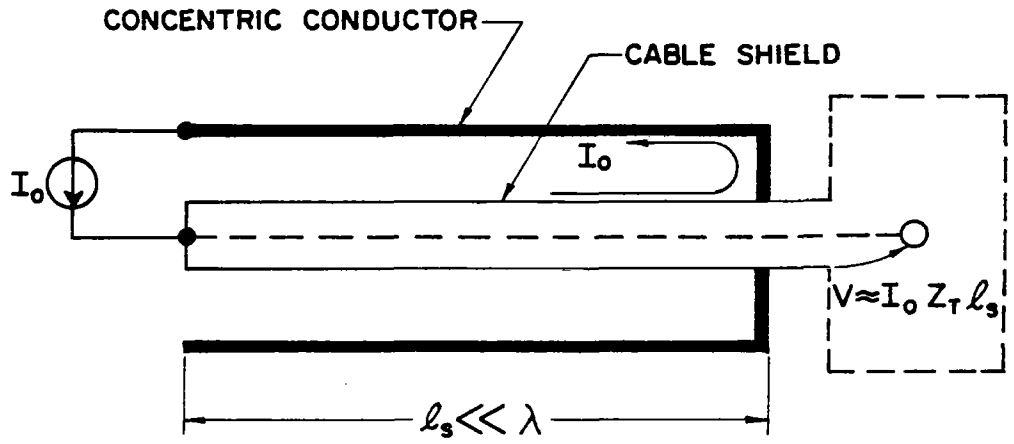

Fig. 3.17. An experimental configuration to determine Z_T (open-circuit form).

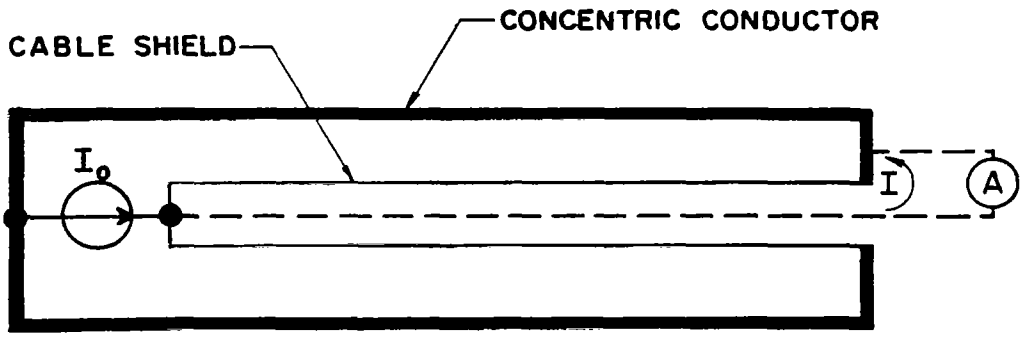

Fig. 3.18. An experimental configuration to determine Z_T (short-circuit form).

equation in Eq. 3.1 with $K(z) = Y_T V_t$, we have

$$\frac{dI}{dz} = -YV - Y_T V_t \tag{3.71}$$

from which it is evident that

$$Y_T = -\frac{1}{V_t}\frac{dI}{dz}\bigg|_{V=0} \tag{3.72}$$

An experimental configuration based on eq. (3.72), is shown in Fig. 3.19. The cable sample is mounted again in a concentric conducting cylinder. The center conductor is shorted to the shield at each end and the current measured at one end. At the opposite end, a voltage source drives the cable and the concentric conductor. If the source voltage is V_o with polarity as shown and the measured short-circuit current is I, then

$$Y_T = \frac{I}{V_o \ell_s} \tag{3.73}$$

where ℓ_s again denotes the length of the cable sample, which is assumed to be short with respect to wavelength over the frequency range of interest.

Lee and Baum (Ref. 3.3) have proposed an alternate configuration shown in Fig. 3.20. This configuration is based on the equation

$$Y_T = -Y\frac{V}{V_t}\bigg|_{I=0} \tag{3.74}$$

The experimental procedure suggested is to again place the cable sample in a concentric cylindrical conductor, drive the shield with a voltage source, and measure the open-circuit voltage at one end of the cable. If the driving voltage is V_o with polarity as shown in Fig. 3.20 and the measured value of the open-circuit voltage is V, then

$$\Gamma_T = \frac{V/V_o}{C_o/C - V/V_o} \tag{3.75}$$

in which C_o denotes the capacitance per unit length between the outer cylindrical conductor and an equivalent ideal (i.e., aperture-free) shield and C is the capacitance per unit length between the center conductor and the same equivalent ideal shield. "Quadraxial" test procedures have also been developed (Refs. 3.20, 3.21), and will be discussed in chapter IV.

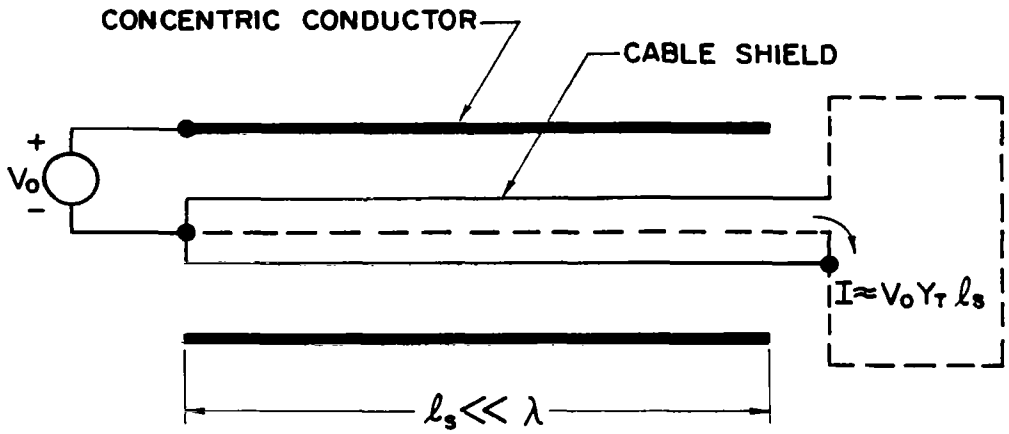

Fig. 3.19. An experimental configuration to determine Y_T (short-circuit form).

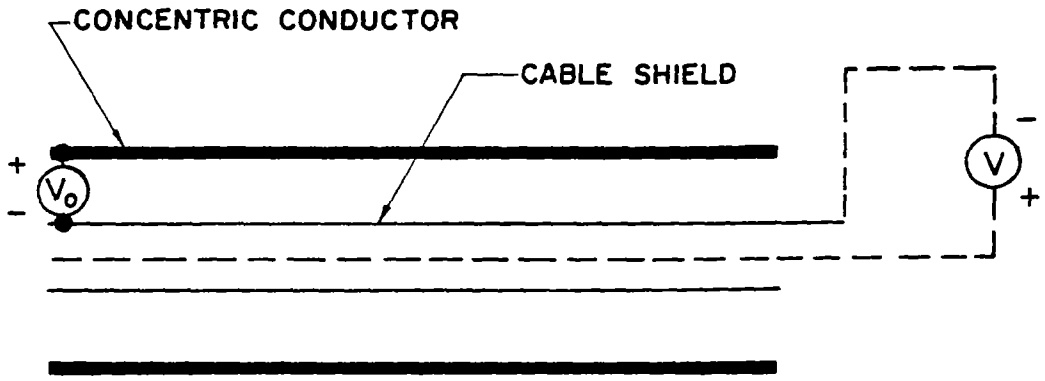

Fig. 3.20. An experimental configuration to determine Γ_T (open-circuit form).

G. Summary and Concluding Remarks

Coupling to the interior of a shielded cable by an external source of electromagnetic energy occurs via two mechanisms: diffusion of the electromagnetic field through the imperfectly conducting shield and penetration of apertures in the shield. When these phenomena occur over the entire length of a cable, we speak of distributed coupling; coupling at isolated points can also occur.

The analysis of the induced internal currents and voltages on an imperfectly shielded transmission line is based on the transmission-line equations. The source terms in these equations are related to the total current and the total charge per unit length induced on the cable by an external electromagnetic field. The determination of these total quantities is a problem for which no general and relatively simple solution exists. However, for well-shielded cables these quantities may be calculated assuming that the shield is perfect: thus the cable may be externally represented by a perfectly conducting cylinder whose radius is small in comparison to wavelength over the EMP frequency range.

The central problem in the analysis of coupling from the exterior to the interior of an imperfectly shielded cable is in determining, either analytically or experimentally, the coupling parameters in the transmission-line equations. Such analysis has been carried out in a reasonably complete fashion for cables with tubular shields without apertures, for braided-shield cables (whose shields possess a nearly uniform distribution of apertures), and for helically shielded cables. The analysis of ferromagnetic effects is less well developed because of the non-linear nature of the field equations.

The analysis of multiconductor cables within a shield is in a much more rudimentary stage than that of coaxial cables, because of the greater complexity of the multiconductor problem. However, substantial progress has been made in recent years, and the reader is referred to Refs. 3.22 - 3.24 for access to some of the relevant literature. The approach involves generalizing the transmission-line equations to the form

$$\frac{d\bar{V}}{dz} = -\bar{\bar{Z}}\cdot\bar{I} + \bar{E}(z)$$

$$\frac{d\bar{I}}{dz} = -\bar{\bar{Y}}\cdot\bar{V} - \bar{J}(z) \qquad (3.76)$$

in which $\bar{I}$ and $\bar{V}$ are column vectors whose elements are the currents and voltages with respect to the shield on each of the internal conductors, $\bar{\bar{Z}}$ and $\bar{\bar{Y}}$ are "series impedance" and "shunt admittance" matrices, and $\bar{E}(z)$ and $\bar{J}(z)$ are vector sources which depend upon the total current and the total charge per unit length induced on the multiconductor cable by an external source.

References

3.1. R. W. Latham, "An approach to certain cable shielding calculations," Interaction Notes, Note 90, January 1972.

3.2. E. F. Vance, "Shielding effectiveness of braided-wire shields," IEEE Trans. Electromagn. Compat., Vol. EMC-17, pp. 71-77, May 1975, and also Interaction Note 172, April 1974.

3.3. K. S. H. Lee and C. E. Baum, "Application of modal analysis to braided-shield cables," IEEE Trans. Electromagn. Compat., Vol. EMC-17, pp. 159-169, August 1975, and also Interaction 133, January 1973.

3.4. E. F. Vance, "Prediction of transients in buried shielded cables," Interim Technical Report, Contract DAEA18-71-A-0204, Stanford Research Institute, March 1973.

3.5. P. R. Barnes, "The axial current induced on an infinitely long, perfectly conducting, circular cylinder in free space by a transient electromagnetic plane wave," Interaction Notes, Note 64, March 1971.

3.6. L. Schlessinger, "Currents induced by a plane wave on an infinite wire above a flat earth," IEEE Trans. Electromagn. Compat., Vol. EMC-17, pp. 156-158, August 1975.

3.7. S. A. Schelkunoff, "The electromagnetic theory of coaxial transmission lines and cylindrical shields," Bell Syst. Tech. J., Vol. 13, pp. 532-579, October 1934.

3.8. S. Ramo, J. R. Whinnery, and T. Van Duzer, Fields and Waves in Communication Electronics, New York: John Wiley and Sons, pp. 286-303, 1965.

3.9. R. Ferber and F. J. Young, "Enhancement of EMP shielding by ferromagnetic saturation," IEEE Trans. Nuclear Sci., Vol. NS-17, pp. 354-359, December 1970.

3.10. D. E. Merewether, "Design of shielded cables using saturable ferromagnetic materials," IEEE Trans. Electromagn. Compat., Vol. EMC-12, pp. 138-141, August 1970.

3.11. H. Kaden, Wirbelströme und Schirmung in der Nachrichtentechnik, Berlin: Springer-Verlag, 1957.

3.12. R. W. Latham, "Small holes in cable shields," Interaction Notes, Note 118, September 1972.

3.13. L. Marin, "Effects of a dielectric jacket of a braided-shield cable on EMP coupling calculations," Interaction Notes, note 178, May 1974.

3.14. K. F. Casey, "On the effective transfer impedance of thin coaxial cable shields," IEEE Trans. Electromagn. Compat., Vol. EMC-18, pp. 110-116, August 1976, and Interaction Note 267, March 1976.

3.15. E. F. Vance, "Coupling to Cables," DNA Handbook Revision, Ch. 11, Stanford Research Institute, December 1974.

3.16. E. F. Vance, "Shielding effectiveness of the liquid tight flexible conduit from transient tests," Tech. Memo, No. 13, Stanford Research Institute, May 1971.

3.17. K. S. H. Lee, "Localized penetration through cable shields," Proc. 1974 FULMEN Meeting, pp. 126-134, AFWL, Kirtland AFB, New Mexico, April 1974.

3.18. E. F. Vance, "Cable transfer impedance measurements," Tech. Memo, No. TM-4, Stanford Research Institute, July 1970.

3.19. E. F. Vance and W. C. Wadsworth, "Cable shield test facility," Tech. Memo, No. TM-25, Stanford Research Institute, October 1973.

3.20. E. D. Knowles and L. W. Olson, "Cable shield effectiveness testing," IEEE Trans. Electromagn. Compat., Vol. EMC-16, pp. 16-23, Feb. 1974.

3.21. P. L. E. Uslenghi and J. E. Bridges, "Electromagnetic field penetration through the shield of a coaxial cable," paper presented at 1976 USNC/URSI Meeting, Amherst, Massachusetts, October 1976.

3.22. F. M. Tesche, "A general multi-conductor transmission line model," paper presented at 1976 USNC/URSI Meeting, Amherst, Massachusetts, October 1976.

3.23. C. E. Baum, "Coupling into coaxial cables from currents and charges on the exterior," paper presented at 1976 USNC/URSI Meeting, Amherst, Massachusetts, October 1976.

3.24. S. Frankel, "Terminal response of braided-shield cables to external monochromatic electromagnetic fields," IEEE Trans. Electromagn. Compat., Vol. EMC-16, pp. 4-16, February 1974.

CHAPTER IV
CONNECTORS

A. Introduction

Electromagnetic energy induced on the outer shell of a connector can be coupled into the shielded inner conductors because of the imperfect connection between plug and receptacle connectors. Indeed, the connector can be viewed as part of a "cable shield" that may contain cracks, slits or lossy contacts through which external electromagnetic fields may penetrate into the internal (shielded) region of the "cable". Most analytical efforts (Refs. 4.1, 4.2) so far have been very limited and have suffered from inadequate physical description of the apertures in a connector. As a result, these efforts have only derived quantities that are meaningful to determine experimentally. Recently, a simple analytical expression has been derived for field leakage through conduit connectors (Ref. 4.3).

Most of the available results have been the experimentally determined shielding effectiveness of some specific types of connectors at either the low frequency region (for EMP evaluation) or the RF region. However, most of these results are for coaxial connectors and only very limited data are available for multipin connectors.

For cables and connectors, the popular definition of shielding effectiveness S is the ratio of power flowing in a path including the exterior of the shield to the power induced in a path including the interior of the shield, expressed in dB. When performing measurements, it is arranged so that the impedance associated with the interior path and the exterior path are equal. In this case

$$S = 20 \log_{10} \left(\frac{\text{outer conductor current}}{\text{inner conductor current}} \right) \text{ dB} \qquad (4.1)$$

This definition is used throughout this chapter.

B. Coaxial Connectors

1. Construction of coaxial cable connectors

Connectors for aircraft and missile application must be small in physical size, of minimum weight, and carry as much electrical power as possible. For EMP hardening purposes, they must also have high shielding effectiveness. Frequency of mating and demating also decides the type of connectors suitable for one particular application.

In Fig. 4.1, the constructions of a few popular connectors (Ref. 4.4) are presented. These connectors satisfy the specification of MIL-C-39012 (Ref. 4.5). In Fig. 4.2, the construction details of the MIL-C-38999 Series II connector, which satisfy the requirements for missile application, are illustrated. The magneform attachment method (Ref. 4.6) as shown with a "Z" shaped cup to ground the tine attachment to the plug body is superior for EMP protection over the conventional soldering method of grounding tine attachment. However, the soldering method is still widely used, even among MIL-C-38999 suppliers.

2. Analytical treatment

Analytical treatment of electromagnetic leakage through coaxial cable connectors has not been very successful due to uncertainties in the physical description of the imperfect connection between plug and receptacle connector shells. A few theories have been developed to understand the leakage mechanisms as well as to derive quantities that are important to measure. A simple expression for the leakage of electromagnetic field through a conduit connector has recently been derived (Ref. 4.3).

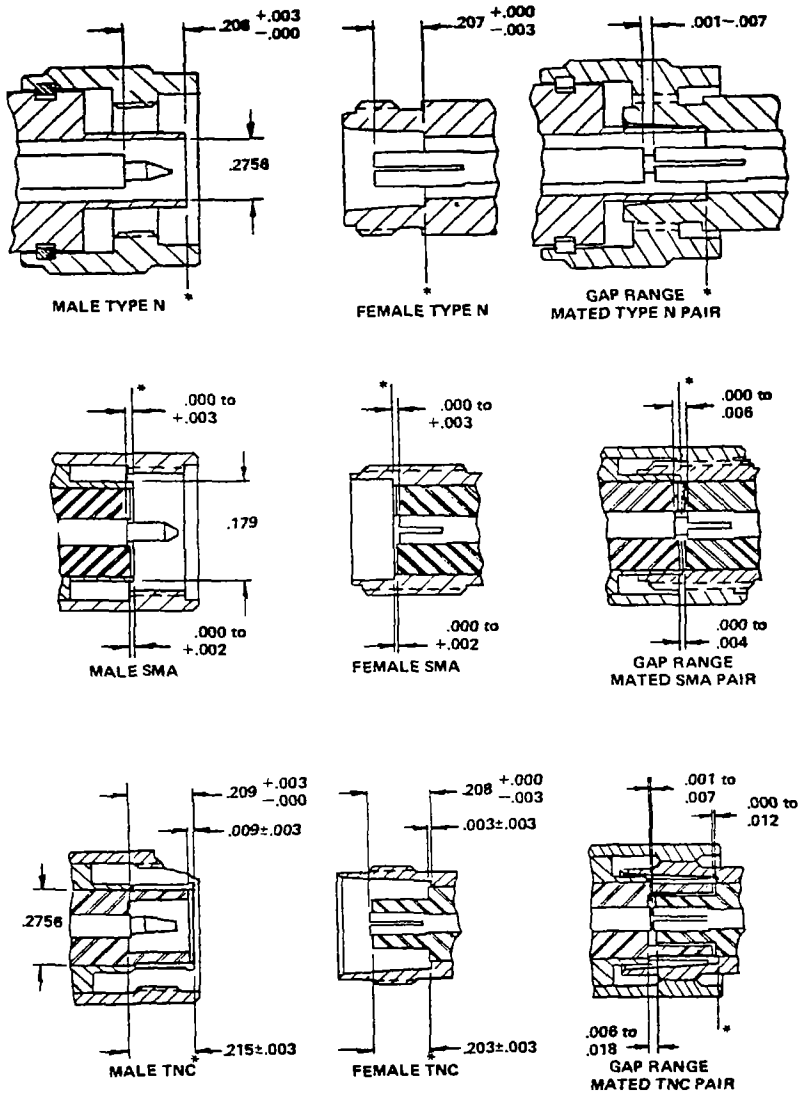

Fig. 4.1 Construction of some popular coaxial connectors

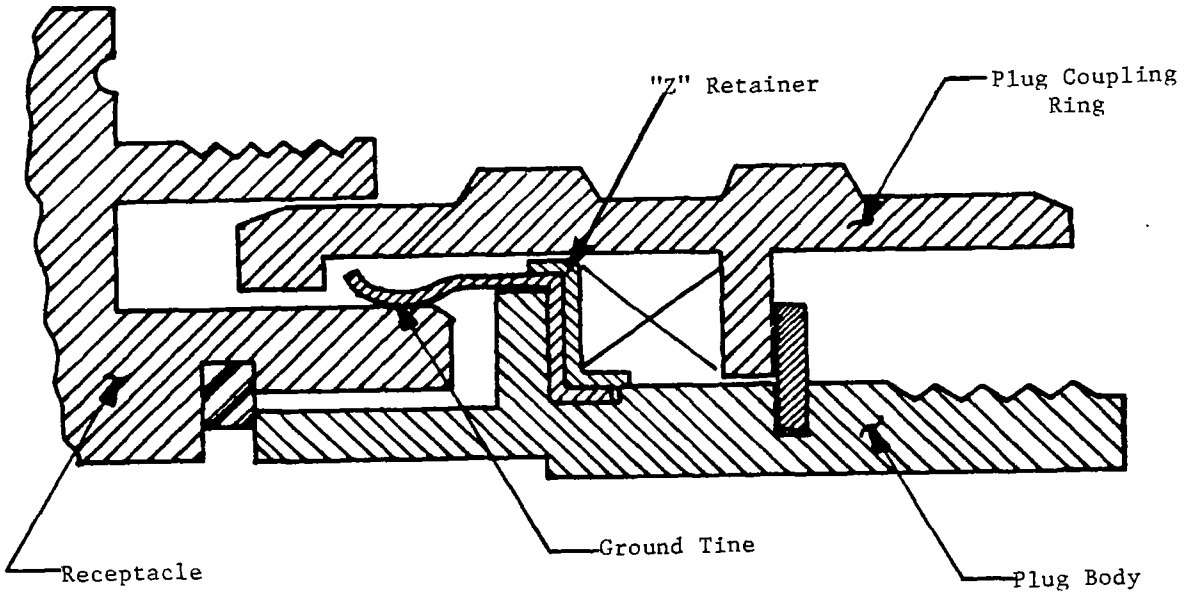

Fig. 4.2 Construction of MIL-C-38999 Series II connector

a. Cable connectors

Modeling a leaky connector by a double concentric coaxial line with a number of apertures on the middle conductor, and using the iris-coupled transmission line theory for the source geometry with one aperture, the equivalent circuit of the connector in Fig. 4.3 is derived (Refs. 4.1, 4.2). The admittances Y_a and Y_b are the input admittances to the left and to the right, respectively, of the connector. The transfer impedance Z_T relates the leakage voltage source driving the inner circuit to the connector shell current I_o. Similarly, the current source driving the inner circuit is related to the voltage V_o between the connector shell and the surrounding structure by the transfer admittance Y_T. The series impedance Z_c and the shunt admittance Y_c usually are negligible unless the load admittances are very large or very small. Also, the transfer admittance Y_T is usually negligible for good shielded cable connectors, particularly for connectors mounted on bulkheads where the electric fields are weak. Thus, the transfer impedance Z_T is the quantity to measure for the determination of leakage through connectors.

b. Conduit connectors

Conduits of permalloy material are used in some aircraft such as the B-1 to shield cables from EMP. Two conduits are jointed by a connector which consists of a metallic ring coupler (see Fig. 4.4) being held tightly over the conduit segments by two outer rings. An idealized model of the connector, as shown in Fig. 4.4, is used to derive an expression for the field leakage through the conduit connector (Ref. 4.3).

At EMP frequencies, penetrations through the connector by the electric field and the longitudinal component of the magnetic field (along the conduit axis) are negligible. The magnetic field at A just inside the conduit is given by

$$\frac{H}{K_{sc}} \approx \frac{Y_{int}}{Y_s + Y_{int} + Y_{ext}} \tag{4.2}$$

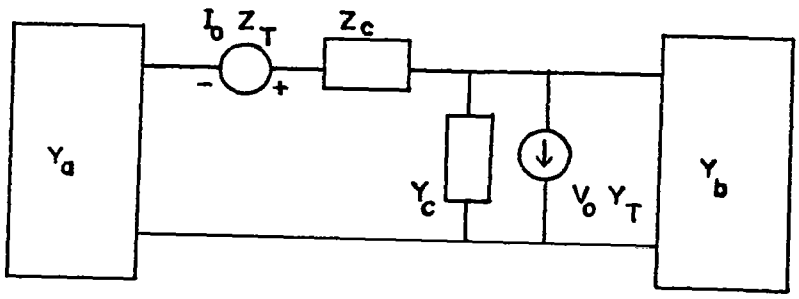

Fig. 4.3 Equivalent circuit of a connector

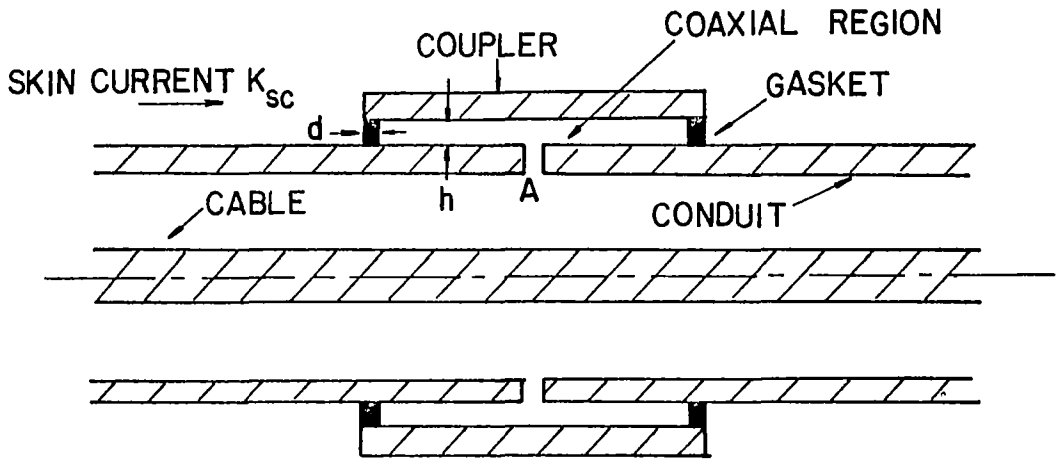

Fig. 4.4 Geometry of the shielding elements in the B-1 cable conduit connector

where

H = magnetic field at A

K_{sc} = short-circuit surface current density on the conduit surface

$Y_{int} = 1/(2Z_o)$

$Z_o = 377\,\Omega$ is the intrinsic impedance of free space

$Y_s = \sigma d$

σ = conductivity of gasket

d = thickness of gasket

$$Y_{ext} = \frac{j\omega \varepsilon_o h}{\pi} \ln \frac{1}{|kh|}$$

ω = angular frequency

ε_o = permittivity of free space

h = separation between coupler and conduit

$k = \omega$/velocity of light is the wavenumber.

3. Experimental treatment

a. Measurement technique

(i) Triaxial configuration

The most popular method of measuring the leakage through connectors is the triaxial configurations, a setup of which is shown in Fig. 4.5 (Refs. 4.7, 4.8). The connector is incorporated in a uniform transmission line which is terminated in a matched load. This coaxial system is embodied within a cylinder to form a second coaxial system which is terminated at one end in an adjustable short-circuiting plunger, and at the other end in a tapered transition to a matched detector. The short-circuit position is adjusted for each measurement to assure a low impedance associated with the equivalent leakage generator. This setup is useful for measurements up to the frequency where higher order modes can propagate in the outer coaxial line.

The leakage power ratio r_p is defined here as the ratio of the power detected in the matched detector at the output of the triaxial

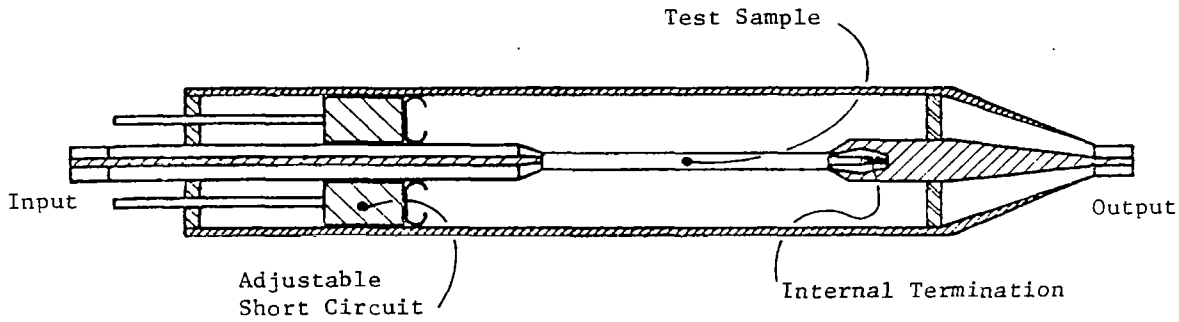

Fig. 4.5 Triaxial configuration of measuring leakage through coaxial connectors

unit to the power flowing through the internal connector system. If the inner and outer coaxial systems have the same characteristic impedance Z_o, this leakage power ratio, when expressed in dB, is the shielding effectiveness. The transfer impedance Z_T of the matched system is simply the product of the characteristic impedance and the square root of the leakage power ratio, i.e.,

$$Z_T = Z_o \sqrt{r_p}$$

(ii) Quadraxial configuration

Another very useful method of measuring the leakage through connectors is the quadraxial configuration illustrated in Fig. 4.6. Here, the driven (signal) path and the receiver (leakage) path are matched at all frequencies from dc up to where higher order modes propagate in the coaxial lines. The addition of the third coaxial system (formed by the driven tube and the guard tube) thus eliminates the need for an adjustable shorting ring, as used in the triaxial system.

Since this frequency range can be achieved without mechanical adjustment, a swept frequency source and a self-tuned detector can be used to reduce measurement time and provide continuous data as a function of frequency.

b. Shielding effectiveness and transfer impedance

Only a limited amount of data on coaxial connector shielding effectiveness and transfer impedance is available. Some of these data are measured for RF evaluation and may not be directly applicable to EMP assessment. In Figs. 4.7 - 4.8 are presented the measured results of a number of coaxial connectors, some of which are the popular commercial types (Ref. 4.7) such as Type BNC, N, GR 874-B, GR 874-BL; some are mainly for military applications (Ref. 4.9).

C. Multipin Connectors

1. Analytical treatment

The mechanisms of electromagnetic energy leakage through shielded multipin connectors are similar to those of coaxial connectors. Iris-coupled transmission line theory again yields the same equivalent circuit as that of Fig. 4.3 for each pin in the connector. In principle, separate values of Z_T, Y_T, etc., are required by measurements; in practice, one can seldom specify a multiconductor system

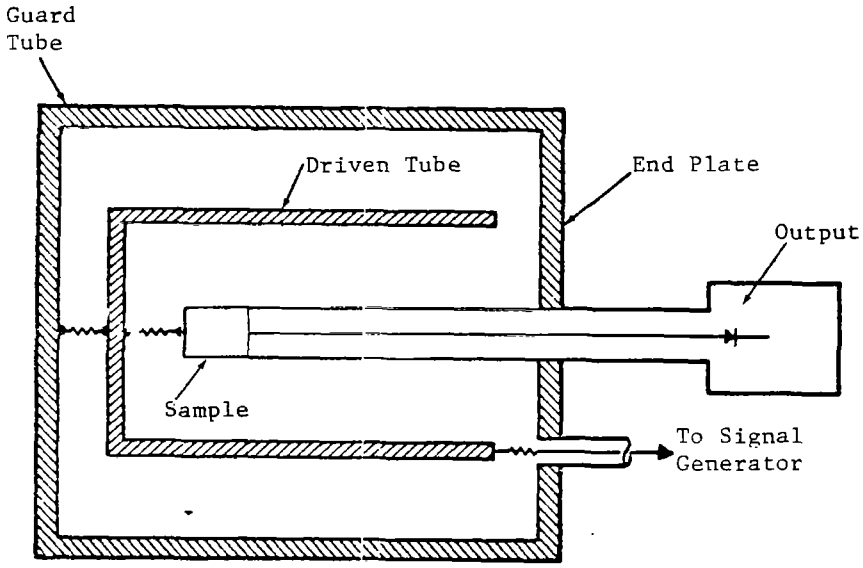

Fig. 4.6 Quadraxial configuration of measuring leakage through coaxial connectors

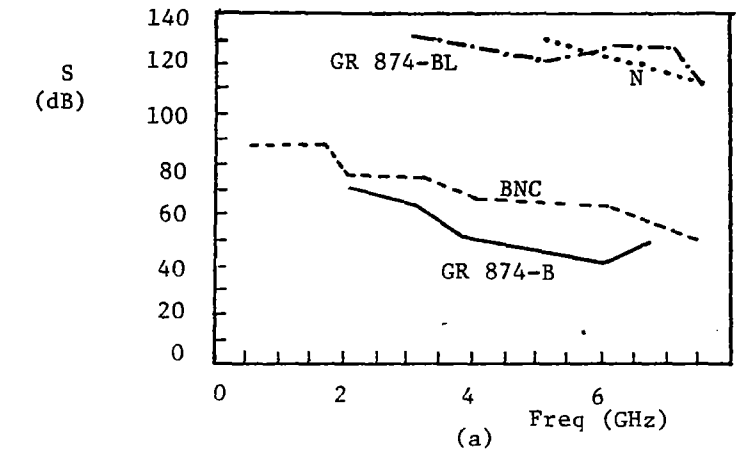

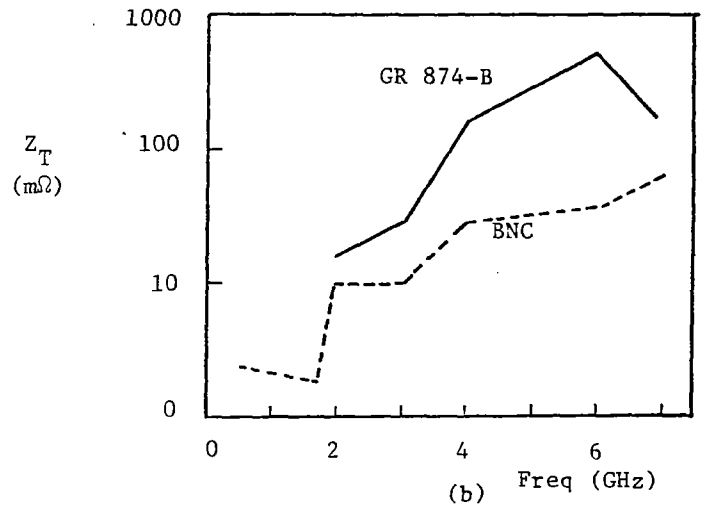

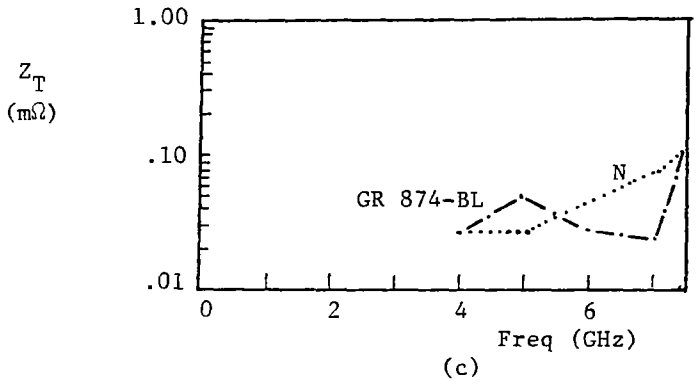

Fig. 4.7 Shielding effectiveness and transfer impedances of some coaxial connectors

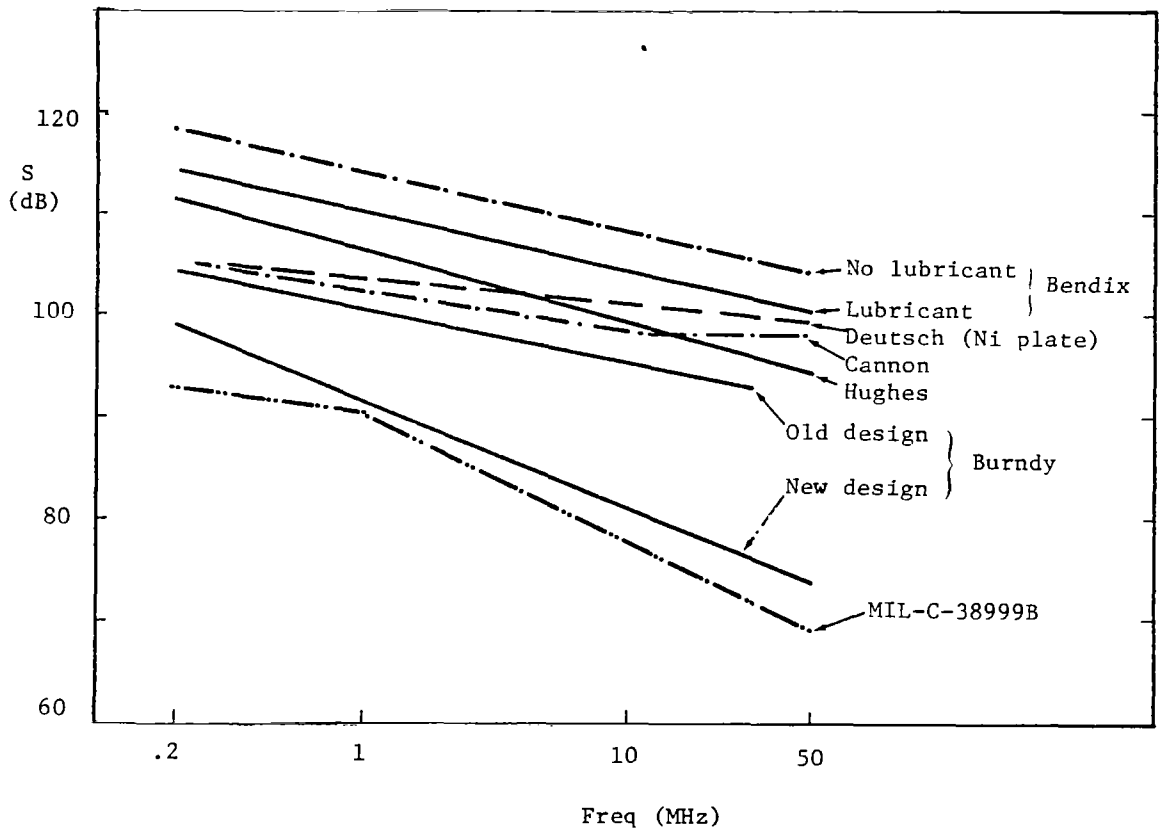

Fig. 4.8 Shielding effectiveness of some military connectors

with sufficient accuracy to warrant this detail in determining the connector properties (Ref. 4.2). Therefore, it is usually sufficient to specify Z_T, Y_T, etc., for a typical pin and assume that this value applies to all pins in the connector. Again, as in the coaxial connector case, usually only the transfer impedance Z_T is important and the resulting equivalent circuit is shown in Fig. 4.9.

2. Experimental results

In Fig. 4.10, the shielding effectiveness for a number of connectors are presented

D. Other Construction Effects

Electrical, mechanical and material properties of the connector construction can affect the leakage effect through the connector.

1. Contact resistance

The connector often has a lumped series resistance associated with the contact resistance of the mating surfaces. Thus, a current through the connector produces a series IR drop as well as a magnetic field penetrating to the internal conductors (Ref. 4.2). The shielding effectiveness decreases with the increase in the shell-to-shell resistance (Ref. 4.9).

The contact resistance of two aluminum surfaces with various platings and coatings is presented in Fig. 4.11 as a function of pressure. It is clearly shown that different coatings/platings have vastly different contact resistances. In Fig. 4.12 the shielding effectiveness of a connector with different surface finishes is shown. The conducting finishes all give essentially the same performance. However, the anodized finish over aluminum, which meets most environment requirements, decreases the shielding effectiveness.

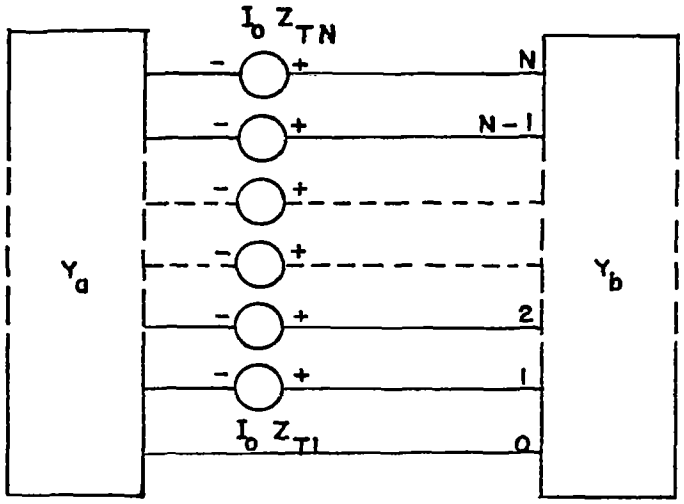

Fig. 4.9 Equivalent circuit for a multipin connector

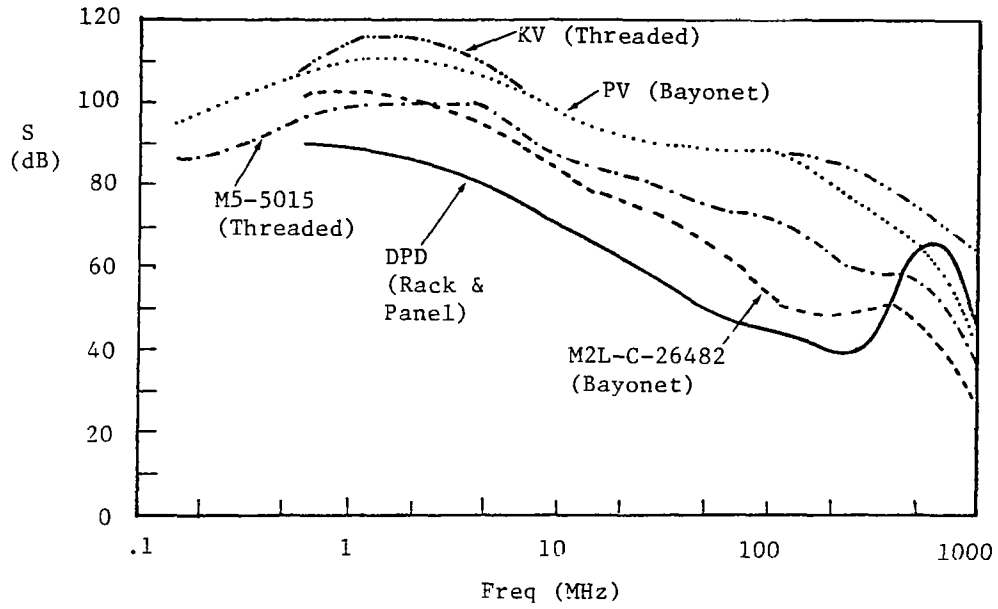

Fig. 4.10 Shielding effectiveness of some connectors

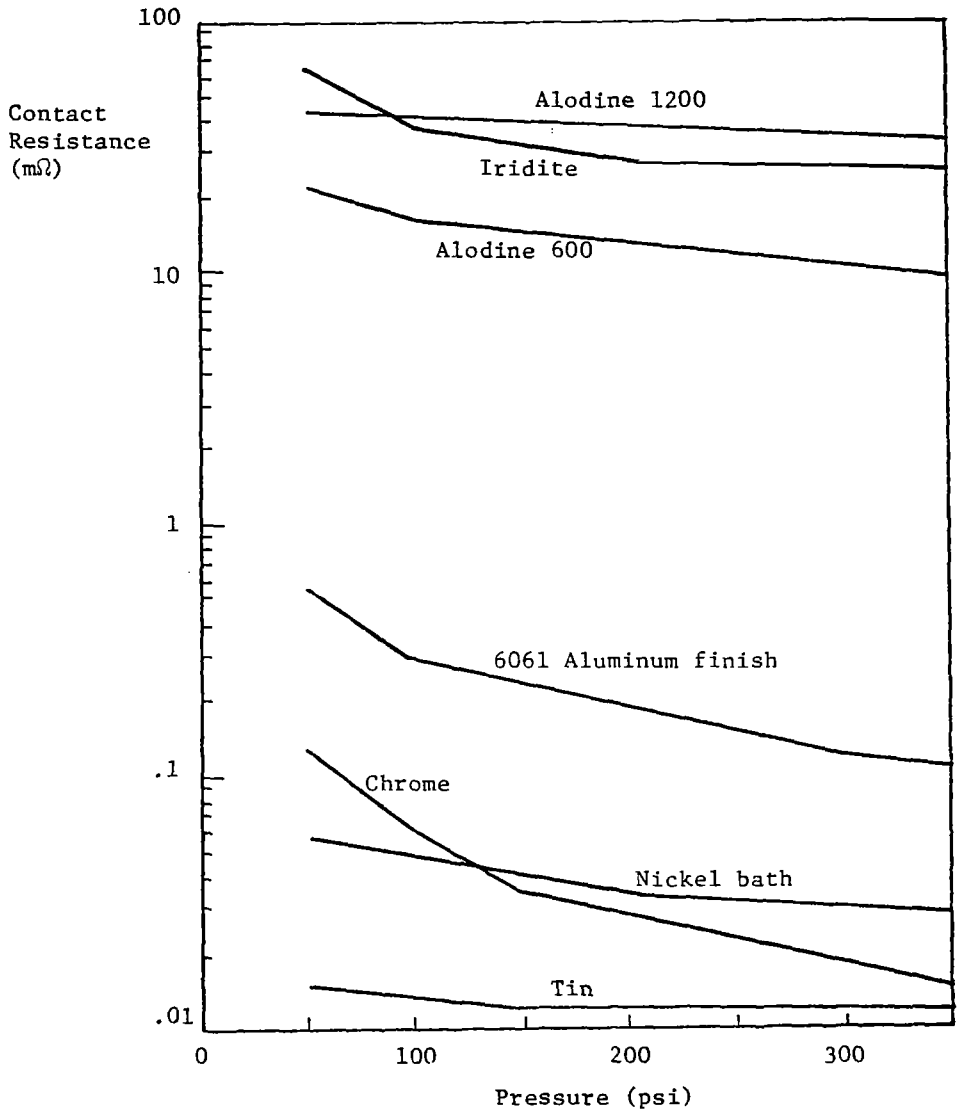

Fig. 4.11 Contact resistance of conductive coatings on aluminum

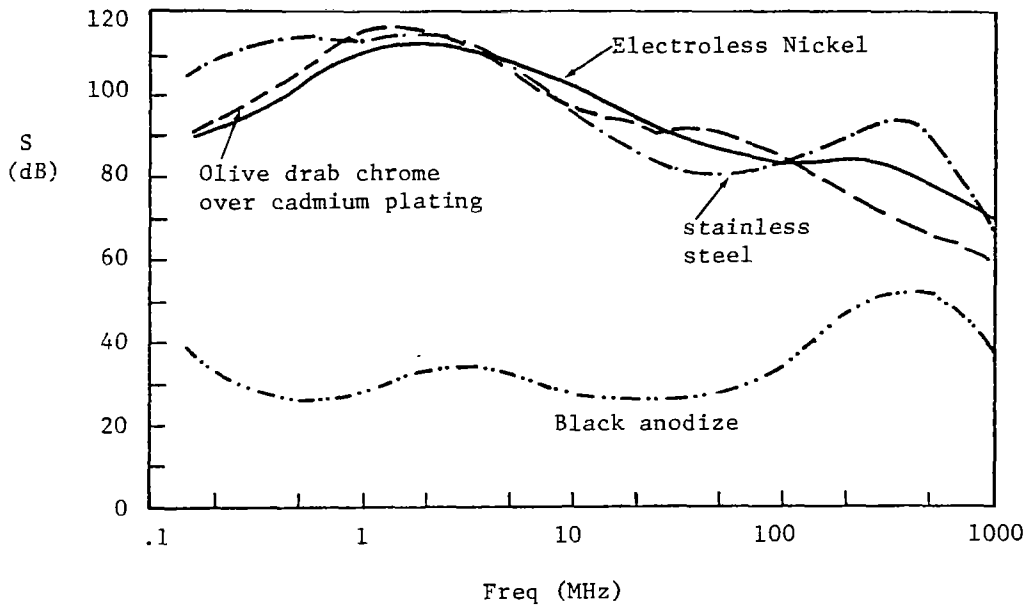

Fig. 4.12 Shielding effectiveness of connectors with various finishes

2. Threaded and bayonet coupling

Similar connectors using threaded coupling exhibit slightly better shielding than those with bayonet coupling. This is illustrated in Figure 4.10.

3. Tightening torque on threaded coupling connectors

Figure 4.11 shows that the contact resistances decrease with increasing pressure. For threaded coupling connectors, shielding effectiveness increases for higher tightening torque, as is evident by test results shown in Figure 4.13 for the static case (Ref. 4.11)

The shielding effectiveness of connectors under dynamic testing conditions to simulate vibration is presented in Figure 4.14 (Ref. 4.11), also as a function of the tightening torque. It is evident that shielding effectiveness is less during vibration.

4. Peripheral spring fingers

Figure 4.13c shows that connectors with peripheral spring fingers have significantly higher shielding effectiveness than those without fingers. In bayonet connector shells with fingers, the shielding effectiveness is plotted in Figure 4.15 versus percentage slot width (Ref. 4.9) which is the percentage of the slot width over the total of the finger and slot widths. This suggests that more effective shielding is achieved with decreasing slot width.

In Figure 4.16 the improvements of adding spring fingers are shown for both the bayonet coupling connectors and the threaded coupling connectors. The improvements of the threaded coupling types is not great since it already gives adequate shielding.

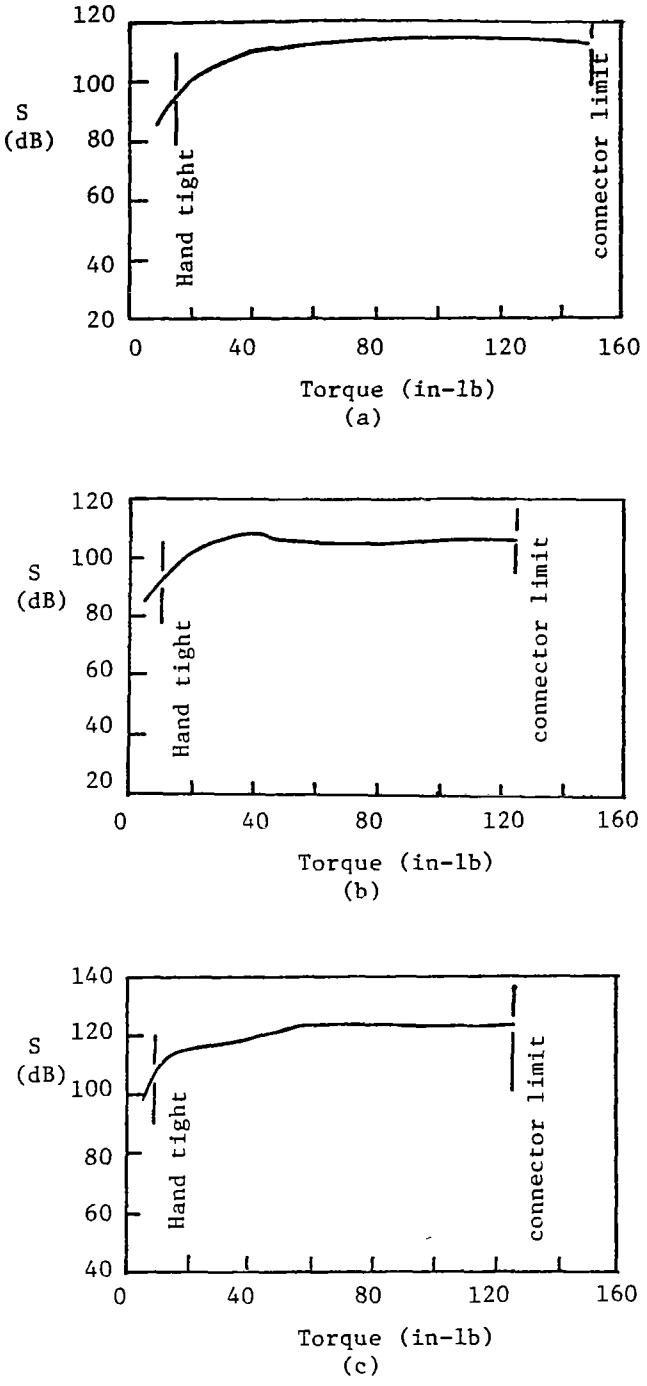

Fig. 4.13 Effect of tightening torque on shielding effectiveness for three shell sizes: (a) shell size 12, (b) shell size 10, (c) shell size 10 with RF fingers

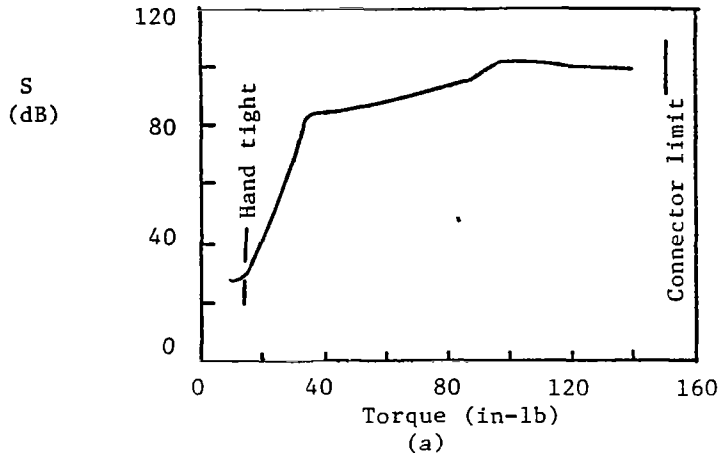

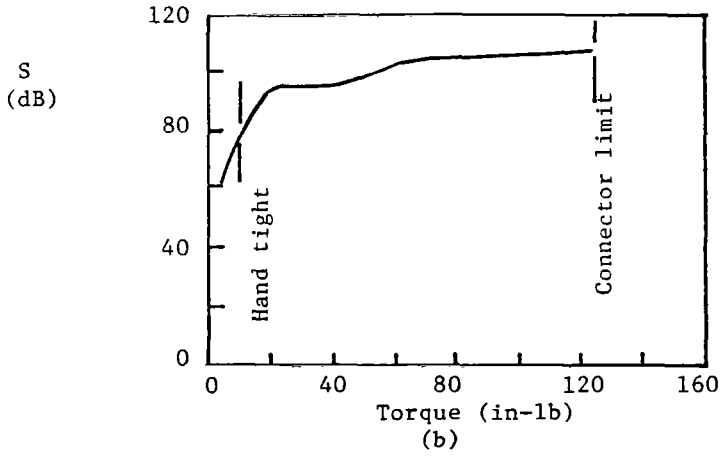

Fig. 4.14 Effect of tightening torque on shielding effectiveness during vibration for (a) shell size 12, and (b) shell size 10

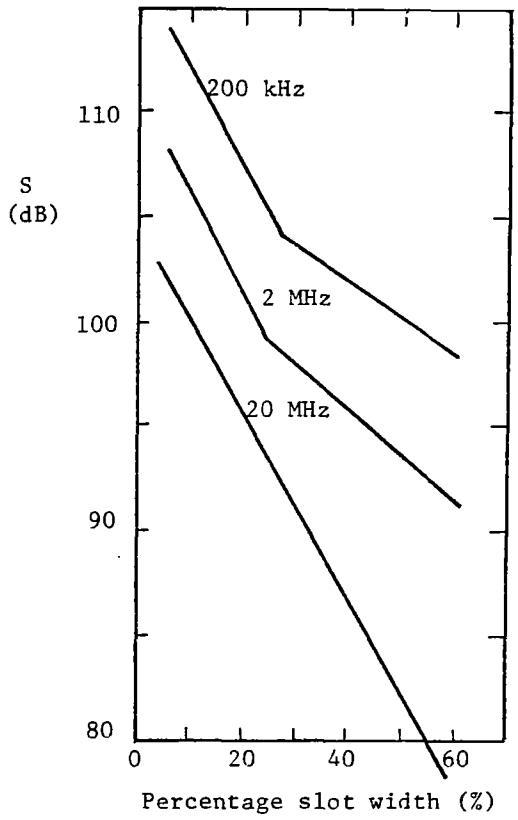

Fig. 4.15 Effect of slot width on shielding effectiveness of bayonet coupling connectors

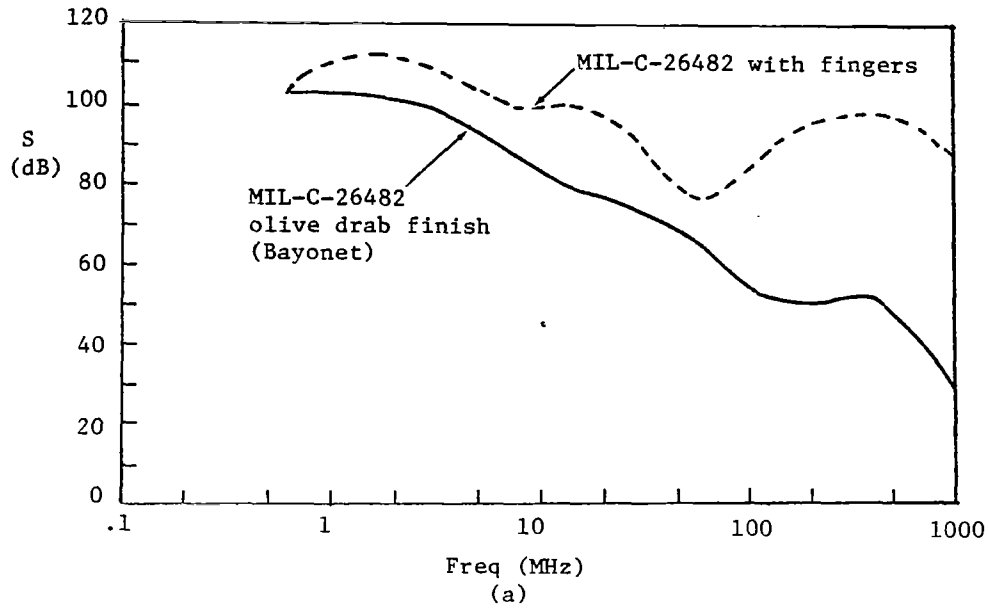

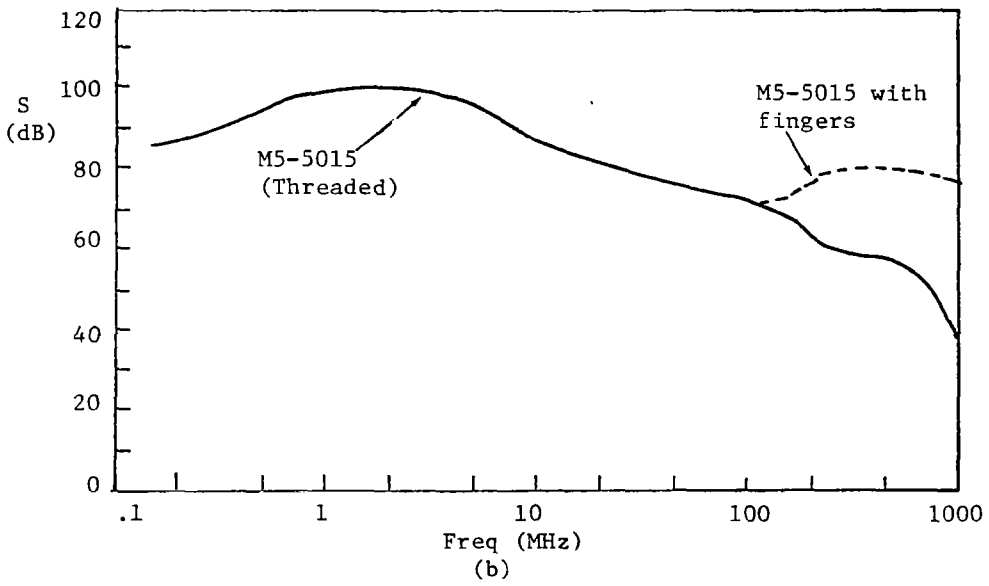

Fig. 4.16 Effect of added spring fingers on shielding effectiveness of (a) bayonet coupling connectors and (b) threaded coupling fingers

5. Shielding gaskets

Connectors using shielding gaskets between the interfaces also increase the shielding effectiveness. The effect is illustrated in Fig. 4.17 when a woven-wire mesh gasket is used. Also metalistic gaskets (woven wire and rubber) can be used.

6. Conductor position

The position of the shielded conductors causes some difference in the electromagnetic coupling from the shell. In Fig. 4.18 the shielding effectiveness of a pair of conductors near the center is about 5 dB over that of a pair of conductors near the shell. Also, the shielding effectiveness is known to increase for a decrease in the spacing between the two conductors.

7. Magnetic field shielding

Magnetic field shielding is important at frequencies below 10 kHz. For the particular materials shown in Fig. 4.19, ferromagnetic materials offer better shielding at low frequencies, whereas above 10 kHz, aluminum offers ample protection.

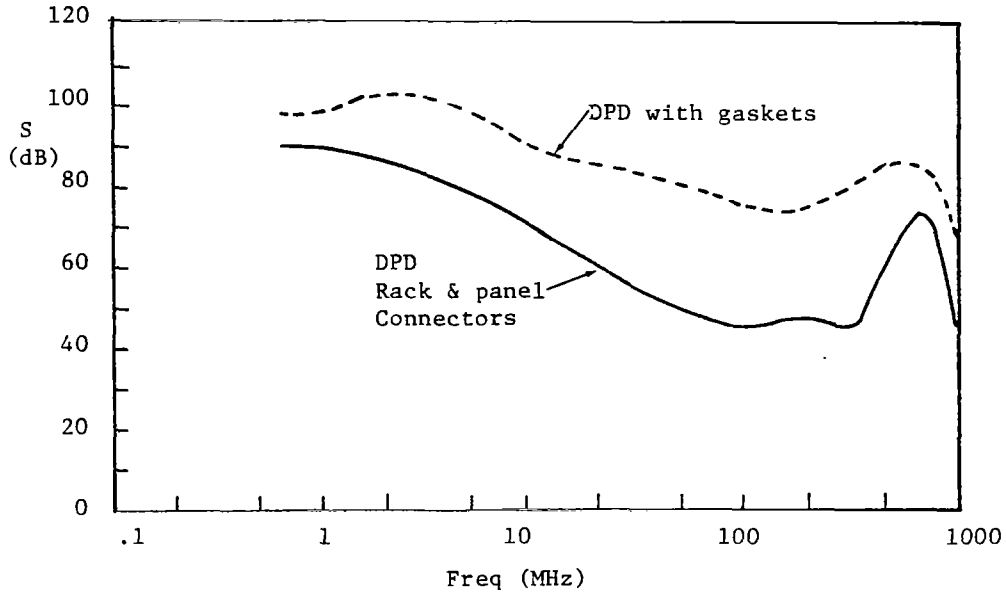

Fig. 4.17 Effect of added shielding gaskets on shielding effectiveness of connectors

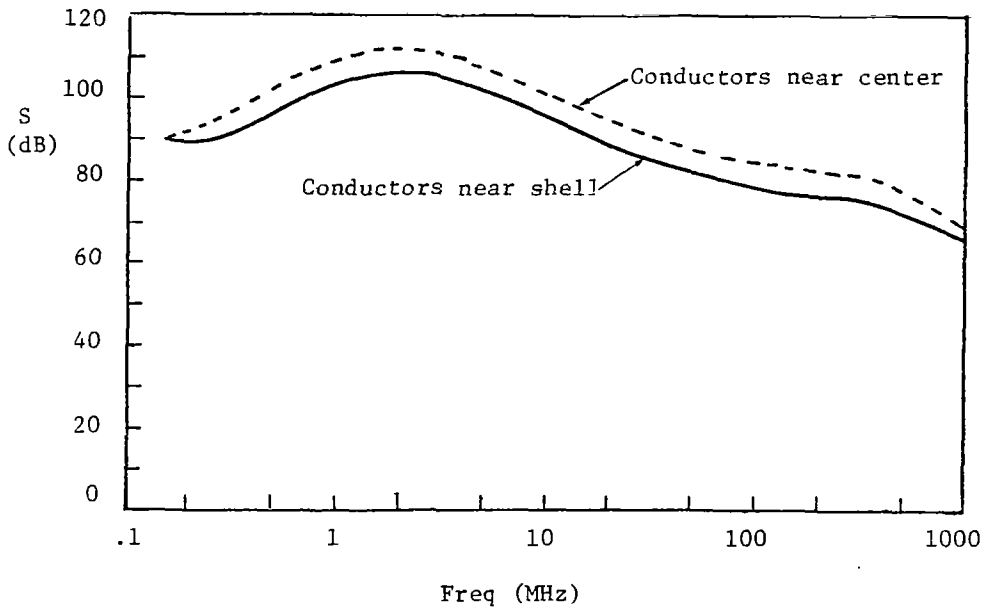

Fig. 4.18 Effect of shielded conductors' positions on shielding effectiveness

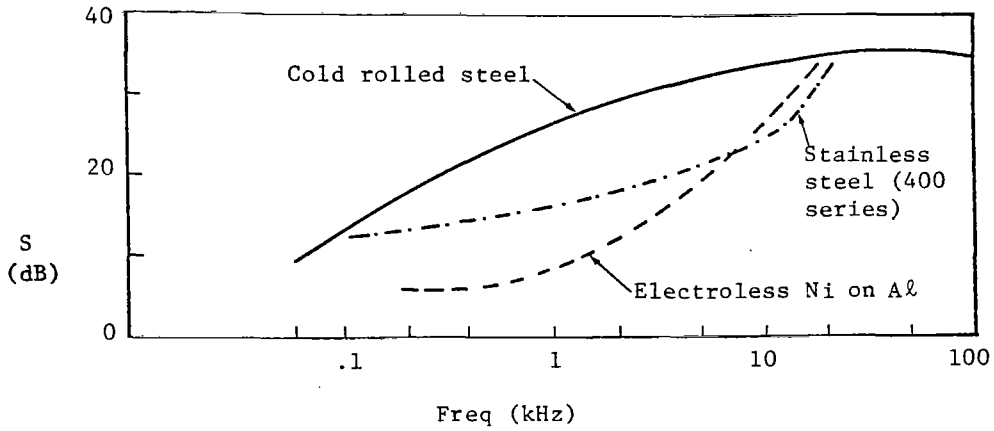

Fig. 4.19 Effect of shield materials on shielding effectiveness of connectors

References

4.1 S. Dairiki, "Considerations in shielding analysis of joints and connectors in cable systems," AFWL-TR-73-73, March 1972.

4.2 E.F. Vance and S. Dairiki, "Leakage through cable connectors," S.R.I. Technical Memo. 26, October 1973.

4.3 J. Lam, "Analysis of EMP penetration through the B-1 cable conduit connector," AFWL AIP Memo 5, November 1976.

4.4 "US coaxial m/w connector state of the art," Microwave Journal, Vol. 18, pp. 35-36, January 1975.

4.5 MIL-C-39012B Amendment 1, October 1972, "Military specification, connectors, coaxial, radio frequency, general specifications for."

4.6 D.F. Cook, "Connector design and test practices," Protection Engineering and Mangement Note PEM-17.

4.7 J. Zorzy and R.F. Muehlberger, "RF leakage characteristics of popular coaxial cables and connectors, 500 MC to 7.5 G C," Microwave Journal, Vol. 4, pp. 80-86, November 1961.

4.8 P.J. Madle, "Cable and connector shielding attenuation and transfer impedance measurements using quadraxial and quintaxial test methods," Protection Engineering and Management Note PEM-45, November 1975.

4.9 J.S. Miller, "Test report on conducted current shielding effectiveness of bayonet connector shells with fingers," Protection Engineering and Management Note PEM-12.

4.10 F.W. Schor, "Measurement of RF leakage in multipin electrical connectors," IEEE Trans. on Electromagnetic Compatibility, Vol. EMC-10, pp. 135-141, March 1968.

4.11 E.D. Knowles and J.C. Brossier, "Measuring connector shielding effectiveness during vibration," Protection Engineering and Management Note PEM-15.

CHAPTER V
SKIN PANELS

A. Introduction

Due to the finite conductivity of the walls (or skin panels on aircraft, missiles, etc.) of a structure, electromagnetic energy can penetrate into the interior of the structure by the process of diffusion. Skin panels of various shapes and various materials are discussed in this chapter; however, most of the formulas presented are restricted to (a) low frequencies where most EMP energy is contained, and (b) structures with thin walls. The first condition requires the characteristic dimensions of the structure to be small compared with the free space wavelength λ_o. The second condition requires the wall thickness to be small compared with the characterisitc dimensions of the structure.

Panels of planar geometry are discussed in detail. This geometry is relevant to many practical configurations where the wall thickness is small in comparison with the local radii of curvature.

A popular measure of the effect of a skin panel on electromagnetic fields is the shielding effectiveness. Define first the shielding factor as the ratio of electric or magnetic field strengths at a point after and before the placement of the shield in question. For most cases of interest, the fields before the placement of the shield are the same as the incident fields outside the shield (Ref. 5.1). Thus, the magnetic shielding factor η_M^o is defined by

$$\eta_M^o = \frac{\text{amplitude of magnetic field inside the shielded space}}{\text{amplitude of magnetic field incident on the shield}} \qquad (5.1a)$$

and the electric shielding factor η_E^o is defined likewise for the electric fields, i.e.,

$$\eta_E^o = \frac{\text{amplitude of electric field inside the shielded space}}{\text{amplitude of electric field incident on the shield}} \quad . \qquad (5.1b)$$

The superscript o indicates that the shielding factors are defined with respect to the incident field.

Note that η_M^o and η_E^o depend on the polarization of the incident wave. The shielding effectiveness is defined as the reciprocal of the absolute value of the corresponding shielding factor and is expressed in dB. Hence, the magnetic shielding effectiveness S_M^o is

$$S_M^o = 20 \log_{10}[1/|\eta_M^o|] \text{ dB} \qquad (5.2a)$$

and the electric shielding effectiveness S_E^o is

$$S_E^o = 20 \log_{10}[1/|\eta_E^o|] \text{ dB} \qquad (5.2b)$$

It is clear that the higher the shielding effectiveness is, the less electromagnetic field energy can penetrate into the shielded space.

In the literature, some authors prefer to measure the effect of a shield by the ratio of penetrated field to the **total** local field outside the shield (incident field + reflected field). For instance, for a parallel-plate cavity with a normal incident field, expression for the ratio: magnetic field inside the shielded space/total magnetic field just outside the plate is given (Ref. 5.2). This quantity has the advantage that once the total local magnetic field (i.e., the skin current on the panel) is known or measured, one can then estimate the penetrated field. However, definitions in Eqs. 5.1 to 5.2 enable one to estimate the penetrated field once the free field is known. Usually, for a finite-sized object, the free field can be readily measured at a distance from the object.

Quantities similar to those in Eqs. 5.1 to 5.2 are defined with superscript T to denote that they are associated with the total field strength, i.e.,

$$\eta_M^T = \frac{\text{amplitude of magnetic field inside the shielded space}}{\text{amplitude of total magnetic field outside the shield}} \qquad (5.3a)$$

$$\eta_E^T = \frac{\text{amplitude of electric field inside the shield space}}{\text{amplitude of total electric field outside the shield}} \qquad (5.3b)$$

and

$$S_M^T = 20 \log_{10} [1/|\eta_M^T|] \text{ dB} \tag{5.4a}$$

$$S_M^T = 20 \log_{10} [1/|\eta_E^T|] \text{ dB} \tag{5.4b}$$

Throughout this report, formulas for both definitions (i.e., the one involving incident field and the one involving total field) are given. Either the shielding factor and/or the shielding effectiveness is presented, but it will be carefully pointed out whether the formula involves incident fields or total fields.

B. Panels of Planar Geometry

When the local radii of curvature are large compared with the skin panel wall thickness, the formulas presented in this section for panels of planar geometry often apply.

1. Panels of conducting materials

a. Skin effect

Skin effect is a phenomenon which tends to concentrate currents on the surfaces of conductors that are nearest to the field sources producing them. Penetration of fields into the conductors decreases gradually. For a good conductor (with conductivity $\sigma >> \omega\varepsilon$; ε being the dielectric constant) of semi-infinite extent, the electric field of the normal incident plane wave is attenuated according to

$$E(z) = E(0)\, e^{-z/\delta}\, e^{-jz/\delta} \tag{5.5}$$

where $E(0)$ is the electric field at the surface $z = 0$, z being the axis normal to the surface. Magnetic field and current density

obey the same relationship as Eq. 5.5 . The quantity δ is known as the skin depth, or the depth of penetration; it is given by

$$\delta = 1/\sqrt{\pi f \mu \sigma} \qquad (5.6)$$

Here μ and σ are respectively the permeability and conductivity of the conductor, and f is the frequency of the incident wave.

The skin depth is the distance at which fields and current densities have decreased to $1/e$ ($= 0.368$ or 8.69 dB) of their value at the surface for plane solids, or for conductors of other shapes with radii of curvature much larger than δ . However, δ as defined above may be considered simply a material constant at frequency f , and it is a useful parameter for other geometrical configurations when evaluating their shielding effectiveness (Ref. 5.3).

Regardless of the plane wave's direction of incidence, the fields within a <u>good conductor</u> of infinite extent are transverse (parallel to the plane interface), the ratio of electric field to magnetic field is independent of position and is defined as the intrinsic impedance Z_i of the medium, given by

$$Z_i = R_s(1 + j) \qquad (5.7)$$

where the surface resistivity R_s (or sometimes called the resistance per square) is given by

$$R_s = \sqrt{\pi f \mu / \sigma} = 1/(\sigma\delta) \qquad (5.8)$$

R_s is another material constant. Equation 5.8 also states that the skin effect resistance of the semi-infinite plane conductor is the same as the dc. resistance of a plane conductor of depth δ.

In table 1 , the skin depth and surface resistivities for several materials are presented.

Table 1

SKIN DEPTH AND SURFACE RESISTIVITY OF METALS

	CONDUCTIVITY Mhos/meter σ	PERMEABILITY Henrys/meter μ	SKIN DEPTH Meters δ	SURFACE RESISTIVITY Ohms R_s
Silver	6.17×10^{7}	$4\pi\times10^{-7}$	$0.0642/\sqrt{f}$ *	$2.52\times10^{-7}\sqrt{f}$
Copper	5.80×10^{7}	$4\pi\times10^{-7}$	$0.0660/\sqrt{f}$	$2.61\times10^{-7}\sqrt{f}$
Aluminum	3.82×10^{7}	$4\pi\times10^{-7}$	$0.0815/\sqrt{f}$	$3.17\times10^{-7}\sqrt{f}$
Brass	1.57×10^{7}	$4\pi\times10^{-7}$	$0.127/\sqrt{f}$	$5.01\times10^{-7}\sqrt{f}$
Solder	0.706×10^{7}	$4\pi\times10^{-7}$	$0.185/\sqrt{f}$	$7.73\times10^{-7}\sqrt{f}$
Steel	6.38×10^{6}	$110\times4\pi\times10^{-7}$	$0.0190/\sqrt{f}$	$8.25\times10^{-6}\sqrt{f}$

*f is the frequency in Hz

b. Shielding of plane waves by a plane of finite thickness

For normal incidence, the ratio of the amplitudes of transmitted and incident electric fields (the electric shielding factor η_E^o) due to an infinite conducting plane (medium 2) of thickness d (see Fig. 5.1) is (Ref. 5.4 and 5.5)

$$\eta_E^o = \frac{E_t}{E_o} = \frac{2\,Z_o\,Z_i}{2\,Z_o\,Z_i\cosh(kd) + (Z_o^2 + Z_i^2)\sinh(kd)} \quad . \qquad (5.9)$$

where the media on both sides of the shield are air, and

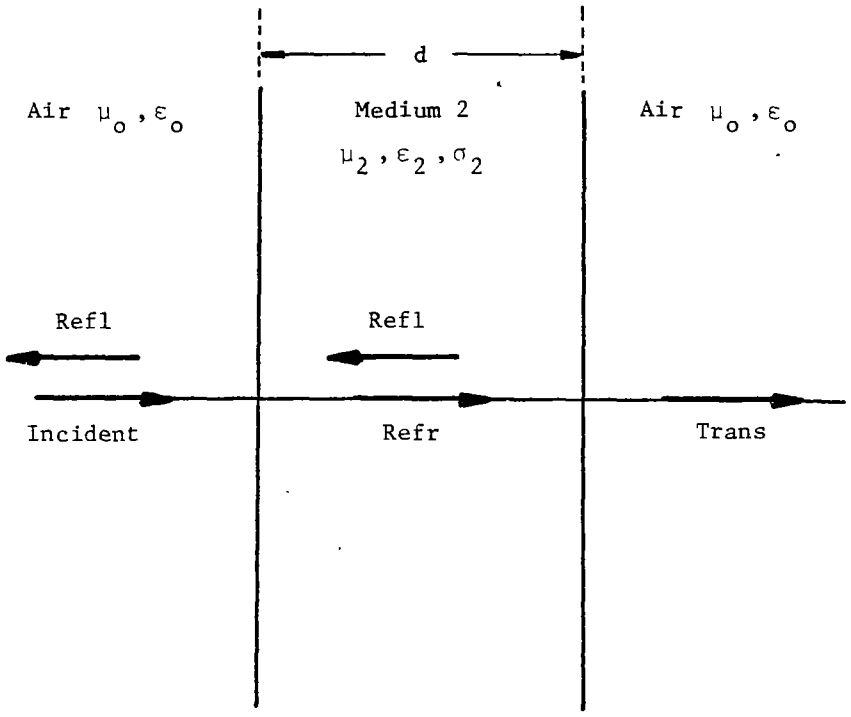

Figure 5.1 Reflection and transmission of plane waves by a plane sheet of thickness d

E_t , E_o = amplitudes of transmitted and incident electric fields at the boundaries

$Z_o = 377\ \Omega$ is the intrinsic impedance of air

$Z_i = (1 + j)/(\sigma_2 \delta_2)$ is the intrinsic impedance of medium 2

$k = (1 + j)/\delta_2$ is the propagation constant of medium 2

$\delta_2 = 1/\sqrt{\pi f \mu_2 \sigma_2}$ is the skin depth of medium 2

μ_2 , σ_2 = permeability and conductivity of medium 2

d = thickness of the panel

The electric shielding effectiveness S_E^o , defined by Eq. 5.2b can be written as

$$S_E^o = A + R_1 + R_2 \quad \text{dB} \tag{5.10}$$

where

$A = 8.68\ d/\delta$ dB is the attenuation loss due to the shield

$R_1 = 20 \log_{10}[|1 + Z_o/Z_i|^2/(4|Z_o/Z_i|)]$ dB is the reflection loss due to the initial reflections at both interfaces of the shield

and

$R_2 = 20 \log_{10} |1 - [(Z_o/Z_i - 1)^2/(Z_o/Z_i + 1)^2]\ e^{-2jkd}|$ dB is a correction term to account for all reflections not contained in R_1 .

The decomposition of the shielding effectivenss into the three components is useful in dealing with more complicated problems (Ref. 5.6). This

method is attributed to Schelkunoff (Ref. 5.7) who called it the "transmission theory of shielding".

It is observed that the attenuation loss A is inversely proportional to the skin depth and, hence, is proportional to the square root of frequency. The reflection loss R_1 becomes larger for lower frequencies. Thus, at low frequencies, usually the reflection loss R_1 is more important. The correction term R_2 is usually small compared with A, and for $A \geq 15$ dB, R_2 is neglected.

Equation 5.10 states that the attenuation loss A is proportional to $\sqrt{\mu\sigma}$. The higher permeability of a ferromagnetic material is often offset by the lower conductivity so that the attenuation loss is not substantially higher than a conductor at low frequencies. However, the reflection loss R_1 depends strongly on the ratio Z_i/Z_o --the closer the ratio to one, the smaller R_1 is. As $Z_i \propto \sqrt{\mu/\sigma}$, ferromagnetic materials have higher intrinsic impedance and, hence, usually lower reflection loss.

In Fig. 5.2 are presented the shielding effectiveness of a few panels of thickness 1.5 mm. The cases of good conductors (copper, aluminum and titanium) show increasing effectiveness for higher conductivity. However, steel (with $\mu_r = 110$, $\sigma = 0.11\ \sigma_{copper}$) has lower shielding effectiveness at low frequencies but exhibits better shielding properties at higher frequencies.

The ratio of the amplitudes of transmitted and <u>total</u> electric fields is given by (Ref. 5.5)

$$\eta_E^T = \frac{E_t}{E_e} = \frac{1}{\cosh(kd) + (Z_i/Z_o)\sinh(kd)} \tag{5.11}$$

where E_e is the total external tangential electric field (incident + reflected) in the unshielded space. Other quantities are defined in Eq. 5.9 .

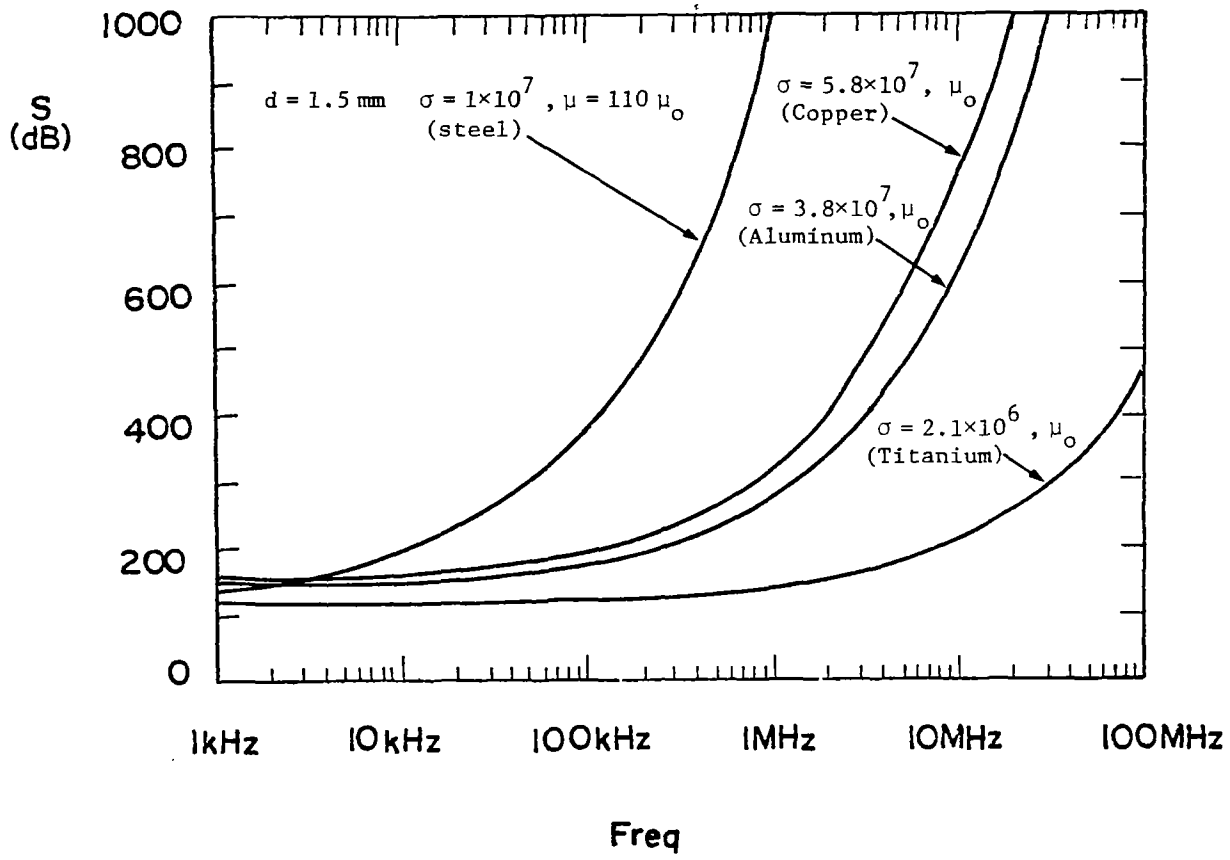

σ in mho/meter

Figure 5.2 Shielding factor of a plane panel of thickness 1.5 mm of various materials.

The expressions for magnetic fields are given in the following equations. The magnetic shielding factor η_M^o which involves the incident field with amplitude H_o, is

$$\eta_M^o = \frac{H_t}{H_o} = \eta_E^o \tag{5.12}$$

η_E^o is given in Eq. (5.19).

The ratio of amplitudes of transmitted and <u>total</u> magnetic fields is (Ref. 5.8)

$$\eta_M^T = \frac{H_t}{H_e} = \frac{1}{\cosh(kd) + (Z_o/Z_i)\sinh(kd)} \tag{5.13}$$

where H_e is the amplitude of the total external magnetic field (incident + reflected).

c. Shielding of a loop

For a circular loop carrying current near a conducting metal wall or chasis, as shown in Fig. 5.3, voltage will be induced in circuits on the other side of the wall. The loop may be wires in circular form, or objects conveniently represented by small magnetic dipoles. This configuration (Fig. 5.3) is also widely used to measure the magnetic shielding effectiveness and is known as the "flat-plate magnetic shielding effectiveness technique". In that case, the shielding effectiveness is defined as the ratio of the flux density (voltage) <u>without</u> the plate to that with the plate, as picked up by a second coaxial circular loop (Ref. 5.9). The results are presented in various ranges of parameter values due to different approximations in evaluating an integral (Ref. 5.6).

$$S_M = 8.686\ d/\delta + 20\ \log_{10}\left[\frac{r'}{8.485\ \mu_r \delta}\frac{r'}{D-d}\left(\frac{r'}{r}\right)^3\right] \quad \text{dB}$$

$$10\ \delta < r' < 10\ \lambda_o, \quad d > 2\ \delta \tag{5.14}$$

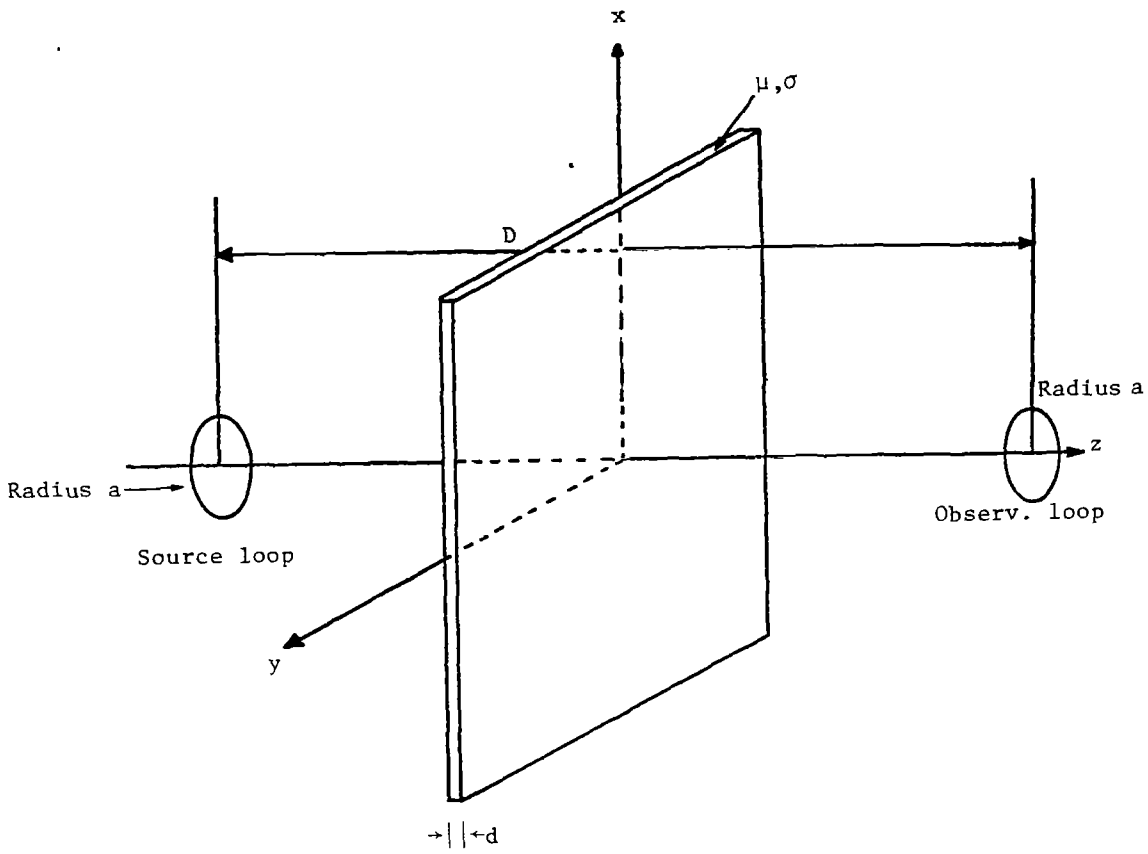

Figure 5.3 Shielding of a loop by a planar conductor

$$S_M = 8.686\ d/\delta + 20\ \log_{10}\left[\frac{\mu_r \delta\ r'(r' + D-d)}{5.657\ r^3}\right]\ dB$$

$$10\ \delta < r' < 10\lambda_o\ ,\quad d > 2\ \delta\ ,\quad r' < 0.1\ \mu_r\delta \qquad (5.15)$$

where

d = thickness of the conducting plate

D = distance between the two loops

$r = \sqrt{a^2 + D^2}$

a = radius of the source loop

$r' = \sqrt{a^2 + (D-d)^2}$

μ_r = relative permeability of the panel

δ = skin depth of the conductor

$= 1/\sqrt{\pi f \mu \sigma}$

μ , σ = permeability and conductivity of the metal

λ_o = wavelength in air.

For the special case that the loop separation is large compared with the conductor thickness d and the source loop radius a, then

$$S_M = 8.686\ d/\delta + 20\ \log_{10}\left[\frac{0.354\ \mu_r \delta}{D} + \frac{0.118\ D}{\mu_r \delta} + 0.408\right]\ dB$$

$$r' < 10\ \lambda_o\ ,\ d > 2\delta\ ,\quad D >> a\ ,\quad D >> d \qquad (5.16)$$

Note that the above expressions are in the form of Schelkunoff's transmission theory that the shielding effectiveness is the sum of an attenuation term and a combined reflection term.

For a thin plate, i.e., the condition $d > 2\delta$ (as required in Eqs. 5.14 to 5.15) is no longer required, the shielding effectiveness becomes (Ref. 5.10)

$$S_M = 10 \log_{10} \left\{ 1 + \left[\frac{1}{3} \left(\frac{d}{\delta} \right)^2 \left(\frac{D}{d} \right) \left(\frac{r}{D} \right)^2 \right]^2 \right\}$$

$$r > 10\,\delta \qquad (5.17)$$

In Fig. 5.4 are presented the results of shielding effectiveness of three metals with approximately 1/16" (1.59 mm) thickness: Copper, aluminum and steel. Clearly, the shielding effectiveness so defined is much less than that for the plane wave case. The calculated values agree with the measured ones to within 1 dB (Ref. 5.6, 5.10).

2. Panels of ferromagnetic materials

The magnetic shielding factor of a normally incident plane wave by a panel of ferromagnetic material is given by Eq. 5.12 provided the panel is assumed to have a constant permeability μ, given by

$$\mu = \mu_r \mu_o$$

where

μ_r = relative permeability

$\mu_o = 4\pi \times 10^{-7}$ H/m is the permeability of free space.

The case of constant μ occurs if the incident energy is not too large. The level of field energy necessary to drive the ferromagnetic shield into a nonlinear μ region or even into saturation depends on the material.

When the shield operates in the linear region, the shielding effectiveness depends strongly on the skin depth δ, which is defined in Eq. 5.6, i.e.,

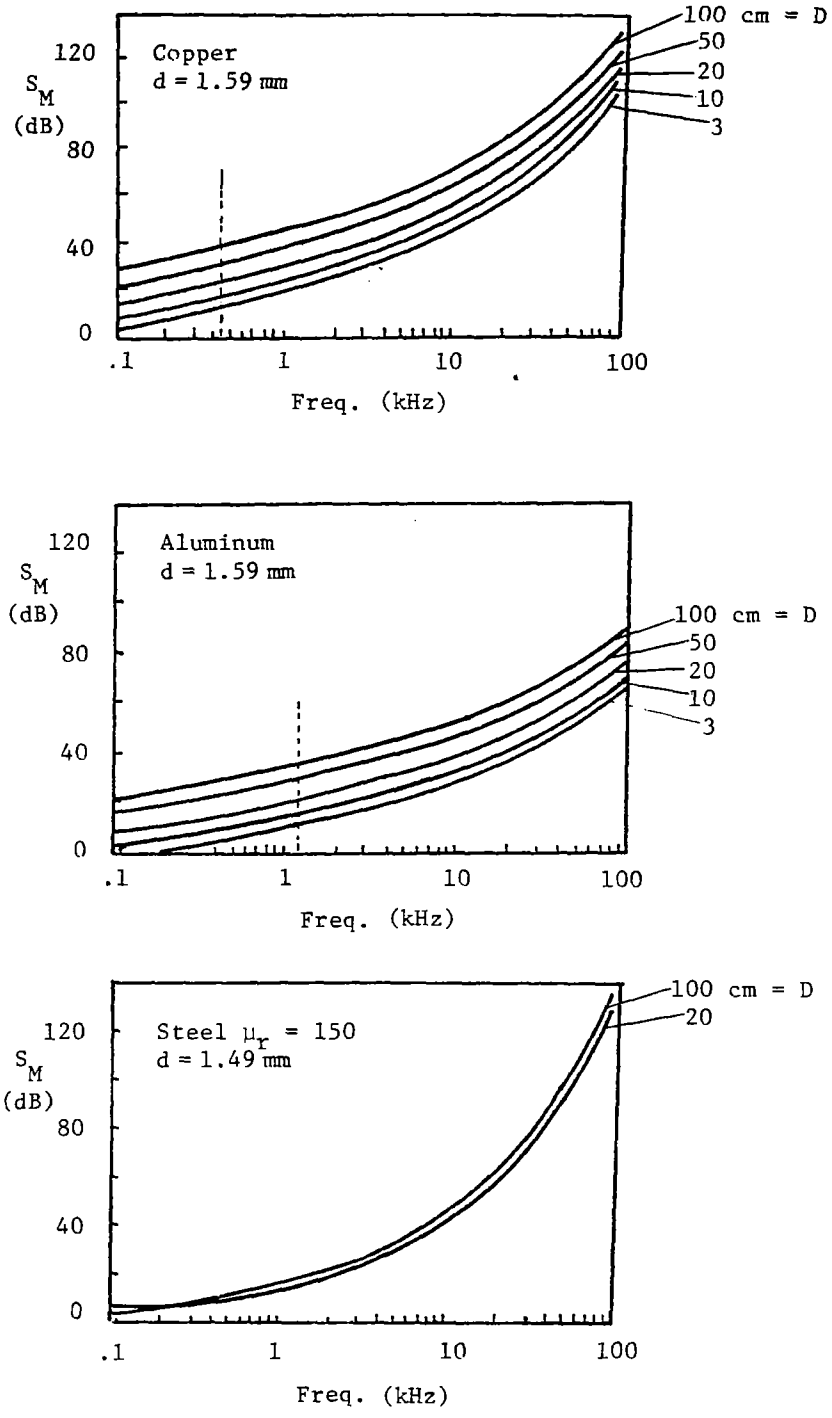

Figure 5.4 Shielding effectiveness of a loop by planar conductors (for configuration, see Fig. 5.3)

$$\delta \propto 1/\sqrt{\sigma\mu}$$

The depth of penetration is decreased by an increase in permeability, but this is usually offset by the poor conductivity of many high permeability materials. Figures 5.2 and 5.4 show that steel has poorer shielding effectiveness at low frequencies than copper or aluminum because of less reflection losses, but it is better at high frequencies due to higher attenuation loss.

For panels with saturable ferromagnetic materials, usually it is difficult to specify the B-H curve precisely. One technique of solving this nonlinear problem is to use numerical methods (finite-difference technique) to solve the nonlinear differential equations as derived from Maxwell's equations (Ref. 5.11).

The shielding effectiveness as measured of a few practical ferromagnetic materials is shown in Fig. 5.5 (Ref. 5.12).

3. Shielding by wire mesh

For a plane wire mesh made up of two planar arrays of perpendicular wires (see Fig. 5.6), the application of the so-called averaged boundary conditions (Ref. 5.13) yields the following equivalent sheet admittance Y_s for the square wire mesh at low frequencies such that the wire grid spacings are small compared with wavelengths

$$Y_s \simeq \frac{j\omega \mu_o d}{2\pi} [\ell n(d/a) - \ell n(2\pi)] \qquad (5.18)$$

where

d = grid spacing of a square mesh

a = wire radius

In the above equation, the junctions are assumed to be bonded.

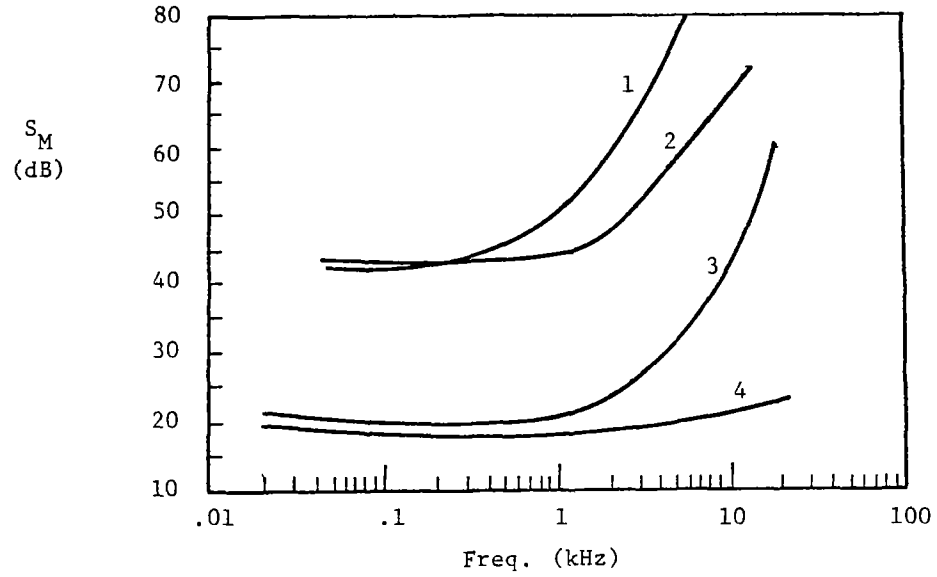

1. Hy-mu .031"×24"×24"
2. AMPE-65 .014"×6.25"×24"
3. Galvanealed Steel .028"×10.75"×10.75"
4. Mu-metal .014"×12"×24"

Figure 5.5 Measured shielding effectiveness of high permeability sheets

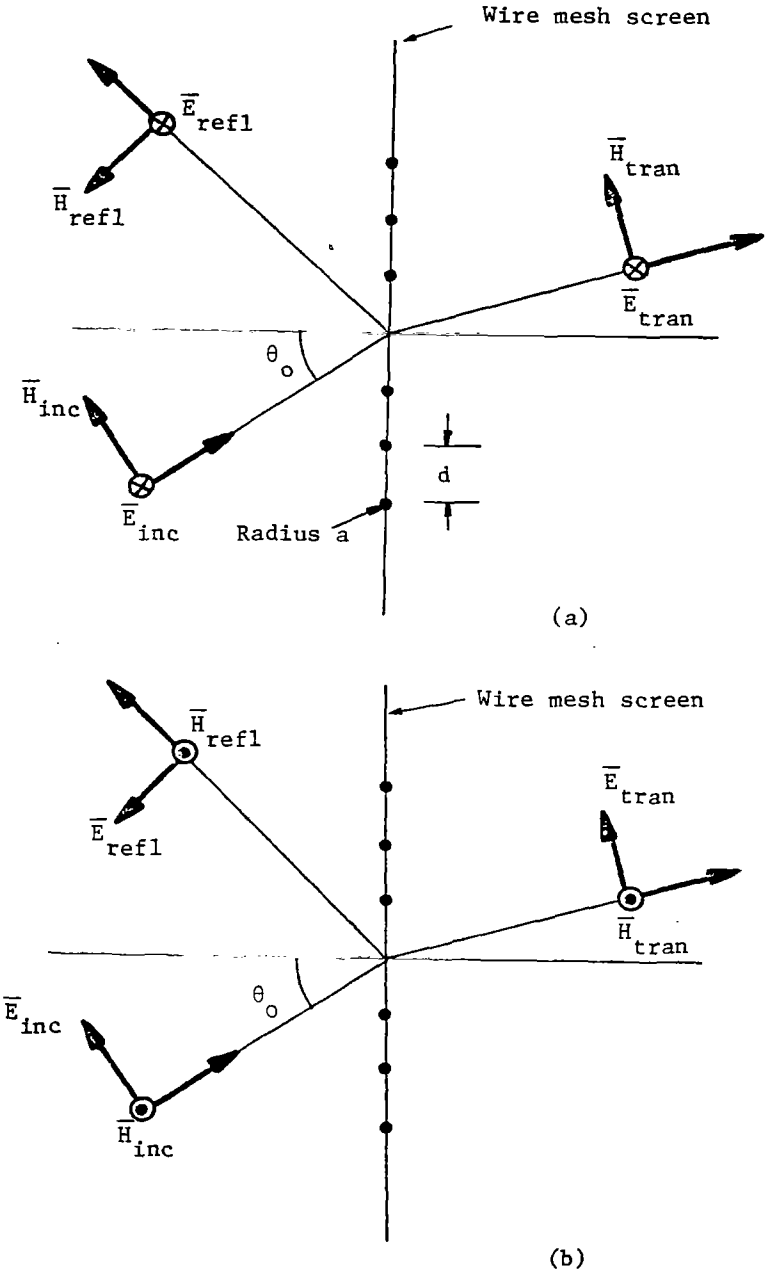

Fig. 5.6 Penetration through wire screen
(a) $\vec{E}$ normal to the plane of incidence
(b) $\vec{E}$ in the plane of incidence

a. Incident electric field normal to the plane of incidence (Ref. 5.14)

The electric shielding factors (referred to the incident fields) are given by

$$\eta_E^o = \frac{2\cos\theta_o}{2\cos\theta_o + Z_o Y_s} \tag{5.19}$$

and

$$\eta_M^o = -\cos\theta_o \, \eta_E^o$$

where

θ_o = angle of incidence

Z_o = intrinsic impedance of free space

b. Incident electric field in the plane of incidence

The shielding factors are

$$\eta_E^o = \eta_M^o = \frac{2\sec\theta_o}{2\sec\theta_o + Z_o Y_s} \tag{5.20}$$

The above equation assumes θ_o is not too close to 90°.

For the more general case of unbonded wire mesh and wire mesh with rectangular geometry, the articles listed in the Bibliography should be consulted.

4. Shielding by advanced composites

Panels of advanced composite materials have found increasing usage in aircraft design, etc. A panel is made up of several laminae (or thin sheets) bonded together, each of which consists of a one-dimensional array of fibers embedded in epoxy. The fibers are graphite (which is a fair conductor) in graphite composites, or boron in boron-epoxy composites. Also available are Kevlar 49 and sapphire fibers; however, these are not viable competitors for graphite and boron fibers (Ref. 5.15).

Due to the one-dimensional array configuration of fibers in each lamina, the electrical property is essentially anisotropic. By making practical assumptions it is possible to reduce the final shielding results to rather simple forms.

a. Graphite composites

Usually the fibers in alternate laiminae are oriented at different directions. In Fig. 5.7, the fibers are oriented at right angles, and the configuration is referred to as a 0° - 90° layup. The graphite itself is a fair conductor, but the fibers are insulated from each other by the epoxy. In the following, only the 0° - 90° layup configuration is considered.

(i) Incident electric field normal to the plane of incidence

In this case, the electric field is parallel to the laminae. The graphite laminate behaves as an isotropic conducting slab of effective conductivity σ_t. The shielding factors (referred to the incident fields) are

$$\eta_E^o = \frac{1}{\cosh(kd) + [Z_o\sigma_t/(2k)]\ \sec\theta_o \sinh(kd)} \tag{5.21a}$$

and

$$\eta_M^o = -\cos\theta_o\ \eta_E^o \tag{5.21b}$$

where

$$k = (1 + j)/\delta$$

$\delta = 1/\sqrt{\pi f \mu_o \sigma_t}$ is the effective skin depth of the graphite composite

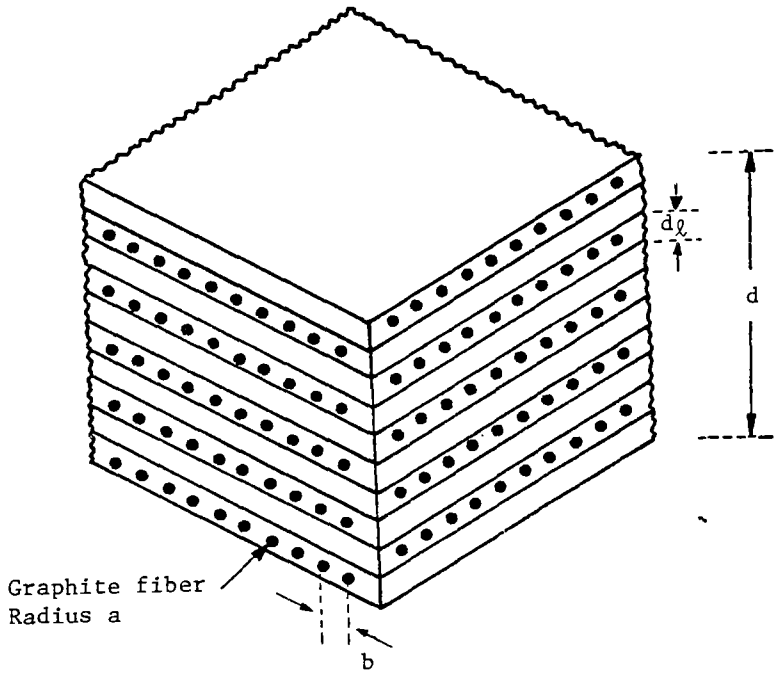

Figure 5.7 0°-90° layup graphite composite panel

$\sigma_t = \frac{1}{2} q \sigma_g$ is the effective conductivity of the graphite composite

σ_g = conductivity of the graphite fiber

q = ratio of the volume occupied by graphite fibers to the volume of the lamina

d = thickness of the whole panel

θ_o = angle of incidence

This is the generalized form (for arbitrary incidence) of Eq. (5.9), assuming the intrinsic impedance of the graphite composite is considerably less than the intrinsic impedance of free space Z_o.

(ii) Incident electric field parallel to the plane of incidence

In this case, the magnetic field is parallel to the laminae. For θ_o not too close to 90° (i.e., not the glazing incident case), the shielding factors are given by

$$\eta_E^o = \eta_M^o = \frac{1}{\cosh(kgd) + Z_o\sigma_t/(2kg)\ \cos\theta_o \sinh(kgd)} \tag{5.22}$$

where

$g = \sqrt{1 - \sin^2\theta_o \varepsilon_\ell/\varepsilon_o}$

$\varepsilon_\ell = \varepsilon_m \frac{1 + 2q(1 + \pi d_\ell/6b)}{1 + q\ \pi d_\ell/3b}$ is the effective permittivity normal to the panel

ε_m = permittivity of the surrounding medium (epoxy)

d_ℓ = thickness of one lamina

b = distance between two graphite fibers

Other symbols are defined in Eq. 5.21

b. Screened boron-epoxy composites

Since the boron-epoxy composites are poor conductors, a metal wire mesh screen is sometimes embedded in one surface of the laminate before it is cured in order to improve its shielding effectiveness. Such a screened laminate is shown in Fig. 5.8 with the screen in the very outside surface of the panel.

(i) Incident electric field normal to the plane of incidence

The shielding factors referred to the incident fields are

$$\eta_E^o = \frac{2\cos\theta_o}{2\cos\theta_o + Z_o Y'_{se}} \tag{5.23a}$$

and

$$\eta_M^o = -\cos\theta_o \, \eta_E^o \tag{5.23b}$$

where

$Z_o = 377\ \Omega$ is the intrinsic impedance of free space

θ_o = angle of incidence

$Y'_{se} = Y_s + j\omega d\,(\varepsilon_t - \varepsilon_o)$ is the equivalent sheet admittance of the screened laminate

ε_t = permittivity of the composites in the direction parallel to the panel surface

$Y_s = [j\omega\,\mu_o\, hL/(2\pi)]^{-1}$ is the sheet admittance of the wire-mesh screen

$L = -\ell n\,[1 - e^{-2\pi\, a/h}]$

h = distance between two adjacent wires

a = radius of the wires

d = thickness of the whole panel

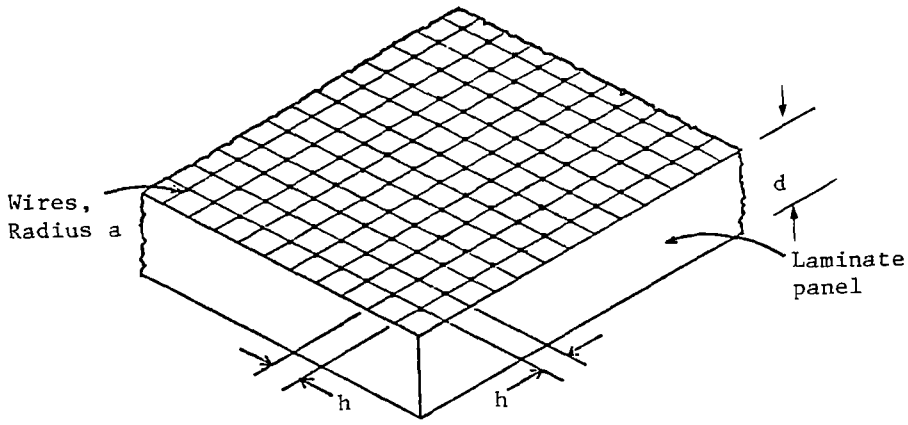

Figure 5.8 A screened laminate. The wire mesh is square and junctions are assumed to be bonded.

(ii) Incident electric field in the plane of incidence

For the incident angle not too near 90°, the shielding factors are

$$\eta_E^o = \eta_M^o = \frac{2 \sec\theta_o}{2 \sec\theta_o + Z_o Y''_{se}} \tag{5.24}$$

where

$$Y''_{se} = Y''_s + j\omega d (\varepsilon_t - \varepsilon_o)$$

$$Y''_s = Y_s \left[1 - \frac{\sin^2\theta_o}{1 + \sqrt{\varepsilon_\ell \varepsilon_t}/\varepsilon_o} \right]^{-1}$$

$$\varepsilon_\ell = \varepsilon_m \frac{1 + 2qp(1 + \pi d_\ell/6b)}{1 + qp\ \pi d_\ell/3b}$$

d_ℓ = thickness of one lamina

b = distance between two adjacent boron fibers

ε_m = permittivity of epoxy

$$p = \frac{\varepsilon_f - \varepsilon_m}{\varepsilon_f + \varepsilon_m}$$

ε_f = permittivity of boron

q = ratio of the volume occupied by boron fibers to volume of the lamina

Other symbols are given in Eq. 5.23 .

C. Cavities Enclosed by Panels

EMP penetrations into cavities enclosed by skin panels are considered in this section. These include cavities formed by two parallel panels, hollow cylinders and hollow spheres. Only the practical configurations of thin-walled structures are considered.

1. Parallel-plate cavities

For a cavity formed by two parallel plates of infinite extent and thickness d, separation $2b$, immersed in an incident field with symmetric magnetic fields which are oriented parallel to the plate surfaces (see Fig. 5.9), the magnetic shielding factor η_M^o (with respect to the incident field) at low frequencies ($\lambda_o >> b$) is (Ref. 5.16)

$$\eta_M^o = \frac{H_i}{H_o} = \frac{2}{\cosh(kd) + (\mu_o/\mu)\, kb \sinh(kd)} \tag{5.25}$$

where

H_o = amplitude of the incident magnetic field

H_i = amplitude of the magnetic field inside the cavity

d = thickness of each plate

$k = (1 + j)/\delta$

$\delta = 1/\sqrt{\pi f \mu \sigma}$ is the skin depth of the plate

μ = permeability of the plate

σ = conductivity of the plate

b = half distance between the inner surfaces of the parallel plates.

When referred to the <u>total</u> external magnetic field H_e at low frequencies, the magnetic shielding factor η_M^T is (Refs. 5.2, 5.16)

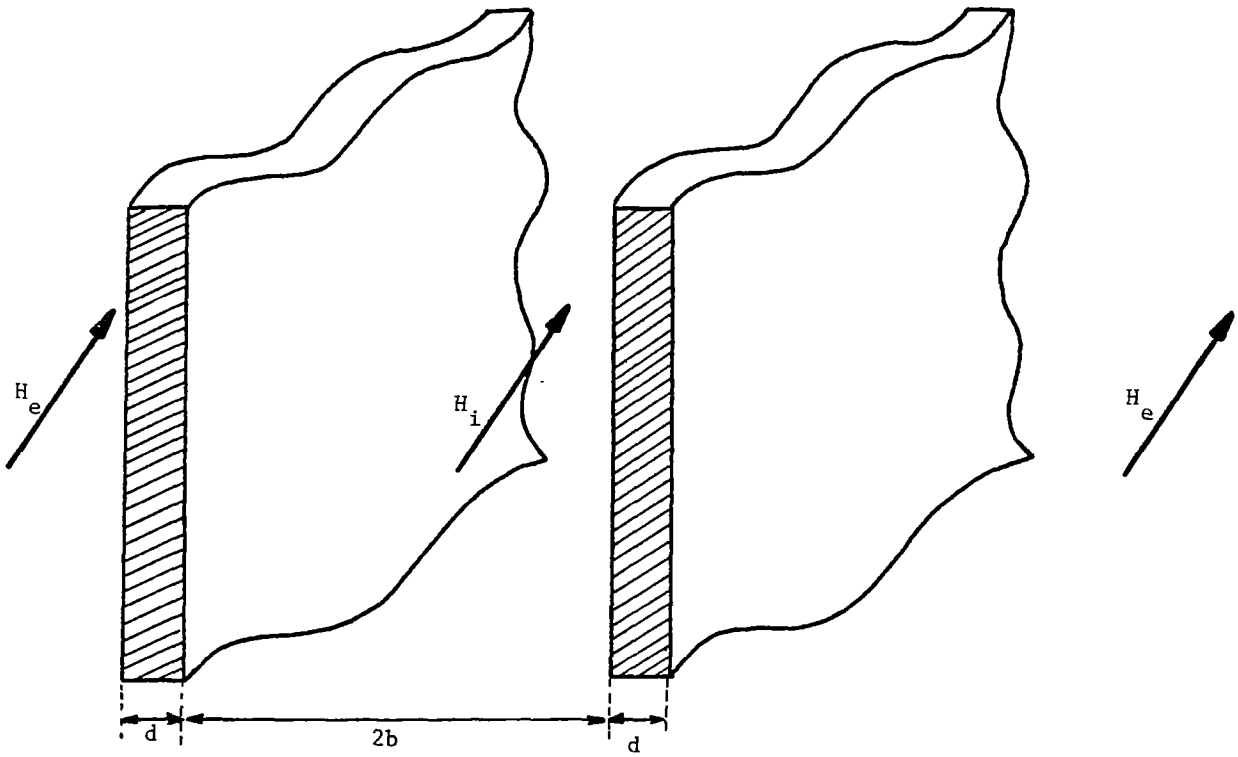

Figure 5.9. Cavity formed by two parallel plates.

$$\eta_M^T = \frac{H_i}{H_e} = \frac{1}{\cosh(kd) + (\mu_o/\mu)\ kb\ \sinh(kd)} \tag{5.26}$$

Expressing this ratio in dB, i.e., let

$$S_M^T = -20 \log_{10} |H_i/H_e| \quad \text{dB}$$

then, for a desired value of S_M^T (which measures the shielding effectiveness of the parallel-plate cavity with respect to the total external magnetic field), the thickness d of the plates is given by the following formulas in two different frequency ranges:

$$d = \begin{cases} \dfrac{\mu}{\mu_o} \dfrac{\delta^2}{2b} \left[10^{0.1\ S_M^T} - 1\right]^{1/2} & d < \delta \\ \dfrac{\delta}{8.686} \left[S_M^T - 20 \log_{10}\left(\dfrac{\mu_o\ b}{\sqrt{2}\ \mu\ \delta}\right)\right] & d > \delta \end{cases} \tag{5.27}$$

The first condition ($d < \delta$) corresponds to the region of low frequencies in which the current is distributed practically uniformly over the thickness of the plate. The second condition ($d > \delta$) corresponds to the region of high frequencies in which the current is distributed outward to the plate surfaces.

2. Thin-walled cylindrical cavities

Two cases are distinguished here (Refs. 5.2, 5.17). One is when the disturbing magnetic field is oriented parallel to the cylinder axis (Fig. 5.10a) and the other when the magnetic field is perpendicular to the cylinder axis (Fig. 5.10b). For both cases, the cylinder shell thickness d is assumed to be thin, i.e., $d \ll a$ where a is the inner radius of the cylinder.

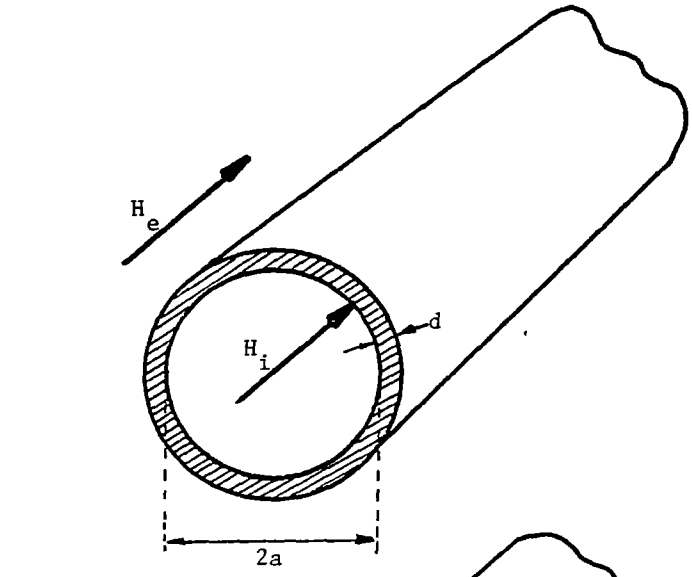

(a)

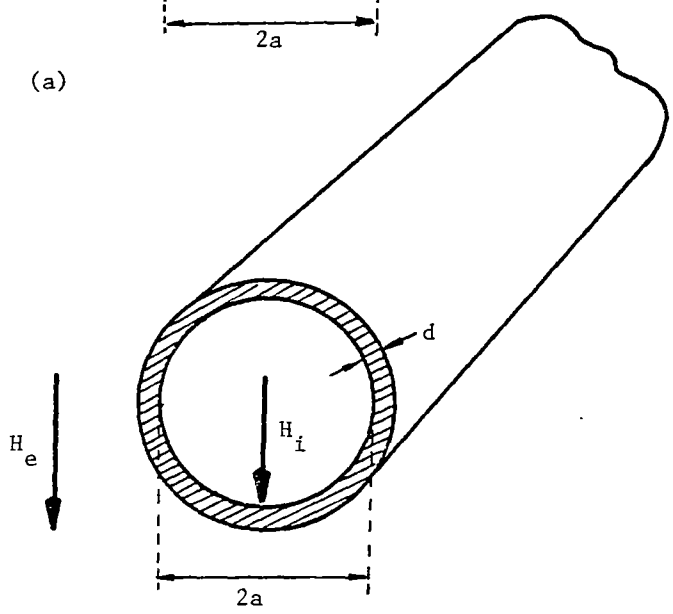

(b)

Figure 5.10 Hollow cylinder with
(a) Longitudinal excitation field
(b) Transverse excitation field

a. Longitudinal magnetic field

For an external magnetic field with <u>total</u> strength H_e parallel to the cylinder axis (see Fig. 5.10a) the internal magnetic field is also parallel to the cylinder axis. For low frequencies so that $\lambda_o >> a >> d$, the magnetic shielding factor η_M^T (with respect to the total external magnetic field) is

$$\eta_M^T = \frac{H_i}{H_e} \approx \frac{1}{\cosh(kd) + (\kappa/2)\sinh(kd)} \tag{5.28}$$

where

d = wall thickness

$k = (1 + j)/\delta$

$\delta = 1/\sqrt{\pi f \mu \sigma}$ is the skin depth of the shell material

μ = permeability of the shell material

σ = conductivity of the shell material

$\kappa = (\mu_o/\mu)\, ka$

a = inner radius of the cylinder

b. Transverse magnetic field

For an external <u>incident</u> magnetic field H_o perpendicular to the cylinder axis, as in Fig. 5.10b, the magnetic shielding factor for the low frequency case $(\lambda_o >> a >> d)$ is

$$\eta_M^o = \frac{H_i}{H_o} \approx \frac{1}{\cosh(kd) + \frac{1}{2}(\kappa + 1/\kappa)\sinh(kd)} \tag{5.29}$$

where all symbols have been defined in Eq. 5.28 . The reactive factor W, which is useful for multilayer shielding problems, is given by

$$W = \frac{\frac{1}{2}\,(\kappa - 1/\kappa)\,\sinh(kd)}{\cosh(kd) + \frac{1}{2}\,(\kappa + 1/\kappa)\,\sinh(kd)} \tag{5.30}$$

Note that the external reactive factor (for external interference field) and the internal reactive factor (for internal interference field) are the same and they are given by Eq. 5.30 .

3. Thin-walled spherical cavities

Although shielding envelopes are in practice only rarely designed as hollow spheres, the latter are of importance to assess the shielding effects of objects which have approximately the same dimensions for all three coordinates (Ref. 5.2).

For a thin-walled sphere (see Fig. 5.11), the inner radius a is much larger than the wall thickness d. In the case of an incident external magnetic field with strength H_o, the internal magnetic field H_i is also parallel to the external field, and

$$\eta_M^o = \frac{H_i}{H_o} = \frac{1}{\cosh(kd) + \frac{1}{3}\,(\kappa + 2/\kappa)\,\sinh(kd)} \tag{5.31}$$

where

d = thickness of the shell

$k = (1 + j)/\delta$

$\delta = 1/\sqrt{\pi f \mu \sigma}$ is the skin depth of the shell material

μ = permeability of the shell material

σ = conductivity of the shell material

$\kappa = (\mu_o/\mu)\ k\ a$

a = inner radius of the sphere

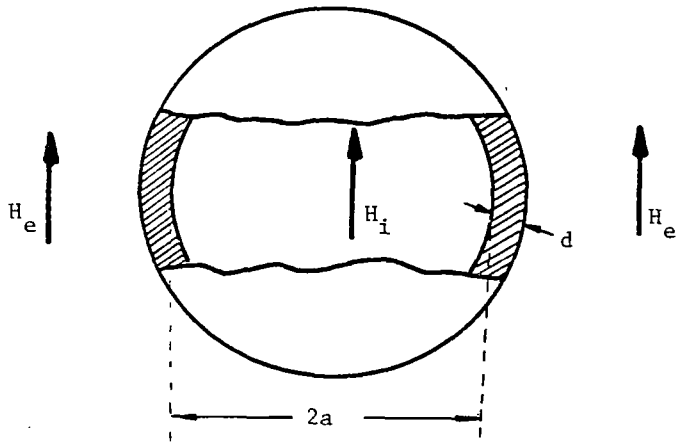

Figure 5.11 Hollow sphere

The above equation is valid at low frequencies such that $\lambda_o >> a >> d$. The reactive factors, which are useful for multilayer shielding problems are given in the following:

The external reactive factor (for external interference field) is

$$W_e = \frac{\frac{1}{3}(\kappa/2 - 2/\kappa)\sinh(kd)}{\cosh(kd) + \frac{1}{3}(\kappa + 2/\kappa)\sinh(kd)} \tag{5.32a}$$

The internal reactive factor (for internal interference field) is

$$W_i = \frac{\frac{2}{3}(\kappa - 1/\kappa)\sinh(kd)}{\cosh(kd) + \frac{1}{3}(\kappa + 2/\kappa)\sinh(kd)} \tag{5.32b}$$

4. *Cavities with laminated shields*

The overall shielding factor η of a laminated (or multilayer) shield is given by (Ref. 5.2)

$$\eta = \frac{\eta_1 \eta_2}{1 - W_{i2} W_{e1}} \tag{5.33}$$

where η_1, η_2 = shielding factors of layers 1 and 2 (referred to the incident field), layer 3 is the outside layer.

W_{e1}, W_{e2} = external reactive factors of layers 1 and 2

W_{i1}, W_{i2} = internal reactive factors of layers 1 and 2

The resulting external reactive factor due to a field incident on layer 2 is

$$W_e = W_{e2} + W_{e1} \frac{\eta_2^2}{1 - W_{i2} W_{e1}} \qquad (5.34)$$

The above two equations are not valid for very low frequencies when $|\eta_1|$ and $|\eta_2|$ are not small compared with 1.

For more than two layers, one evaluates the resultant η and W_e of the first two layers at a time, and reapplies Eqs. 5.33 and 5.34 using these new values and those of the third layer. The process is repeated until the overall η is obtained.

a. Multilayer cylindrical shield

Consider a double layer shield with the inner layer (layer 1) being of high conductivity metal, and the outer layer (layer 2) of ferromagnetic material. For frequencies not too low, $W_1 \simeq 1$, $W_2 \simeq -1$, and with transverse magnetic field

$$\eta \simeq \frac{1}{2} \eta_c \eta_s = \frac{2 \kappa_s}{\kappa_c \sinh(k_c d_c) \sinh(k_s d_s)}$$

where the subscripts c and s denote quantities in layers 1 (conductive) and 2 (ferromagnetic), respectively. The quantity κ is defined in Eq. 5.28. The overall shielding effectiveness is

$$S_M = -20 \log_{10} |\eta|$$

$$= -20 \log_{10} (\pi f \mu_s \sigma_c d_c d_s) \quad \text{dB} \qquad (5.35)$$

$$\text{for } d_c < \delta_c, \quad d_s < \delta_s$$

For constant total wall thickness d ($d = d_c + d_s$), maximum shielding effectiveness is when $d_c = d_s = d/2$. It is noteworthy that the shielding effectiveness is independent of the shield radius.

b. Multilayer spherical shield

For a double-layer spherical shield, there are two different cases: ferromagnetic layer on the outside and ferromagnetic layer on the inside. The reactive factors for the two cases are different. They are given by Eqs. 5.32a and 5.32b.

(i) Ferromagnetic layer on the outside

In the outer layer (layer 2), $\mu >> \mu_o$. Here $W_{e1} = 0.5$ and $W_{i2} = -1$, and

$$\eta \simeq \frac{2}{3}\eta_c \eta_s = \frac{\kappa_s}{\kappa_c \sinh(k_c d_c)\sinh(k_s d_s)}$$

and the shielding effectiveness is

$$S_M = -20 \log_{10} [(2/3) f\pi \mu_s \sigma_c d_c d_s] \quad \text{dB} \qquad (5.36)$$

(ii) Ferromagnetic layer on the inside

In the inner layer (layer 1), $\mu >> \mu_o$. Here $W_{e1} = -1$ and $W_{i2} = 2$, and

$$\eta = \frac{1}{3}\eta_s \eta_c = \frac{3}{2}\frac{\kappa_s}{\kappa_c \sinh(k_s d_s)\sinh(k_c d_c)}$$

and

$$S_M = -20 \log_{10} [(4/3) \pi f \mu_s \sigma_c d_c d_s] \quad \text{dB} \qquad (5.37)$$

Comparing Eqs. 5.35, 5.36 and 5.37, the shielding effectiveness of a double layer cylinder is greater than that of the sphere with the ferromagnetic layer on the outside by 8.1 dB, but less than that of the sphere with the ferromagnetic layer in the inside by 5.8 dB. It is advisable to arrange the conductive layer on the outside since it offers higher reflection loss.

D. Skin-Panel Joints and Seams

The boundary between two skin panels forms a slit (seam, or slot) that enables coupling of electromagnetic fields into the otherwise enclosed region. Often the skin panels are riveted together to form a stringer joint or a lap joint. Sometimes conductive gaskets are installed around the slits or joints to reduce electromagnetic field penetration.

Only a limited amount of useful formulas are available for these types of problems. An infinitely long slot between two conductive planes is one that has a useful engineering formula for frequencies such that the slot width is small compared with the wavelength (Ref. 5.2). Some preliminary work (Ref. 5.18) has been done on the subject of penetration through skin panel joints. Very little analytical work has been performed on the shielding by gaskets.

Seams between two conducting planes

The seam or slot is considered to be long (i.e., the length is much larger than the width b). The surrounding panels are considered to be plane and with conductivity σ and thickness d. The configuration is illustrated in a two-dimensional drawing in Fig. 5.12. At low frequencies ($\lambda_o >> b$, $\lambda_o >> d$), for a disturbing magnetic field with strength H_o parallel to the surface and perpendicular to the slot (see Fig. 5.12), the magnetic shielding factor η_M^o (with respect to the incident magnetic field H_o) is given by (Ref. 5.2)

$$\eta_M^o = \frac{H_i}{H_o} = \frac{pg^2}{r^2}\left[1 + \frac{2}{kb}\psi\left(\frac{d}{b}\right)\right] \tag{5.38}$$

where

r = distance from the center of the bottom of the slot (see Fig. 5.12)

b = slot width

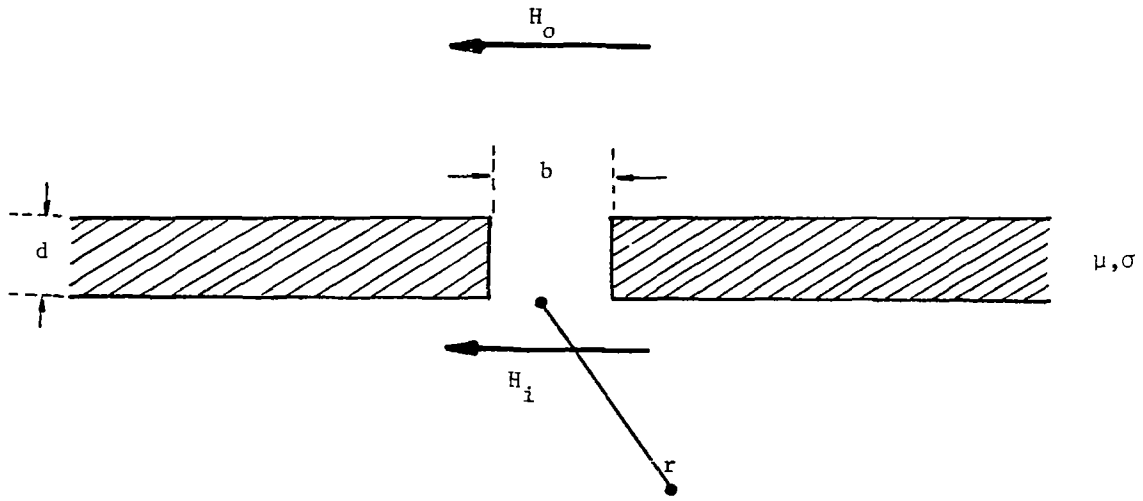

Figure 5.12 Two-dimensional illustration of a slot formed by two joining panels

d = panel thickness

$k = (1 + j)/\delta$ is the propagation constant in the panel

$\delta = 1/\sqrt{\pi f \mu \sigma}$ is the skin depth of the panel

μ = permeability of the panel

σ = conductivity of the panel

p and g are two parameters given in graphical form in Fig. 5.13a

$\psi(d/b)$ is given in Fig. 5.13b

For certain ranges of d/b values, the following approximations for pg^2 and ψ are valid

$$pg^2 = \begin{cases} (b/4)^2 & \text{for } d = 0 \\ (2b/\pi)^2 \exp(-\pi d/b - 2) & \text{for } d \geq 0.4\ b \end{cases} \tag{5.39}$$

and

$$(d/b) \simeq 2 + \pi + d/b \qquad \text{for } d \geq 0.5\ b \tag{5.40}$$

From Eq. 5.38 it is noted that the penetrating magnetic field is composed of two parts: one due to the penetration through the gap (the first term), and the other due to diffusion through the panels (the second term). Indeed, for perfectly conducting panels ($\sigma \to \infty$), the second term in Eq. 5.38 , corresponding to the diffusion process, vanishes. Equation 5.38 also indicates that the penetrating magnetic field is proportional directly to the square of the slot width, and inversely to the square of the distance from the gap.

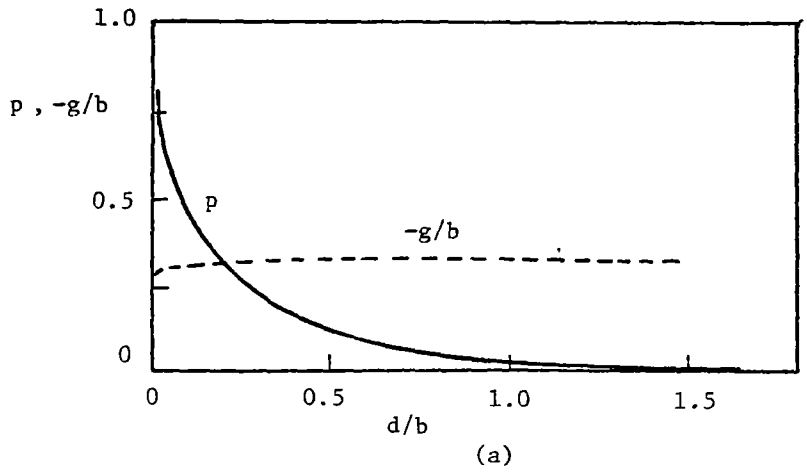

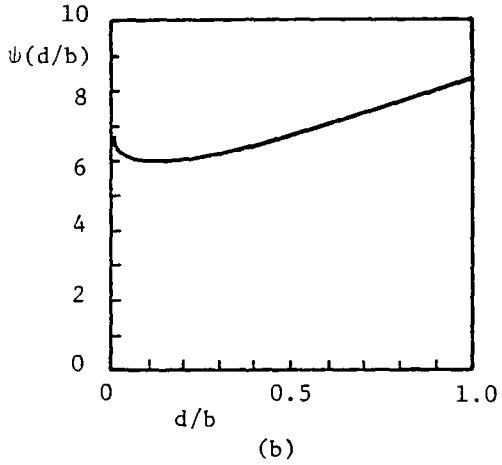

Figure 5.13 Parameters p,g and ψ versus d/b for slot case

References

5.1 IEEE Standard Dictionary of Electrical and Electronics Terms, Wiley-Interscience, 1972.

5.2 H. Kaden, Wirbelströme and Schirmung in der Nachrichtentechnik, (Eddy Currents and Shielding in Telecommunications Technology), Springer-Verlag, 1957.

5.3 S. Ramo, J.R. Whinnery and T. Van Duzer, Fields and Waves in Communication Electronics, John Wiley and Sons, Ch. 7, 1965.

5.4 J.A. Stratton, Electromagnetic Theory, McGraw-Hill, pp. 490-511, 1941.

5.5 C.W. Harrison, Jr., "Transient electromagnetic field propagation through infinite sheets, into spherical shells, and into hollow cylinders," AFWL Interaction Note 32, May 1964.

5.6 P.R. Bannister, "New theoretical expressions for predicting shielding effectiveness for the plane shield case," IEEE Trans. on Electromagnetic Compatibility, Vol. EMC-10, pp. 2-7, March 1968.

5.7 S.A. Schelkunoff, Electromagnetic Waves, Van Nostrand Co., Chs. 7, 8, 1943.

5.8 G. Bedrosian and K.S.H. Lee, "EMP penetration through metal skin panels and into aircraft cavities," Interaction Note 314, August 1976.

5.9 J.R. Moser, "Low-frequency shielding of a circular loop electromagnetic field source," IEEE Trans. Electromagnetic Compatibility. Vol. EMC-9, pp. 6-18, March 1967.

5.10 P.R. Bannister, "Further notes for predicting shielding effectiveness for the plane shield case," IEEE Trans. on Electromagnetic Compatibility, Vol. EMC-11, pp. 50-53, May 1969.

5.11 D.E. Merewether, "Electromagnetic pulse transmission through a thin sheet of saturable ferromagnetic material of infinite surface area," IEEE Trans. on Electromagnetic Compatibility, Vol. EMC-11, pp. 139-143, November 1969, Interaction Note 38, November 1969.

5.12 R.B. Schulz, "ELF and VLF shielding effectiveness of high-permeability materials," IEEE Trans. on Electromagnetic Compatibility, Vol. EMC-10, pp. 95-100, March 1968.

5.13 M.I. Kontorovich, V. Yu. Petrun'kin, N.A. Yesepkina and M.I. Astrakhan, "The coefficient of reflection of a plane electromagnetc wave from a plane wire mesh," Radio Eng. Elect. Phys., Vol. 7, pp. 222-231, February 1972.

5.14 K.F. Casey, "EMP penetration through advanced composite skin panels," Interaction Note 315, December 1976.

5.15 C.L. Blake, "Composites - their electrical and electromagnetic impact," IEEE 1976 International Symposium on Electromagnetic Compatibility Record.

5.16 C.W. Harrison, Jr., M.L. Houston, R.W.P. King and T.T. Wu, "The propagation of transient electromagnetic fields into a cavity formed by two imperfectly conducting sheets," AFWL Interaction Note 31, April 1964.

5.17 L.V. King, "Electromagnetic shielding at radio frequencies," Phil. Mag. J. Sci., Vol. 15, pp. 201-223, February 1933.

5.18 J. Lam, "Analysis of EMP penetration through skin panel joints," AFWL AIP Memo 3, August 1976.

Bibliography

The formulas presented in this chapter are mostly for skin panels with thin walls at low frequencies. Formulas for more general cases are available, but usually their solutions involve the use of complicated mathematical procedures or computers, or the results may not be directly applicable to the EMP problems. A list of bibliography is given here for these papers and reports.

Planar panels of conducting materials

R.B. Schulz, V.C. Plantz and D.R. Brush, "Shielding theory and practice," Proc. 9th Tri-Service Conf. on Electromagnetic Compatibility, Chicago, Ill., 1963.

J.R. Wait, "Shielding of a transient electromagnetic dipole field by a conductive sheet," Can. J. Phys., Vol. 34, pp. 890-893, July-August 1956.

N.R. Zitron, "Shielding of transient electromagnetic signals by a thin conducting sheet," J. Res. NBS-D. Radio Propagation, Vol. 64D, pp. 563-567, September-October 1960.

Planar panels of ferromagnetic materials

F.J. Young and W.J. English, "Flux distribution in a linear magnetic shield," IEEE Trans. on Electromagnetic Compatibility, Vol. EMC-12, pp. 118-133, August 1970.

Shielding by wire mesh

M.I. Astrakhan, "Averaged boundary conditions on the surface of a lattice with rectangular cells," Radio Eng. Elect. Phys., Vol. 9, pp. 1239-1241, 1964.

D.A. Hill and J.R. Wait, "Electromagnetic scattering of an arbitrary plane wave by two nonintersecting perpendicular wire grids," Can. J. Phys., Vol. 52, pp. 227-237, 1974.

D.A. Hill and J.R. Wait, "Electromagnetic scattering of an arbitrary plane wave by a wire mesh with bonded junctions," Can. J. Phys., Vol. 54, pp. 353-361, February 1976, and also Section II of Sensor and Simulation Note 231, 10 June 1977.

M.I. Kontorovich, "Averaged boundary conditions at the surface of a grating with square mesh," Radio Eng. Elect. Phys., Vol. 8, pp. 1446-1454, 1963.

S.W. Lee, "Scattering by dielectric-loaded screen," IEEE Trans. on Antenna Propagat., Vol. AP-19, pp. 656-665, September 1971.

H. Val McAdams, Jr., "Electromagnetic field penetration of wire screens," AFWL Interaction Note 46, January 1970.

Shielding by advanced composites

J.T. Kung and M.P. Amason, "Lightning protection design concepts for advanced composite structures," IEEE 1976 International Symposium on Electromagnetic Compatibility Record.

C.D. Skouby, "Effects of advanced composites on shielding and antenna performance," IEEE 1976 International Symposium on Electromagnetic Compatibility Record.

D. Strawe and L. Piszker, "Interaction of advanced composites with electromagnetic pulse (EMP) environments," Air Force Materials Laboratory, Technical Report AFML-TR-75-141, September 1975.

Cylindrical shells

R.H. Duncan and C.W. Harrison, Jr., "Radio-frequency leakage into missiles," AFWL Interaction Note 14, April 1963.

D. Schieber, "Shielding performance of metallic cylinders," IEEE Trans. on Electromagnetic Compatibility, Vol. EMC-15, pp. 12-16, February 1973. Also comments by C.W. Harrison, Jr., IEEE Trans. on Electromagnetic Compatibility, Vol. EMC-15, p. 150, August 1973.

S. Shenfeld, "Shielding of cylindrical tubes," IEEE Trans. on Electromagnetic Compatibility, Vol. EMC-10, pp. 29-34, March 1968.

D.A. Still, "Interaction of magnetic fields and ferromagnetic shields," IEEE Trans. on Electromagnetic Compatibility, Vol. EMC-13, pp. 45-50, May 1971.

T.K. Wu and L.L. Tsai, "Shielding properties of thick conducting cylindrical shells," IEEE Trans. on Electromagnetic Compatibility, Vol. EMC-16, pp. 201-204, November 1974.

T.K. Wu and L.L. Tsai, "Shielding properties of thick conducting cylindrical shells with an obliquely incident plane wave," IEEE Trans. on Electromagnetic Compatibility, Vol. EMC-17, pp. 189-191, August 1975.

T.K. Wu and L.L. Tsai, "Time domain shielding properties of conducting cylindrical shells," IEEE Trans. on Electromagnetic Compatibility, Vol. EMC-17, pp. 191-193, August 1975.

Spherical shells

D.G. Dudley and J.P. Quintenz, "Transient electromagnetic penetration of a spherical shell," J. Appl. Phys., Vol. 46, pp. 173-177, January 1975.

C.W. Harrison, Jr. and C.H. Papas, "On the attenuation of transient fields by imperfectly conducting spherical shells," AFWL Interaction Note 34, July 1964.

General Cavities

W.W. Cooley, "Low-frequency shielding effectiveness of nonuniform enclosures," IEEE Trans. on Electromagnetic Compatibility, Vol. EMC-10, pp. 34-43, March 1968.

W. Jarva, "Shielding tests for cables and small enclosures in the 1- to 10-GHz range," IEEE Trans. on Electromagnetic Compatibility, Vol. EMC-12, pp. 12-24, February 1970.

D.A. Miller and J.E. Bridges, "Geometrical effects on shielding effectiveness at low frequencies," IEEE Trans. on Electromagnetic Compatibility, Vol. EMC-8, pp. 174-186, December 1966.

Seams

W.E. Ackerknecht, III and C.L. Chen, "The scattering of electromagnetic pulse by a slit in a conducting screen," IEEE Trans. on Antennas Propagat., Vol. AP-23, pp. 368-376, May 1975.

R.A. Hurd and B.K. Sachdeva, "Scattering by a dielectric-loaded slit in a conducting plane," Radio Sci., Vol. 10, pp. 565-572, May 1975.

Gaskets

"EMI/RFI gasket design manual," Chomerics, Inc., Woburn, Mass, 1975.

J.E. Ehrreich and M. Nimoy, "R.F. Shielding performance on reinforced metal filled conductive plastic flat gaskets," IEEE Trans. on Electromagnetic Compatibility, Vol. 7, pp. 50-54, March 1965.

SUBJECT INDEX